Technische Universität München
Lehrstuhl für Leichtbau

Shape Memory Polymers in Fiber Composite Structures for Shape Adjustment

Stephan Rapp

Vollständiger Abdruck der von der Fakultät für Maschinenwesen der Technischen Universität München zur Erlangung des akademischen Grades eines

Doktor-Ingenieurs (Dr.-Ing.)

genehmigten Dissertation.

Vorsitzender: Univ.-Prof. Dr. rer. nat. Ulrich Walter

Prüfer der Dissertation:

1. Univ.-Prof. Dr.-Ing. Horst Baier
2. Univ.-Prof. Dr.med., Dr.-Ing. habil. Erich Wintermantel

Die Dissertation wurde am 14.02.2011 bei der Technische Universität München eingereicht und durch die Fakultät für Maschinenwesen am 30.06.2011 angenommen.

Abstract

The manufacturing of fiber composite parts leads to residual curing stresses resulting in warpage and spring-in effects. Even with cure cycle optimization, iterative mould adjustment and the use of advanced tooling, small distortions remain, which might affect the performance of high precision composite parts. In order to compensate these distortions a post manufacturing shape adjustment process using shape memory polymer actuator patches can be applied. To determine necessary actuation properties an experimental method is developed. Methods for the 3D shape sensing are introduced. Finite element models are used for the investigation of the structure-actuator interface for these soft actuator materials. An optimization process for the determination of optimal actuator configurations for the shape error minimization is developed. For several types of composite parts simulation results are verified with experiments in which significant shape error reductions are achieved.

Kurzfassung

Faserverstärkte Verbundbauteile weisen nach der Fertigung aufgrund von Eigenspannungen Verzüge auf. Mit optimierten Aushärtezyklen, iterativer Anpassung der Formwerkzeuge und der Verwendung von formstabilen Werkzeugen, wird versucht diese Verzüge zu minimieren. Trotzdem können kleinste Verzüge, die die Funktionalität hochpräziser Verbundbauteile einschränken können, nicht verhindert werden. Eine weitere Möglichkeit ist die Verzügereduktion nach der Fertigung mit Hilfe von Formgedächtnispolymer Aktor-Patches. Für die Bestimmung der dafür erforderlichen Aktoreigenschaften wird eine experimentelle Methode entwickelt. Verfahren zur 3D Oberflächenvermessung werden vorgestellt. Mit Hilfe von Finite Elemente Modellen wird die mechanische Schnittstelle zwischen Aktor und Struktur für diese weichen Aktorwerkstoffe untersucht. Ein Optimierungsprozess zur Bestimmung optimaler Aktorkonfigurationen zur Formfehlerminimierung wird entwickelt. Die Simulationsergebnisse werden für verschiedene Verbundbauteile mit Experimenten verifiziert. Dabei werden deutliche Verzügereduktionen erreicht.

Acknowledgement

This thesis was written during my employment as a research assistant at the Institute of Lightweight Structures.
I thank Prof. Dr.-Ing. Horst Baier for his support regarding my work and also sportive and social activities. I thank my colleagues not only for their help and collegiality but also for their friendship. Further acknowledgement goes to my students for their contributions and the helpful discussions. Additionally I would like to thank Mr. Alexander Höhn and his wife for their help.
I thank my parents for their support and giving me the opportunity to study aerospace engineering at TUM. Special thanks go to my girlfriend Verena.

Contents

List of Figures

List of Tables

Nomenclature

Acronyms

1D	1 dimensional
2D	2 dimensional
3D	3 dimensional
AFC	active fiber composite
CFRP	carbon fiber reinforced plastic
CTE	coefficient of thermal expansion
DE	differential equation
EAP	electro active polymer
FBG	fiber Bragg grating
FE	finite element
FEM	finite element method
GA	genetic algorithm
LISA	Lightweight Inter-Satellite Link Antenna
LLB	Institute of Lightweight Structures
RMS	root mean square
RT	room temperature
SLV	standardized linear visco-elastic
SMA	shape memory alloy

SMC . . . . . shape memory composite

SME . . . . . shape memory effect

SMM . . . . . shape memory material

SMP . . . . . shape memory polymer

UAV . . . . . unmanned aerial vehicle

UD . . . . . unidirectional

UMAT . . . . . user material subroutine

Symbols

A . . . . . actual cross-sectional area

A_0 . . . . . initial cross-sectional area

α_T . . . . . coefficient of thermal expansion

C_M . . . . . shape memory coefficient

E_{eff} . . . . . stimulation parameter

ε_r . . . . . recovery strain

ε_{r_0} . . . . . recovery strain related to permanent shape

ε_{prog} . . . . . programming strain related to permanent shape

ε_{res} . . . . . residual strain related to programmed shape

ε_{free} . . . . . free recovery strain

$\dot{\varepsilon_r}$ . . . . . recovery strain rate

ε_T . . . . . thermal strain

ε_u . . . . . remaining strain after unloading

F_r . . . . . recovery force

ζ . . . . . fixation ratio

L_0 . . . . . initial actuator length

L_{prog} . . . . . actuator length after programming

L_{res} . . . . . actuator length after recovery (residual length)

ρ . . . . . material density

η . . . . . recovery ratio

σ_{act} . . . . . actuation stress

σ_{block} . . . . . blocking stress

σ_{prog} . . . . . stress after straining (hot state)

σ_r . . . . . actual recovery stress

σ_{r_0} . . . . . recovery stress related to initial cross-section

Ψ . . . . . stiffness ratio

t_a . . . . . actuator thickness

T . . . . . temperature

T_r . . . . . recovery temperature

T . . . . . thickness ratio
t_r . . . . . recovery time
t_s . . . . . storage time
T_{prog} . . . . . programming temperature
t_s . . . . . thickness of structure
T_{trans} . . . . . transition temperature
W_r . . . . . recovery energy density
w_r . . . . . specific recovery energy density
W_{r_0} . . . . . technical recovery energy density
w_{r_0} . . . . . technical specific recovery energy density
$\hat{w}$ . . . . . actual out-of-plane coordinate
$\overline{w}$ . . . . . desired out-of-plane coordinate

1. Introduction

1.1. Motivation

Fiber composites are receiving more and more interest. Due to their outstanding mechanical properties in terms of stiffness, strength and thermo-elastic stability, they are an attractive alternative to metals. Especially for space applications very high stiffness to mass ratios, low coefficients of thermal expansion (CTEs) and high shape precision are of interest. However, due to curing stresses, resulting in warpage and spring-in effects, carbon fiber reinforced plastic (CFRP) parts show distortions after manufacturing. Small distortions remain after demoulding even if the mould shape is iteratively adjusted and the curing process optimized. Hence, a post manufacturing shape adjustment process is suggested in this thesis. Using shape memory polymer actuator patches, applied to the structural surface, distortions can be compensated.
For this single-step shape adjustment application, shape memory polymers (SMPs) are well suited. The material does not need a continuous energy supply to provide the actuation stress, is compatible with CFRP, lightweight, easy to manufacture into arbitrary shape and shows attractive actuation properties.

1.2. Scope and Objective of Thesis

The objective of this work is the development of a post manufacturing process to adjust the shape of fiber composite parts using shape memory polymer patch actuators. Specifically different measurement techniques to determine the 3 dimensional (3D) shape of distorted parts are investigated and necessary actuation properties of shape memory polymers are determined. A newly developed experimental method allows the simultaneous determination of actuation force and stroke of SMPs. Novel finite element models including the active properties of shape memory polymers are employed for parametric studies. Furthermore, these finite element models are used in optimization processes for the best actuator location and geometry determination. An application and stimulation process for SMP patch actuators is established. Using curved shells, planar plates and a rectangular waveguide sample, the methods are verified by simulations and experiments.

1.3. Outline

Chapter 2 describes the state of the art in the fields of dimensional stability of composite parts, static shape control and shape memory polymers. Chapter 3 provides the fundamentals and background about the dimensional stability of composite structures, shape adjustment using patch actuators, and shape memory polymers. Chapter 4 introduces measurement techniques to determine structural shapes. Chapter 5 concentrates on the definition of actuation properties of shape memory polymers and their experimental determination. Chapters 6 and 7 introduce the methods for modeling, applying, stimulating and straining of shape memory polymer actuator patches. A parametric invesitgation of the structure-actuator interface for soft actuators is shown in Chapter 8 and Chapter 9 introduces an optimization algorithm for the shape error minimization. Chapter 10 briefly describes the operation of SMP equipped parts and describes properties such as creep and thermal distortions. Chapter 11 shows three examples of different composite parts. Chapter 12 summarizes and concludes the thesis. Figures 1.1 and 1.2 illustrate the process of the introduced shape adjustment in two flowcharts and can be seen as an outline of the thesis. Figure 1.1 focusses on the methods and Figure 1.2 shows some representative results.

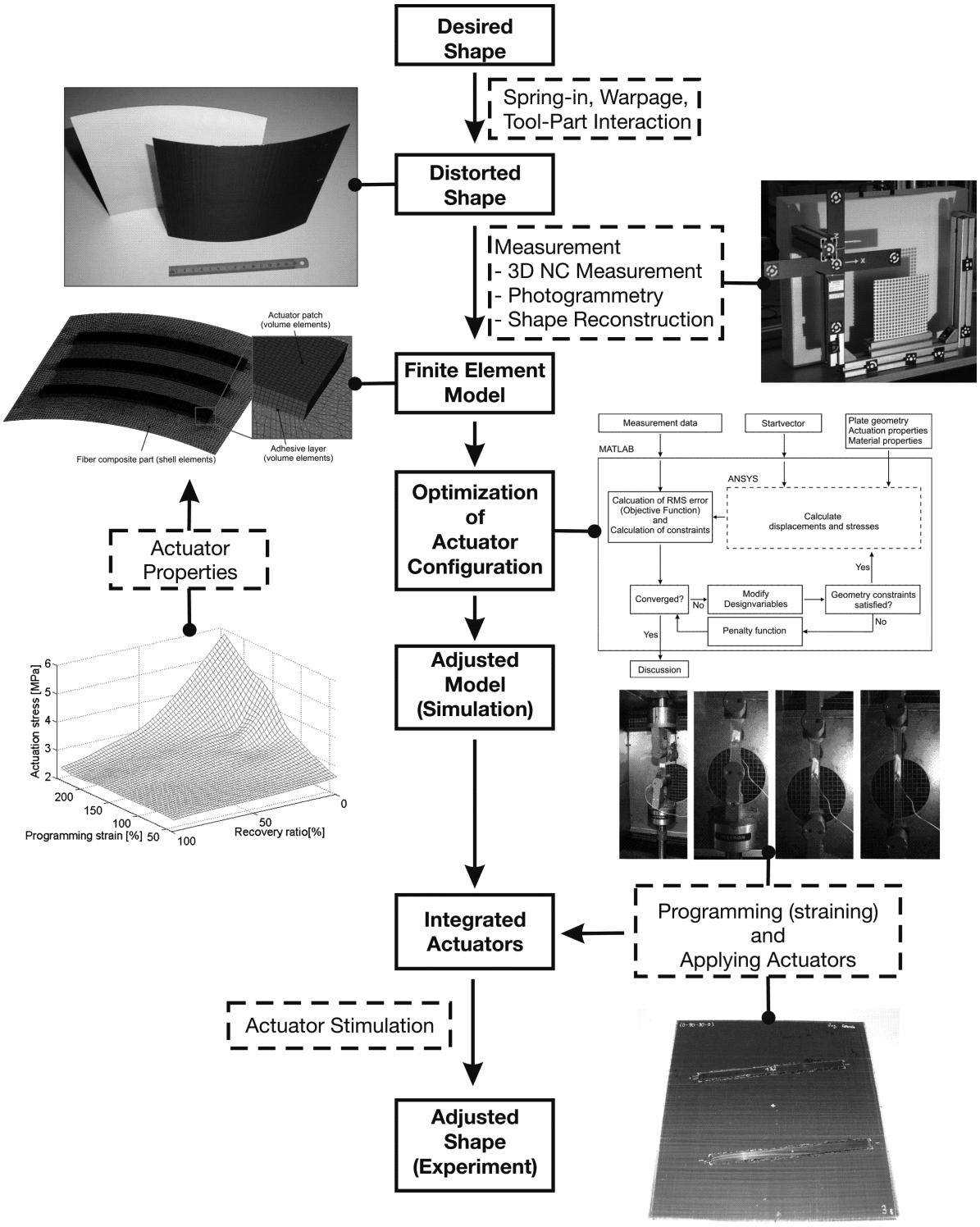

Figure 1.1.: Flowchart of the process of shape adjustment with the focus on the methods.

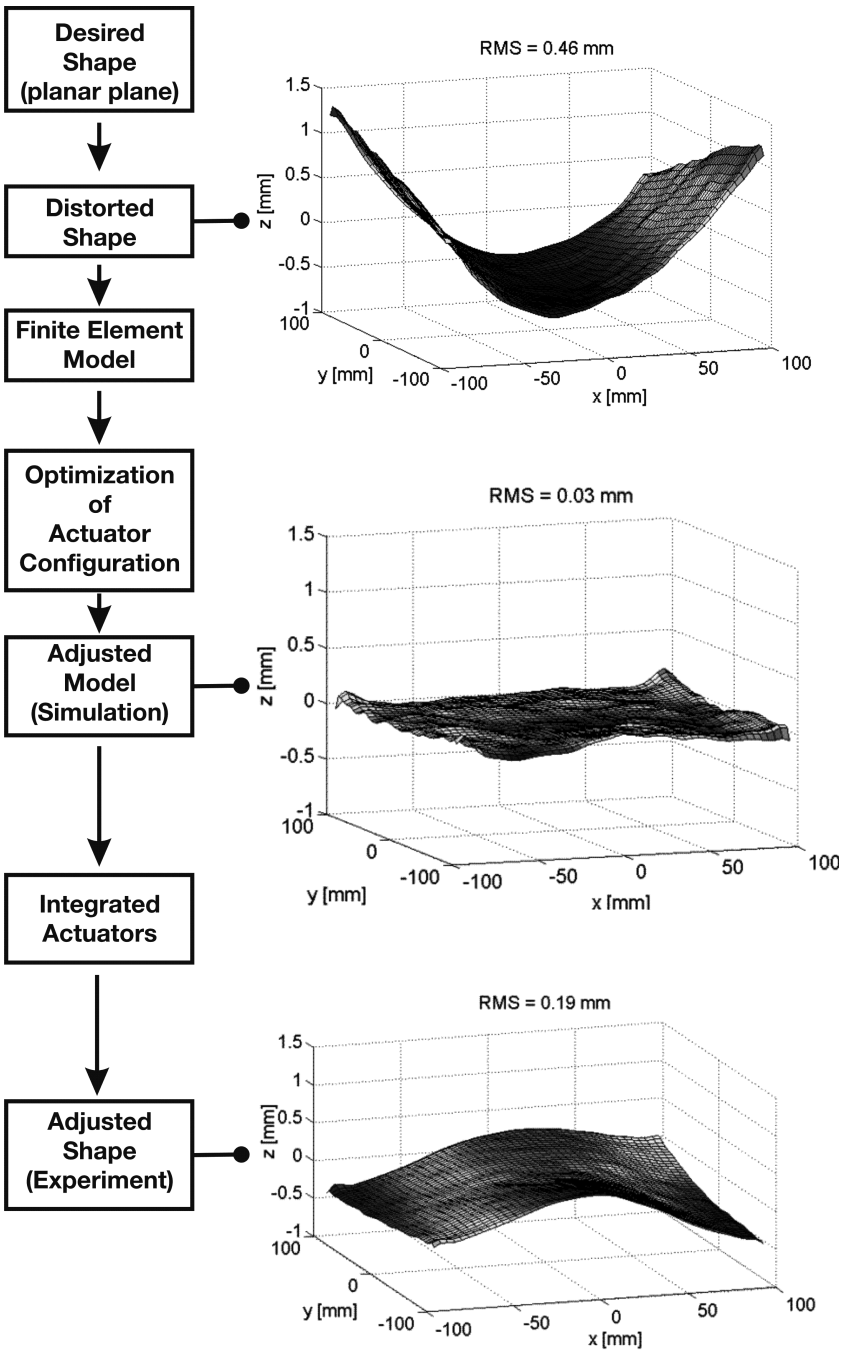

Figure 1.2.: Flowchart of the process of shape adjustment with the focus on representative results.

2. State of the Art

The discussion of the state of the art begins with a review of literature on the dimensional stability of fiber composite structures. Effects leading to warpage, modeling of curing processes and methods to minimize these effects are included. This is followed by a review of static shape control including methods, actuators, optimization algorithms and applications. Finally the research field of shape memory polymers is reviewed. Literature on the chemical structures, thermomechanical properties and characterization, modeling and applications is cited.

2.1. Dimensional Stability of Fiber Composite Parts

The dimensional stability of fiber composite parts is affected by different environmental influences such as processing, thermal or humidity loads. Here the effects of manufacturing, expecially the curing processes on the dimensions of composite parts are considered. Other keywords used in the literature to describe the same effect are dimension fidelity, shape distortions or residual stresses. Actually, residual stresses are built up during the curing process of composites, which partly are released during demoulding by warping. While residual stresses may lead to a reduction of the load carrying capacity, warpage and spring-in effects lead to a reduction of the precision of the parts geometry. While *warpage* describes the concave deformation of planar parts away from the tool (Figure 2.1 (a) and (c)), *spring-in* is the reduction of the included angle of curved parts (Figure 2.1 (b) and (d)).

For some applications such as reflecting surfaces of space reflectors or other radio frequency devices such as waveguides, the geometric precision, however, is essential for the performance. Several different causes for the warpage effects were found, modeled and simulated. Using this knowledge shape error reduction methods were developed.

Causes for warpage and spring-in

Basically three causes for warpage and spring-in can be distinguished: Anisotropy of the laminate, cure shrinkage and tool-part interaction. Usually these effects occur in combination. Darrow and Smith [52] isolated different components of process-induced warpage of composite parts. The three mentioned main causes can be further subdivided.
The most obivous anisotropy in laminates is apparent for asymmetric layups, which leads to saddle or bistable cylindrical shapes of the parts. Radford and Diefendorf [96] developed a mathematical model to predict shape instabilities in composites resulting from laminate

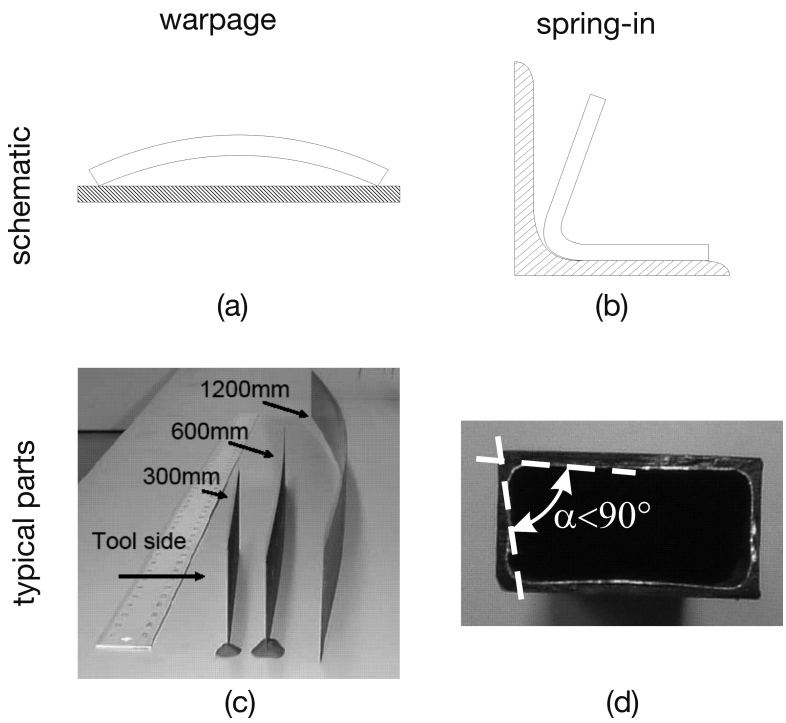

Figure 2.1.: Effects of warpage and spring-in; (a,b) Schematics of warpage and spring-in; (c) Warped rectangular composite parts [121]; (d) Spring-in in a rectangular waveguide cross-section.

anisotropy and verified it with experiments. Another reason for anisotropies are the local orientation differences of the fibers [57]. Furthermore, the always present anisotropy in thickness direction of 2 dimensional (2D) composite parts compared to the x-y-plane, causes spring-in effects [96, 110]. A further reason for an asymmetric layup is a gradient in the fiber volume fraction through thickness, which is caused by resin accumulation at the tool side and resin take out at the bleeding ply [95].

The cure shrinkage can be subdevided in a chemical shrinkage due to cross-linking and a thermal shrinkage due to thermal compression after curing. Svanberg and Holmberg [108] experimentally investigated the influence of different cure cycles on the spring-in effect. Svanberg and Holmberg determined that a model to predict the spring-in must at least incorporate thermal compression, chemical shrinkage and frozen-in effects. Fernlund et al. [33] investigated experimentally and numerically the effect of cure cycles on the dimensional stability of composites, using the software *COMPRO* to simulate the degree of cure, resin flow and residual stresses.

The tool-part interaction is based on the CTE mismatch of the tool and the part. Fernlund et al. [32] experimentally investigated effects on the warpage due to tool-part interaction. In this paper a strong relationship between the aspect ratio, the cure cycle, and the warpage is reported. However, the effect of the tool material was found to be negligible. Albert and Fernlund [5] performed a comprehensive experimental investigation on a large number of parameters influencing spring-in and warpage. The part thickness, the laminate layup,

the part shape, the cure cycle, the release agent and the included angle were investigated. Twigg et al. [120] experimentally investigated different curing pressures and related sticking and sliding conditions to the measured data. It was pointed out that the aspect ratio has a much higher influence on the warpage effect than the curing process parameters [121]. Figure 2.2 summarizes the different factors causing warpage or spring-in.

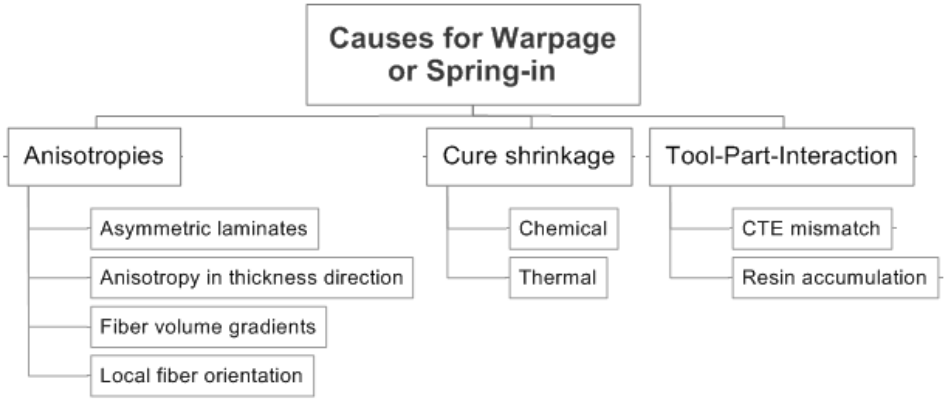

Figure 2.2.: Factors causing warpage or spring-in.

Modeling of warpage and spring-in

Since the goal is to reduce the distortion effects, modeling and simulation techniques were developed to predict the shape distortions or residual stresses. Jain and Mai [47] used a modified shell theory to predict the degree of spring-in in composite shells. Spring-in ratios regarding radius to thickness ratios and ply directions were calculated. White and Hahn [128] included a cure kinetics model, a residual stress model, a strain history model and mechanical properties in a simulation process called *LamCure* for the residual stress prediction. Prasatya et al. [92] developed a viscoelastic model for predicting isotropic residual stresses built up during cure. Prasatya et al. determined that elastic models overestimate residual stresses and thus viscoelastic modeling cannot be neglected. Furthermore, the influence of the heating rate and the cure temperature were investigated. While the heating rate hardly showed an effect, an increasing gelation temperature led to a strong increase of the residual stresses.
Besides these analytical models, material models were developed and implemented in finite element software for the calculation of distortions and residual stresses. Svanberg and Holmberg [109] developed a simplified linear viscoelastic material model to predict shape distortions due to thermal expansion, chemical shrinkage and frozen-in deformations. The material model was implemented in the commercial FE software *ABAQUS*. Experimental validation of the model and an analysis of the curing cycle and boundary conditions were performed [110]. A contact boundary condition showed better agreement with experimental results than a free or fully constrained boundary condition. However, in general the predicted distortions were overestimated. Svanberg used this model for the validation of the spring-in of a C-Spar [107]. Spröwitz et al. [104] simulated the manufacturing process with a hybrid finite element model using the software *MSC/NASTRAN*. Sweeting et al. [111] used two different finite element approaches to simulate the distortions after manufacturing of a circular

flange structure. Shrinkage effects were integrated by initial strain conditions. A fiber shear model with solid elements was compared with a simplified in-plane isotropic model. The results showed almost no differences, however, the comparison with an experiment showed differences of up to 100%. Twigg et al. [122] used an additional shear layer between the part and the tool to simulate the shear stress transfer. Good agreement between simulation and experiment was achieved after tuning the shear stiffness. Johnston et al. [50] developed a linear elastic plain-strain model for the prediction of process-induced deformations. This model captured the thermal strain, the cure shrinkage, the gradient of the degree of cure and temperatures, the resin flow and the tool-part interface. The model predictions and the experimental data showed good agreement. The most comprehensive 3D-thermo-chemo-viscoelastic model was developed by Zhu et al. [137]. Using this complex model the residual stress development could be captured throughout the entire curing cycle. The influence of laminate thickness, laminate layup, tool geometry and curing process parameters were accurately predicted.

Countermeasures

White and Hahn [129] presented an experimental study on the influence of cure cycles on residual stresses and possible improvements. It was determined that reducing the cure temperature decreased the residual stresses, while increasing dwell times maintained the mechanical properties. White and Hahn suggested a three step cure cycle and slower cool down rates. Olivier and Cottu [88] used an optimization formulation to find optimal cure cycle parameters to minimize residual stresses. The optimization variables were the second dwell time and the second dwell temperature. Olivier and Cottu used their process also to optimize the cure cycle to minimize residual stresses in two different composites which were cured simultanously. Using optimized cure cylces, the warpage effects could be reduced, however, not eliminated.
Another principle is the compensation of the resulting distortions by adjusted moulds. Radford [95] compensated the influence of the fiber volume fraction gradient using this approach. Zhu et al. [138] also used the effect of male and female parts and different coefficients of thermal expansion of the tool material to adjust the mould shape and reduce distortions. An optimization approach for L-shaped parts was shown by Zhu et al. [138]. Capehart et al. [17] used a comprehensive chemical-thermal-mechanical finite element model to capture distortions due to manufacturing. An algorithm was developed, which iteratively adjusted the mould shape thus changed node locations of the finite element net until a convergence criterion was achieved. The approach was demonstrated at a curved car door. In the simulation, a reduction of the out-of-plane deformation of several orders of magnitude from 11.6 mm to less than 0.01 mm was achieved. However, in an experiment only a reduction of 52% from 29 mm to 14 mm was achieved.
Another approach is the use of locally asymmetric laminates to compensate spring-in [96]. Huang and Yang [45] used this approach to improve advanced composite tool shapes. Tuttle et al. [119] introduced a technique to prestress fibers in laminates which reduced the residual stresses and distortions. While the ultimate strength was not improved, the number of microcracks could be reduced.

It can be concluded that a lot of effort was spent in the last two decades on the understanding and improvement of the dimensional stability of composite parts after manufacturing. However, contradictory statements on the effects can still be found, and a lot of the developed methods for prediction and reduction of distortions are expensive and time intensive. Furthermore, with most methods the distortions can only be reduced but not avoided, and small distortions, which might be unacceptable for high precision structures, remain. Therefore, a post manufacturing shape adjustment approach, such as suggested in this thesis, seems to be an attractive alternative or complement to the existing methods. Fundamentals on the dimension stability of composite parts are given in Section 3.1.

2.2. Shape Adjustment

In this thesis the notation of *shape adjustment* is used for the single adjustment of a structural shape after manufacturing. This is a special case of the more comprehensive field of *shape control*, which tends to the multiple necessary adjustments of structural shapes due to external loads.
Shape control includes dynamic as well as static shape control. Dynamic shape control or vibration control governs the bulk of the research including for example vibration control of aerospace and automotive structures, noise reduction in aircrafts or the shape control of large space telescopes. There are comprehensive books [78, 93] and review papers [46] on that topic.
The static shape control or shape adjustment respectively describes the process of compensating mechanical or thermal loads, or manufacturing errors in structures, to maintain the desired functional shape. This was investigated for truss structures, (composite) beams, plates and shells, aircraft wings and space reflectors. Different smart materials, such as piezoelectric materials, shape memory alloys (SMAs) or electro active polymers (EAPs), were suggested for actuation. These materials were used as patch, stack or tendon actuators. Using different optimization methods and algorithms, actuator input voltages and locations were determined. Figure 2.3 illustrates the structure of the research field of static shape control, reviewed in this section.

Haftka et al. [44] introduced an analytical investigation which showed the shape control capability of introduced forces and thermally expanding actuator elements in large space antenna truss structures. The use of such thermal active elements, thus elements with a higher coefficient of thermal expansion (CTE) than the host structure, is a simple method for actuation. The shape control of other truss structures was shown by Salama et al. [100] and Sofla et al. [101]. In [100] the wording *shape adjustment* was used for the shape control of an erectable truss structure. By optimizing the forces of active members (lead screw actuators) in the truss structure, the root mean square (RMS) error of specified truss nodes was minimized. As an additional parameter, the number of active members was varied. In [101], an adaptive hinged truss structure was introduced. Using novel spherical-pivotal joints and antagonistic operating SMA wires a morphing bipyramid element was built. Although the

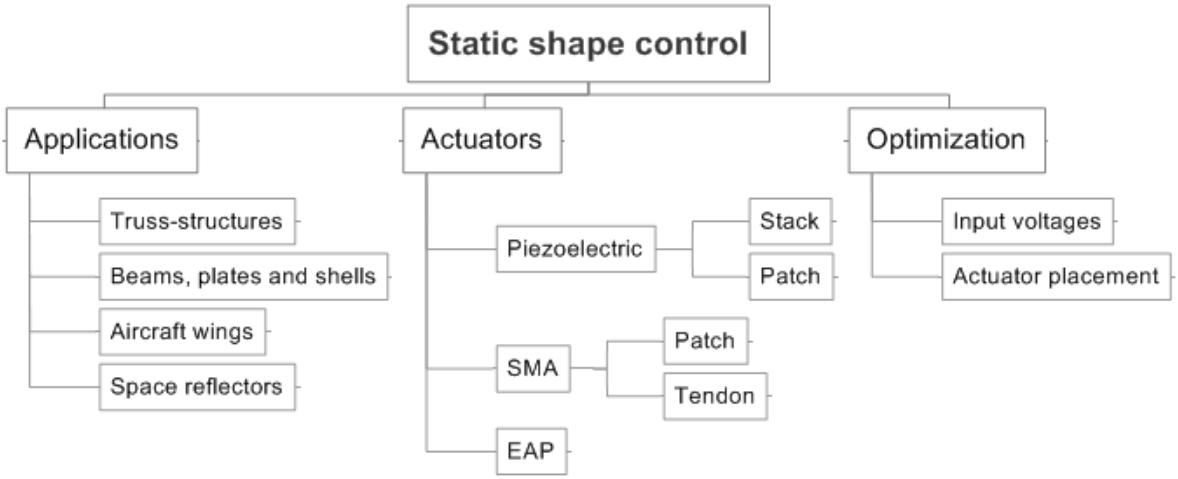

Figure 2.3.: Structure of the research field of static shape control

truss structures built the starting point for the shape control, most research was carried out for (composite) beams, plates and shells. Analytical models of laminated plates integrated with actuator patches were developed in the late 80's and the 90's.
Crawley and Luis [23] presented an analytical model for piezoelectric patches for intelligent structures. Embedded and surface mounted patches were considered as well as a bonding layer. The effectivity and the shear lag were investigated. The analytical model was verified with experiments using aluminum, GFRP and CFRP beams in dynamic tests. Crawley and Lazarus [24] developed an analytical model for the strain induced actuation of isotropic and anisotropic plates. Experiments with cantilever plates verified the method. Crawley and Anderson presented the developement of a detailed model of piezoelectric actuated beams [22]. Parameters such as the thickness ratio, the shear parameter and creep effects were investigated. Koconis et al. [56] developed an analytical method to determine optimal actuator input voltages to achieve a desired shape of different structures. The model of Koconis was very comprehensive and included solid plates and beams as well as sandwich constructions in flat, curved or asymmetric shape. A weighted multiobjective function including voltage input and shape error was optimized by solving a linear equation system. Agrawal et al. [3] used the elastic plate theory and an implementation in a finite difference formulation to model plates integrated with piezoelectric actuator patches. Desired plate shapes were achieved by optimally determined actuator voltages and locations regarding a quadratic shape error. Agrawal and Treanor [2] presented the static shape control of a beam using piezoelectric actuators. An analytical model based on the Euler-Bernoulli beam model was introduced. An optimization process included the actuator location and voltage inputs as design variables and the beam shape as cost function. Tan [113] introduced a simulation procedure for the compensation of thermal deformations in CFRP parts, with a set of governing equations for a curved piece of a shell of revolution. Using a control scheme, based on strain measurement and the nulling of the strain, the distortions of beams, plates and parabolic shells could be reduced. Tan compared his results with experiments of Crawley and Luis [24] and a finite element analysis of Ha et al. [42]. The results showed that for a parabolic shape, densly

distributed sensors and actuators (they were collocated in Tans case) are necessary. Furthermore, dependent on the load case, circumferential or radial actuation was advantageous. Lin et al. [69] proposed sine shaped sensors and actuators for the static shape control of beam plates as Preumont [93] did for dynamic applications. Clamped-clamped and simply supported beam plates were loaded with different static loads. Using different sensor/actuator configurations and optimized input voltages, the shapes were controlled. Chen et al. [19] presented a static shape control method incorporating not only displacement requirements, but also stress requirements. The results showed a decrease in the displacement quality, but a smoothening of the shape and a reduction of stresses.
The analytical models were complemented by the then arising finite element models. Ha et al. [42] presented a finite element formulation for the modeling of composites integrated with piezoelectric sensors and actuators. Ha showed numerical examples of static and dynamic shape control of composite plates and beams, which were compared with experimental results of Crawley [24] and himself. Although the total plate was covered with sensors and actuators the shape predictions showed shortcomings. Ghosh and Batra [39] presented a finite element analysis of shape control of simply supported and cantilever plates using piezoelectric elements. Wang et al. [125] introduced a new piezoelectric plate bending element, which was used for static shape control of plates. Sun and Tong [106] presented an algorithm for static shape control including piezoelectric non-linearities and energy constraints. Lagrange multipliers were used to determine optimal input voltages for equally distributed piezo-patches. Sun and Tong [105] introduced a finite element model incorporating a host structure, an adhesive layer and piezoelectric actuator patches. An adhesive element considering peel and shear stresses was introduced. The developed finite element model was used for the optimization of input voltages for the static shape control of cantilever beams and plates. Every patch was modeled using one element. The results showed that the adhesive layer is not negligible. Jin et al. [49] showed an approach for static shape control of repetitive structures such as symmetrical, rotational periodic or chain structures. The approach was illustrated with a finite element analysis of a cantilever plate with symmetric and antisymmetric distortions. Binette [11] demonstrated the static shape control of thermally distorted fiber composites using active fiber composite (AFC) patches. Finite element models with solid elements were built and the simulation results were compared with experiments. A control loop was applied using strain gages to attenuate thermally induced distortions.
Most of the studies on shape control concentrated on the actuation using piezoelectric actuator patches. However, shape memory alloys were also used for this application. Especially for quasi-static or static applications, SMAs show advantages. Due to their two stable states, electric creep effects are avoided, which are documented for piezoelectric actuators [22]. Song et al. [103] showed an experiment, in which the shape of a sandwich beam was statically controlled by integrated SMA wires. A proportional derivative control and a robust compensator were introduced by Song et al. [102, 103]. Balta et al. demonstrated the static shape control of a composite sample with embedded SMA wires [8]. Fiber Bragg grating (FBG) sensors were used as feedback signals in a PID controler. Peng et al. [89] introduced the shape control of a membrane structure using SMA wires for tensioning. The group developed a genetic algorithm (GA)-based optimization algorithm for the determination of the wire tensions. As a further example for shape control using SMA actuators, the morphing

wing mechanism developed by Manzo and Garcia [76] can be mentioned. The camber of an unmanned aerial vehicle (UAV)-sized segmented wing was actuated using SMA tendons. The load carrying capability was shown by wind tunnel tests.
Austin et al. [6] introduced a theoretical method to control flexible structures by internal displacement actuation. The introduced method was applied to an adaptive wing, where the cross-section was modified to reduce drag and shock waves. A demonstrator was built using 14 mechanical ball-screw actuators.
The shape control of space reflectors and mirrors was reported for example by Bushnell [15], Tabata [112] and Lang [61].
In Crawley's overview of intelligent structures for aerospace different shape control applications are mentioned as well as a strain actuator comparison [21].

Shape control is a widly investigated field with a focus on vibration control and the application of piezo-electric patch or stack actuators. Optimization algorithms using input voltages or discrete actuator locations as input variables and the shape error as the objective function are well established. The post manufacturing shape adjustment, the use of continuously optimized actuator configurations and SMP actuator patches, as it is introduced in this thesis, will contribute to expand the field of shape adjustment.

2.3. Shape Memory Polymers

The shape memory effect (SME) describes a macroscopic shape change of a material due to an external stimulus in which the material returns to a previous shape. These effect was first discovered in alloys by Chang and Read [18]. The most popular representative is the *NiTi* alloy introduced by Buehler et al. [14]. In alloys the shape transformation is caused by diffusionless phase transformations. Also other materials show a memory effect, such as ceramics and polymers. A comprehensive review on shape memory materials can be found in [126, 127]. Here the focus is on shape memory polymers (SMPs).
Shape memory polymers were already known in the 1960s [62] as heat shrinkable materials and were used for packaging and isolating electric components for decades. However, due to the lack of attractive mechanical properties, at first they were not taken into account for mechanical engineering applications. Only in the 1990s the attention increased in the smart materials community [71], because of two reasons: The polymeric tailoring and the fiber composite technology. The polymeric tailoring enables the combination of several properties within one polymer, which opens a wide field of possible applications. The development of the fiber composite technology enables the improvement of the mechanical properties of these polymers by fiber reinforcements. In the meanwhile a lot of research was carried out on chemical structures, thermomechanical characterization, modeling and applications. Comprehensive reviews can be found in [62, 71, 98]. One of the first summarizing books on this new smart material was edited by Jinseong Leng [63].
Different chemical structures are used for the composition of shape memory polymers. There

are thermoplastic as well as thermoset SMPs based on a wide variety of polymers. As most popular representatives, polyurethanes, polystyrenes and epoxy resins have to be mentioned [62, 63, 130]. The most comprehensively investigated SMP might be the polyurethane, which was intensively studied by the group of Tobushi [115, 116, 117]. More information about the chemical structures can be found in Section 3.3.

From an engineering point of view the thermomechanical characterization of SMPs is an important step into the direction of industrial application. Besides conventional material parameters, shape memory parameters play a key role. Several experimental investigations on these parameters were performed in the past. Tobushi et al. [115, 117] determined thermomechanical properties of polyurethane SMP. Baer et al. [7] also performed a comprehensive experimental study on the shape memory properties of polyurethanes. Ni et al. [85] characterized shape memory nano composites. Ji et al. [48] determined actuation properties of SMP fibers. Liu et al. [72] investigated the thermomechanical behavior in flexure and Gall et al. [36] the mechanical behavior of nanocomposite SMPs.

The fiber composite technology was also applied to the shape memory polymers. The influence of continuous fibers on the recovery behavior was investigated by Gall et al. [37], Lake et al. [58] and Tupper [118]. The focus in these studies was on the kinematics of the integrated fibers during bending or folding processes. The buckling behavior of the fibers within the soft matrix above its glass transition temperature was investigated analytically. Furthermore, the influence of the integrated fibers on the recovery performance was investigated regarding the bending radius for example. Much more attention, however, was paid to the shape memory polymers with fillers or short fiber reinforcement. First of all fillers are used to make the polymers conductive for stimulation. Using an electrically conductive filler such as Nickel or carbon black, the SMP can be stimulated by an applied electric current. Especially the group of Prof. Leng at the Harbin Insititute of Technology (HIT) investigated such shape memory polymer composites [64, 65, 66, 67]. Especially the development of resistivity with increasing powder content as well as the recovery behavior were investigated. Meng et al. [79] incorporated multi-walled carbon nano-tubes into SMPs to improve the conductivity. The large majority of the shape memory polymers only show the *one-way* shape memory effect, which only allows a single switching triggered by an external stimulus. However, recently there were reports on dual- or even trippel-shape effects [63], which describe the behavior of a two-step recovery dependent on two different transition temperatures. And 2008 even a two-way shape memory effect in polymers was reported [20].

The majority of the shape memory polymers is stimulated by heat although other stimuli exist. Using the afore mentioned fillers the thermally induced shape memory effect is triggered by an electrical current, thus a kind of electro activated shape memory polymer is formed. Some polymers show a shape memory effect triggered by solutions or infrared light [63, 64].

Besides the experimental surveys of the scientists also theoretical work was conducted and models were set up to simulate the polymers behavior. Since SMPs show a 3D, non-linear viscoelastic material behavior the material modeling is complex. Tobushi et al. [116] set up a constitutive model based on a standard viscoelastic model with an additional temperature dependent slip element. Abrahamson et al. [1] used an addaption of the visco-plastic Valanis model to describe the thermomechanical behavior of shape memory composites. Qi et al. [94] developed a 3D constitutive model which was implemented in an *ABAQUS* user mate-

rial subroutine (UMAT) for a finite element analysis. Qi et al. implemented a hyperelastic model for the stress development and incorporated relationships for the volume fractions of glassy and rubbery state as well as transformation rules. Nguyen et al. [84] incorporated an Adam-Gibbs formulation for the structural relaxation and a modified Eyring model for the viscous flow into this finite-deformation model. Diani et al. [28] also developed a 3D thermo-viscoelastic model for finite strain. Liu et al. [73] developed a 1D small strain constitutive model and compared it with good agreement with experimental results. Zhou et al. [136] introduced another mechanical constitutive equation to describe the stress-strain-temperature behavior of SMPs. Also Böl and Reese [12] introduced a finite element implementation of the shape memory behavior of polymers.
The suggested applications for SMPs show a wide variety. The most popular ones are medical devices, such as stents or suturals [12, 63] for minimal invasive surgeries and deployable space structures. Both applications fit well to SMPs due to the low required forces. While for the medical devices a lot of investigations were carried out on biocompatible pure SMPs, for the space deployable applications shape memory composites were foreseen. Two strategies were followed. The first is the use of the material as an energy storage and an additional device such as a hinge [9, 59, 60]. This approach minimizes the risk of uncomplete or inaccurate deployment since the shape of the deployed rigid part is given and the deployment stroke and force can be designed with some margin. This approach led to the first space application of an SMP deployable part [9]. Another approach is the use of the shape memory resin as the matrix material of the deployable composite structure. This approach leads to a higher degree of integration, less moveable parts and higher reliability. However, the recovery ratio and predictability have to be very good. Especially for the application for high performance parts such as space reflectors this seems at the moment too challenging. For structures such as booms or habitat structures, which not have to be accurate in a micrometer range, this approach might be successful. Cadogan et al. [16] presented 2002 the use of SMP composite gossamer inflatable structures. Lake et al. [58] pointed out necessary fundamentals on this topic as well as Tupper et. al. [118]. Other suggested applications are the use as a skin material in morphing wings with temperature dependent Young's modulus [134] or as the active member [135]. The use of shape memory mandrels for the manufacturing of hollow composite parts might be introduced in industrial application soon [63]. More unconventional applications such as shape memory cloths or the use of shape memory foams can be found in [63].

In summary it can be stated that since 1990 a lot of research was carried out in the field of shape memory polymers. The scientists concentrated on the thermomechanical characterization, the modeling of the complex material behavior, the integration of fillers and deployment applications. However, very little can be found on the characterization in terms of actuation properties and the application of the material as patch actuators. Some fundamentals on shape memory polymers, their chemical structures, thermomechanical behavior, modeling and applications can be found in Section 3.3. Chapter 5 will give a more comprehensive overview on their actuation properties.

2.4. Summary

From the literature review of the three fields of warpage and spring-in, shape control and shape memory polymers, the following conclusion for the suggested shape adjustment approach can be drawn.
Warpage and spring-in are a widely investigated and well understood phenomenon based on several causes. The modeling and simulation techniques are well developed and can predict shape distortions well. This leads to the capability of cure cycle optimization and mould corrections, which is sucessfully done. Systematic shape errors can be minimized to a certain distinct with this approach. However, local effects cannot be considered in the already complex models, and the complete compensation of distortions is only achieved in simulations. Hence, the post manufacturing shape adjustment for high performance composite parts is an attractive addition.
The necessary shape control is an established and widely investigated field of research. However, a majority of the work is concentrated on dynamic shape control and vibration control. Static shape control can be found basically for truss structures. Static shape control of planar parts is basically focused on the reduction of thermal distortions, which is mostly a temporary case. Approaches for the post manufacturing correction of composite parts can hardly be found. One reason could be the lack of proper active materials. Since this application is a static application with a long duration, a bi-stable material should be used which does not require permanent power input. Thus only shape memory materials come into consideration. The relatively new (1990s) class of smart materials, the shape memory polymers (SMPs), has been well characterized in the meantime. Especially the disciplines of chemical structures, chemical and physical effects and compositions with different fillers. Also, a large number of papers can be found on the thermomechanical charaterization and modeling techniques. Suggested applications are mainly medical devices and space-inflatable structures. However, the characterization in terms of actuation properties and the use as actuation patches, as introduced in this thesis, is believed to be a novel approach.

3. Fundamentals and Background

3.1. Dimensional Stability of Composite Parts

The motivation for the research presented in this dissertation is the reduction of distortions in composite parts caused by the manufacturing process. This chapter provides background information and fundamentals on the dimensional stability of composite parts, and introduces the terminology used in the composite society. The underlying mechanisms for the distortions are presented and the state of the art of modeling and simulation for these processes is given. The actual countermeasures against the shape distortion are summarized.

3.1.1. Warpage and Spring-in

In the first instance the term *warpage* describes any kind of distortion of any part of any material caused by manufacturing. However, in the field of fiber composite manufacturing *warpage* describes the more special effect of the concave out-of-plane deformation of a originally desired planar shape after manufacturing. The effect especially applies for thin-walled structures. Radford [95], Radford and Rennick [97], and Fernlund et al. [32] mentioned gradients of the fiber volume fraction, asymmetric peel ply, asymmetric layups and tool-part interaction as possible reasons. Figure 3.1 illustrates such deformed parts.

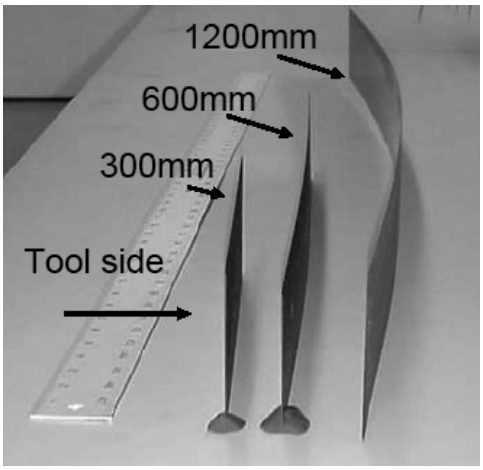

Figure 3.1.: Warpage of thin-walled fiber composite parts [121].

The terminology of *spring-in* is used for the deformation of curved parts, if the included angle of the part does not conform to the mould after demoulding. According to Radford [95] and Radford and Reinnick [97] the main cause for this behavior are material anisotropies in thickness and in-plane directions. While the fibers constrain shrinkage effects during curing in in-plane direction, there is no hindering in out-of-plane direction. This different behavior reduces the included angle of the part, which leads to the terminology of *spring-in*. Note that warpage effects are always overlaid. The included angle for spring-in only can be calculatd by Equation 3.1 [96].

$$\Delta\Theta = \Theta(\frac{(\alpha_l - \alpha_t)\Delta T}{1 + \alpha_t \Delta T}) + \Theta(\frac{\Phi_l - \Phi_t}{1 + \Phi_t}) \tag{3.1}$$

where Θ is the desired part angle, $\Delta\Theta$ is the change of the desired angle, ΔT is the temperature change, Φ_l, Φ_t are the in-plane and out-of-plane cure shrinkage and α_l, α_t are the in-plane and out-of-plane coefficients of thermal expansion (CTEs). Figure 3.2 illustrates the spring-in behavior in a sketch and a hybrid CFRP-copper waveguide.

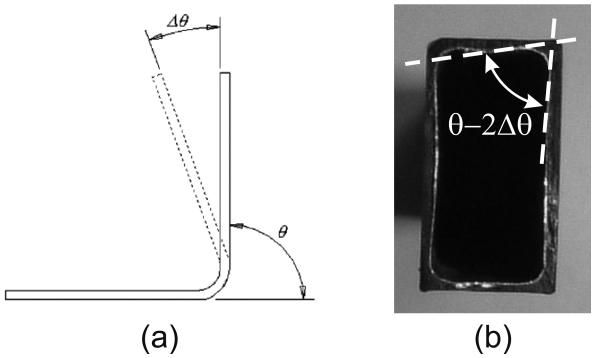

Figure 3.2.: Spring-in: (a) Angle definition [108]; (b) Spring-in in a rectangular hybrid CFRP-copper waveguide (see Section 11.3).

The effect of warpage or spring-in is caused by residual stresses, which built up during the curing and cooling processes due to different causes. Demoulding leads to a partial release of these stresses through warping. Figure 3.3 illustrates qualitatively a typical development of residual stresses in a composite during a typical two-step cure cycle.

During the first heating of the resin a compression stress builds up due to thermal expansion (I). During the dwell and initial gelation, a tensile stress builds up (II). Further heating decelerates this effect (III), before a second dwell for the full curing of the material increases the tensile stresses until a saturation is achieved (IV). Cooling down the sample leads to a strong increase of tensile stresses due to thermal contraction (V). Demoulding leads to a partial release of the stresses through warping.
In the following the causes for this effects and their modeling and simulation will be presented.

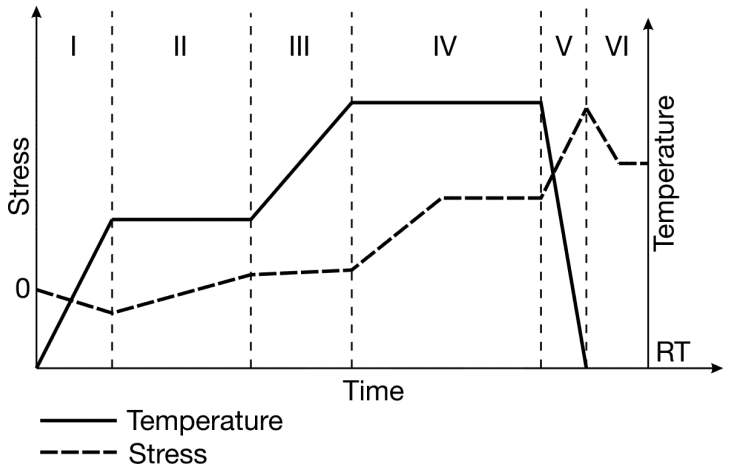

Figure 3.3.: Qualitative development of residual stresses. (I) heating; (II) first dwell; (III) second heating; (IV) second dwell; (V) cooling; (VI) demoulding.

3.1.2. Causes for Warpage and Spring-in

The three most important causes for warpage and spring-in are the CTE mismatch or anisotropy, the cure shrinkage (chemical and thermal) of the matrix, and a tool-part interaction (Figure 3.4).

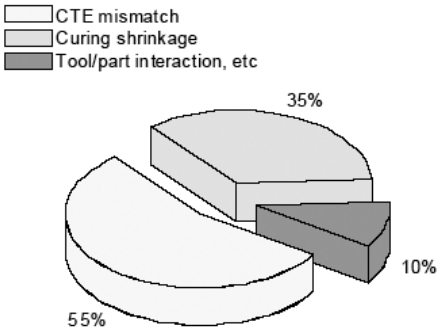

Figure 3.4.: Causes for warpage and spring-in: CTE-mismatch, curing shrinkage and tool-part interaction [30].

There are other mechanisms, such as gradients in the fiber volume fraction, local fiber orientation and the part geometry. Darrow and Smith [52] isolated different influences and related them to the laminate thickness. Their representative results are illustrated in Figure 3.5.

It can be seen that there is a constant influence due to thickness shrinkage, which adds to the effects of a fiber volume gradient and the mould stretching (tool-part-interaction), which both increase with decreasing part thickness. The fiber volume fraction is only affected by

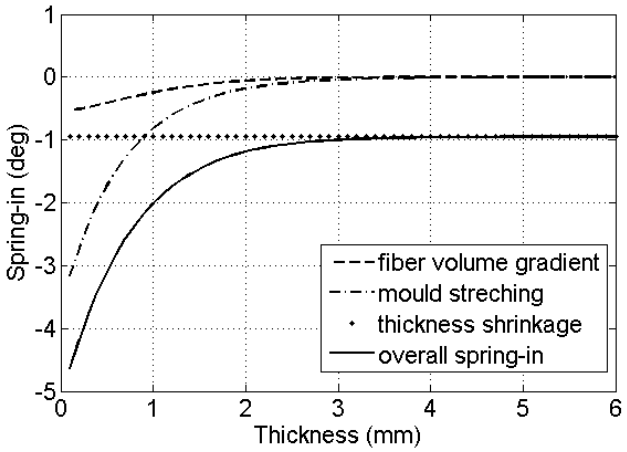

Figure 3.5.: Different influences on spring-in angle related on the laminate thickness [52].

the mould and the bleed layer at the outer layers. Therefore, the thicker the laminate, the more inner layers with no effect are included. The characteristic of the mould stretching can be explained with the interlaminar slippage. Thus only the layers near the tool are affected. This means the thicker the laminate, the less the overall influence.

Anisotropies

Fiber composites, which generally do not have a reinforcement in thickness direction, always show an anisotropy regarding in-plane and out-of-plane direction. While this anisotropy does not play a role for planar parts, for curved parts it is a cause for distortions, called spring-in. Since a laminate shows similar properties in 90^o direction as in thickness direction, the spring-in effect is small if the laminate is oriented parallel to the curvature vector. However, if the 0^o direction is in circumferential direction, the spring-in effect is clearly present [32, 47]. The spring-in effect can be explained by geometric considerations of a 90^o bend of a laminate such as shown in Figure 3.6

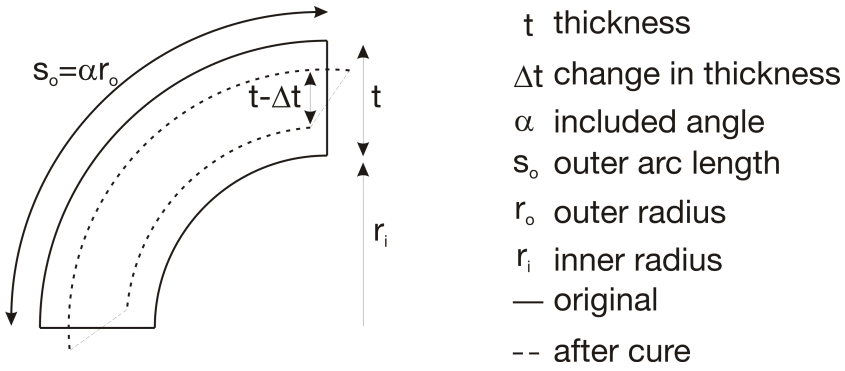

Figure 3.6.: Schematic illustration of the spring-in effect.

A very low shrinkage and thermal compression in arc length direction is assumed due to the

fiber reinforcement in this direction. Thus the reduction of arc length s can be neglected. However, the shrinkage and thermal compression in radial direction Δt is high because the resin properties dominate.
The arc length s is defined as:

$$s = \alpha r \tag{3.2}$$

where α is the included angle and r is the radius. The angles α_i at the inner and α_o at the outer side are calculated to:

$$\alpha_i = \frac{s_i}{(r_o - t)} \quad \text{and} \quad \alpha_o = \frac{s_o}{(r_i + t)} \tag{3.3}$$

If the thickness t is reduced during curing while the arc lengths s remains constant, it can be seen from Equation 3.3 that the outer angle α_o increases, while the inner angle α_i decreases. This change in geometry leads to the spring-in effect caused by out-of-plane anisotropy.

Not only the anisotropy in thickness direction causes distortion, but also in-plane anisotropy. This is obvious for asymmetric laminates regarding their midplane. In this case the chemical shrinkage and the thermal shrinkage are not constant through the thickness. The extreme of such anisotropy is the $[0^o/90^o]$ laminate, which is well investigated. For such laminates different stable geometries exist after curing. Figure 3.7 summarizes these shapes.

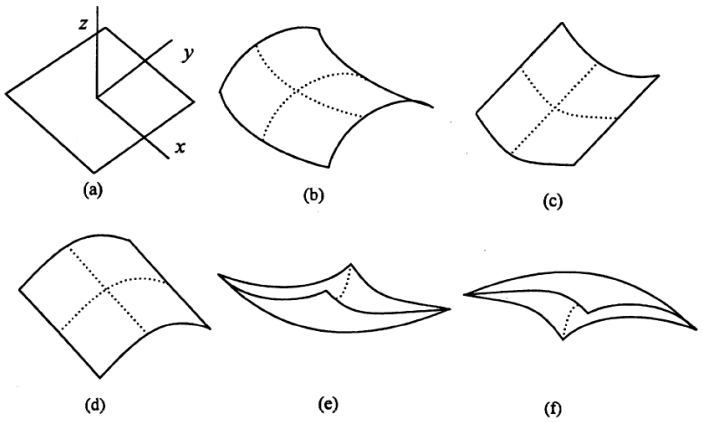

Figure 3.7.: Distorted shapes due to asymmetric layups; (a) original; (b) saddle shape; (c,d) cylindrical shapes (snap-through); (e),(f) rotated cylindrical.

While cross laminates with a small in-plane to thickness ratio lead to saddle shapes (a,b), cross laminates with larger in-plane dimensions show cylindrical shapes (c,d). This cylinders, however, show the snap-through phenomenon. Thus there are two stable cylindrical shapes with curvatures about the x- or y-axis. For angled laminates, angled cylindrical shapes are formed (e,f). These effects reduce with increasing laminate thickness. These effects can be avoided using symmetric laminates. However, even in symmetric laminates an anisotropy in

thickness direction can occur due to different fiber volume fractions. If prepregs are used for the manufacturing, usually it is necessary to remove excessive resin by an absorbtion fabric. The absorbtion fabric usually is applied on the side not facing the tool of the laminate only. Hence, resin is mainly removed on that side, while resin accumulation might occur at the tool side. This process causes a gradient of fiber volume fraction. While the chemical and thermal shrinkage is hindered by the high volume fraction at the top side of the laminate, the laminate at the tool side shows high shrinkage because of a low volume fraction. This leads to a concave warpage of the parts.

Curing shrinkage

Two types of shrinkage are distinguished - thermal and chemical. While the first is dependent on the coefficient of thermal expansion of the resin, which is a function of temperature and the level of cure, the second is a chemical property of the resin. During a curing process macromolecules are formed by a cross-linking process. Since these macromolecules show a higher molecule density than the originals, the volume of the polymer shrinks. This chemical shrinkage is assumed to be linearly dependent on the level of cure and the most important parameters are time, temperature and pressure [129]. The incorporated fibers hinder the chemical shrinkage in laminates, and residual stresses occur. This inherent stresses lead to distortions after demoulding. Chemical shrinkages of some polymers are summarized in Table 3.1.

Table 3.1.: Chemical shrinkage of several polymers.

Polymer	Chemical shrinkage [%]	Reference
Vinylester	> 6	[132]
Epoxy	$< 2 - 6$	[132]
Polyester	$5 - 10$	[132]
Phenole	$2 - 4$	[132]
Polystyrol	$0.3 - 0.8$	[38]

Svanberg und Holmberg [109] investigated experimentally the influence of the chemical shrinkage. Their results can be summarized as follows: A high percentage of the chemical shrinkage appears before the gelification, thus in the liquid phase. Because of that no stresses can be built up. This means that the higher the level of cure at the gelification point, the lower the shrinkage after gelification and the resulting residual stresses. Furthermore, Svanberg and Holmberg [109] related the shrinkage to the density development during curing. Figure 3.8 illustrats the density development during the curing process.

During the heating of the polymer the density decreases due to the thermal expansion (A-B). While the cross-linking takes place (B-C) the density increases. Cooling down the cured material (C-D) an increase of the density can be noticed due to the thermal contraction. Besides the shrinkage due to cross-linking a second chemical effect plays a role. The coefficient of thermal expansion is changed during curing, which is expressed in different slopes of the straight lines (A-B) and (C-D). The model for the overall volume shrinkage ΔV_m^c developed

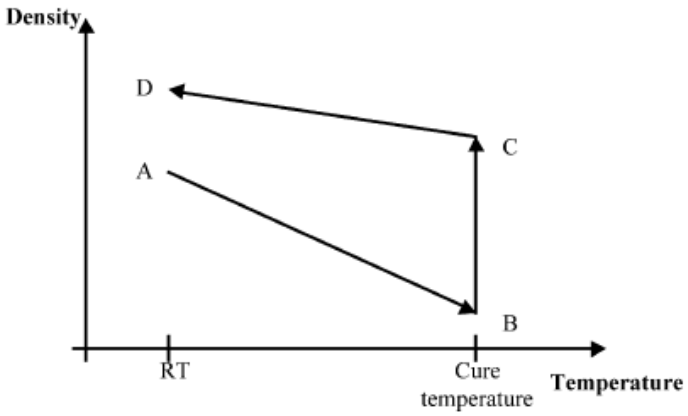

Figure 3.8.: Density development during curing. A-B: heating; B-C: curing; C-D: cooling [110].

by Svanberg and Holmberg based on this relationship can be described by Equation 3.4 and shows the temperature dependancies.

$$\Delta V_m^c = \frac{\rho_m^{liquid}(T_{cure}) - \rho_m^{cured}(T_{cure})}{\rho_m^{cured}(T_{cure})} \frac{1}{X(T_{cure})} \tag{3.4}$$

where ρ_m^{liquid} and ρ_m^{cured} are the mass densities of the resin before and after curing, T_{cure} is the curing temperature and X is the level of cure.
Another mechanism which leads to distortions is the temperature gradient of the composite during curing. Such a gradient might occur due to the external heating of the autoclave or the internal exothermic reaction of the polymer.

Tool-part interaction

The tool material used, is basically determined by the manufacturing process used. Especially if pressure and vacuum are applied, materials with high strength and stiffness have to be used to sustain the pressures of about 0.9 bar. Therefore steel or aluminum is often used as a mould material. However, these materials have coefficients of thermal expansion (CTEs) of about $12 \cdot 10^{-6}[1/K]$ to $20 \cdot 10^{-6}[1/K]$, which is much higher than those of carbon fiber composites (typically $1 \cdot 10^{-6}[1/K]$). If the part is compressing against the tool due to the elevated pressure and the tool and the part expand due to thermal expansion, the part is tensioned due to the high thermal expansion of the tool. Because of the friction between the tool and the part especially the layers near the tool are tensioned, while layers further away are hardly tensioned due to interlaminar slippage. This leads to a stress gradient in the laminate which is fixed during the curing. After demoulding the part will deform concavely due to the resulting bending moment M (Equation 3.5, Figure 3.9).

$$M = \frac{t}{2} \alpha_T \Delta T E b d_m \tag{3.5}$$

where t is the laminate thickness, b is the laminate width, α_T is the tool CTE, ΔT is the temperature change, E is the laminate Young's modulus and d_m is the laminate thickness influenced by the tool-part interaction. Darrow and Smith [52] determined d_m experimentally

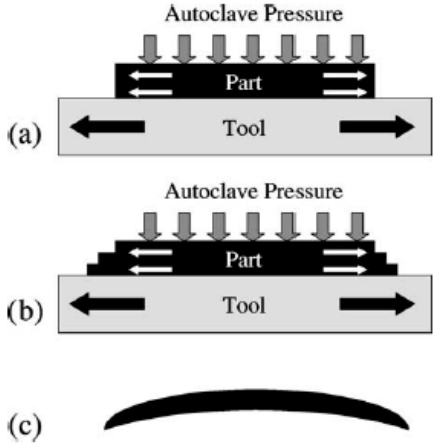

Figure 3.9.: Principle of the tool-part interaction. (a) Tensioning due to thermal expansion; (b) Stress reduction due to interlaminar slippage; (c) Warpage after demoulding [121].

to be 0.004 m, which is smaller than a fiber diameter. The physical explanation might be the slippage of the part on the tool and the reduced tensioning of the fibers with respect to the matrix. The quantity of the resulting warpage due to tool-part interaction is dependent on different process and material parameters such as pressure and temperature, or resin age and viscosity. A model predicting the out-of-plane deformation w_{max} due to tool-part interaction was developed by Twigg et al. (Equation 3.6).

$$w_{max} = \frac{2\tau_{Net}L^3}{E_{part}t_{Lam}^2} \tag{3.6}$$

where τ_{Net} is the difference of the stress transferred between tool and part and the stress transferred between the layers, L is the x-coordinate (x=L) at the part, t_{Lam} is the laminate thickness and E_{part} is the Young's modulus of the part. The curing pressure P is accounted for by Equation 3.7.

$$w_{max} \propto \frac{P^{0.2}L^3}{t^2} \tag{3.7}$$

Thus the tool part interaction strongly depends on the tool-part interfacial shear stress [122]. Therefore if the friction between tool and part can be reduced, the warpage can be reduced also. Furthermore, the tool geometry plays a significant role for the spring-in effect. For both, male and female tools, a spring-in effect is induced due to the out-of-plane contraction.

However, for a male part this effect is amplified by the tool-part interaction and the fiber volume fraction gradient. For a female tool, however, the spring-in effect is balanced (Figure 3.10). This effect is used as a countermeasure for the warpage effects (see Section 3.1.4).

Influence of the part geometry

The geometry of a part does not influence the appearance of warpage or spring-in effects, however, it has an influence on the magnitude of the warpage effect. Especially the x-y-direction to thickness ratio plays a key role. In general thicker parts show less distortions than thin-walled structures [5, 97]. Furthermore, it can be seen in Equation 3.1 that curved structures with increasing outer part angle Θ show increasing spring-in, which was verified by Huang [45], who investigated different angles of angle brackets regarding their spring-in angle.

Locally different fiber orientation

This effect plays only a secondary role for reinforcements with continuous fibers, however, short fiber reinforced materials are strongly affected. Different parameters such as the geometry, injection- and process factors and material properties were investigated by Kukula et al. [57].

Summary

In Table 3.2 the discussed causes, their principles, influences and controllability are summarized.

Table 3.2.: Summary of causes of manufacturing distortions.

Cause	Principle	Sensitivity	Controllability
Anisotropies	In-plane and out-of plane anisotropies lead to warpage and spring in.	very high	Hardly controllable in one layer and out-of plane. Symmetric layups
Chemical shrinkage	Chemical and thermal shrinkage lead to volume reduction of the resin. Not shrinking fibers lead to residual stresses.	very high	Only by choice of matrix material.
Tool-Part-Interaction	CTE mismatch between tool and part. Shear stress transfer to the part.	high	Tool material. Friction between tool and part.
Gradient of fiber volume fraction	Asymmetric behavior due to varying fiber volume fraction through thickness	high	Choice of manufacturing process.
Part geometry	Geometry has influence on warpage and spring-in magnitude	moderate	Limited by functional requirements.
Local fiber orientation	Inhomogenious material behavior caused by flow of material.	only in short fiber reinforced plastics	By geometry, injection and process factors.

3.1.3. Simulation of Cure Induced Shape Errors

To model the behavior of composite parts during the manufacturing process until demoulding, a lot of models have to be coupled. Mechancial, chemical, material, thermal and fluidic models are necessary to govern all effects. Most approaches neglect the fluidic and thermal models, thus the resin flow and the heat generation [133], conductivity and convective processes during cure. The fluidic models are especially relevant for short fiber reinforced plastics and their local fiber orientation, which has a negligible influence. These effects will not be considered further, since other effects, governed by the other disciplines, dominate. The mechanical models used are based on shell or classical laminate theory (CLT), or finite element formulations are used. The used chemical models might include the heat generation of exothermic cross-linking reactions and the relationship between degree of cross-linking and the glass transition temperature called DiBenedetto Equation [86] (Equation 3.8).

$$\frac{T_g - T_{g0}}{T_{g0}} = \frac{[\frac{\epsilon_X}{\epsilon_M} - \frac{F_X}{F_M}]X_C}{1 - (1 - \frac{F_X}{F_M})X_C} \tag{3.8}$$

where T_g and T_{g0} are the glass transition temperature and a reference glass transition temperature, ϵ_X/ϵ_M is the ratio of lattice energy for cross-linked and non-cross-linked polymers, F_X/F_M is the ratio of the segmental mobilities and X_C is the mole fraction of monomer units which are cross-linked in the polymer. This relationship is used in material models which consider temperature and the degree of cure-dependent coefficients of thermal expansion and coefficients of chemical shrinkage. There is a wide variety of models and their degree of idealization as has been pointed out in Section 2.

The implementation of geometry, material model and boundary conditions in finite element software is performed differently. Shell models [111] as well as solid [137] or hybrid models, to reduce the computational effort [104], were used. Depending on the geometry, shell models agree very well with solid models [111].
The boundary conditions between the mould and the part can be modeled in four different ways.

- **Free**
  The part is modeled free with only a constraint of the rigid body modes, thus there is no effect of the mould. This modeling technique in general overestimates the spring-in angles [107].
- **Fully constrained**
  The part is fully constrained at all nodes and simulates a full sticking to the mould. Regarding Svanberg [107], this kind of boundary condition agrees well with experimental data.
- **Contact elements**
  Using contact elements with a peel strength, the tool-part-interaction might be modeled in an accurate way [110].

- **Shear layer**
  It is possible to include a layer of elements between the part and the mould representing the shear stiffness. Tuning the shear stiffness, such a model can be well adjusted to experimental data [122].

The chemical cure shrinkage might be taken into account by an adjusted coefficient of thermal expansion in conventional finite element software. If a more complex material model is implemented, which is for example possible using the *UMAT* routine in the software *ABAQUS*, additional cure shrinkage coefficients can be implemented. The non-linear behavior of the material properties during the curing cylce have also been implemented in the material models of finite element codes by Svanberg et al. [109].

3.1.4. Countermeasures

There are several approaches to avoid or reduce warpage and spring-in effects which can be structured as follows:

- Improvement or optimization of the cure cycle.
- (Iterative) adjustment of the mould shape.
- Compensation of distortions by changing the layup.
- Use of composite mould.
- Pretensioning of fibers.

The **improvement of the cure cylce** was investigated already 20 years ago by White and Hahn [129]. By changing cure temperatures and dwell times, distortions were reduced up to 30%. The basis for this approach is the developement of the glass transition temperature and the other material properties such as the coefficient of thermal expansion and the Young's modulus during the curing process. During a typical two step curing process a first curing temperature is achieved in which the gelation takes place. At that time, the glass transition temperature is still very low. Thus, in a second step, the post cure which is at a higher temperature, the glass transition temperature is shifted higher and the material freezes in. Furthermore, relaxation effects play a role if the dwell times increase. In general the residual stresses increase with increasing cure temperatures, not only because of the increasing thermal shrinkage, but also because of increasing freezing-in stresses. However, it has to be guaranteed that at least a degree of cure of 95% is achieved to maintain the mechanical properties [129]. This can be achieved with longer dwell times.
While White and Hahn [129] investigated cure cycle parameter influences by a trial and error approach, Olivier and Cottu [88] applied an optimization formulation based on analytical models.
The **adjustment of the mould shape** can either be based on modeling and simulation or

on a trial and error approach, which leads to the iterative adjustment of the mould. Especially for angle brackets, the effects of tool-part interaction and the possible compensation approaches can be shown descriptive. Generally, female moulds are advantageous to reduce the distortions of curved parts. This can be traced back to the superposition of the warpage effect and the spring-in effect. The warpage effect always shows a convex distortion away from the tool, caused by tool-part interaction or fiber volume gradients. The spring-in effect, however, always leads to a reduction of the included angle, independent of the type of mould. This leads to a compensation of distortions for female tooling and an amplification of distortions for male tooling (Figure 3.10).

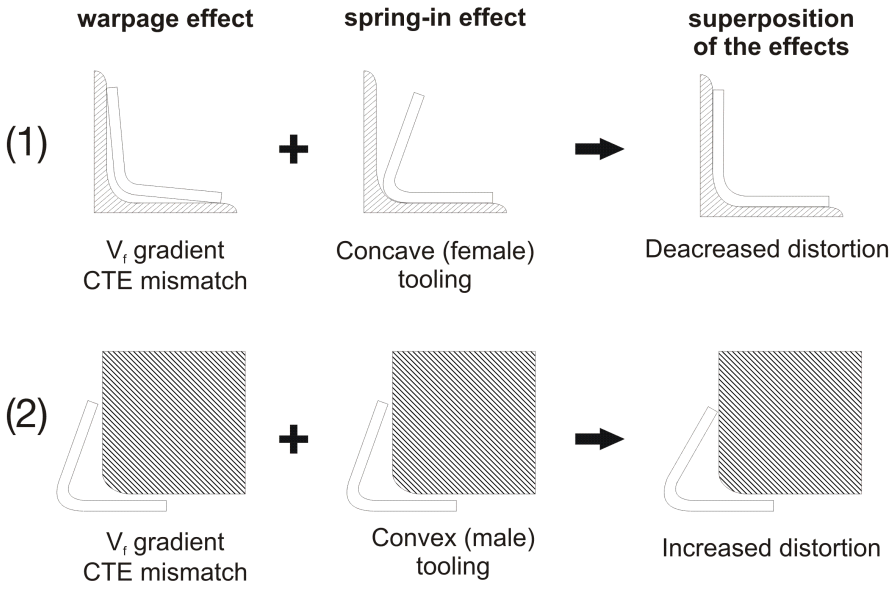

Figure 3.10.: Compensation (1) and amplification (2) of distortions through choice of tool.

This effect can be used to reduce spring-in angles by using proper tool materials with appropriate tool CTEs. Zhu et al. [137] reduced the spring-in angle from 0.72^o to 0.01^o by using a female mould with a CTE of $\alpha_{mould} = 25 \cdot 10^{-5}[1/K]$. The application of composite moulds makes use of the same effect. If the mould shows the same properties as the part, tool part CTE mismatch can be avoided.
Radford [96] and Huang [45] successfully demonstrated the approach of locally **changing the layup** to compensate spring-in.
The **pretensioning of fibers** during the curing process to reduce residual stresses and distortions is an expensive method. Furthermore, it is difficult to implement and not applicable for every structure.

3.2. Shape Adjustment using Patch Actuators

Depending on the structure, the necessary forces, and strokes, different actuator materials and devices can be used for structural control or shape adjustment. Different smart materials will be introduced in Chapter 5. A brief introduction for different mechanical principles for shape adjustment is given before concentrating on the used patch actuation.

3.2.1. Basic Actuation Principles

Two basic principles exist for the shape control of structures, which are used depending on the structure. For truss structures single rods are replaced by active rods. Their location is dependent on the controllability. The mechanical principle is the generation of internal forces in single truss members, which act directly on the truss nodes. A typical actuator which is used for this kind of actuation is the piezo-electric stack actuator. A sketch of this kind of actuation can be seen in Figure 3.11 (a).
If volumetric or 2D parts are considered the integration of such stack actuators is hardly possible. Especially for thin-walled structures, the actuators have to be attached from the outside to the structure or have to be very small. Furthermore, for thin-walled structures, the out-of-plane deformation usually is of interest, thus the in-plane load introduction in the neutral axis is useless. Two approaches to create this out-of-plane deformations can be applied - a perpendicular force F, or a bending moment M. Figures 3.11 (b) and (c) illustrate these two principles for a simply supported beam structure.

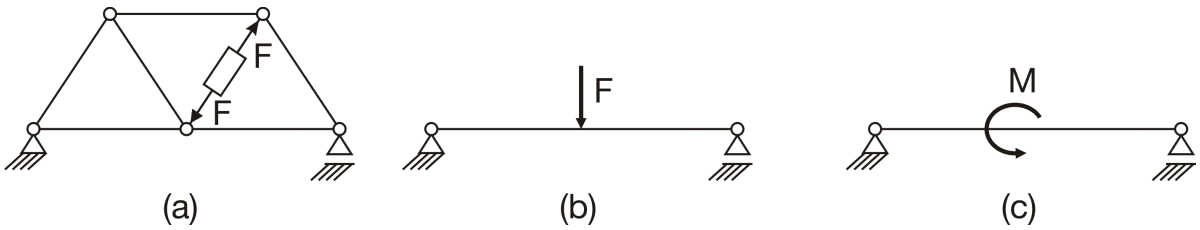

Figure 3.11.: Possible load introduction strategies for shape adjustment; (a) active strut (a) out-of-plane forces; (b) in-plane bending moments.

Classical actuators to introduce out-of-plane forces are stack actuators. However, a support for the actuator is needed, which is not possible in a lot of applications. For vibration attenuation *sky hook* dampers can be used, which use their inertia to create compensating forces. For the static shape control investigated here, the introduction of bending moments is advantageous. These moments can be introduced by forces parallel to the structural surface with a certain lever arm. For structures with a finite thickness, this is already the case for the load introduction at the surface, since there is a distance to the neutral axis of the structure. This mechanical relationship leads to the approach of patch actuators, which will be discussed in the following section in detail. Using such distributed actuator patches, it is possible to deform the structure and adjust its shape regarding the desired shape.

3.2.2. Mechanics of Patch Actuators

Patch actuators are small plates consisting of the actuation material, which are applied to or integrated in structures. Expanding or contracting, triggered by an external stimulus, they introduce forces F and bending moments M into the structure. The basic mechanical principle of patch actuation is illustrated in Figure 3.12.

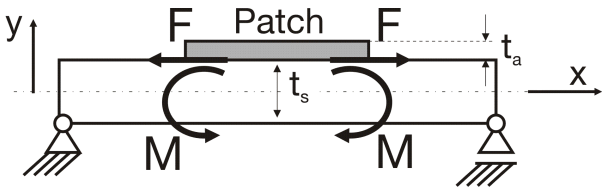

Figure 3.12.: Sketch of load introduction of a patch actuator into a beam structure including normal forces and bending moments.

Actuator patches are either surface mounted or integrated in structures, which is only possible for composite structures. Actuator patches which are integrated right below the structural surface have the advantage of an optimal load introduction due to the reduced structural stiffness and a maximum lever arm [31]. However, the focus here will be on surface mounted patch actuators due to the considered thin-walled structures, the better accessability, the simpler application process, and the limited minimal actuator thickness due to manufacturing restrictions. Surface mounted actuator patches are mostly attached by a structural adhesive. Thus there is an assembly of three materials with different properties and thicknesses. This leads to a design space which, for the general case, cannot be captured analytically. However, depending on different assumptions and restrictions, different analytical models can be established. Figure 3.13 shows assumed strain distributions for the different models.

Figure 3.13 (a) and (b) illustrate a model of constant strain in the actuator patches. This is valid for normal strain only or bending if the structure is much thicker than the actuator patch. Furthermore, a perfect bonding is assumed in this model, and shear deformation of the structure and the actuator is neglected. Figures 3.13 (c) and (d) show the Euler-Bernoulli theory incoorporating linear strain distribution in the actuator patches for the bending case. Again, a perfect bonding is assumed and shear is neglected. Figures 3.13 (e) and (f) incorporate the shear effect, which cannot be described analytically. For this case finite element models can be used. To describe the mechanical behavior of such a load introduction, and to introduce the necessary parameters, the simplest case of the model with constant strain distribution is considered first. The following considerations and analytical derivations are an excerpt of a book of Elspass and Flemming [31].

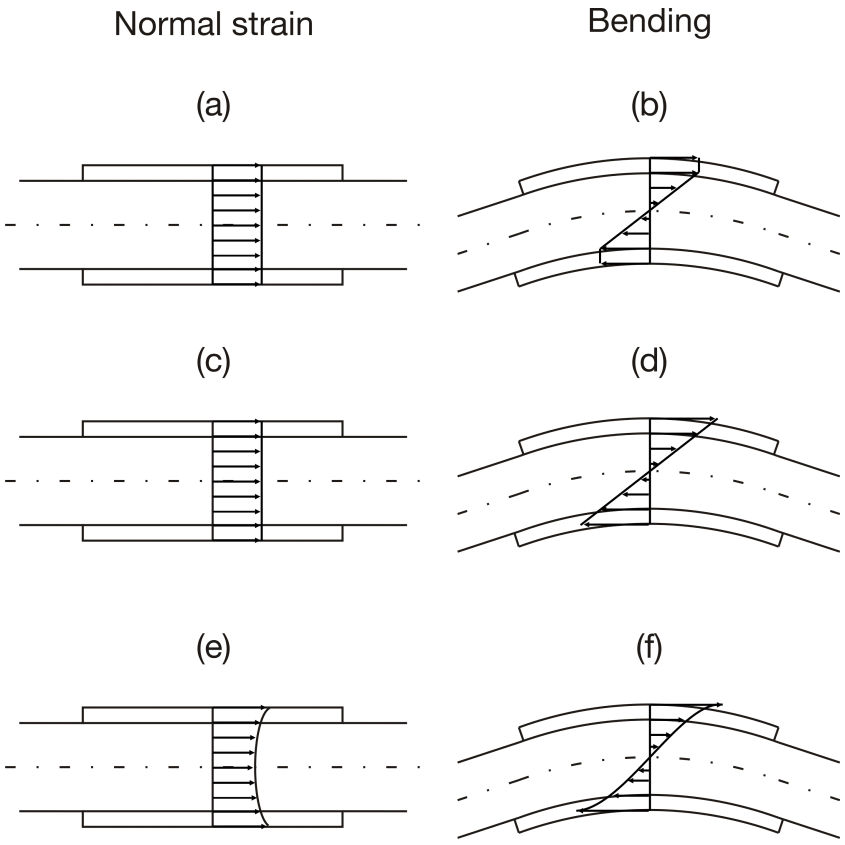

Figure 3.13.: Model assumptions for the strain distribution in beams for normal strain and bending; (a,b) constant strain in actuator; (c,d) Euler-Bernoulli beam; (e,f) including shear

Constant strain
Assumptions:

- Infinite stiffness of bonding layer.
- Strain is constant in actuators; bending stiffness of actuator is neglected.
- Shear deformations are neglected.

Consider a structure-actuator setup as shown in Figure 3.13(b). A structure with a thickness t_s is equipped with two actuator patches a, at the top and bottom side. The actuator patches are operated in opposing directions (compression and tension) and introduce forces F into the structure. Assuming infinite shear stiffness and infinite bonding stiffness the resulting bending moment M can be calculated by Equation 3.9.

$$M = -Ft_s \tag{3.9}$$

The bending stress in a beam is defined as:

$$\sigma_s(z) = -\frac{MzE_s}{(EI)_s} \tag{3.10}$$

where z is the thickness and I is the moment of intertia of the structure. The corresponding strain is:

$$\varepsilon_s = \frac{\sigma_s}{E_s} \tag{3.11}$$

The actuator stress can be defined as:

$$\sigma_a = -\frac{F}{A_a} \tag{3.12}$$

where A_a is the cross-section of the actuator patch. The actuator strain ε_a is composed of an elastic component and the actuation strain Λ:

$$\varepsilon_a = \frac{\sigma_a}{E_a} + \Lambda \tag{3.13}$$

At the interface, the compatibility requirement 3.14 applies:

$$\varepsilon_s \stackrel{!}{=} \varepsilon_a, \text{ for } z = \frac{t_s}{2} \tag{3.14}$$

Inserting Equations 3.9 to 3.13 into Equation 3.14, leads to the resulting force F of:

$$F = \frac{\Lambda}{\frac{t_s^2}{2(EI)_s} + \frac{1}{(EA)_a}} \tag{3.15}$$

Inserting 3.15 into Equation 3.11 leads to the actuator strain and the structural strain at the surface (Equation 3.16).

$$\varepsilon_a = \varepsilon_s(\frac{t_s}{2}) = \frac{\Lambda}{1 + \frac{2(EI)_s}{(EA)_a t_s^2}} \tag{3.16}$$

If a rectangular cross section of the structure is assumed, the moment of intertia I is:

$$I = \frac{A_s t_s^2}{12} \tag{3.17}$$

A stiffness ratio Ψ can be defined as:

$$\Psi = \frac{12(EI)_s}{t_s^2(EA)_a} = \frac{(EA)_s}{(EA)_a} \tag{3.18}$$

Thus, Equation 3.16 simplifies to:

$$\varepsilon_a = \varepsilon_s(\frac{t_s}{2}) = \frac{6\Lambda}{6+\Psi} \tag{3.19}$$

For pure bending the curvature of the structure can be calculated by:

$$\kappa = \frac{\varepsilon(t_s/2)}{t_s/2} = \frac{2}{t_s}\frac{6\Lambda}{6+\Psi} \tag{3.20}$$

It can be noticed that the introduced curvature κ, and therefore strain ε, increases with decreasing structural thickness t_s and stiffness ratio Ψ. This relationship is shown in Figure 3.14 for a range of interest.

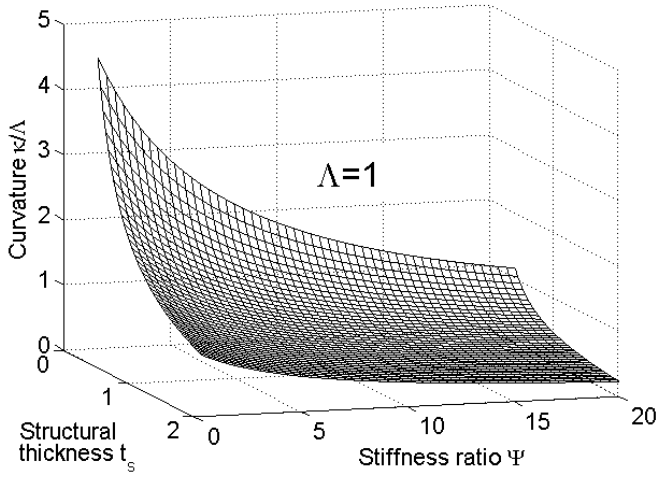

Figure 3.14.: Normalized curvature introduced by patch actuators as a function of structural thickness t_S and stiffness ratio Ψ (constant strain model, $\Lambda = 1$).

Euler-Bernoulli model
Assumptions:

- Infinite stiffness of bonding layer.
- Bending stiffness of actuator is considered.
- Shear deformations are neglected.

With the same calculating steps as for the constant strain model and the integration of the bending stiffness of the actuator, the introduced curvature calculates to:

$$\kappa = \frac{\varepsilon(t_s/2)}{t_s/2} = \frac{6(1+\frac{1}{T})\Lambda(\frac{2}{t_s})}{(6+\Psi)+\frac{12}{T}+\frac{8}{T^2}} \tag{3.21}$$

This equation is similar to Equation 3.20 for the model with constant strain, however, it includes additional terms of the thickness ratio T:

$$T = \frac{t_s}{t_a} \tag{3.22}$$

where t_a is the actuator thickness and t_s is the structural thickness. If the actuators are thin compared to the structure (large T), these terms have negligible influence and Equation 3.21 simplifies to Equation 3.20. When the actuator thickness increases (small values of T), the influence increases and the possible introduced curvature becomes zero. This behavior is illustrated in Figure 3.15. Furthermore, the decreasing curvature with an increasing ratio of Young's moduli can be seen.

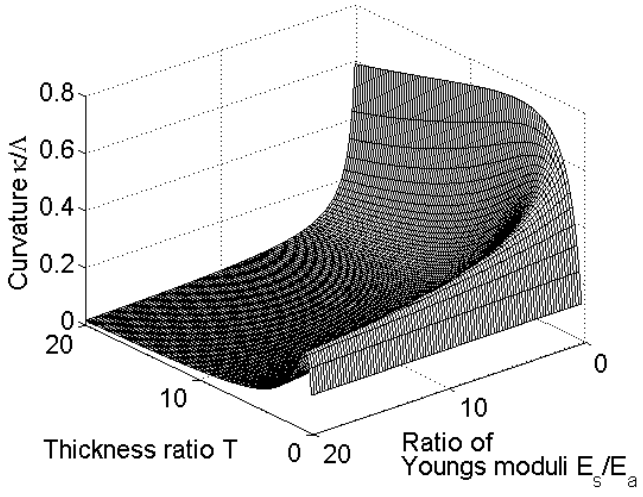

Figure 3.15.: Normalized curvature introduced by patch actuators as a function of the thickness ratio T and the ratio of Young's moduli E_S/E_A (Euler-Bernoulli model).

From Figure 3.16 it can be seen that for large thickness ratios T, the constant strain model predicts almost the same load introduction as the Euler-Bernoulli model. However, for small thickness ratios T the models diverge. For the Euler-Bernoulli model the considered increase of the bending stiffness due to the actuator patch leads to the reduction of the introduced curvature. For the constant strain model this decay is not apparent and the introduced curvature further increases due to higher actuation forces.

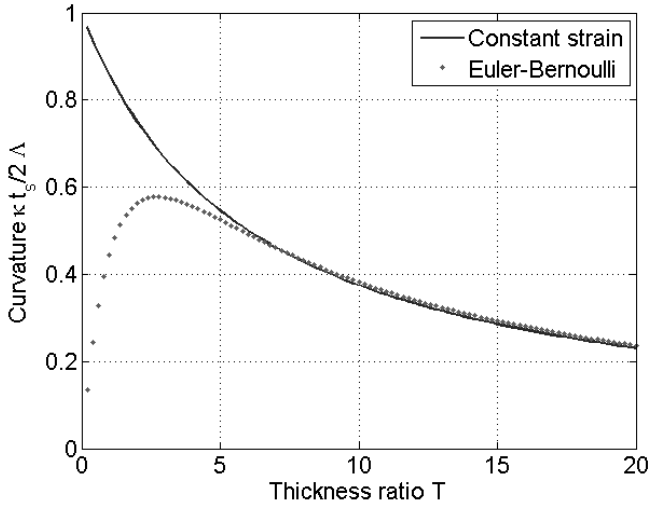

Figure 3.16.: Normalized curvature introduced by patch actuators as a function of the thickness ratio T for a constant strain model and the Euler-Bernoulli model.

Shear lag in the bonding layer

The influence of the bonding layer is included by a shear coefficient Γ. For the constant strain model, it is defined as:

$$\Gamma^2 = \frac{\frac{G_b t_b}{E_a t_a}}{(\frac{t_b}{l_a})^2}(\frac{2+\Psi}{\Psi}) \tag{3.23}$$

where G_b and t_b are the shear modulus and the thickness of the bonding layer respectively, and l_a is the length of the actuator. For the Euler-Bernoulli model, the shear coefficient is defined as:

$$\Gamma^2 = \frac{\frac{G_b t_b}{E_a t_a}}{(\frac{t_b}{l_a})^2}(\frac{6+\Psi+12/T+8/T^2}{\Psi(1+1/T)}) \tag{3.24}$$

It can be seen that with increasing bonding layer shear stiffness G_b, and decreasing thickness ratio of the bonding layer t_b/l_a, the shear coefficient increases, which is beneficial for the load introduction (see Equation 3.25 and Figure 3.18).

The influence of the thickness ratio T and the stiffness ratio Ψ on the shear coefficient is illustrated for the Euler-Bernoulli model in Figure 3.17.

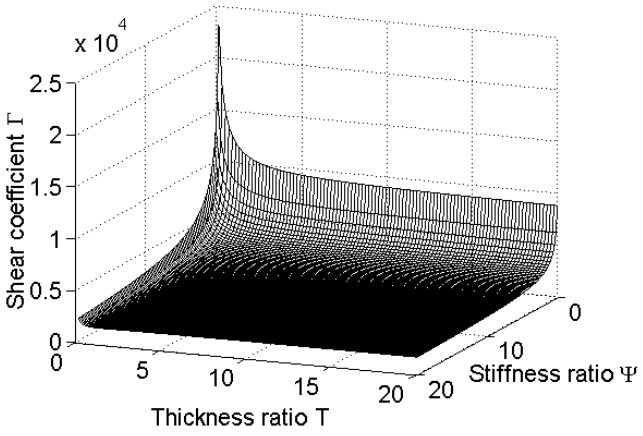

Figure 3.17.: Shear coefficient vs. the stiffness Ψ and thickness ratios T.

It can be seen that decreasing stiffness and thickness ratios lead to decreasing shear lag coefficients. For conventional stiffness ratios and bonding layer properties, the shear coefficient is still high enough to neglect the bonding layer influence. For very high stiffness ratios the behavior changes as shown in Chapter 8. The influence of the shear coefficient on the introduced curvature can be described by Equation 3.25:

$$\frac{\kappa_{shear}}{\kappa} = 1 - \frac{1}{\Gamma} \cdot \frac{sinh(\Gamma)}{cosh(\Gamma)} \tag{3.25}$$

Figure 3.18 illustrates this relationship.

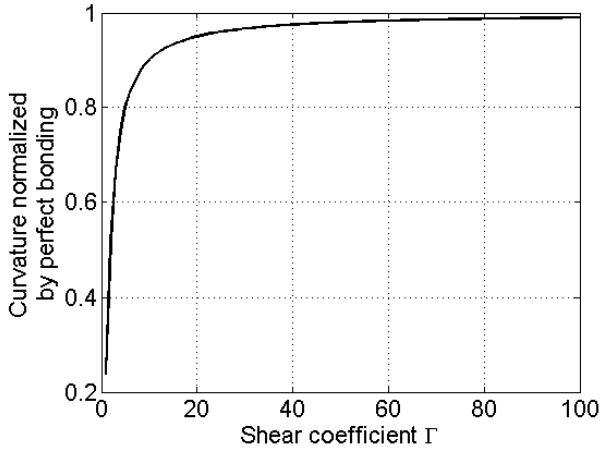

Figure 3.18.: Influence of the shear coefficient on the introduced curvature.

With an increasing shear coefficient, the influence of the bonding layer can be neglected.

To summarize, patch actuation is a well understood and established method for shape adjustment purposes (see also Chapter 2). However, all introduced applications, investigations and analytical models are based on several assumptions, which do not apply for soft actuation materials and very low thickness ratios $T < 1$ which are present for the SMP actuator patches. In Chapter 8 the case of the SMP - fiber composite interface will be discussed in detail, and it will be shown that finite element models considering shear lag and the adhesive layer are necessary.

3.3. Shape Memory Polymers (SMPs)

In this section, the fundamentals of shape memory polymers (SMPs) will be introduced. An overview of SMPs is given first, followed by the introduction of different chemical structures. In a further subsection, the thermomechanical behavior is described in detail before, in subsection 3.3.4, the modeling of this behavior is discussed. Finally, shape memory composites (SMCs) and different applications are introduced.

3.3.1. Overview

The shape memory effect describes a macroscopic shape change of a material due to an external stimulus. The *one-way* shape memory effect (SME) was discovered by Chang and Read [18] in the 1950s. Chang and Read discovered diffusionless phase changes in a gold-cadmium alloy. However, much more attention was paid to the shape changing properties of these materials when, in 1963, Buehler et. al. [14] introduced the *two-way effect* in titanium-nickel alloys (Nitinol). Due to phase changes between the martensitic and austenitic phase, the alloys undergo macroscopic shape changes. This phenomenon is triggered by heat or mechanical stress. Besides this most popular class of shape memory materials, there are others such as ceramics or the polymers discussed here. Comprehensive overviews on the topic of shape memory materials can be found in the review papers of Wei and Sandström [126, 127]. The focus of this work is on shape memory polymers (SMPs), which are a relatively new class of smart materials. Although the qualitative macroscopic behavior of shape memory polymers (SMPs) and shape memory alloys (SMAs) is very similar, the underlying physical and chemical processes and the thermomechanical properties are different.
Shape memory polymer (SMP) development started in the 1960s with shape changing properties, called *shrinkable materials* [62]. In recent years, polyurethane- and polysytrene-based systems as well as epoxies, are treated as shape memory polymers. The shape memory effect in polymers is a result of the structure, the morphology, and the processing of the material. Its macroscopic behavior can be described by a thermomechanical cycle. Figure 3.19 shows a thermomechanical cycle of a SMP sample stimulated by integrated heating wires. Heated above a transition temperature T_{trans}, the sample is deformed mechanically. Mechanically

constrained cooling below T_{trans} leads to the freezing of the sample in its temporary, programmed shape. (*Programming* describes the process of mechanically deforming the shape memory material into its temporary shape.) After a storage time t_s the sample is stimulated by a temperature above T_{trans} and the sample returns to its permanent shape (recovery). The thermomechanical cycle will be described in detail in Section 3.3.3.

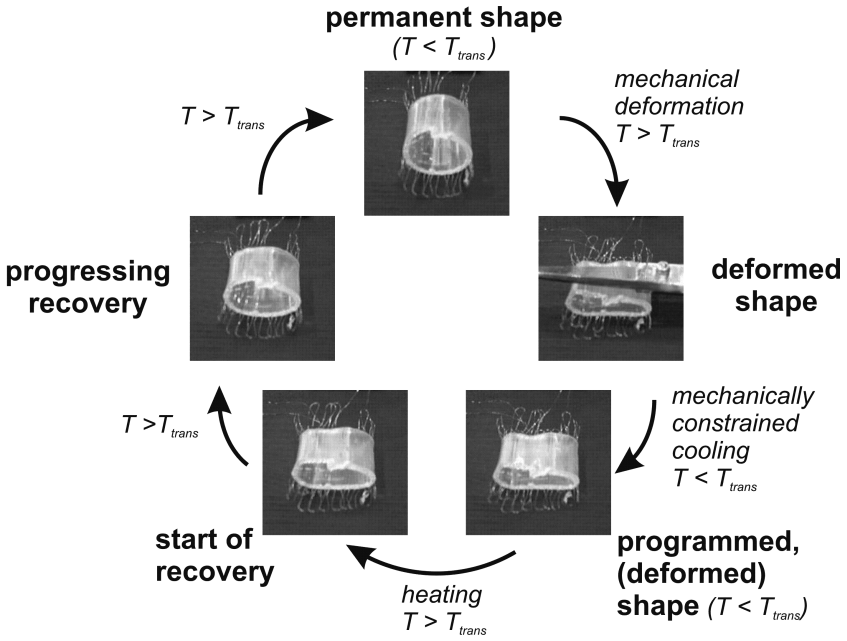

Figure 3.19.: Unconstrained recovery cycle of an SMP sample with integrated heating wires.

The molecular mechanism behind the shape memory effect in polymers is the use of network chains as molecular switches. This is possible if the stiffness of the segments is a function of the temperature. One possibility is a transition from the stiff to the flexible state at a transition temperature T_{trans}. After deforming the polymer in its flexible state and switching to the stiff state by cooling, the crystallized segments avoid the immediate return to the permanent shape. Lendlein and Kelch [62] gave a comprehensive overview of the underlying physical and chemical processes for different types of shape memory polymers. Section 3.3.2 will give an introduction on the underlying chemical structures. Although, infrared light, electricity and chemical solutions can be used as a stimulus [64, 66], the most common stimulus is heat.
Shape memory polymers show some unique properties, which make them an interesting class of smart materials. They are able to recover large strain of typically up to 400%. The achieved recovery stresses are typically in the range of 5 MPa. With the low mass density of approximately 1 g/cm^3 this leads to specific energy densities of about 0.1 J/g, which is competitive with other smart materials (Shape memory alloys: $\approx$ 0.15 J/g, Piezoelectric stack actuators: $\approx$ 0.002 J/g). Their lightweight properties are advantageous, especially for space applications. Since conventional curing processes for polymers can be used, their manufacturing into arbitrary shapes is easy and cheap. The field of polymer chemistry furthermore offers the possibility of tailoring the properties of SMPs. The variety of properties

make the material very interesting in the use of a variety of applications.
Especially significant applications have arisen in medical devices and space applications in recent years. For example tailoring biocompatible polymers with shape memory properties led to shape memory polymer stents. In addition the very high recovery strains and low mass density led to the investigation and application of space deployable structures. Reinforcement with carbon fibers, resulting in shape memory composites (SMCs), leads to a great potential in the area of deployed structural members.

3.3.2. Chemical Structures of SMPs

To avoid missunderstanding of the terminology, it shall be noted that in this chapter the terminology *structure* denotes the chemical structure of a polymer. Some basic information about the chemical structure of SMPs will be given in this section. There are two structural requirements which have to be fulfilled by an SMP.

1. Primary cross-links for distinct shape
For shape memory polymers to be used as active members of a smart stucture they have to be solid and show a distinct shape. In polymers this is achieved by cross-linking several polymer chains. The primary cross-links are either covalent networks (chemical bondage) leading to thermoset materials, or physical networks leading to thermoplastic polymers. The first exhibit irreversible polymer networks, while the second can be thermally and solvent processed due to their strong interactions of the chain cross-links. Figure 3.20 illustrates such polymer networks.

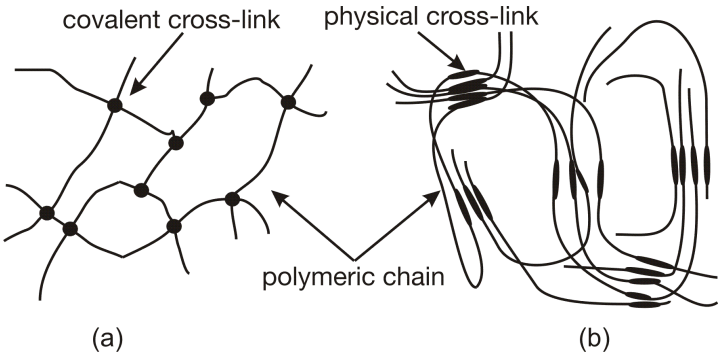

Figure 3.20.: Polymer networks; (a) covalently cross-linked; (b) physically cross-linked

2. Polymer segments and secondary cross-links

The second component which is responsible for the behavior of SMPs are the polymer segments between the primary cross-links. In an unconstrained state and above the glass transition temperture T_g, these segments pull the network points to each other to achieve the entropically favored state of low order. Deforming the material leads to an orientation of these segments in load direction. The fixation of the segments in the reoriented state is

the main principle of the shape memory effect in polymers. Within the polymeric chains, different segment types can be found. The soft segments, with their low glass transition temperature, are responsible for the highly elastic nature of SMPs. The hard segments are glassy for the whole desired temperature range and are responsible for the solid shape of the polymer. The switching segments, however, change their properties when triggered by a stimulus. This might be UV-light, solvents or radiation, but mostly heat is used. The mobility of these switching elements is changed with the crossing of its glass transition temperature or melting temperature. Both leads to the building of secondary physical cross-links, which are temporary and responsible for the fixation in the deformed state. This fixation is often called *freezing*. Figure 3.21. illustrates such a switching mechanism in an SMP. Comprehensive overviews about chemical structures and chemical and physical mechanisms of SMPs are given in [62, 63].

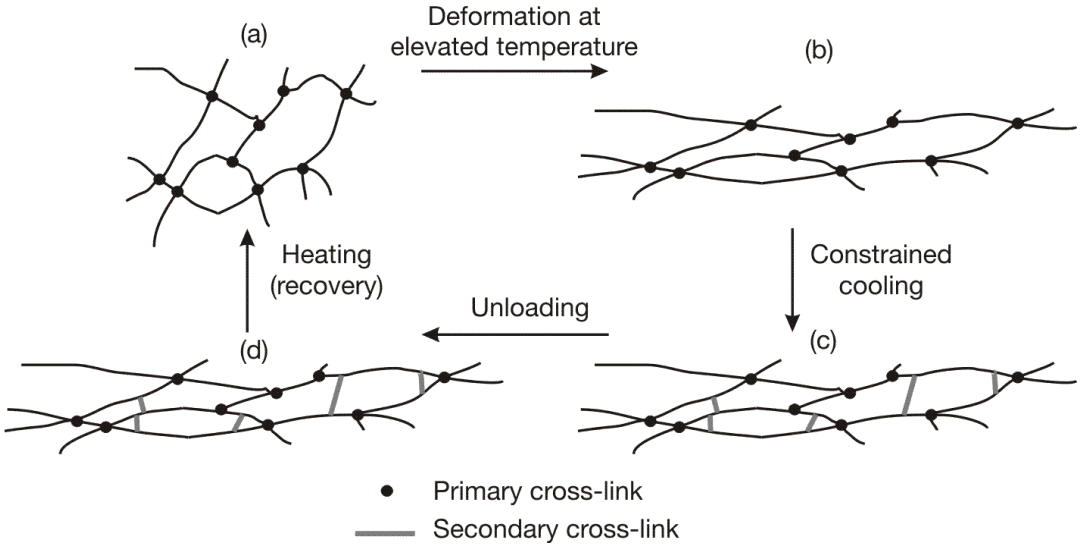

Figure 3.21.: Micromechanism of building secondary cross-links in the thermomechanical cycle of SMPs; (a) permanent shape; (b) deformed shape; (c) building of secondary cross-links; (d) frozen, temporary shape.

Covalently cross-linked SMPs

Due to their covalent primary cross-links, this type of SMP shows permanent cross-links leading to very attractive properties. In comparison with thermoplastic (physically cross-linked) SMPs they hardly show creep or relaxation effects. This leads to very good recovery properties such as the fixation ratio, recovery ratio and energy densities. SMPs based on polyolefines, polyurethanes, polyacrylates, polystyrene and polysiloxanes are reported [63].
Polyolefines are one of the first reported materials with heat-shrinkable properties, which appeared in the 1960s. Membranes and tubes were manufactured for different applications such as packaging of food or isolation of electrical cables. Polyurethanes (PUs) possess a large variety of properties, which they gain through a large number of possible additives and components, which make PUs the most common SMPs. Especially for medical applications, PUs are attractive due to their biocompatibility and their high definition properties. Simi-

larly polystyrenes (PSs) show a large variety in their possible copolymers which make them attractive for different applications as well. Throughout this work, the polystyrene based shape memory polymer called *Veriflex* manufactured by *CRG Industries* is used, which is a covalently cross-linked, thermoset polymer. The material is available as a two part resin system, or as wrought material as quadratic cured plates of the dimensions of 300 mm $\times$ 300 mm $\times$ 3 mm. *CRG Industries* quotes the composition given in Table 3.3.

Table 3.3.: Composition of *Veriflex* resin.

Component	Amount [%]
Styrene monomer	50
Styrene block copolymer	< 50
Proprietary mixture	< 20

Additional information about the properties can be found in the material datasheet provided by *CRG Industries* (Appendix A.7).

Physically cross-linked SMPs
Several types of SMPs of this group have been reported [63]. For example, polyurethanes (PU)- and polystyrene (PS)-based SMPs can be found. PU is the most discussed foundation of SMPs in the community of smart materials. Due to their versatile structure, PUs offer a lot of possibilities of polymeric tailoring and a large variety of shape memory properties. PU-SMPs were discovered by Mitsubishi Heavy Industry in the 1980s, their difference to conventional PUs is the composition of hard and soft segments in the polymer chains. Two classes can be distinguished - segmented PUs and multiblock PUs. Segmented PUs are synthesized from three raw materials. These are di-iso-cyanate, long chain polyether and a short-chain chain extender. While the di-iso-cyanate and the long chain extender build the hard segment, the long chain polyether builds the soft segment. The class of multiblock PUs are built by di-iso-cyanate, a long chain polyether with a high glass transition temperature for the hard segment, and a long chain polyether with a low glass transition for the soft segment. Further information, including the synthesis steps and the exact chemical compositions, can be found in [63].

3.3.3. Thermomechanical Characterization of SMPs

The shape memory effect in polymers can be described by a thermomechanical cycle. Depending on the mechanical boundary conditions, different thermomechanical cylces can be observed. At first the unconstrained, free recovery cycle of a tensile sample is introduced. In this case there is no mechanical constraint of the material during the recovery. Figure 3.22 illustrates this case.

After conventional curing, leading to the permanent shape of the polymer, it is heated well above its transistion temperature T_{trans} (I). Tensile straining (programming) (1) of the

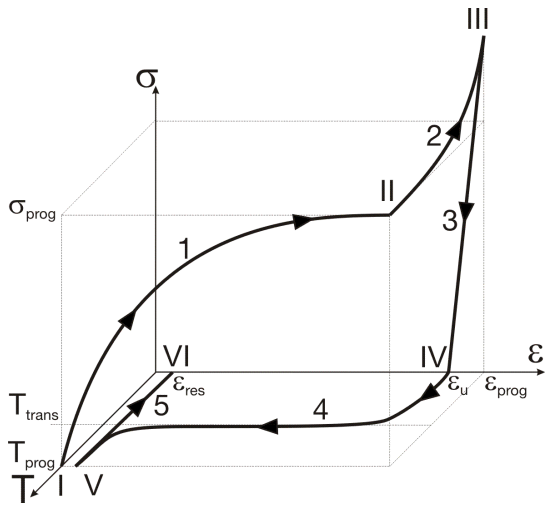

Figure 3.22.: Illustration of a free recovery cycle of a tensile sample in a stress-strain-temperature diagramm; 1: programming, 2: freezing, 3: unloading, 4: recovery, 5: cooling

sample leads to an increasing stress σ, ending up with the programming strain ε_{prog} and programming stress σ_{prog} (II). Constrained cooling (2) leads to an increase of the stress due to thermal contraction (III). Unloading (3) leads to a slight reduction of the deformation due to the elasticity of the material. After this *programming* procedure the sample shows the unconstrained programming strain ε_u (IV). Mechanically unconstrained heating (4) and subsequent cooling (5) leads to a free recovery of the sample resulting in a residual strain ε_{res} (VI).
The ratio of the unconstrained programming strain ε_u and the programming strain ε_{prog} is called fixation ratio ζ and is defined as:

$$\zeta = \frac{\varepsilon_u}{\varepsilon_{prog}} \tag{3.26}$$

Tobushi et al. [115] investigated the fixation ratio by thermomechanical cycling tests. They found out that the shape fixation ratio is about 99% for high programming strain ε_{prog}. The same is observed for the experiments performed during this study. Hence, in the following, the deformation reduction due to elasticity is neglected, and the programming strain ε_{prog} is used as reference strain for the recovery. More information about the residual strain ε_{res} and the resulting recovery strain ε_r and their definitions will be given in Chapter 5.
The other extreme of the thermomechanical cycle is the fully constrained recovery. This case is illustrated in Figure 3.23 for a tensile sample. Steps 1 to 3 are the same as for the free recovery cycle. Starting from the programmed state (IV), the mechanically fully constrained sample is heated well above T_{trans} to the recovery temperature T_r, which is not necessarily the same as the programming temperature T_{prog} (4). During this process the memory effect and the thermal expansion are superimposed, which might lead to compression stresses or

buckling of samples at the beginning of the recovery. Ending up with the blocking stress σ_{block} (Equation 5.3) (V) the recovery is completed. Cooling (5) the sample to room temperature (RT $\approx 21^oC$) leads to an increase of the tensile stress due to thermal contraction. The resulting stress σ_{act} (Equation 5.5) is used for the patch actuation in the shape adjustment process. The highly non-linear behavior of the process, depending on the temperature-dependent Young's modulus $E(T)$, the coefficient of thermal expansion (CTE), the shape memory effect and a tensile or compression mode, will be discussed in more detail in Section 5.

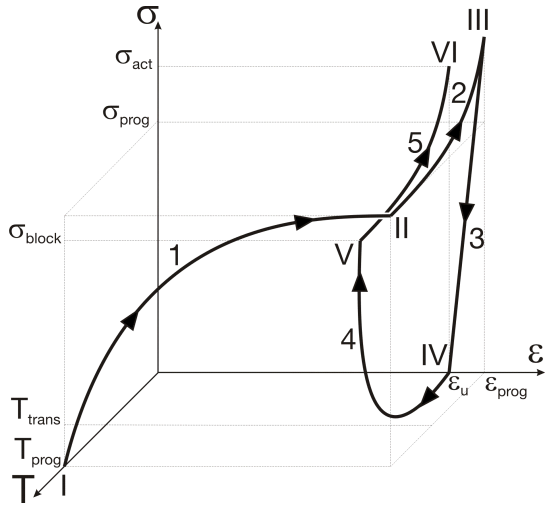

Figure 3.23.: Illustration of a fully constrained recovery cycle of a tensile sample in a stress-strain-temperature diagramm; 1: programming, 2: freezing, 3: unloading, 4: recovery, 5: cooling

These two thermomechanical cycles are the most common ones and usually found in the literature. However, in real applications, a balance between recovery stress and recovery strain is achieved depending on the applied load. The result is a recovery cycle between the two extremes of free recovery or fully constrained recovery. Figure 3.24 illustrates such a cycle for a tensile sample. Steps 1 to 3 are the same as before. However, with beginning recovery, recovery strain and stress progress (4), ending up at an arbitrary point on the load curve with a recovery stress σ_r and a residual strain ε_{res} (V). The cooling (5) to room temperature (RT $\approx 21^oC$) leads to a new balance of stress and strain (VI).

This loaded cycle is hardly found in the literature. However, it is essential to determine actuation properties of shape memory polymer actuators and the resulting energy densities. Since energy is a product of force and stroke, thus stress and strain respectively, a fully constrained recovery or a free recovery always leads to an energy output of zero. Only if loaded recovery is performed a real energy output is generated. In Section 5 an experimental procedure is introduced which is capable of determining energy outputs of shape memory polymer actuators for arbitrary working points.
The three introduced, typical thermomechanical cycles, are shown for the tensile mode. For compression, however, the behavior is different. While for tension the shape memory effect

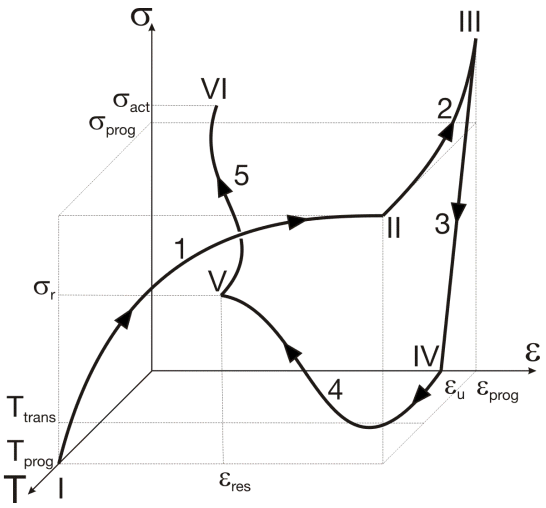

Figure 3.24.: Illustration of a loaded recovery cycle of a tensile sample in a stress-strain-temperature diagramm; 1: programming, 2: freezing, 3: unloading, 4: recovery, 5: cooling

and the thermal compression add during freezing, for compression the two effects counteract each other. This effect is shown for a representative, fully constrained recovery cycle (Figure 3.25). The absolute values of stress and strain are plotted for better comparison with the tensile case.

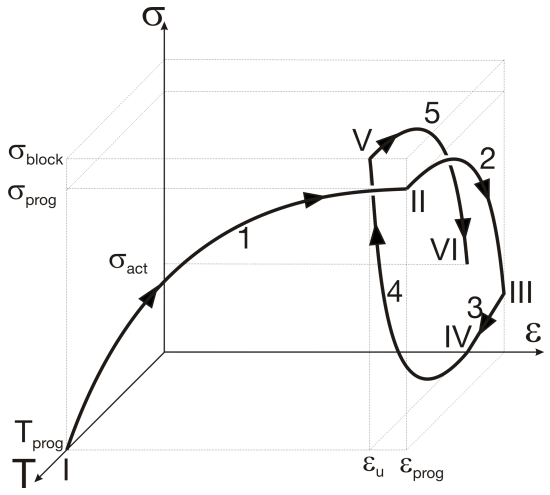

Figure 3.25.: Illustration of a fully constrained recovery cycle of a compression sample in a stress-strain-temperature diagramm; 1: programming, 2: freezing, 3: unloading, 4: recovery, 5: cooling

Compression at the elevated temperature T_{prog} (1) leads to the programming strain ε_{prog} and the programming stress σ_{prog} (II). Freezing in (2), the deformation, however, leads in contrast to the tensile case to a reduction of the stress due to the thermal compression (III). Unloading

the sample leads to the unconstrained programming strain ε_u (IV). Due to the superposition of thermal expansion and the compression shape memory effect, the recovery (4) leads in general to higher blocking stresses σ_{block} for compression than for tension (V). However, due to cooling to room temperature (5), the stress decreases to the actuation stress σ_{act}, which is used for the patch actuation. Hence, in general, compression actuation stresses are smaller than tensile actuation stresses. This is one of the reasons, why compression actuators are disadvantageous for patch actuation. However, compression actuators have other advantages, which lead to a complementary mode to tensile actuators and an extended working field of the material.
More details on thermomechanical properties, experimental procedures and figures of merit of SMPs are given in Chapter 5.

3.3.4. Modeling of the Thermomechanical Behavior of SMPs

In this subsection different constitutive models, which were developed in the past, are introduced.
All described models are based on viscous models, called standardized linear visco-elastic (SLV) models, including elasticity and damping (Figure 3.26).

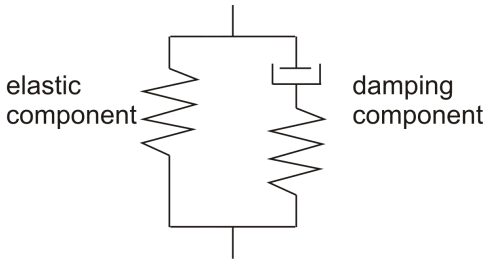

Figure 3.26.: Standardized linear viscoelastic (SLV) model

The system contains three elements. An elastic element and a parallel spring-damper system. The differential equation to describe such a model is:

$$\dot{\varepsilon} = \frac{\dot{\sigma}}{E} + \frac{\sigma}{\mu} - \frac{\varepsilon}{\lambda} \tag{3.27}$$

where ε is the strain, σ is the stress, E is the Young's modulus, μ is the viscosity of the material, and λ is the retardation time. This model was adapted to the behavior of SMPs by Tobushi et. al. [116].

$$\dot{\varepsilon} = \frac{\dot{\sigma}}{E} + \frac{\sigma}{\mu} - \frac{\varepsilon - \varepsilon_S}{\lambda} + \alpha\dot{T} \tag{3.28}$$

where ε_S, α and $\dot{T}$ denote the creep irrecovery strain, the CTE and the temperature change. The coefficients of this model are dependent on the ratio of temperature T and transition

temperature T_{trans}. This model is simple to implement and the computational effort is small. However, only 1D elements can be modeled and it was only verified in a strain range of up to 10%. A 3D thermomechanical model was developed by Liu et al. [73]. This model is based on the storage of the entropic strain energy in the frozen state and the release during heating. The frozen fraction function was determined by 1D experiments. A 3D finite strain model was developed by Diani et al. [28].
Another visco-plastic model, developed by Abrahamson [1], is a modification of the *Valanis Model* (see fig. 3.27). The model was modified in such a way that the parameters are temperature dependent.

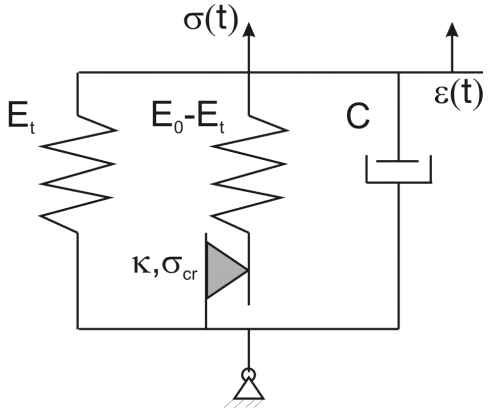

Figure 3.27.: Visco-plastic model [1]

The model incorporates two elastic elements, a viscous damping element and a friction slider element. Depending on the parameter κ which is restricted in the range of $0 \leq \kappa \leq 1$, the friction slider element is either fixed or free. The slip-stick stress σ_{cr} describes the transition from elastic to a plastic state and depends on the temperature. For a temperature $T \geq T_{trans}$ the slip-stick stress σ_{cr} diminishs. The *Valanis Model* is governed by the following differential equation.

$$\dot{\sigma}(t) = E_0\dot{\varepsilon}(t)\{\frac{1+\frac{sgn(\dot{\varepsilon}(t))}{\sigma_{cr}}(E_t\dot{\varepsilon}(t)-\sigma(t))}{1+\frac{\kappa sgn(\dot{\varepsilon}(t))}{\sigma_{cr}}(E_t\dot{\varepsilon}(t)-\sigma(t))}\} - C\ddot{\varepsilon}(t) \tag{3.29}$$

This model is able to describe plastic deformations for a constant temperature T. The implementation is simple and the numerical effort is small. However, it is not appropriate for the implementation in a finite element code.
For the modeling and simulation of more complex structures making use of the polymeric shape memory effect, finite element models were implemented. This was done for example by Qi et al. [94]. A 3D-thermomechanical model was developed, where the constitutive equations are separated for the rubbery, the glassy and the frozen-in state. Their constitutive model was implemented in the user material subroutine (UMAT) of the FE software *ABAQUS*. The model was experimentally verified with a compression sample. Böl and Reese [12] showed a finite element simulation of a deploying stent.

3.3.5. Shape Memory Composites

SMPs are polymers, thus they are dielectric materials. Furthermore, they show mechanical properties which are not sufficient for most engineering applications. Numerous investigations were carried out to enhance SMP properties either by fillers or reinforcements. These two classes of SMP composites are combined in this section, whereby fillers describe the addition of powders such as carbon black or metallic powders and reinforcements are represented by short carbon fibers or continuous fibers. Carbon nanotubes can be classified either as a filler or a reinforcement.

Shape memory polymers with fillers
The intention mostly found in the literature for the addition of fillers is the change of the conducting properties of SMPs. Since they are a dielectric material, resistive heating is not possible. Increasing the electrical conductivity of the polymer by conductive fillers, the electrical triggering becomes feasible. Some fillers and their influence on the physical and shape memory properties are summarized in the following.

- **Nickel powder:** The integration of Ni powder and Ni powder chains was investigated by the group of Jinsong Leng [66, 67]. A PU based SMP was doped with Ni powder to increase electric conductivity. The Ni chains were manufactured using an applied magnetic field during the curing process at which the Ni particles were aligned. The results achieved by Leng can be summarized as follows: With increasing volume fraction, the resistivity drops down by magnitudes for both randomly and chained particles. As an example the resistivity given for a Ni powder volume fraction of 10% for randomly distributed particles is $2.36 \times 10^4\ \Omega cm$, in transverse direction of chained samples $2.93 \times 10^6\ \Omega cm$, and in chain direction $12.18\ \Omega cm$. The storage modulus increases with the Ni content of up to about 40% below T_{trans}, while above T_{trans}, the modulus hardly is affected.

- **Carbon particles:** Leng et al. [65] added carbon nano-powder (30 nm) to a shape memory polymer to improve the mechanical and electrical properties. A reduction in resistivity was found for a volume fraction of 0.04, where the resistivity decreases from $10^{14}\ \Omega cm$ to $10^2\ \Omega cm$. The storage modulus increases continuously with increasing volume fraction from 1500 MPa for pure SMP to 2000 MPa for a volume fraction of 10%. Leng et al. also investigated SMP composites with a combination of Ni and carbon particle fillers [67].

- **Carbon nanotubes:** Carbon nanotubes (CNTs) are a new class of materials which have arisen in recent years. They show outstanding mechanical properties with elastic moduli in the range of 1 TPa and a strength of around 200 GPa. Ni et al. [85] added weight fractions of CNTs of up to 5% to a PU-SMP to increase its mechanical and

recovery properties. An increase of 186% of the Young's modulus can be observed for a volume fraction of 5% and a temperature of 65^{o}C (T_g=45^{o}C). The strength for the same sample increases about 132%. The shape fixation of the shape memory composite is almost constant for increasing weight fractions. For the recovery stress an optimal weight fraction of CNTs of 3.3% leads to a recovery stress, which is twice as high as for the bulk material. Meng et al. [79] investigated electro-active shape memory fibers with integrated multi-walled CNTs. The resistivity drop is $10^7\ \Omega cm$ for a weight fraction between 3% and 7%. Fibers with an elongation of 50% and a CNT weight fraction of 6% show a fixation ratio ζ of 75% and a recovery ratio η of about 77%.

- **Silicon carbide (SiC) particles:** Gall et al. [36] investigated SMP with integrated silicon carbide (SiC) nano-particles. Compression samples were used for thermomechanical cyling tests. A recovery stress of about 6 MPa is reported.

Fiber reinforced shape memory polymers

The much higher effect on the mechanical properties is achieved by continuous fibers, when compared to fillers.

- **Short carbon fiber reinforced SMPs**

  Although the integration of short carbon fibers (SCF) is widely discussed in the community of lightweight composite parts, for SMPs this reinforcement is hardly discussed. Mainly Leng et al. [65] investigated SMPs with different filler combinations including SCFs. The focus of this study was the influence on the transition temperature and the resistivity. While pure SMPs show a resistivity of $1 \cdot 10^{16}\ \Omega cm$, SMP filled with 6% volume fraction of carbon black result in a resistivity of $1 \cdot 10^8\ \Omega cm$, which further decreases to 2.3 Ωcm by using a combination of 5% carbon black and 2% of SCFs.

- **Continuous fiber reinforced SMPs**

  While the particle fillers or short fibers lead to a slight improvement of the mechanical properties in the same order of magnitude and are basically used for the reduction of the resistivity and stimulation purposes, the integration of continuous carbon fibers leads to a material, which is mechanically very different from pure SMP. The stiff continuous fibers lead to an increase of magnitudes of the material stiffness and strength, however, prevents large strain. This leads to a mechanically completely different behavior and the devices have to be designed differently. While pure SMP mostly is used in tension with very high strain of several hundred percent, shape memory composites can only be used in bending due to the limited strain of the continuous fibers. However, the advantage is a material with reasonable mechanical properties for engineering applications in its permanent shape with very good recovery properties in bending. Several applications were based on this material which will be introduced in Section 3.3.6.
  For continuous fiber reinforced SMPs the programming process includes additional challenges which were adressed by different researchers [37, 58, 118]. Even for bending

application of SMCs the programming has to be peformed carefully not to damage the integrated fibers, and to avoid influence between each other. Therefore programming is only possible well above T_{trans} to allow sufficient curvatures of the fibers in the soft matrix and avoid fiber breakage. Gall et al. [37] investigated experimentally the out-of-plane buckling of integrated fibers during programming. Lake et al. [58] gave fundamentals on the design with SMC addressing bending radii and fiber buckling. Also Tupper et al. [118] addressed the bending radius of SMCs regarding the application of SMC for spacecraft deployable structures.

Own contributions complement this section. The results of experimental investigations regarding the recovery properties of SMC are summarized. For the experiments, samples with the dimensions of 100 mm $\times$ 10 mm $\times$ 1.6 mm of the material *Veritex*, distributed by *CRG Industries* are used. This material is a woven fabric impregnated with *Veriflex* resin. Bending recovery tests with different bending radii are performed using these samples . The samples are bent to $\Theta = 180^o$ in a steel mould during the *programming* process. After cooling and demoulding, the sample is recovered unconstrained, and the residual angle Θ_{res} (see Figure 3.28 (a)) is measured. The recovery cycle is repeated to investigate the influence of the integrated fibers on the recovery. Figure 3.28 (a) shows a bent sample in its programmed shape, and a recovered sample with its residual angle Θ_{res}. The results are summarized in Figure 3.28 (b).

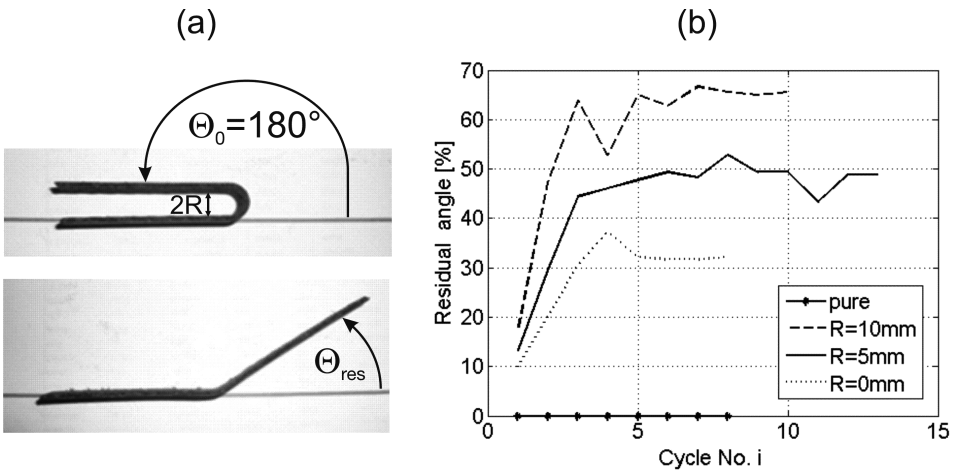

Figure 3.28.: Bending recovery test for the shape memory composite *Veritex*;(a) Recovery of sample; (b) Residual bending angle regarding the cycling iterations.

It can be seen that pure SMP shows no noticable residual angle for any number of cylces, thus 100% of bending recovery. The behavior is different for the shape memory composite. The integrated fibers affect the recovery performance and a residual strain (here a residual bending) remains after recovery. This residual angle increases with increasing bending radius. With an increase of the cycle number, a *learning effect* (see also Chapter 5) occurs and the residual strain converges to a value between 30% and 65% depending on the bending radius R. This behavior can be explained with a

negative influence of the fibers on the shape memory effect, because of the reduction of active mass and a disturbance of the recovery. The improvement with decreasing bending radius can be explained with increasing stored elastic energy in the fibers. However, it has to be kept in mind that with very small bending radii, fiber breakage might occur.
Similar tests are performed for a sample twisting of $\Theta = 180^o$. Figure 3.29 (a) shows such a programmed sample inside a thermal chamber. The resulting residual strains are summarized in Figure 3.29 (b).

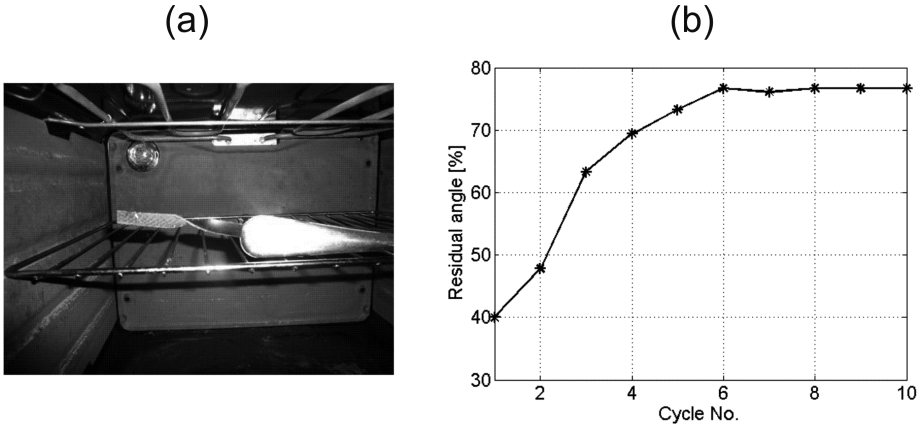

Figure 3.29.: Twisting recovery test for the shape memory composite *Veritex*; (a) Twisting sample; (b) Residual twisting angle with respect to the cycling iterations.

For twisted samples a *learning effect* can also be observed. However, the residual angles are much higher than for bending. This might be explained with the small strain energy storage in the carbon fibers due to the twisting load.
In summary it can be noted that the influence of the fibers for the used shape memory carbon fiber fabric *Veritex* is very high and disadvantageous. Because of the woven fabric a high amount of fiber volume fraction does not account for the strain energy storage, but only for the reduction of memory material volume fraction. Furthermore, the friction between the perpendicular rovings might cause losses and sticking. For unidirectional (UD) layers the behavior could be much better because a high elastic strain energy is stored if it is bent in fiber direction and almost no interaction between the fibers occur in perpendicular direction.

- **Triaxially reinforced shape memory polymer**

  Besides commercial SMCs another type of shape memory composite is investigated qualitatively. The triaxially reinforced shape memory polymer (SMT) is a material consisting of triaxially woven carbon weaves impregnated with *Veriflex* resin. Figure 3.30 shows this material during a deployment process. This triaxially reinforced material has unique mechanical properties in terms of very low CTE, and very low mass density. This material is used in combination with a rubbery matrix as surface materials for deployable space reflectors [25, 141]. Because of the porose structure, the

material is very lightweight and is almost immune regarding solar pressure, which is important for large space deployable structures [26]. The reflectors investigated so far at the Institute of Lightweight Structures (LLB) are deployed mechanically by a deployment mechanism, driven by conventional actuators such as springs or electric motors. The combination of this know-how and a shape memory matrix could lead to very lightweight deployable space reflectors. The use of the stored shape memory energy makes additional actuators unnecessary and the lack of a lot of moving parts would make such a system more reliable. First recovery tests are performed with small rectangular samples (see Figure 3.30).

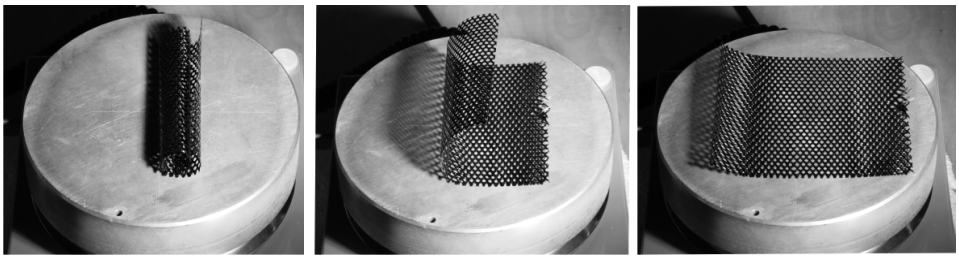

Figure 3.30.: Triaxially reinforced shape memory composite sample deploying triggered by a heat lamp.

3.3.6. Applications

The large variety of SMPs and their properties led to a large variety of applications. However, since the material is relatively new and not as established as for example SMAs, the applications were limited to academic examples, demonstrators or non-critical engineering elements. In this large amount of suggested applications two fields are standing out.
Bio-medicine is one of the most investigated and mentioned applications for SMPs. The possible tailoring of polymer properties led to biocompatible SMPs, which are well suited to different bio-medical applications [7]. The most popular example is the stent to expand arteries. With its outstanding recovery strains, helix-like or cylindrical structures can be compressed to very small diameters and inserted into human bodies with minimal invasive surgery. Triggered by body temperature or heating wires, the stent deploys and expands the artery [12, 63]. Other medical applications could be kneets for wound closing or micro tools to remove a thrombus [63].
The second large field of possible applications are space structures. Especially deployable structures suffer from high additional mass, integration effort, complexity and limited reliability because of their deployment systems, therefore the SMPs with their very high recovery strains were considered for deployment applications. Especially in the combination with fiber reinforcement and the resulting improvement of the mechanical properties, this approach led to lightweight, simple and reliable mechanisms. Two strategies were followed for the design of shape memory deployable structures. Rigid parts were deployed by deployment energy providing shape memory actuators. Such devices were put into practice by different researchers.

Lan et. al. [60] introduced a deployable shape memory hinge and its application for the deployment of solar arrays [59]. The same approach was followed by the company *Composite Technology Development* and the *Air Force Research Laboratory* using a different hinge design [9]. This development culminated in the first (and to our knowledge, the only) space proven application of SMPs. The developed hinge was flown on two missions in December 2006. Cyclic deployment testing was performed on the international space station, while in the TecSat 2 mission a non-critical, additional solar array was deployed by this shape memory hinge. Another approach was the use of shape memory material as the matrix material of the structure to deploy itself. This was introduced basically for deployable boom structures [16, 70, 118]. In this case, the combination of space rigidization and inflation techniques is often mentioned. The incorporation of these new technologies led to a decrease in reliability. However, for structures which do not have to deploy very accurately, such as booms, this might be an attractive approach. The same approach was also used for the deployment of space reflectors [70]. For this application very high deployment accuracies are required to achieve the desired reflector surface shape. However, the stored elastic energy in the integrated carbon fibers lead to very good deployment properties.
Other applications mentioned in the literature are morphing wings. It has to be mentioned, that for morphing wings, SMPs cannot be used as the active material since SMPs exhibit the one-way-effect only. However, it could be used for deployment of wings [135] or as a skin material with changing Young's modulus [134]. The second is believed to be one of the most promising approaches in recent years to achieve the long-term goal of the morphing wings. There have been concepts for the actuation mechanisms and materials for more than hundred years (The Wright brothers used a morphing wing), however, solutions for flexible skins were not found. For this morphing application, the effect of the pseudo-plasticity of SMPs and the temperature depending stiffness are used. The remaining difficulty is the load carrying capacity of the material for high cruising speeds and aerodynamic loads [134]. However, keeping the gaps for the SMP skin small and improving the mechanical properties, could lead to the first laminar flow wings. For this application, materials with low in-plane normal and shear stiffness and high out-of-plane stiffness are required.
Another application, which could be industrially realized in short term, is the use of SMP as mould material for mandrels for the CFRP part manufacturing [63]. One difficulty in manufacturing hollow CFRP parts such as tanks is the removal of the mould. Using SMP, a cylindrical tube can be expanded during the programming process. After programming, a winding process can be applied on the cyclindrical mould with increased diameter. After the curing process the mandrel can be recovered and the cylindrical, permanent shape of the mould can be removed easily. The challenge in this application is the adjustment of the recovery and curing temperatures.
Two wrougth materials should be mentioned, within the wide range of applications. Shape memory textiles were manufactured based on PU SMPs for the application of smart cloths. Wrapping of sleeves in sunlight and the tightening of bras while doing sports were reported [63]. Shape memory foams manufactured by cold hibernated elastic memory (CHEM) technology were reported also for a wide range of applications such as deployable wheels for Mars rovers or deployment of sandwich structure core materials.

4. 3D Shape Sensing

One of the keys for the post manufacturing shape adjustment is the accurate measurement of the structural shape. For an accurate measurement the resolution of the measurement system has to be sufficient enough to capture relevant distortions, which are on the order of magnitude of 0.005 mm to 0.5 mm. The accessability is another limiting factor for the shape measurement. In addition to any geometric limitations from the part itself, the applied adjustment process limits the measurement region as well. In this early scientific stage at least, where the distortion before and after the adjustment process needs to be known, a measurement before and after actuator application must be possible. Furthermore, the measurement method should not, or only by a negligible amount, affect the measurement itself. A simple measurement technique is desirable in order to minimize the effort for the shape adjustment process. In this chapter the following three measurement techniques are introduced.

- 3D-NC Shape Measurement
- Photogrammetry
- Strain Based Displacement Field Reconstruction

Independent of the measurement technique, a quantitative measure is necessary to evaluate the structural shape before and after adjustment. This measure should be independent of the structural geometry. Such a general and common measure is the quadratic error of a best fit shape with respect to the measurement data - also known as a best fit root mean square (RMS) shape error (Equation 4.1).

$$RMS = \sqrt{\frac{\sum_{i=1}^{n} (\overline{w}_i - \hat{w}_i)^2}{n}} \tag{4.1}$$

where n is the number of evaluation points, $\overline{w}$ are the desired out-of-plane coordinates and $\hat{w}$ are the actual out-of-plane coordinates, either distorted or adjusted, of every point i.
For most of the following examples this measure will be used for the shape evaluation.

4.1. 3D-NC Shape Measurement

3D numerical controlled (NC) shape measurement is the state of the art method for conventional parts. Using computer controlled robots with a sensing arm and a sensing ball at its tip, a programmed sequence of measurement points can be established. A force sensor inside the sensing tip indicates when the structural surface has been touched. This measurement technique is very fast, well established, and has a resolution of the magnitude of 0.01 mm. Figure 4.1 shows the measurement of an antenna waveguide sample (see Section 11.3) using a 3D-NC measurement machine.

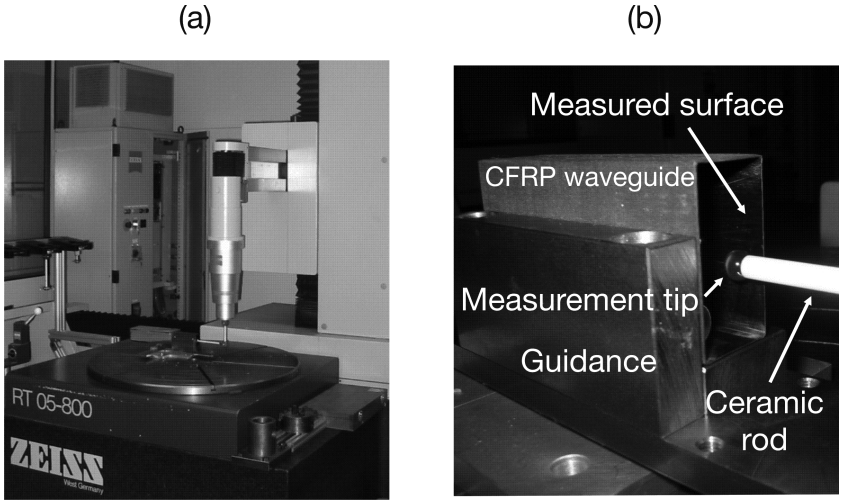

Figure 4.1.: 3D-NC measurement. (a) Measurement machine; (b) Measurement tip and waveguide sample.

The inherent drawback is the presence of a necessary sensing force, which might disturb the measurement by a significant amount. For classical, often metallic, parts with a certain wall thickness this effect does not play a role. However, for thin-walled composite parts with wall-thicknesses smaller than 1 mm, this effect must be considered. Examining the two examples, introduced in Sections 11.2 and 11.3, the first is a quadratic plate with the dimensions of 200 mm $\times$ 200 mm and a thickness of approximately 1 mm. The goal is to reduce the out-of-plane distortions. A finite element model is built to investigate the influence of a representative sensing force of 0.1 N, which is the minimal sensing force of the measurement machine used. To avoid a deformation of the part by the clamping used for the measurement, only the four corners are clamped (Figure 4.2 (a)). A perpendicular point force of 0.1 N is applied in the middle of the plate. The laminate is a symmetric $[0/90/90/0]$ layup with UD plys from SGL (SIGRATEX PREPREG CE 1250-230-39). The material properties can be found in Appendix A.4. Figure 4.2 (b) shows the deformation contour plot (not to scale).

The resulting out-of-plane deformation is 0.045 mm, which is within the range of the assumed root mean square (RMS) shape error. Thus another measurement techique should be applied for these composite plates. The second example is a rectangular antenna waveguide with the

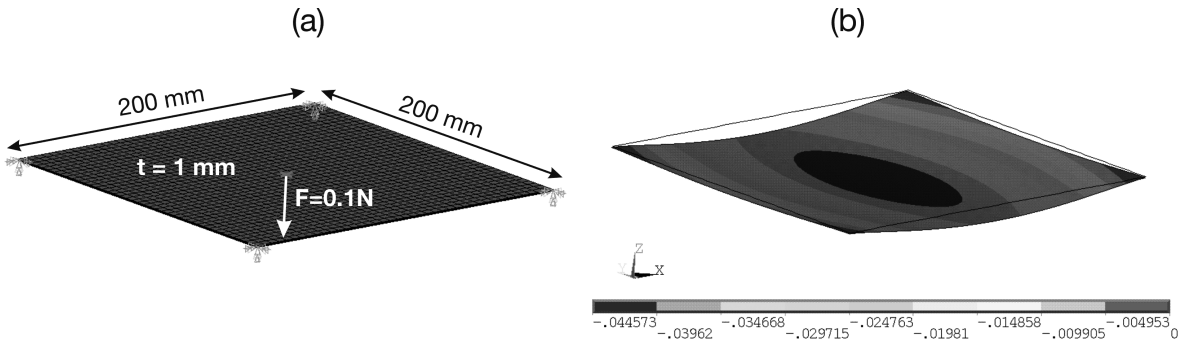

Figure 4.2.: Assumed deformation of a composite plate due to a sensing force of 0.1 N. (a) FEM model; (b) Deformation contour plot.

inner dimensions of 47.5 mm $\times$ 23.7 mm and a corner radius of 1 mm. The wall thickness is 1 mm with a symmetric $[0/90/90/0]$ layup with UD plys from SGL (SIGRATEX PREPREG CE 1250-230-39). The length of the waveguide sample is 100 mm. The waveguide inner side wall is measured. During the measurement it is fixed with strong permanent magnets at the bottom and at the guidance opposite the measurement surface. To reduce computational effort a finite element model is built using the waveguide symmetry. The boundary conditions are modeled as clamped at the symmetry lines. This is feasible because the waveguide is clamped with the magnets at the bottom, and at the top the waveguide is loaded with tensile forces due to the measurement which only have negligible effect. The most critical location for the sensing force is the middle of the waveguide edge. The force in this case is applied to the inner surface. This is necessary because the inside measurement is needed, since the actuator application will occur on the waveguide outer side. The resulting deformation contour plot (not to scale) can be seen in Figure 4.3 (b).

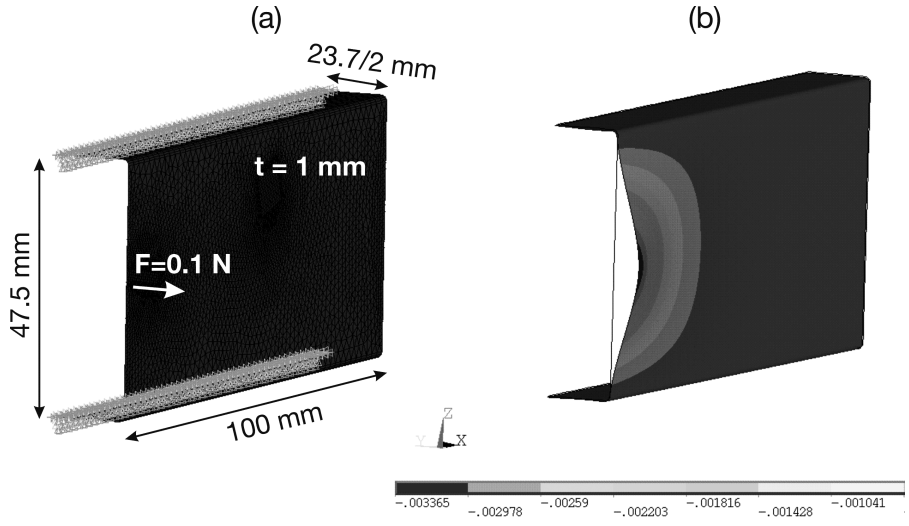

Figure 4.3.: Assumed deformation of a composite waveguide due to a sensing force of 0.1 N. (a) FEM model; (b) Deformation contour plot.

The resulting out-of-plane deformation is 0.0033 mm, which is well below the expected RMS error range and can be neglected. Thus for the measurement of parts with a certain bending stiffness this measurement technique provides an established, accurate and cheap technique for the shape measurement. As long as the surfaces are easily accessible, this technique can be used. A possible alternative is a non-contact measurement technique, which avoids interactions between the measurement tool and the part.

4.2. Photogrammetry

Photogrammetry is a method to calculate 3D-coordinates out of 2D-photos, using a triangulation method. A common measurement system of this type is a one camera system produced by the company *AICON*. The orientation is achieved by the use of additional scales and coded targets. The shape measurement is performed in four basic steps.

- Acquisition
- Target evaluation
- Pre-orientation of camera position and attitude
- Determination of 3D coordinates

Acquisistion
The data acquisition is accomplished by taking photographes from several different positions and orientations. The quality is dependent on the camera quality, resolution, the target size, the number, position, and orientation of pictures, and the contrast. There are two types of targets commercially available: White targets and retro-reflective targets. The second type provides sharp contrast and good pictures. These targets are circular stickers with diameters of 0.4 mm to 25 mm, which are attached to the structural surface. Note that the attachment might affect the part or possibly add an offset of the sticker thickness. Another possibility to apply targets, is the projection onto the structural surface [99]. In this case the structure is not affected by the measurement. However, because black circular targets are projected onto a matt white surface, it is necessary to pre-treat the structural surface by coating. It is questionable wheter this approach is practial. However, for scientific purpose and accurate measurement without introducing structure-measurement interaction, it is a very attractive alternative.
The camera settings, focussing and distance to the targets are sensitive parameters which require some preparation before measuring, as does the projection pattern in terms of projector distance, target size, etc.. Figure 4.4 shows a typical measurment setup.

Target evaluation
After data acquisition, the pictures are processed automatically with the *AICON 3D Visual Studio* software. As a first step, the targets are evaluated. The elliplical centers of the targets and the coded targets are determined based on contrast gradients.

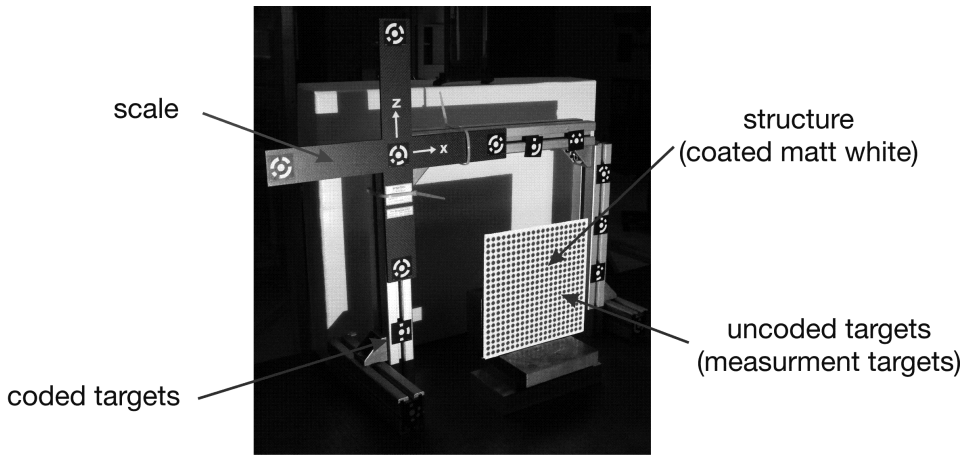

Figure 4.4.: Measurement setup for the dot projection photogrammetry.

Pre-orientation of camera position and attitude
From the pictures of the coded targets and their known scales, the locations and attitudes of the camera positions are determined.

Determination of 3D coordinates
From the different camera positions the measurement target locations can be determined via triangulation. This technique is based on trigonometric functions. For the 2D space the intersection of two image vectors can be calculated easily and the intersecting point indicates the target location. For the 3D space the skewed vectors never cross each other exactely. However, by measuring from several different locations, a linear equation system can be used to calculate the target location. Additionally, a measurement error can be calculated since the linear equation system is over-determined. Standard deviations for the measurement points between 0.0027 and 0.02 mm can be achieved. After these steps the 3D coordinate data can be exported to post-processing software. In this work the post-processing is performed with *Matlab*.

The contact-free measurement technique of dot projection photogrammetry is well suited for the measurement of thin-walled structures since there is no measurement-structure interaction. However, the target surface must be easily accessible and must have a matt white surface. Thus for academic purposes this method is well suited. For industrial applications however, it is not well suited because compared to 3D-NC measurements it is more labor intensive.

4.3. Strain Based Displacement Field Reconstruction

Sometimes it is not possible to measure the structural shape directly. This might be the case in hazardous or isolated environment, moving systems or environments with limited space. Especaially for moving systems, such as aircraft wings or satellite structures, a fixed reference

system is absent, not allowing the measurement of the structural shape directly. In these cases the approach of indirect shape measurement can be followed. Figure 4.5 illustrates this approach.

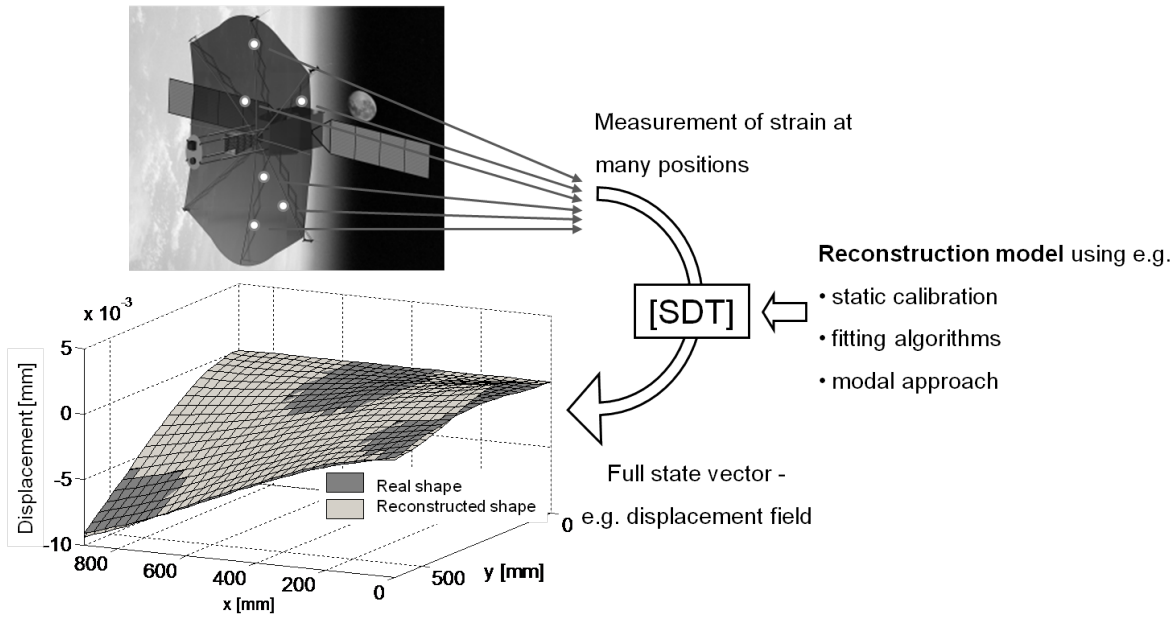

Figure 4.5.: Illustration of the strain-based shape reconstruction.

It should be noted that only elastic deformations can be reconstructed using strain data. Rigid body motions of the structure cannot be captured. Within the research field of strain based displacement field reconstruction, two main areas can be distinguished.

- Algorithms for the displacement field reconstruction
- Measurement techniques and sensor configurations

In the following subsections, these two research fields will be introdcued and discussed.

4.3.1. Displacment Field Reconstruction Algorithms

Displacement field reconstruction algorithms can be structured in two groups.

Displacement field reconstruction based on local shape functions: This kind of reconstruction method is often used for beam or cable like structures. The structures are segmented into N nodes at which the strain is measured. Using the displacement and strain data at node k, the displacement at node $k+1$ can be calculated. Using a clamped end as a strating point, the displacement of the whole structure can be determined sequentially. This method, however, shows a systematic error increasing at each point from the clamped end to the free end.

Displacement field reconstruction based on global shape functions: This type of reconstruction method is based on approximation functions of the displacement field $\vec{u}$ and strain field $\vec{\varepsilon}$ of the total structure. Using these shape functions a transformation matrix $[SDT]$ can be determined, which relates displacements to strains (Equation 4.2).

$$\hat{\vec{u}} = [SDT] \cdot \vec{\varepsilon} \tag{4.2}$$

where $\hat{\vec{u}}$ is the reconstructed displacement field. The $[SDT]$ matrix can be obtained via simulation or experimentally. Several methods to determine the $[SDT]$ matrix were reported:

- Static calibration of strain signals for known force vectors
- Double integration of a strain field
- Shape reconstruction using a modal basis
- Determination of shape functions from modal analysis (experimental)

The **static calibration method** is an established technique for known static loads, which was reviewed by Giesecke [40]. However, for unknown or dynamic loads this method is not well suited because of aliasing effects due to higher modes [74].

The method of **double integration of a strain field** was described by Jones et al. [51] using the example of a cantilever sandwich plate. The strain-displacement relationship used for this type of reconstruction, is derived from the classical plate theory, where the double integration of the strain ε results in the displacement u (Equation 4.3).

$$\varepsilon_y = -z\frac{\delta^2 u}{\delta y^2} \tag{4.3}$$

where ε_y is the normal strain in y-direction and z is the distance to the neutral axis of the structure. The polynomial function of the strain field $\varepsilon_y(x, y)$ was chosen such as:

$$\varepsilon_y(x, y) = a_1 + a_2 x + a_3 y + a_4 xy + a_5 y^2 + a_6 xy^2 + a_7 y^3 + a_8 xy^3 \tag{4.4}$$

where x and y are the in-plane coordinates and a_1 to a_8 are the polynominal coefficients. These coefficients were determined by the use of a least-squares fitting algorithm minimizing the error function E:

$$E[\varepsilon(x, y)] = \sum_{i=0}^{N} [\varepsilon_y(x_i, y_i) - \epsilon_{yi}] \tag{4.5}$$

where E is the sum of the differences of the calculated and the measured strains ϵ_{yi} at the measurement locations $i...N$. The integration of this fitted function with respect to Equation

4.3 led to the determination of the displacements u.

The **displacement field reconstruction using modal shape functions** was demonstrated by Foss et al. [34]. The approach is capable of estimating dynamic and static shape deformations. Using k displacement mode shapes $\vec{\Phi}$ and strain mode shapes $\vec{\Psi}$, a strain-displacement matrix $[SDT]$ is determined. Both N displacements $\vec{u}_{N\times1}$ and M mechanical strains $\vec{\varepsilon}_{M\times1}$ can be expressed as a weighted sum of mode shapes (equations 4.6 and 4.7).

$$\vec{u}_{N\times1} = [\Phi]_{N\times k} \cdot \vec{q}_{k\times1} \tag{4.6}$$

$$\vec{\varepsilon}_{M\times1} = [\Psi]_{M\times k} \cdot \vec{q}_{k\times1} \tag{4.7}$$

where $\vec{q}_{k\times1}$ is the vector of k weighting factors, modal coordinates respecively. Modifying Equation 4.7 leads to:

$$\vec{q}_{k\times1} = ([\Psi]^T_{M\times k} \cdot [\Psi]_{M\times k})^{-1} \cdot [\Psi]^T_{M\times k} \cdot \vec{\varepsilon}_{M\times1} \tag{4.8}$$

Inserting Equation 4.8 into Equation 4.6 leads to:

$$\hat{\vec{u}}_{N\times1} = \underbrace{[\Phi]_{N\times k} \cdot ([\Psi]^T_{M\times k} \cdot [\Psi]_{M\times k})^{-1} \cdot [\Psi]^T_{M\times k}}_{[SDT]} \cdot \vec{\varepsilon}_{M\times1} \tag{4.9}$$

The modal approach was verified for the static case by Kirby et al. [55] using a cantilever beam equipped with 6 strain sensors. The tip of the beam was deflected 13.3 cm and the resulting shape error of the total beam was less than 1%. Further examples including an optical mirror with a complex back structure are given by Mueller [80].

4.3.2. Displacement Field Reconstruction based on Strain Measurement using Fiber Bragg Grating (FBG) Sensors

The reconstruction algorithms, previously discussed, are independent of the sensor type, however, strongly dependent on the number of sensors and their distribution, which is only a matter of observability. While Pisoni and Santolini [90] used a cantilever beam structure equipped with two conventional strain gages to predict displacements at any given point, Jones et al. [51] used 8 distributed fiber Bragg grating (FBG) sensors. Li et al [68] suggested the minization of the condition number κ of the modal strain matrix $[\Psi]$ to find optimal strain sensor locations to improve the shape recontruction results.

In general all introduced displacement field reconstruction methods improve with an increasing number of strain sensors. If electrical strain gages are used, this leads to an immense

cabling effort and a high mass due to copper cables and connectors. For space applications where shielded cables must be used and mass is a critical consideration, this is not acceptable. Fiber Bragg gratings (FBGs) offer an attractive alternative. They are lightweight, small in size, thus easy to integrate, electro-magnetically immune, and they show a very good multiplexing capability. It is very easy to use high numbers of sensors. Therefore many investigations were carried out on applications for distributed strain and temperature measurement using FBGs [35, 77, 83, 123].

The FBG sensor was first demonstrated by Hill et. al. [87]. Its working principle is based on a periodic change of the refractive index of the core of an optical fiber. If a broadband lightsource is applied to the fiber a certain wavelength, the Bragg wavelength λ_B (Equation 4.10) is reflected at the grating.

$$\lambda_B = 2 \cdot n_e \cdot \Lambda[nm] \tag{4.10}$$

where Λ is the period of the grating and n_e is the effective refractive index of the fiber core. Different grating periods lead to different reflected wavelengths, which allows the wavelength division multiplexing (WLDM). Figure 4.6 illustrates the basic principle of an FBG sensor.

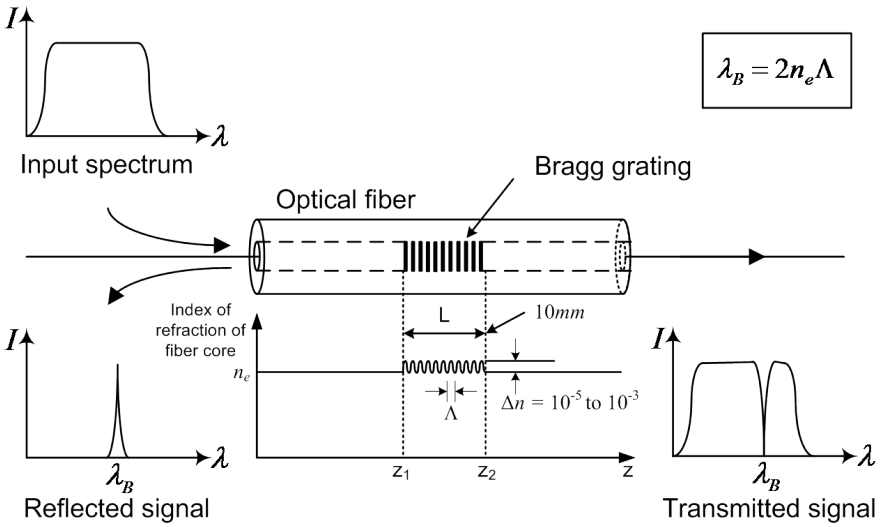

Figure 4.6.: Working principle of an FBG sensor.

If the FBG sensor is applied to or integrated in a structure it is exposed to mechanical strain which compresses or tenses the grating and the reflected wavelength will be changed. This wavelength change $\Delta\lambda$ can be measured by spectrometers. Using the well known equation shown in 4.11, it is possible to calculate applied mechanical strain or temperature:

$$\frac{\Delta\lambda}{\lambda_B} = (1 - p_{eff}) \cdot \Delta\varepsilon + ((1 - p_{eff}) \cdot \alpha_s + \frac{1}{n_e} \cdot \frac{dn}{dT}) \cdot \Delta T \tag{4.11}$$

where p_{eff} is the photo-elastic coefficient, $\Delta\varepsilon$ is the mechanical strain, α_s is the CTE of the structure, $\frac{dn}{dT}$ is the thermal-optic coefficient and ΔT is the temperature change. From Equation 4.11 it can be seen that mechanical strain as well as temperature changes lead to a wavelength change. This implies the necessity to use compenstation methods to distinguish the measured physical parameters [53, 81, 114]. Using such temperature compensated FBG sensors, these sensors are suited very well for shape reconstruction methods due to their multiplexing capability. Foss and Hauges [34] suggested the use of FBGs for the shape reconstruction. High noise and drift levels of electrical strain gages and the multiplexing capability of FBGs are mentioned. Mueller et al. [82] concentrated on the high-precision measurement using FBGs in the shape control process. Kang et al. [54] investigated the dynamic shape reconstruction of a cantilever beam using FBGs.

Invetigations on the dynamic shape reconstruction of a cantilever plate are carried out in this work. Simulations and experiments are performed to investigate the influence of the sensor locations on the quality of the shape reconstruction. For this purpose an acrylate cantilever plate with the dimensions of 600 mm $\times$ 900 mm $\times$ 8 mm is used (Figure 4.7(a)). Different sinusoidal exciations with resonance and off-resonance frequencies are applied (Table 4.1). Different sensor configurations and numbers of sensors are investigated. It is found that a sensor configuaration, which leads to a minimum condition number κ of the $[SDT]$ matrix, gives the best reconstruction results. The simulation of the shape reconstruction is verified with an experiment using 16 FBGs in a condition number optimized configuration. Two sensors are located at each position and oriented perpendicular in x- and y-direction (Figure 4.7 (a)) Four laser sensors are used as reference sensors (see Figure 4.7(b)).

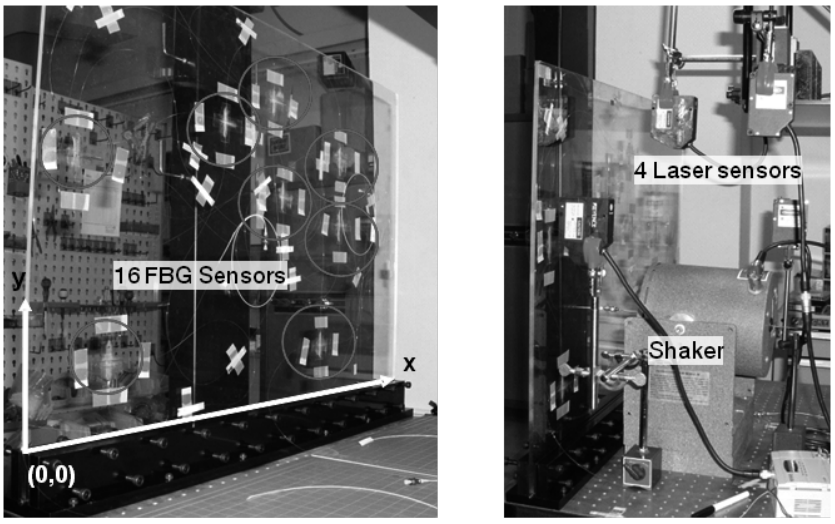

Figure 4.7.: Experimental setup for dynamic shape reconstruction ; (a) Cantilever plate with 8×2 FBGs (marked with circles); (b) Electromechanical shaker and reference laser sensors.

Sucess of the reconstruction is evaluated by calculating the root mean square error of the surface (Equation 4.1). This is done for all discrete points of the simulation and the four reference measurements of the experiment. The results are summarized in Table 4.1. Figure

Table 4.1.: RMS shape errors of the dynamic displacement field reconstruction of a cantilever plate for different harmonic excitations.

Excitation frequency [Hz]		RMS [%]	RMS [%]
Simulation	*Experiment*	(Simulation)	(Experiment)
3.00	3.00	1.72	0.56
6.83(1st)	7.14	0.16	0.44
10.00	10.00	1.28	1.31
12.48 (2nd)	12.84	0.48	0.46
20.00	20.00	4.88	1.12
28.18 (3rd)	31.08	0.57	2.2

4.8 illustrates the reconstructed shapes. The asterisks mark the measured reference data.

It can be seen that the resonance load cases lead to much lower reconstruction errors than the off resonance loads. Furthermore, it can be seen that with increasing excitation frequency the reconstruction becomes less reliable. The extraordinarily high error for the excitation with the 3rd natrual frequency in the experiment can be explained as due to the limited sampling rate and resolution level of the reference measurement system.

This introduction to indirect structural shap measurement methods, shows possible alternatives for applications where direct measurement of the shape is not possible. As mentioned previously the application of the modal approach for static cases, which is apparent for the shape adjustment, was verified by Kirby [55] and Mueller [80]. For the shape adjustment experiments introduced in this thesis, the 3D-NC shape measurement and the photogrammetry proved to be better suited and are used. For industrial applications the indirect shape measurement with integrated strain sensors could be an advantageous, or even necessary, alternative.

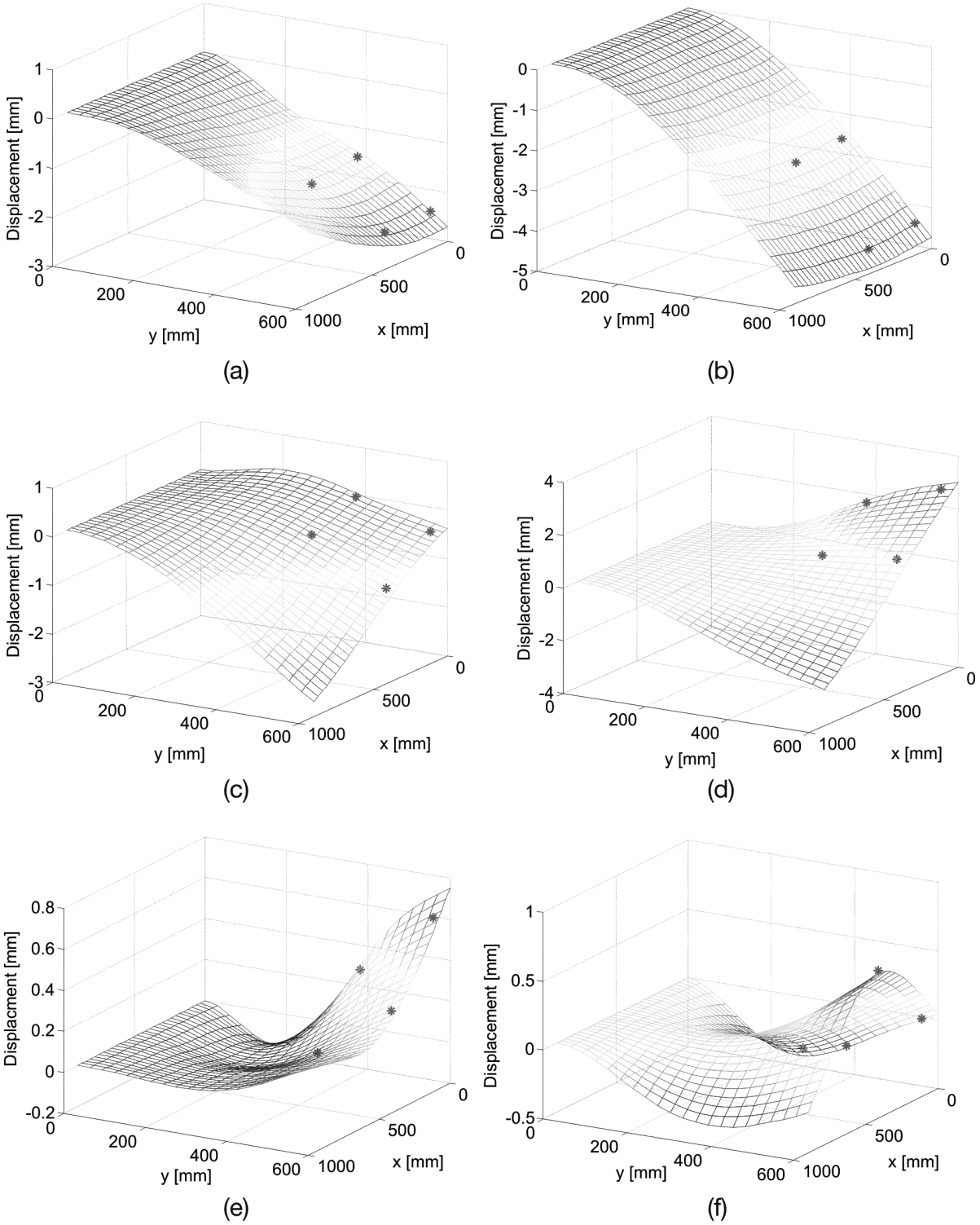

Figure 4.8.: Experimental results of the shape reconstruction of a dynamically excited plate for six harmonic excitation cases; asterisks mark experimental reference measurements.

5. Actuation Properties of Shape Memory Polymers

To perform shape adjustment with SMPs it is necessary to know their actuation properties. This knowledge is necessary for the actuator selection, the actuator simulation and optimization, the application and the stimulation. In this chapter those actuation properties of shape memory polymers are introduced. Figures of merit will be defined and described as they are used in this thesis. After the introduction, a review of recent experimental invetigations will show the necessity of an improvement of experimental techniques to attain more valuable information about the actuation properties. The developed experimental method and the determined actuation properties are presented.

5.1. General Considerations

This section shall give a brief overview on common actuation properties or figures of merit of smart materials and actuators. Since forces and strokes of actuators are scalable if the devices are built smaller or larger, it is necessary to normalize the properties by volume or mass to get representative figures of merit. For smart materials it is even worthy to normalize the properties by the cross sectional area to get information about the actuation stress and strain, which are more generally used than force and stroke. Using these general properties it is possible to design proper actuators in an appropriate size. Stress and strain may not even be the most general properties, since they can be transferred into each other by proper transmissions, if a negligible transmission loss is assumed. Thus a much more valuable actuation property is the energy content W, the product of force and stroke. The maximum energy output of an actuator is achieved at a certain point on the load curve, where the area below the curve achieves a maximum (Figure 5.5). The energy content can be normalized by volume or mass, leading to a work density W and a specific work density w. For static applications this property is the most valuable. However, for dynamic applications the bandwidth of the actuators plays a key role, thus the normalized bandwidth and the power density P are important figures of merit. Table 5.1 gives a summary of the typical actuation properties and their normalized partners.

It shall be pointed out that forces and strokes of actuators provided in data sheets or in the literature generally are the blocking force F_{block} and the free stroke ΔL_{free}. These figures of merit provide the two extremes of an actuator, where it is operated either fully constrained

Table 5.1.: Summary of general actuation properties and their normalized partners

	Normalized by size		Normalized by
Property	Notation	Scaling [91]	cross-section or length
Force $[N]$	Force density $[N/cm^3]$	L^{-1}	Stress $[MPa]$
Stroke $[mm]$	Stroke density $[mm/cm^3]$	-	Strain $[\%]$
Bandwidth $[Hz]$	- $[Hz/cm^3]$	L^{-1} - L^{-2}	-
Energy $[J]$	Energy density $[J/cm^3]$	L^0	Energy density $[J/cm^3]$
Power $[W]$	Power density $[W/cm^3]$	L^{-1} to L^{-2}	Power density $[W/cm^3]$

Where L denotes a characteristic length of the actuator

or without any mechancial constraint. However, in practical applications a balance between force and stroke will always be achieved. For patch actuators such a balance is caculated by Equation 3.15. To evaluate actuators and compare their performance their properties can be ploted in 2D property maps. As two representative examples, a stress-strain and a work density-power density map are shown in Figures 5.1 and 5.2. A comprehensive overview of smart materials and their properties can be found in [91].

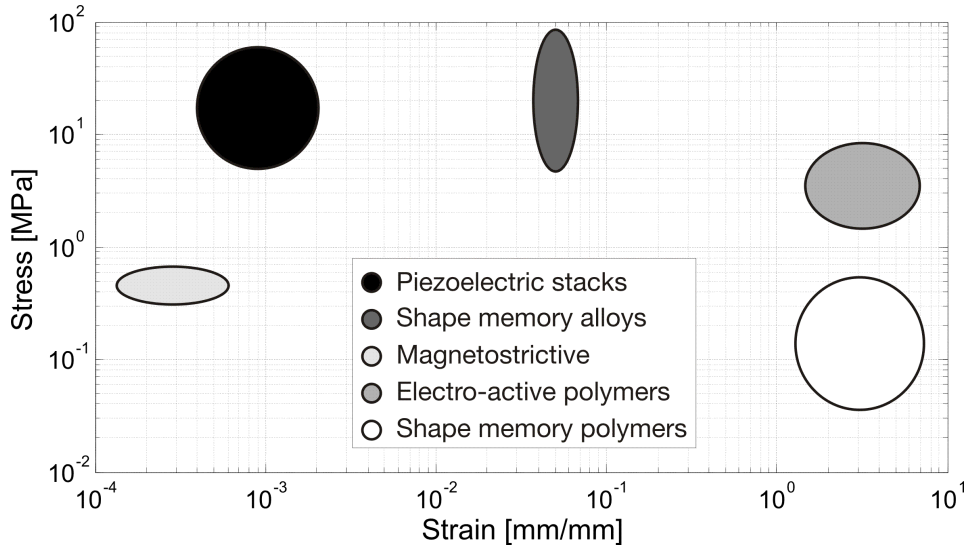

Figure 5.1.: Classification of a selection of smart materials regarding their actuation stress and strain.

It must be added that shape memory polymers actually do not show a power output in terms of bandwidth since only the one-way effect is apparent. For a single step actuation, however, an actuation time can be used for the power calculation.
In general it can be seen that the variety of smart materials offers a very wide range of properties which can be used for different applications. The following section will concentrate

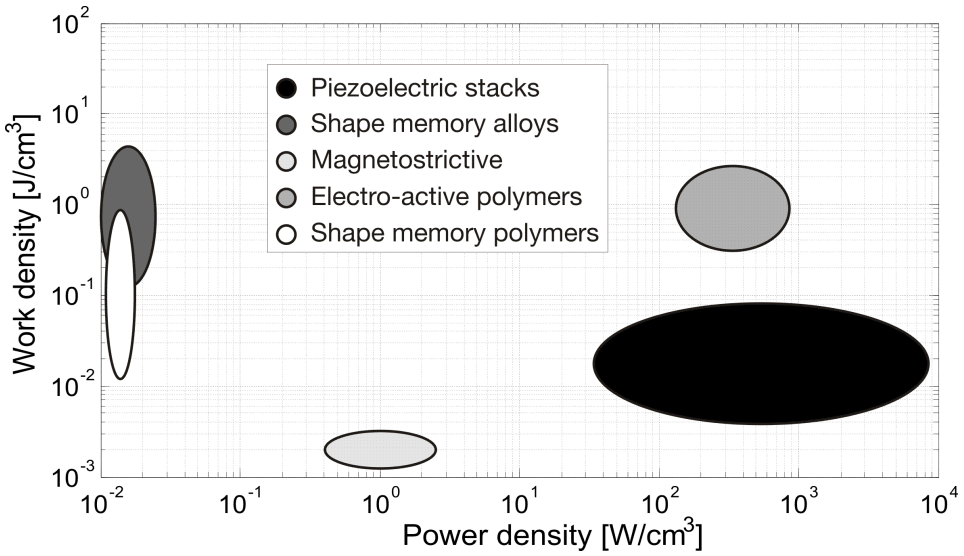

Figure 5.2.: Classification of a selection of smart materials regarding their work and power densities.

on shape memory polymers and their actuation properties. More specifically it will focus on the actuation stress, the actuation strain, the work density and additional properties unique to shape memory materials.

5.2. Figures of Merit

For shape memory materials the actuation stress is denoted as recovery stress σ_r built up during the recovery process due to the external stimulus (Figure 3.24). It can either be related to the original cross section A_0 or the actual cross section A. For the standardized material characterization the relation to A_0 (Equation 5.1) is used. This is more appropriate since most engineering materials do not show large elongations and lateral contractions. However, for shape memory polymers, were elongations of more than 100% and corresponding lateral contractions are expected, the engineering recovery stress σ_{r_0} is substantially different from the actual recovery stress σ_r (Equation 5.2).

$$\sigma_{r_0} = \frac{F_r}{A_0}[MPa] \tag{5.1}$$

$$\sigma_r = \frac{F_r}{A}[MPa] \tag{5.2}$$

where F_r is the recovery force.
For the material characterization and comparison with other smart materials the engineering stress σ_{r_0} is used, while for the determination of the actuation properties and the model input

parameters the actual recovery stresses σ_r must be used. For a fully constrained recovery (Figure 3.23) or actuation the most common figure of merit, the blocking force F_{block} or blocking stress σ_{block} (Equation 5.3), respectively, applies.

$$\sigma_{block} = \frac{F_{block}}{A} \tag{5.3}$$

For the special case of shape memory polymer actuator patches a further stress component must be considered for the actuation. While the actuator patch cools down from the recovery temperature, an additional thermal stress σ_{CTE} builds up which is a function of the coefficient of thermal expansion (CTE) α_T, a temperature dependent Young's modulus $E(T)$ and the temperature change ΔT (Equation 5.4)

$$\sigma_{CTE} = \alpha_T \cdot E(T) \cdot \Delta T \tag{5.4}$$

For both compression and tensile actuators, an additional tensile stress builds up which leads to the actuation stress σ_{act} (Figures 3.24 and 3.25, Equation 5.5).

$$\sigma_{act} = \sigma_r + \sigma_{CTE} \tag{5.5}$$

It is emphasized that this actuation stress σ_{act} is the most relevant figure of merit for the shape adjustment using patch acutators.

The actuation strain is denoted for shape memory materials as a recovery strain ε_r. Since for shape memory polymers there are large strains of more than 100%, different reference lengths must be distinguished. It is possible to relate the recovery strain to the original length L_0 of the permanent shape or to the programmed length L_{prog}. Only L_0 consideres the programming history and is able to give actuation properties related to the original shape. Figure 5.3 illustrates the different definitions of recovery strains for a compression actuator. The recovery strain ε_{r_0} related to the permanent shape is defined as:

$$\varepsilon_{r_0} = \left| \frac{L_{prog} - L_{res}}{L_0} \right| [-] \tag{5.6}$$

where L_{prog} is the programmed length of the actuator, L_{res} is the length after recovery and L_0 is the initial length of the actuator. For the modeling and simulation of actuation, the recovery strain ε_r is related to the progammed shape.

$$\varepsilon_r = \left| \frac{L_{prog} - L_{res}}{L_{prog}} \right| [-] \tag{5.7}$$

In the special case of unconstrained, free recovery (Figure 3.22) the recovery strain is denoted as ε_{free}. The free recovery strain ε_{free} is an important figure of merit for the simulation of the shape adjustment (Chapter 6). This definition of the recovery strain ε_r leads to very

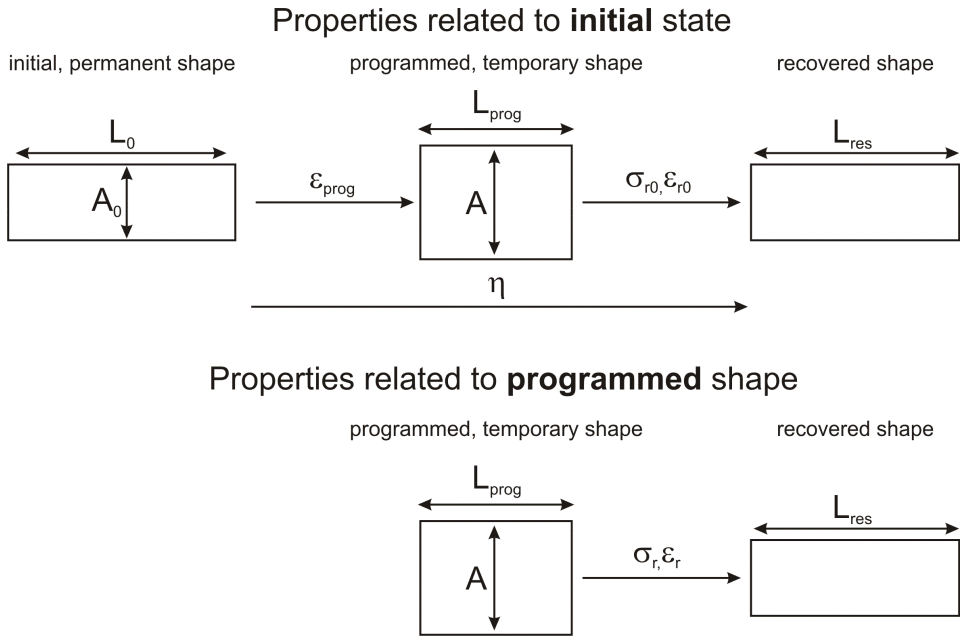

Figure 5.3.: Illustration of different representations of recovery strains and stresses

different characteristics of tensile and compression actuators. While compression actuators cannot be compressed more than 100%, tensile actuators cannnot recover more than 100%. Figure 5.4 illustrates this behavior for the assumption of free recovery with a recovery ratio η of 1 (Equation 5.8).

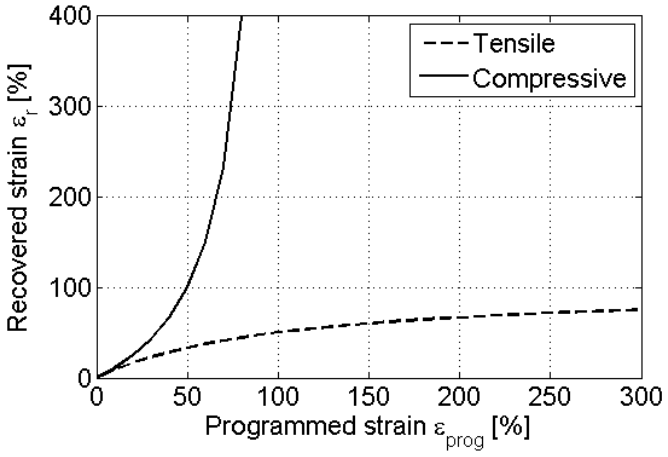

Figure 5.4.: Different characteristics for tensile and compression actuators.

A general figure of merit for shape memory materials is the recovery ratio η (Equation 5.8),

which relates the recovered strain to the programmed strain:

$$\eta = \frac{L_{prog} - L_{res}}{L_{prog} - L_0}. \tag{5.8}$$

The recovery ratio η is a kind of quality measure for the recovery, which indicates how much of the programmed strain is recovered. The recovery ratio is normalized to the range of 0% to 100%. The quality of recovery of different shape memory materials (SMMs) can be compared using this figure of merit, although they may have very different maximum strain capability ε_{prog} (Equation 5.9). This applies for different smart materials as well as for the differences in tensile and compression modes.

$$\varepsilon_{prog} = \left| \frac{L_{prog}}{L_0} - 1 \right| \tag{5.9}$$

The corresponding strain remaining as unrecovered is the residual strain ε_{res}:

$$\varepsilon_{res} = 1 - \eta \tag{5.10}$$

The relationship of σ_r and ε_r can be illustrated as a load line (Figure 5.5).

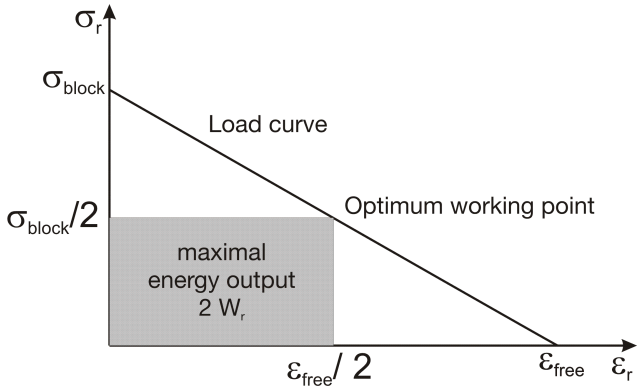

Figure 5.5.: Schematic illustration of a linear actuator load curve and important figures of merit.

The two extremes of blocking stress σ_{block} and free recovery ε_{free} appear at the axis crossings of the linear load curve. The arbitrary working points on the load curve are characterized by a recovery stress σ_r and a recovery strain ε_r. While blocking stress and free recovery do not produce an energy output in the sense of a product of force and stroke, the pairs of σ_r and ε_r in between produce an energy output (marked as a grey area below the working

point). For SMPs a recovery energy density W_r is defined, which might also be related to the permanent or the programmed shape:

$$W_{r_0} = \frac{1}{2} \cdot \varepsilon_{r_0} \cdot \sigma_{r_0} [\frac{J}{cm^3}] \tag{5.11}$$

and

$$W_r = \frac{1}{2} \cdot \varepsilon_r \cdot \sigma_r [\frac{J}{cm^3}] \tag{5.12}$$

While the recovery energy density W_{r_0} is related to the volume, the specific recovery energy density w_{r_0} is related to the mass:

$$w_{r_0} = \frac{1}{2} \cdot \frac{\varepsilon_{r_0} \cdot \sigma_{r_0}}{\rho} [\frac{J}{g}] \tag{5.13}$$

and

$$w_r = \frac{1}{2} \cdot \frac{\varepsilon_r \cdot \sigma_r}{\rho} [\frac{J}{g}] \tag{5.14}$$

where ρ is the mass density of the shape memory material. Generally the work density should be considered in the development process of actuation devices to get a maximum energy output. However, for the shape adjustment application using patch actuators other constraints negate the need for consideration of the energy density. Since the stiffness of the structure is predetermined and transformation mechanisms shall not be considered, a balance of recovery stress and strain arising due to a maximum possible applied stress, must be accepted.

A further figure of merit is the recovery strain rate $\dot{\varepsilon_r}$ (Equation 5.15).

$$\dot{\varepsilon_r}(T_r) = \frac{\varepsilon_r}{t_r} \tag{5.15}$$

where T_r is the recovery temperature and t_r is the recovery time. The fixation ratio ζ (Equation 3.26) defines the capability of the material to maintain the programmed shape and is the ratio of the remaining strain after unloading ε_u and programmed strain ε_{prog} (Equation 3.26). This figure of merit is important for acurate stowage applications. A further property is the *learning effect*, which has been widly investigated in the past. The learning effect describes the recovery behavior regarding several thermomechanical cycles. Although SMPs only show the one-way-effect, the thermomechanical cycle can be repeated by again introducing mechanical energy during the programming step. The SMPs show an

increasing relative recovery ratio $\eta(i)$ (Equation 5.16) with increasing cycle number i, while the overall recovery ratio η related to the initial length L_0 decreases.

$$\eta(i+1) = \frac{L_{prog} - L_{res}(i+1)}{L_{prog} - L_{res}(i)} \quad i = 0, ..., n \tag{5.16}$$

Figure 3.28 illustrates this behavior for a shape memory composite bent to $\Theta = 180^o$ (compare Figure 3.28) for each cycle i. Relating the residual angles to the recovered angle in the cycle before the learning effect becomes obvious (Figure 5.6).

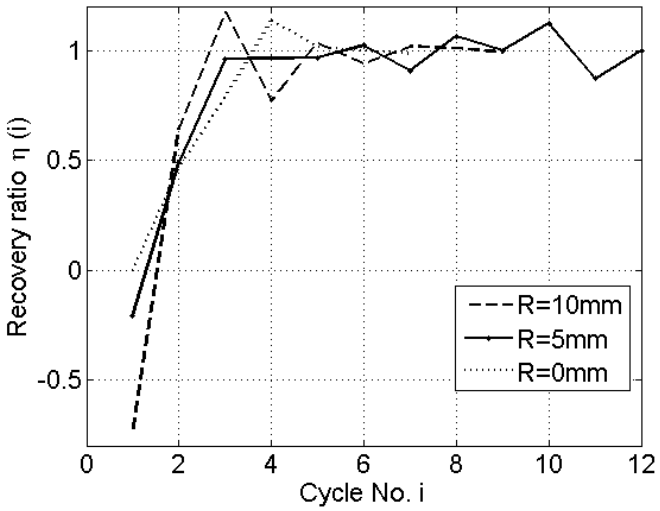

Figure 5.6.: Illustration of the learning effect for shape memory composite bending samples.

Past studies on the thermomechanical actuation properties of SMPs were focused on the strain recovery effect, the learning effect, and the recovery temperature [13, 117]. Most of these studies were performed using tensile test samples only. Tobushi et. al. [115] showed the thermomechanical properties in thin films of polyurethane series using tensile test samples. The focus was on the shape fixation and the *learning effect*. Tobushi [117] furthermore gave numbers for energy densities. However, these results were determined using constant recovery strain rates, which implies an additional constraint. Baer et. al. [7] investigated recovered strain, dependent on the cycle number and the recovery temperature using tensile samples. Liu and Gall [72] showed recovery couplings in a flexure load case with the focus on deformation stress, recovery temperature and heating and cooling rates.

In this work a new experimental method is shown, which is able to determine more valuable figures of merit from an actuation point of view. The method and the determined comprehensive actuation property characteristics for *Veriflex* in tension and compression are shown in the next section.

5.3. Material Properties of SMPs

For the simulation and determination of appropriate experimental processes and process parameters it is necessary to know the conventional material properties of the SMP. In this work, the material *Veriflex* manufactured by the company *CRG Industries* is used.
Three general material properties of SMPs are of interest: The transition temperature T_{trans}, the coefficient of thermal expansion (CTE) α_T and the Young's modulus E.

5.3.1. Transition Temperature

The transition temperatures of SMPs strongly differ depending on their chemical composition. While for epoxy based SMPs for example, the transition temperature is in the range of 70^oC to 115^oC [130], for the polystyrene based *Veriflex* used in the current work, the manufacturer declares a transition temperature of $T_{trans} = 62^oC$. For the determination of actuation properties the thermomechanical cyling tests must be adjusted to the transition temperature. Only at temperatures well above the transition temperature T_{trans} a full recovery can be guaranteed. Furthermore, the drop of the Young's modulus and the change from the elastic to a visco-plastic behavior takes place at this temperature.

5.3.2. Coefficient of Thermal Expansion

The coefficient of thermal expansion (CTE) of polymers is significant and is about 5 to 10 times higher than that of metals. This CTE is responsible for a significant change of the actuation stress σ_{act} (Equation 5.5) by a thermal stress (Equations 5.4). For the used *Veriflex* the CTE is determined in a dilatometer test. Two samples are tested 3 times each. The measurement results can be seen in Figure 5.7.

A slight nonlinearity can be seen in the range between $T = -60^oC$ and $T = +50^oC$. However, for the calculations and modeling, a linearized CTE of $109.5 \cdot 10^{-6}[\frac{m}{mK}]$ is used.

5.3.3. Young's Modulus

For polymers the Young's modulus is not constant but shows significant changes as a result of changes of the temperature and the strain rate $E = f(T, \dot{\varepsilon})$. Increasing strain rates increase the Young's modulus of polymers. This can be explained with relaxation effects which can take place if the deformation is applied slowly. For dynamic loads the sliding of polymer chains cannot occur but the chains may catch each other.
With the change from the glassy to the rubbery state at the glass transition temperature the Young's modulus of polymers drops significantly in magnitudes.
Both effects are investigated experimentally. The tests are performed with standard test samples using *DIN EN ISO 527-1BA* with an *INSTRON 4505* tensile testing machine and

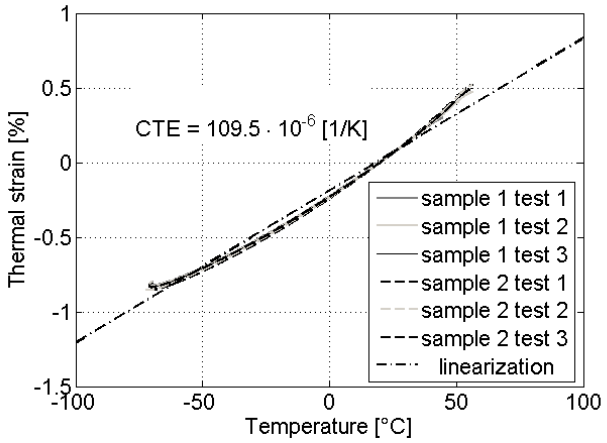

Figure 5.7.: Measurement of thermal expansion for several samples and a linearized CTE of $109.5 \cdot 10^{-6}[1/K]$.

a thermal chamber. The Young's modulus is determined regarding the standard *ISO 527-1* (Equation 5.17).

$$E = \frac{\sigma_2 - \sigma_1}{\varepsilon_2 - \varepsilon_1} \tag{5.17}$$

where $\sigma_{1,2}$ are the measured stresses for the test strains of $\varepsilon_1 = 0.05[\%]$ and $\varepsilon_2 = 0.25[\%]$. If nonlinearities due to the clamping boundary conditions at elevated temperatures occur the strain values are shifted into the linear elastic region.
Because of the high programming strains ε_{prog} of more than 200% at elevated temperature, conventional strain measurement techniques such as extensiomenters and strain gages cannot be used. Since the tests are performed in a thermal chamber a visual auto correlation system cannot be used. Thus the machine displacement is used for the strain measurements. This technique, however, produces large errors as compared to the real strain due to creep effects at the clamping edges. Hence a machine correction factor k_m is necessary in order to correlate the real strain to the machine displacement. For that a parallel measurement with the machine displacement and an extensiometer is performed up to 40% at 60 ^oC. The differences between the measurments are summarized in Figure 5.8.

It can be seen that the differences of the two measurment techniques reduce with increasing temperature which may be explained with the reduction of the applied forces. Thus the machine correction factor k_m is a function of the temperature. For higher strains $\varepsilon > 40\%$, the curve is extrapolated. For the temperature range between 80^{o}C and 90^{o}C, where the thermomechanical cycling tests take place, a machine correction factor of $k_m = 0.85$ is used for the strain calculations to balance the difference of 15%.

The determination of the strain rate dependent Young's modulus is performed at a temperature of 70^oC, using the corrected machine displacement. The test was performed for strain rates of 5, 30 and 62 mm/min. The results are summarized in Table 5.2

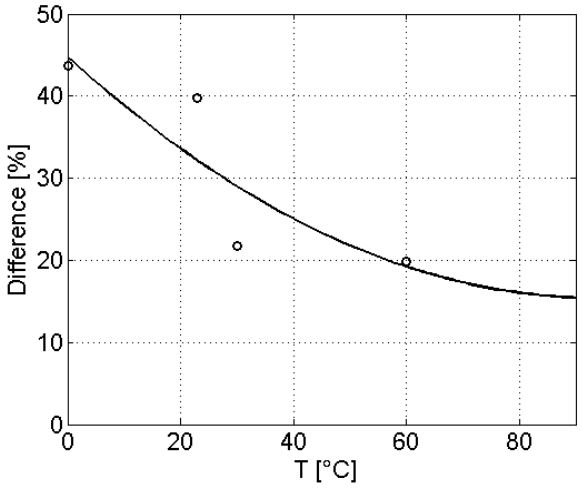

Figure 5.8.: Difference between extensiometer and machine displacement measurements with respect to the temperature; circles indicate measurment data; line is a best fit curve.

Table 5.2.: Young's modulus depending on strain rate at 70 ^oC.

Strain rate $[mm/min]$	Young's modulus $[MPa]$
5	0.48
30	0.74
62	0.81

As expected, a clear increase of the Young's modulus regarding the strain rate can be observed.
Since the standard for polymer testing permits the adjustment of the strain rate and an increased strain rate results in higher recovery stresses and lower testing times, all following tests are performed with a strain rate of $\dot{\varepsilon}$=62 mm/min. However, the standardized strain rate is $\dot{\varepsilon}$=5 mm/min, why for the comparison with material data sheets the strain rate corrected values are used. The same applies for the calculation of the thermal stresses σ_{CTE}, which build up in a slow process. From Table 5.2 a strain rate correction factor of $k_{sr} = 1.69$ between a strain rate of 5 mm/min and 62 mm/min can be calculated.

Thus to calculate the Young's moduli, for reasons of comparability and the determination of thermal stresses, Equation 5.18 can be used. It corrects a Young's modulus E_m, measured with elevated strain rates and the machine displacement, by a strain rate and a machine correction factor to attain representative material properties E.

$$E(T, \dot{\varepsilon} = 5\frac{mm}{min}) = E_m(T, \dot{\varepsilon} = 62\frac{mm}{min}) \cdot \frac{1}{k_{sr}} \cdot \frac{1}{k_m(T)} \tag{5.18}$$

Using this equation the temperature dependent Young's modulus can be determined. The resulting characteristic can be seen in Figure 5.9, where the circles mark strain rate corrected extensiometer measurements and the full line shows an approximated function of the Young's modulus.

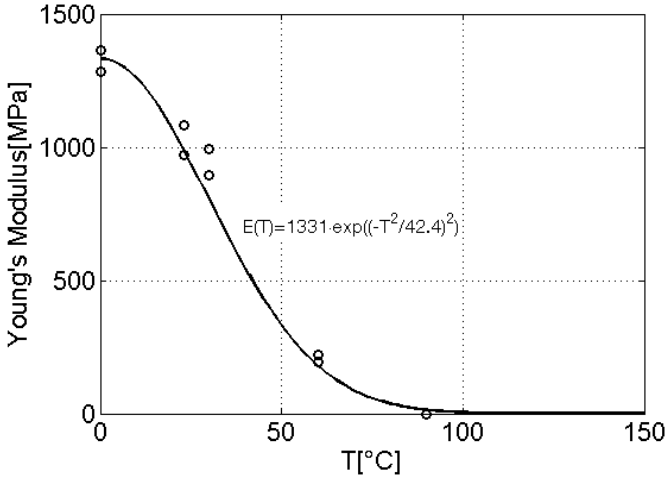

Figure 5.9.: Young's modulus of the Veriflex shape memory polymer with respect to the temperature; circles indicate strain rate corrected extensiometer measurements; full line shows an approximation.

The determined average Young's modulus at room temperature of about 1026 MPa is in the range of the manufacturer specificatoin of 1240 MPa (*CRG industries*). The relationship between the Young's modulus and the temperature is approximated by the following empirical equation:

$$E(T) = 1333.6 \cdot e^{(\frac{-T^2}{42.36})^2} \tag{5.19}$$

For the calculation of the thermal stress σ_{CTE} an averaged Young's modulus $\hat{E}$ has to be calculated in the temperature range between room temperature and the recovery temperature T_r, in which the thermal stress builds up (Equation 5.20).

$$\hat{E}(T_r) = \frac{1}{T_r - 23^oC} \int_{23^oC}^{T_r} E(T)dT \tag{5.20}$$

Using Equation 5.4 and including the averaged Young's modulus $\hat{E}$ and the recovery temperature T_r the thermal stresses σ_{CTE} can be calculated by

$$\sigma_{CTE}(T_r) = \alpha_T \cdot \hat{E}(T_r) \cdot (T_r - 23^oC) \tag{5.21}$$

The results are summarized in Table 5.3

Table 5.3.: Average Young's moduli $\hat{E}$ and resulting thermal stresses σ_{CTE}

Recovery temperature T_r $[^oC]$	Young's modulus $\hat{E}$ $[MPa]$	Thermal stress σ_{CTE} $[MPa]$
50	643.2	1.9
60	536.8	2.17
70	450	2.36
80	381.42	2.38
90	328.16	2.4
100	286.7	2.42

The determined classical material parameters are a basis for the determination of actuation properties, which is introduced in the following.

5.4. Actuation Properties

In Section 5.2 different figures of merit were defined, however, their dependence on each other and on other parameters such as the recovery temperature T_r has not been discussed yet. In this section the experimental determination of actuation properties and their dependencies is shown.

5.4.1. Experimental Setup

The experiments are performed using an *INSTRON* tensile testing machine and an *INSTRON* static thermal chamber. The clamping of the tensile samples is performed with pneumatic clamps to provide a constant clamping pressure despite a sample softening during the thermomechanical cylce. Figure 5.10 shows the test setup.

The strain of the samples is measured by a corrected machine displacement (see previous section). To determine the stress, the force is measured by a load cell with a capacity of 1 kN and a resolution of 0.1 N. From the measured force and the initial cross-section A_0 the stress σ_{r_0} can be calculated as well as σ_r using the actual cross section A. All measures are recorded with the measurement hardware *micromysics* from *National Instruments (NI)* and the measurement software *Famos*. For the tensile tests, conventional, rectangular multipurpose samples with the dimensions of 110 mm $\times$ 12.7 mm $\times$ 3 mm following Grellmann and Seidler [41] and standard samples regarding *DIN EN ISO 527-1BA* are used. The differences in sample geometry are negligible. The sample geometry for the compression test is a 10 mm $\times$ 10 mm $\times$ 8.8 mm cube. This non standard sample geometry is chosen to avoid buckling of the sample without using a protection system. The sample temperature is measured with

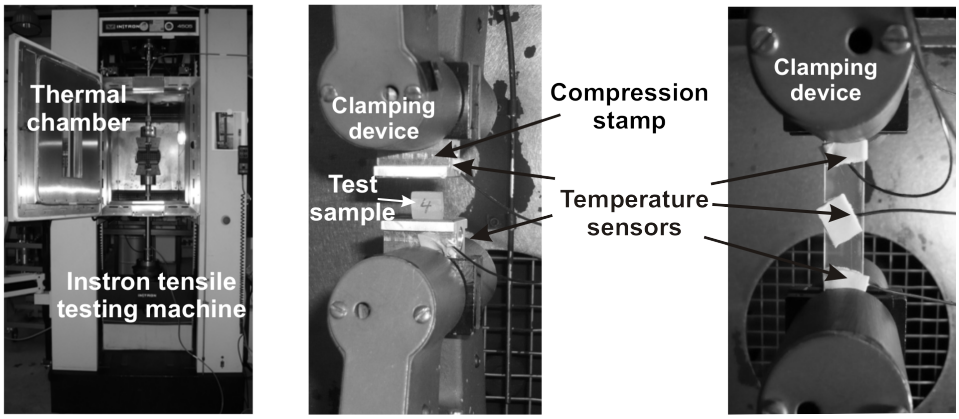

Figure 5.10.: Test setup to determine actuation properties of compression and tensile SMP samples.

thermo-couples at the samples surface. The sample geometries with all dimensions can be found in Appendix A.1.

5.4.2. Experimental Procedure

To determine arbitrary working pairs of recovery strain and recovery stress on the load line, an experimental procedure is developed (see also [150]). The actuation properties are determined by a closed loop, load controlled recovery cycling with the following underlying thermomechanical cycle (Figure 5.11, see also Figure 3.24).

The shown test cycle for a tensile sample is devided in five phases (0-4)(see also Section 3.3.3). In phase 0 the temperature is increased to the programming temperature T_{prog}, while the sample is fully constrained. A compression stress builds up due to the thermal expansion. This stress diminishes when the glass transition temperature is reached and the sample begins to buckle. In phase 1 the designated programming strain ε_{prog} is applied. In phase 2 the sample is mechanically constrained and cooled down to a storage temperature T_s. After a storage time t_s and the unloading of the sample the temperature is increased again (phase 3). Passing the transition temperature T_{trans} the recovery starts (phase 4). In phase 4 the control changes from displacement to load control. After reaching the desired recovery stress level, the closed loop control keeps the stress constant within a small stress range R_σ, while the strain recovery progresses.
Within the fully constrained blocking stress cycles the actuation stress σ_{act}, including an additional thermal stress component, is determined. Figure 5.12 shows a representative blocking stress cycle for a tensile sample (Figure 3.23 illustrates such a cycle qualitatively in a stress-strain-temperature diagramm).

This cycle shows two differences to the previously introduced recovery cycle. It is fully strain controlled, thus after phase 1 the sample remains fully constrained and only a recovery stress builds up. Furthermore, an additional phase 5 is shown in which the build-up of the additional

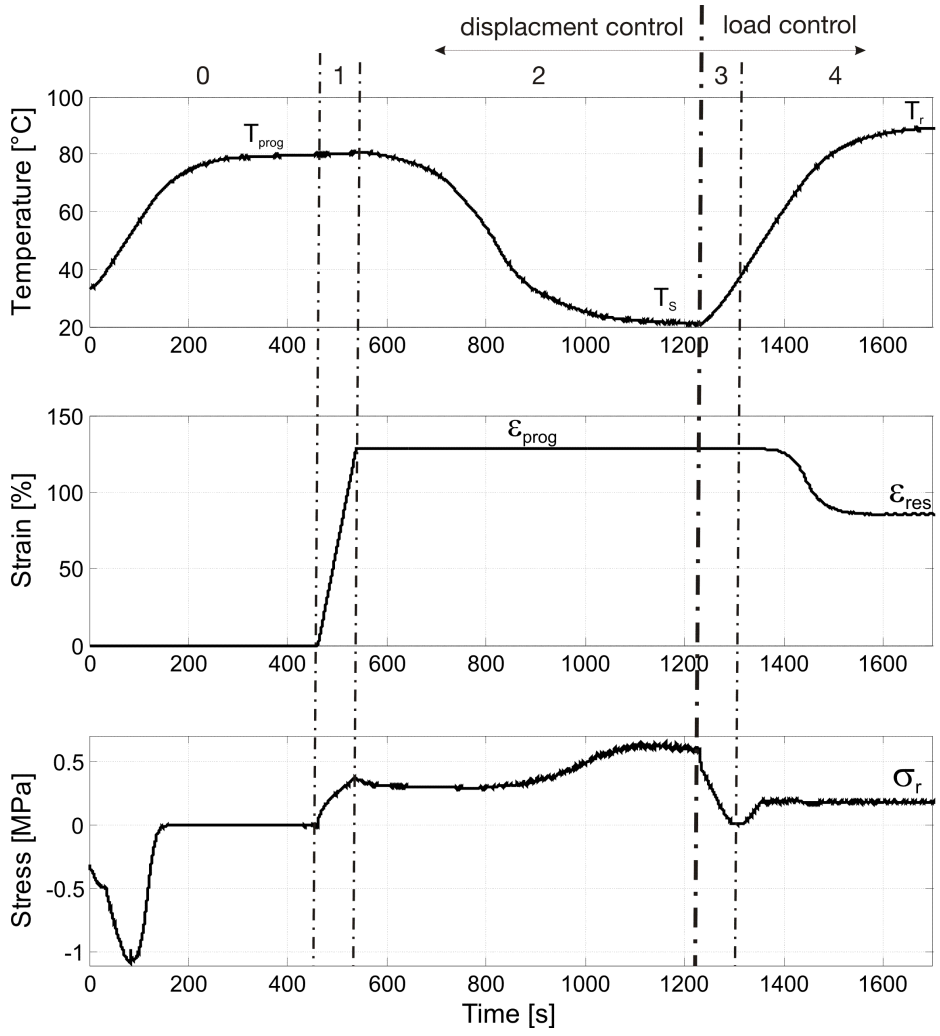

Figure 5.11.: Record of an energy recovery cycle including temperature, strain and stress curves for tension

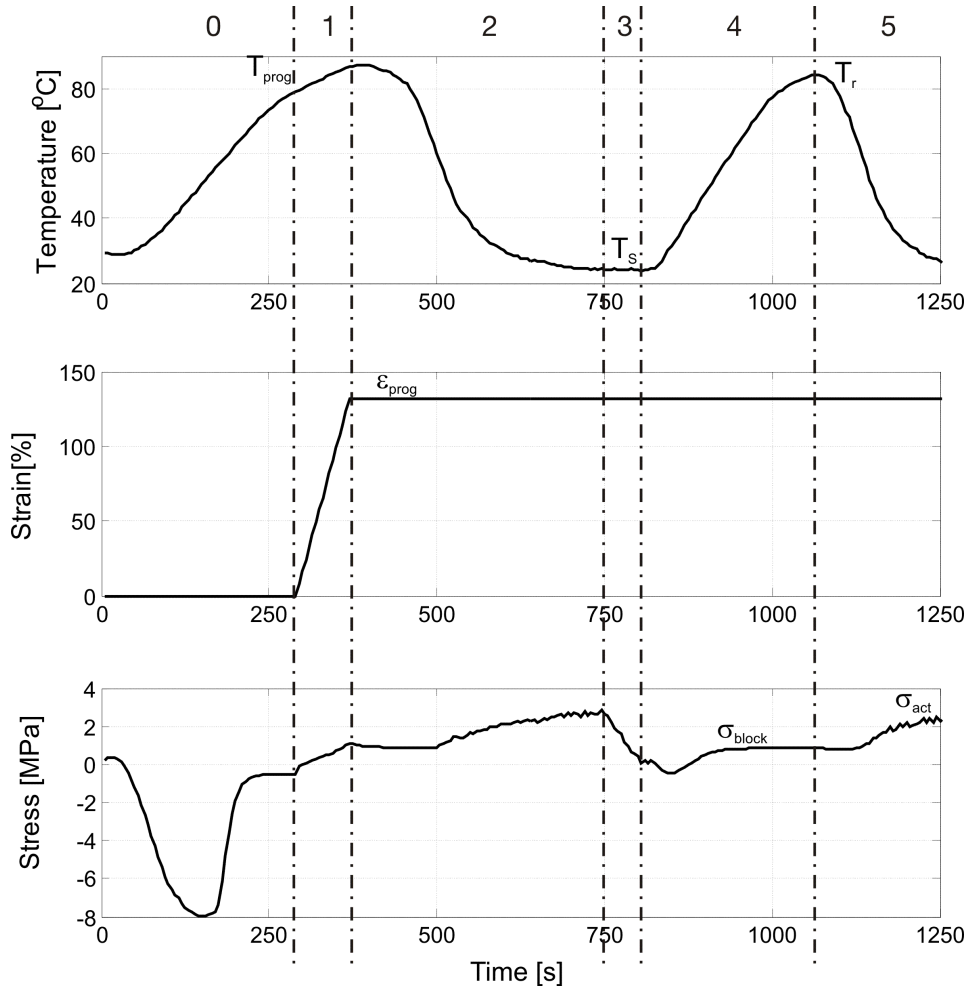

Figure 5.12.: Record of a blocking stress cyle including the actuation stress σ_{act} for 130% of programming strain.

thermal stress σ_{CTE} ends up with the actuation stress σ_{act}.
The details on all test and control parameters can be found in Appendix A.3.

The introduced recovery cycles are used to obtain comprehensive actuator characteristics including arbitrary working points between the extremes of blocking stress and free recovery. The influence of programming strain is introduced as a further parameter, thus the recovery stress, the actuation stress and the recovery energy densities for tension and compression are determined regarding the programming strain and the recovery ratio.

5.4.3. Recovery Stress

The recovery stress is the actuation property which is directly achieved by the stimulation. It is a well known property - hence it is determined for the purpose of comparison with other smart materials. The standard property fields, related to the original actuator cross-section A_0 can be found in [150]. Here the properties related to the actual cross-section A after programming are shown, because those are used for the modeling and simulation of the shape adjustment process. The characteristics in Figure 5.13 and 5.14 summarize the results. The asterisks mark experimental data, the circle indicates an additional extrapolated data point and the surface is a *Matlab* interpolation.

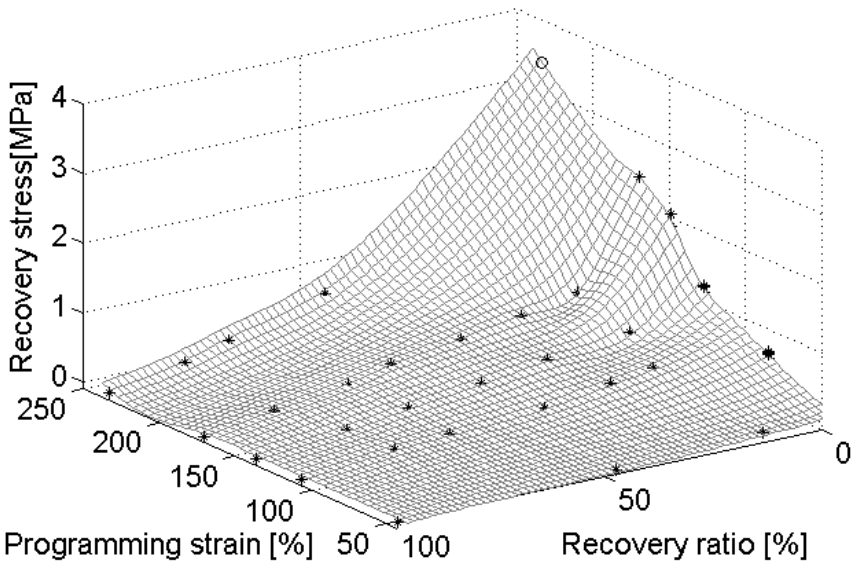

Figure 5.13.: Recovery stress characteristic for the tensile mode.

Several phenomenons can be observed from the actuator characteristic for the tensile mode. A full recovery ratio of about 100% is achieved for all programming strains without a load. The increase in recovery stress develops progressivly with decreasing recovery ratio. Thus for shape memory polymers the linear interpolation between the blocking stress and the free

recovery is not feasible. The second conclusion which can be drawn from the characteristic is the strong increase of recovery stress with increasing programming strain, which also can be seen in Figure 5.16. The maximum achieved programming strain of 233% results in a recovery stress of 0.7 MPa at a recovery ratio of 50%. The maximum measured recovery stress is a blocking stress of 2.38 MPa for a programming strain of 170%. Higher programming strains lead to the failure of the samples during the blocking stress build-up.

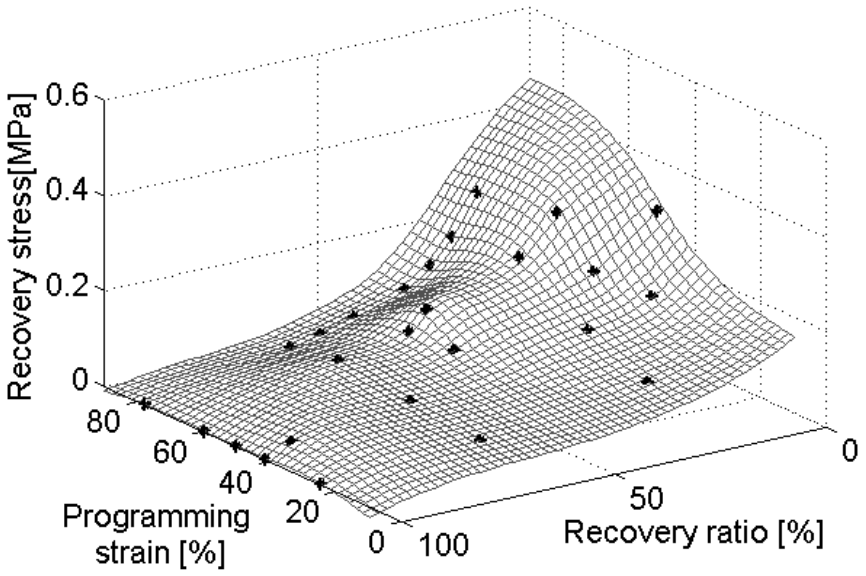

Figure 5.14.: Recovery stress characteristic for the compression mode.

For compression the characteristic is slightly different. While with decreasing recovery ratio the recovery stress increases progresively too, the clear trend of higher programming strain leading to higher recovery stresses can only be observed up to a programming strain of 60%. Above, the recovered stresses reduce again. This might be explained with the very high compression of the samples and possible damage or with the increasing contact surface between the sample and the tool because of the transversal expansion and the increased friction forces hindering the recovery. The overall stress level is with a maximum of 0.3 MPa much lower than for tension. This can be explained with the necessarily higher cross sections for the used cube samples and the limited programming strain. Thus in general the tensile actuators are advantageous in terms of stress output. However, in some applications compression actuators might be necessary. Furthermore, the achieved recovery strains of the compression samples are as high as 400%, which might be highly relevant for some deployment applications.

These determined characteristics provide the necessary actuation properties for the simulation of applications were the additional thermal stresses do not have a significant effect. This is the case for bending recovery as it appears in deployment applications. Large deformations during deployment are achieved by a bending recovery at elevated temperature. The cool down in the deployed state leads to in-plane thermal stresses, which do not affect the shape

significantly.
However, for the actuator patch application the additional thermal stress is a significant factor, which adds to the recovery stress for tension and subtracts for compression actuators.

5.4.4. Actuation Stress

Since for compression, thermal tensile stresses are built up during cool down, which could not be measured with the used test setup, only the actuation stress characteristics for the tensile acutators are shown. Furthermore, the thermal stress adds a significant magnitude of actuation stress to tensile actuators while for compression actuators it has a negative influence (see Section 3.3.3). The actuation stress for tension is measured in blocked recovery cycles with a programming strain of 100 % for different recovery temperatures. The results are summarized and illustrated in Figure 5.15.

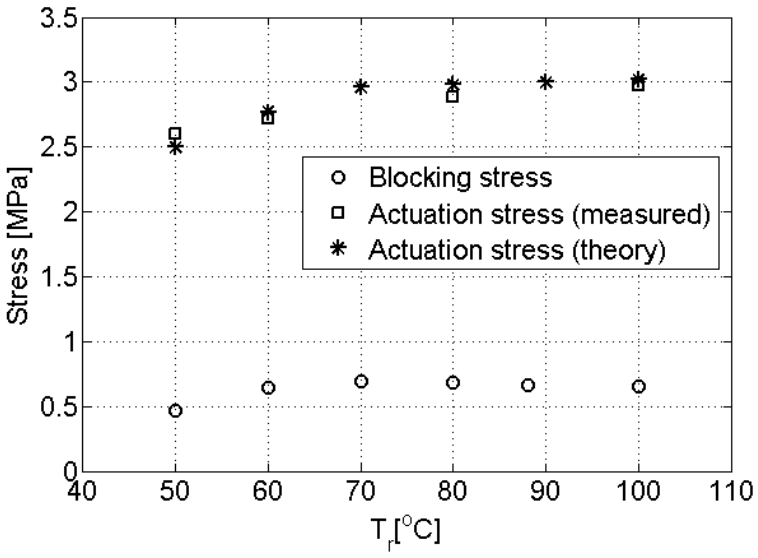

Figure 5.15.: Blocking stress and actuation stress with respect to the recovery temperature for a programming strain of 100%.

It can be seen that the blocking stress is independent of the recovery temperature for $T_r > T_g = 62^oC$. The actuation stress, however, increases with increasing recovery temperature due to the higher thermal strain and stress respectively. The increase, however, converges since the Young's modulus of the material is reduced succesively (Table 5.3). It can be seen that theory and measurement agree very well. This is also verified for different programming strains (Figure 5.16).

For a constant recovery temperature of 88^oC only a parallel shift of the characteristic of 2.4 MPa can be observed. The figure shows a good agreement between measurement and theory. The lower measurements for high programming strains might be explained with

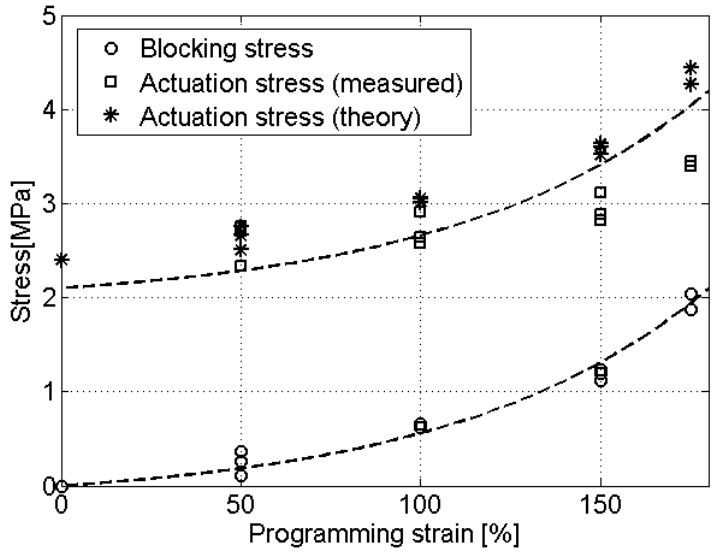

Figure 5.16.: Blocking stress and actuation stress with respect to the programming strain for a recovery temperature of 88^oC.

relaxation effects. The maximum measured actuation stress is 3.5 MPa.
Adding the theoretical values of the thermal strain regarding Table 5.3 to the experimentally determined recovery stresses an actuation stress characteristic can be obtained which is shown in Figure 5.17.

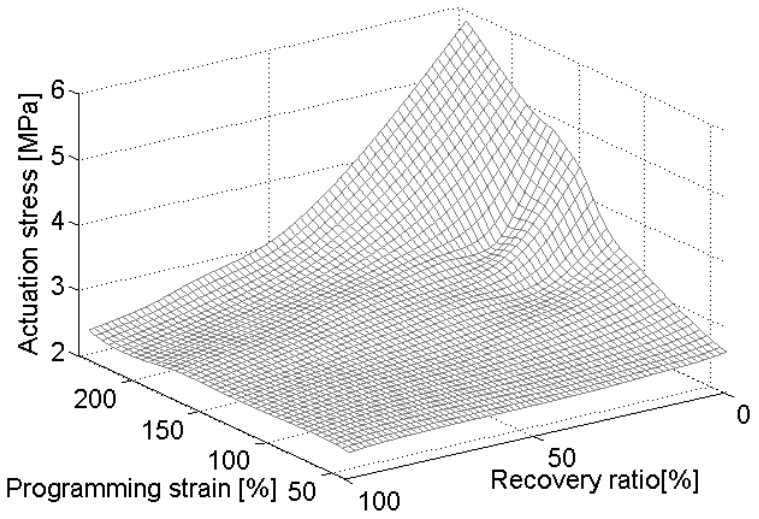

Figure 5.17.: Interpolated actuation stress characteristic for a recovery temperature of 88^oC.

The characteristic is shown for a representative recovery temperature of 88 ^oC. It shows

the same behavior regarding programming strain and recovery ratio as the blocking stress. However, much higher stress levels are obtained. This actuation stress characteristic can be used as a look up table for the modeling and simulation of shape memory polymer actuator patches.

5.4.5. The Recovery Energy Density

For general actuator selection the energy density is the more valuable and general figure of merit. The optimum working point can be found from this characteristic and necessary stroke or force can be produced using proper transmissions. Using Equation 5.14 the energy density characteristic shown in Figure 5.18 is calculated. More detailed information on energy densities can be found in [150].

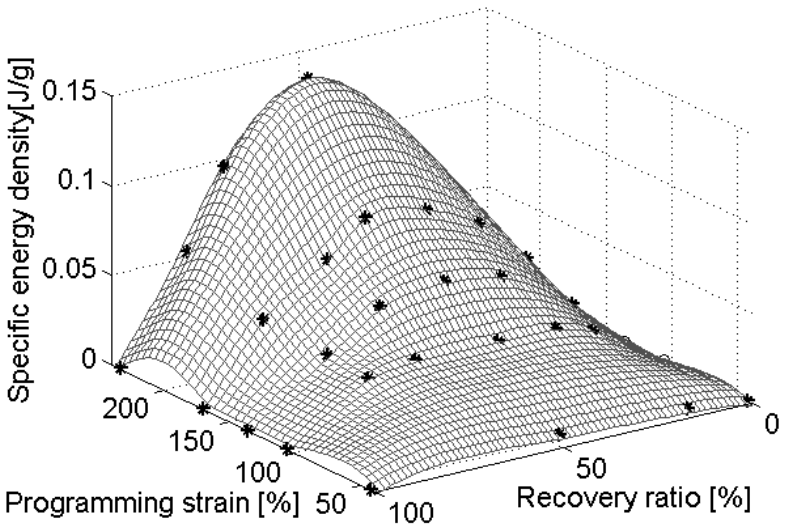

Figure 5.18.: Energy density characteristic with respect to the recovery ratio and the programming strain for tension.

It can be seen that an optimum energy output exists. For the example on hand this optimum is achieved for a programming strain of 233% and a recovery ratio of 50% with a value of 0.138 J/g, which is a competitive value. For fully constrained and free recovery respectively, the product of stroke and stress diminishes if the thermal stress is not considered, which is generally feasible.
For the compression case the characteristic is shown in Figure 5.19.

Although the recovery stresses for compression are smaller than for tension, the achieved energy density is similar for both modes. This can be explained with the much higher recovery strain in compression compared with tension, balancing the smaller recovery stress. The maximum measured specific energy density is 0.15 J/g for a programming strain of 80%

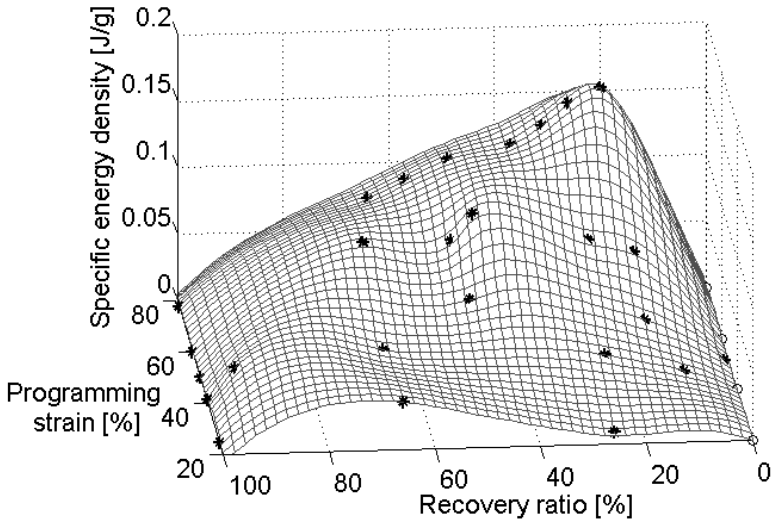

Figure 5.19.: Energy density characteristic with respect to the recovery ratio and the programming strain for compression.

and a recovery ratio of 20%. It shall be noted that the optimum appears at higher stress levels and lower recovery ratios than for the tensile mode. Because of that the two actuation modes are complementary and extend the application range of shape memory polymers.

6. Finite Element Modeling of Shape Adjustment

The finite element method (FEM) is an appropriate method for the modeling of composite structures with integrated actuators, because complex structural geometries, laminate layups and actuation properties can be modeled. Furthermore, effects of the actuator patch load introduction, such as shear in the actuators, can be captured by this method. In Chapter 8 it is shown that unconventional material parameters of the shape memory polymers cannot be treated with existing analytical models. The FEM provides a suitable solution to model and simulate such problems. Hence finite element models are built for the analysis of structural matters, such as the load introduction of SMP actuator patches, and to solve the system equations for the shape error minimization algorithm. The commercial FEM tool *ANSYS 12* is used for pre-processing, computation and post-processing.

6.1. Modeling of Thin-Walled Composite Parts

For thin-walled composite parts, shell elements of the type *shell181* are chosen since shear deformation and stresses in thickness direction are assumed to be negligible. Four node quadrilateral or degenerated triangular elements are chosen. The triangular option is necessary to avoid element warpage of quadrilateral elements. To model the layup of the laminate, the layered shell option is used.
The geometry of the composite parts is modeled regarding the ideal shape. The stiffness change in the part, due to small geometry changes caused by the manufacturing distortions, is assumed to be negligible. To reduce the modeling effort, especially with respect to the applied optimization algorithm, the original shape is modeled in most cases. The same applies for the local gradients of fiber volume fraction and locally different fiber orientations. The part thickness , however, has a significant influence on the part stiffness and the shape adjustment process. The second-most important property, the Young's modulus in fiber direction, is taken from a large number of mechanical tests, which were performed with prepreg laminates of the same batch. The less sensitive material properties are taken from a representative material database of the *Institute of Lightweight Structures*. The material data used for the UD ply can be found in Appendix A.4. The sensitivities of modeling errors of the structure regarding the shape adjustment simulation are investigated using a finite element anlaysis of a representative sample (Example 1.1). The results are summarized in Figure 6.1.

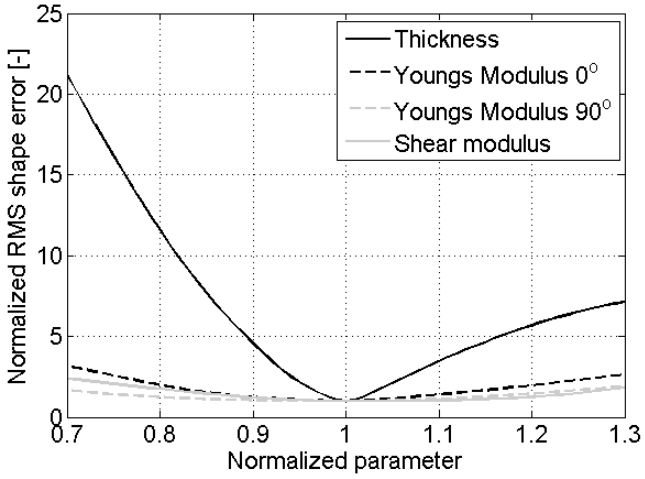

Figure 6.1.: Sensitivity of modeling errors of thickness and moduli on the RMS shape error.

It can be seen that the structural thickness has the most significant influence on the simulation of the shape adjustment. The sensitivity to the material properties is one order of magnitude smaller. The most sensitive material property is the Young's modulus in fiber direction.

6.2. Modeling Shape Memory Polymer Actuator Patches

6.2.1. Finite Element Selection

In contrast to the thin-walled composite parts, the actuator patches, with a relatively high thickness and a high shear deformation, are modeled using 8 node brick elements of the type *solid45*. At least three elements are used in thickness direction. The adhesive layer is also modeled using the same elements with at least three elements in thickness direction. This means that for the used adhesive layer thickness of 0.2 mm an element height of 0.067 mm is used. In order not to violate the thickness to length ratio limit of 1:10, the element width and length for the adhesive layer is limited to 0.67 mm. This leads to a high number of DOFs for the accurate modeling incoorporating an adhesive layer, since the substrate and the actuator are directly coupled to the adhesive layer nodes. Therefore the adhesive layer is modeled for different parametric studies. However, the adhesive layer is neglected for the shape optimization process due to the large computational effort.

6.2.2. Geometry

The geometry of the actuator patches is modeled regarding the design variables (Chapter 9) as bricks with a certain length, width and thickness. The orientation regarding the composite part is also given by the design variables. The thickness is modeled with 2 mm, which is the standard thickness due to manufacturing restrictions. The adhesive layer is modeled as well as a volume with the same dimensions as the actuator and a thickness of 0.2 mm.

6.2.3. Material Model of SMPs

As can be seen in Section 3.3, SMPs show a non-linear 3D-visco-thermo-elastic behavior, which is dependent on the programming history. Using certain assumptions for the application of patch actuators, this model can be significantly simplified and implemented in a linear elastic finite element model.

Assumptions

- Full recovery level is used only.
- Normal actuation strain only (no bending, twisting or shear).
- Isotropic, linear elastic material properties.
- Negligible lateral recovery stress.

The assumption of the use of the **full recovery level** is feasible as long as the recovery temperature and time are high and long enough to ensure the full recovery. This is even desired to obtain the maximum energy output and to reduce actuator mass. Using this assumption the material model becomes independent of the temperature T and time t, and the recovery process itself does not need to be modeled. The non-linear behavior of the SMP is illustrated in Figure 6.2.

The figure shows a non-linear behavior of the recovery level regarding the temperature and time. With increasing temperature, a quasi-discrete switch from no recovery to full recovery takes place at the transition temperature. With increasing time, different behaviors can be observed. Below the transition temperature, no recovery occurs. However, above the transition temperature the recovery increases non-linearly until saturation at the full recovery level is reached. The stationary area of full recovery, which is used in the modeling, is marked with a circle. The height of the recovery level, which is composed of recovery stress σ_r and strain ε_r, is determined by the programming strain ε_{prog}, which should be chosen as high as possible to get the maximum energy output.

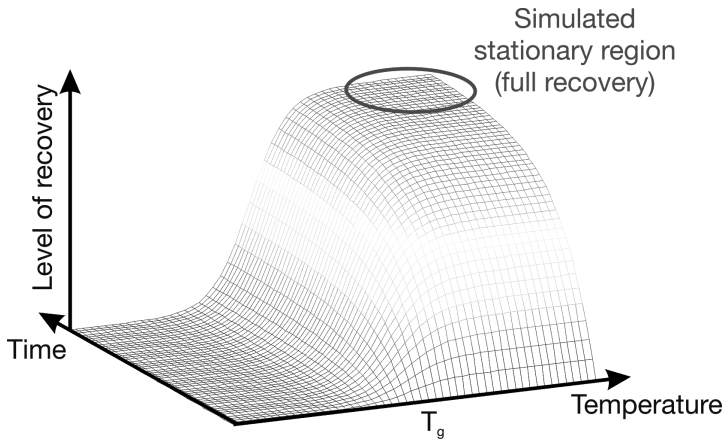

Figure 6.2.: Qualitative physical interpretation of the recovery level regarding recovery temperature and recovery time.

The assumptions of **normal actuation strain only** and **isotropic, linear elastic material properties** lead to a decoupled 3D stress recovery behavior for the patch actuation, described by Equation 6.1:

$$\begin{Bmatrix} \sigma_{rx} \\ \sigma_{ry} \\ \sigma_{rz} \end{Bmatrix} = \frac{E}{1-\nu-2\nu^2} \cdot \begin{bmatrix} 1-\nu & \nu & \nu \\ \nu & 1-\nu & \nu \\ \nu & \nu & 1-\nu \end{bmatrix} \cdot \begin{Bmatrix} \varepsilon_x \\ \varepsilon_y \\ \varepsilon_z \end{Bmatrix} - E_{eff} \cdot C_M \cdot \begin{Bmatrix} \Delta S_x \\ \Delta S_y \\ \Delta S_z \end{Bmatrix} \quad (6.1)$$

where $\sigma_{rx,y,z}$ are the recovery stresses in x-, y- and z-direction, E and ν are the Young's modulus and the Poission's ratio of the actuator material, E_{eff} is the effective Young's modulus for the actuation, C_M is the shape memory coefficient and $\Delta S_{x,y,z}$ are the stimulation parameters. While the shape memory coefficient is a constant, the stimulation parameters are a function of the programming strain $\Delta S = f(\varepsilon_{prog})$. The first term on the right side of the equation describes the mechanical behavior of the actuator, while the second term is the actuation stress. In general, arbitrary stress-strain pairs can be calculated from this equation. However, for the introduced patch actuation, small mechanical strains ε are expected. In this case the first term of Equation 6.1 becomes zero, and the equation simplifies to:

$$\begin{Bmatrix} \sigma_{x,act} \\ \sigma_{y,act} \\ \sigma_{z,act} \end{Bmatrix} = -E_{eff} \cdot C_M \cdot \begin{Bmatrix} \Delta S_x \\ \Delta S_y \\ \Delta S_z \end{Bmatrix} \quad (6.2)$$

which corresponds to a 3D actuation stress σ_{act}.
For the patch actuation, the out-of-plane direction does not lead to a relevant actuation stress, thus this direction is not programmed and stimulated. Both in-plane directions can be used simultanously, if 2D programming is applied, which requires a bi-axial tensile testing machine operated in a thermal-chamber. To avoid this additional equipment requirement,

only 1 dimensional (1D) programming and actuation is considered, which further simplifies the actuation equation to:

$$\sigma_{x,act} = -E_{eff} \cdot \underbrace{C_M \cdot \Delta S_x(\varepsilon_{prog})}_{\Lambda} \tag{6.3}$$

where Λ is the actuation strain represented in case of shape memory polymers by a free recovery strain ε_{free} (Equation 6.5). This 1D relationship is only true with the additional assumption of a **negligible lateral recovery stress**. The feasibility of this assumption can be explained as follows.
For tension actuators, a lateral compression recovery exists. However, the compression actuation stress is very small since the thermal stress is counteracting the shape memory effect. This small stress is further reduced by the factor of the Poission's ratio in lateral direction.
For compression, the lateral expansion during programming is avoided by the mould (see Section 7), thus no lateral recovery appears.
Therefore the lateral recovery is neglected, and the 1-D model is used for the material modeling.
This linear relationship between a stimulus and a resulting strain is well known for thermal expansion (Equation 6.4).

$$\varepsilon_T = \alpha_T \cdot \Delta T \tag{6.4}$$

where ε_T is the thermal strain, α_T is the coefficient of thermal expansion, and ΔT is the temperature change. This analogy can be used in the finite element method for the modeling of actuation properties. For the modeling, this means an introduction of an orthotropic thermo-elastic behavior ($\alpha_x = C_M, \alpha_y = \alpha_z = 0$), and the application of a thermal load ($\Delta T = \Delta S$) as a stimulus. Table 6.1 summarizes the analogy.

Table 6.1.: Summary of *analogy of thermal expansion*.

	Formula	Strain	Coefficient	Stimulus
Thermal expansion	$\varepsilon_T = \alpha_T \cdot \Delta T$	ε_T	α_T	ΔT
Shape memory effect	$\varepsilon_{free} = C_M \cdot \Delta S$	ε_{free}	C_M	ΔS

For the modeling of the shape memory effect using the *analogy of thermal expansion*, a further issue has to be considered. While the shape memory effect shows a volume constancy during programming and recovery by lateral contraction, this is not the case for the thermal expansion, and the corresponding finite element properties. To avoid artificial lateral forces due to the missing volume constancy for the thermal expansion, either a negative CTE in perpendicular direction can be modeled or a Poission's ratio of zero can be used, which is selected for this work.

The determination of the other parameters E_{eff}, C_M and ΔS for the 1D case (Equation 6.3) is described in the following. An overview of this determination process is given in Figure 6.3.

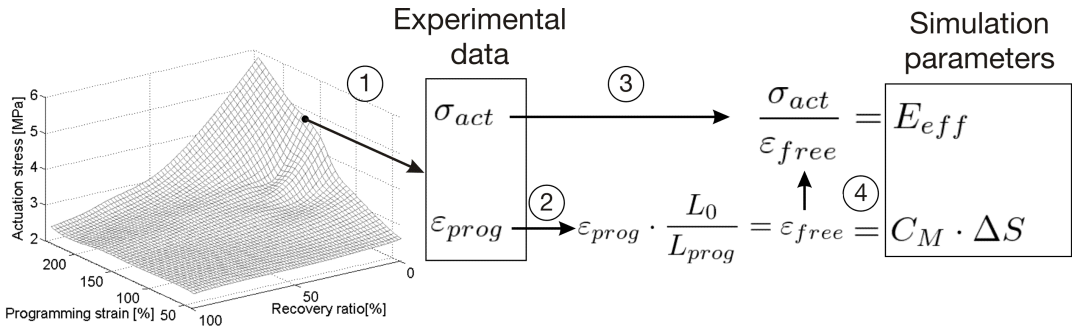

Figure 6.3.: Process flowchart for the determination of simulation parameters.

From the actuation stress characteristic (Figure 5.17), proper actuation stresses and the corresponding actuation strain can be obtained (1). For patch actuation of stiff structures, a low actuation, thus recovery strain is expected. Hence, the actuation stress is chosen from the right edge of the property characteristic. One has to move to the inner region of the stress characteristic, only if larger strains are expected. To get a maximum actuation stress, high programming strains are chosen. From the programming strain, a free recovery strain ε_{free} can be calculated (Equation 6.5) (2).

$$\varepsilon_{free} = \varepsilon_{prog} \cdot \frac{L_0}{L_{prog}} \tag{6.5}$$

Using this free strain and the resulting actuation stress σ_{act}, an effective Young's modulus E_{eff} can be calculated (Equation 6.6) (3), which is one of the input parameters for the finite element simulation.

$$E_{eff} = \frac{\sigma_{act}}{\varepsilon_{free}} \tag{6.6}$$

To achieve the free recovery strain using the analogy of thermal expansion, the parameters C_M and ΔS have to be determined. Since only the stationary, full recovery is modeled, those parameters can be chosen arbitrarily as long as their product results in the determined free recovery strain (4). Here a C_M of $110 \cdot 10^{-6}$ is chosen to be constant and the stimulus parameter ΔS is calculated regarding the free recovery strain (4). All material parameters used for the finite elements of the shape memory polymers can be found in Appendix A.4. Figure 6.4 shows a representative example of the finite element models used.

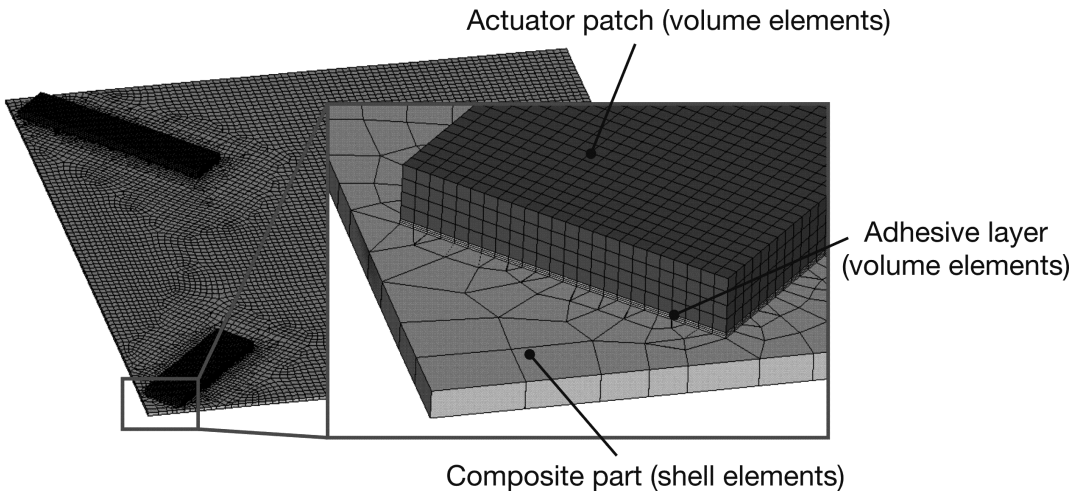

Figure 6.4.: Illustration of a finite element model

7. Application, Stimulation and Programming of SMP Actuator Patches

In this chapter, practical aspects of the shape adjustment process are addressed. In addition to the mentioned 3D shape sensing, the practical part contains the programming, the application, and the stimulation of the actuator patches.

7.1. Programming of SMP Actuator Patches

The first step in the thermomechanical cycle, where the sample is strained to its maximum deformation, is called programming. This is the step in which energy is applied to the actuator, which then is stored during freezing-in in the temporary shape. In most cases the programming is performed well above the transition temperature $T_{prog} > T_{trans}$ to achieve high programming strains ε_{prog}. This is essential for the programming of shape memory composites, otherwise the integrated fibers will break during the typical bending programming. In general shape memory materials can be programmed to any arbitrary shape. Very complex programmed shapes can be found in medical applications or in folding paterns of deployment applications [63]. In addition to the programmed shape, the original shape can also show any arbitrary shape. This leads to a large variety of possible application geometries.
The focus here will be on the programming of rectangular actuator patches. Basically, the programming is focused on a pure contraction or tension. Out-of-plane actuation by bending or twisting of the patches is not considered. For the soft material, this leads to only very small actuation forces. However, it might be necessary to programm small out-of-plane deformations to be compliant with the distorted composite parts. However, in most cases, the out-of-plane deformations can be neglected for the programming and the actuation stresses. Before the programming is applied, the original actuator size has to be calculated to achieve the necessary actuator geometry. From the desired geometry and the applied programming strain, it is possible to calculate, via the volume constancy and the Poission's ratio, the original sample geometry. It is furthermore necessary to account for the lateral contraction during a tensile programming and the pulling out of material from the clamping jigs. The programming of tensile actuators can be performed in a tensile testing machine in combination with a thermal chamber. The process is defined by the steps 1 to 3, indicated in the thermomechanical cycles of Figures 3.22 to 3.25. It shall be noted that an additional

temperature sensor in the middle of the sample or at an additional dummy sample should be used since the chamber air temperature might be up to 5^oC different from the sample temperature. As mentioned in Section 5.3, the necessary measurement using the machine displacement of the tensile testing machine has to be scaled with an extensiometer test to obtain reliable values for the programming strain. The thermomechanical programming cycle ends with the demounting of the sample (IV in Figure 3.22). Before the sample can be applied to the structure the overlaying ends have to be removed from the sample by a cutting machine producing as little heat as possible to avoid preliminary stimulation. Figure 7.1 shows the different stages of the programming of a tensile actuator patch.

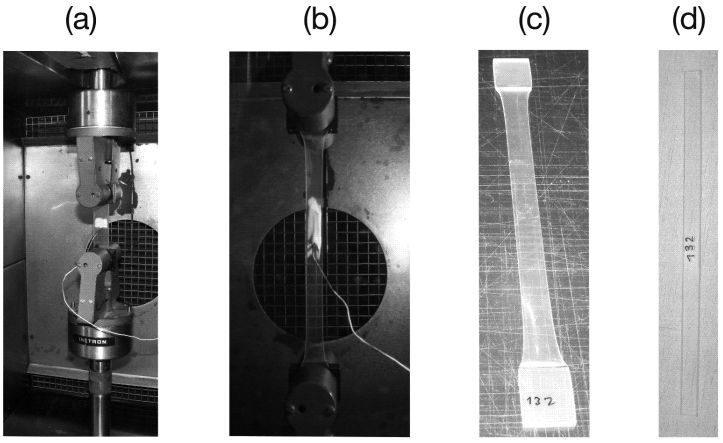

Figure 7.1.: Programming of a tensile actuator: (a) Green body in tensile testing machine; (b) Straining; (c) Programmed sample; (d) Trimmed sample.

An alternative to the caculation of the necessary green body shape is the post programming trimming. However, wasted active material has to be accepted.
To avoid buckling of compression samples during programming a guidance is designed. It consits of a male die and a female mould with the width and height of the final actuator patch. A proper release agent is used for better slippage during programming and demoulding. The green body with its smaller width and height and its longer length can be placed in the mould. The mould including the sample is heated well above the transition temperature in a thermal chamber. After a settling time the mould is removed from the thermal chamber and a compression force is applied. Fixing the sample in this configuration, the mould is cooled down to room temperature. Since the gap between the green body and the mould increases with increasing compressive strain the buckling capability increases as well. Thus, buckling cannot be avoided for more than 50% of programming strain. Using this process the manufacturing limits the theoretically very high (several hundred percent) free recovery strain to about 50%. Figure 7.2 illustrates the programming process for compression samples in the designed mould.

Additional programming in out-of-plane direction can be performed in a subsequent step in an additional mould. For strongly distorted asymmetric plates shown in Section 11.1 this is applied to manufacture curved tensile and compressive actuator patches. A convex mould is

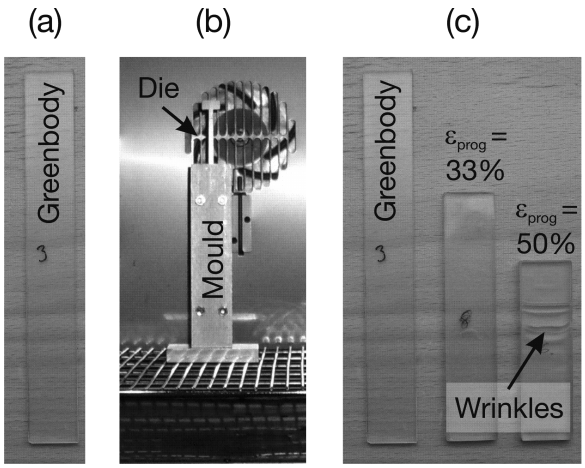

Figure 7.2.: Programming of a compression actuator: (a) Green body; (b) Mould; (c) Porgrammed samples.

manufactured by milling. Different lengths of the patches are adjusted by shims at the end of the mould. A concave die closes the mould and applies the necessary pressure. Heating up the mould, the sample can be pushed in its curved shape. The mould avoids the recovery in length direction during this second programming step. Figure 7.3 shows a sample inside the curved mould.

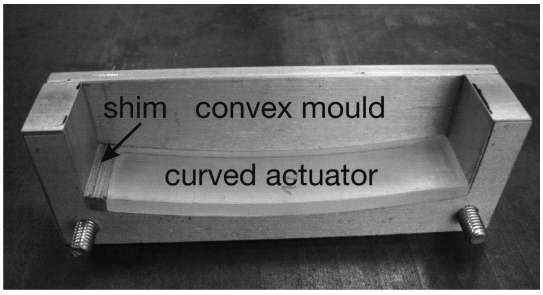

Figure 7.3.: Programming of a curved actuator patch in a mould.

It can be concluded that programming tensile actuators is much easier than compression actuators. Curved patches can be manufactured as well, however, it is an additional programming step which increases the manufacturing effort. For small distortions, however, curved actuators are not necessary.

7.2. Application of SMP Actuator Patches

The common application technique for actuator patches in general is the attachment by a proper adhesive to the structural surface. The load introdcution capability and questions about the adhesion, peel and shear stresses in the adhesive layer will be discussed in Chapter

8. In this section the concenration is on the application process, which consits of the following steps.

- Mechanical treatment of surfaces
- Clean actuator and structural surface
- Mark actuator locations
- Coat structure and actuator
- Place distance wires on the structure
- Apply actuator by avoiding bubbles
- Apply pressure
- Curing

Mechanical treatment of the bonding surfaces is used to improve the bonding strength (see also Section 8.3). For the cleaning of the structure and the actuator surfaces, *Aceton* or *Isopropanol* are used. The attitude of the actuators are marked with pen markers. Using a spatula the thin adhesive layer is applied to the surfaces. Distance wires with a diameter of 0.2 mm are placed in the adhesive layer to ensure the desired adhesive layer thickness. Applying and pushing the actuator to the surface from one end to the other avoids the inclusion of bubbles in the adhesive layer. Using a spatula a neat can be manufactured around the actuator edges. A surface pressure of 0.01 MPa to 0.02 MPa is applied during the curing at room temperature (RT $\approx 21^oC$). For flat samples this can be performed by distributed masses. For curved samples a pressure mould (Figure 7.3) is used. Figure 7.4 illustrates the application process.

7.3. Stimulation of SMP Actuator Patches

In this study heat is used as the stimulus. Heat can be applied either by Joule heating, thus by integrated heating wires or conductive fillers. While wires might reduce the structural load carrying capacity, fillers affect the recovery performance. For systems which have to be triggered in operation, this stimulation approach is the most promising. An alternative could be the triggering by the environment, such as the body temperature for medical applications or sun light and UV radiation for space deployment applications.
For the application introduced here an external stimulation is sufficient, which reduces the integration and system effort significantly. Three methods for external thermal triggering can be distinguished:

- Heat plate
- Heat lamp
- Thermal chamber

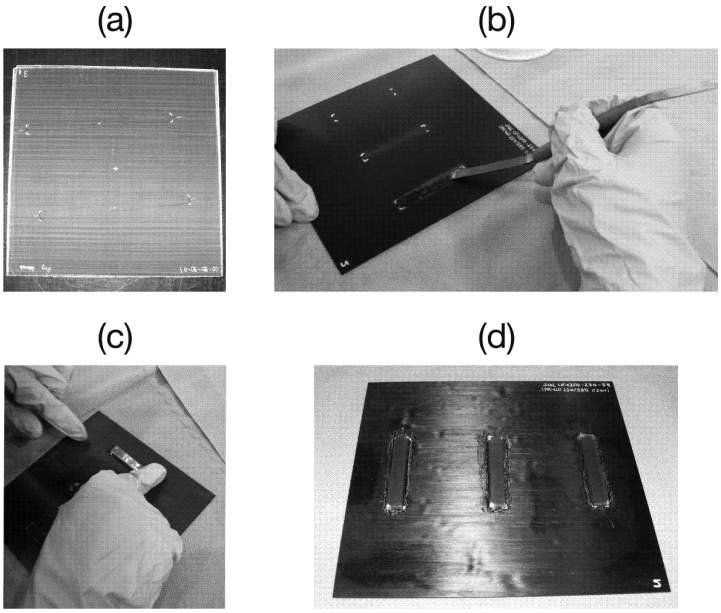

Figure 7.4.: Application process for patches: (a) Cleaning and marking of surfaces; (b) Coating; (c) Application of patches; (d) Curing.

The heat plate is used to trigger deployment of triaxially reinforced shape memory polymer samples (Figure 3.30). Since this method relates basically on the thermal conduction and the direct heat transfer between the plate and the sample, an irregular recovery occurs. This irregularity leads to incomplete recovery. Using a high power heating lamp the deployment of the samples can be accelerated and the quality improves. Using the radiation in combination with the very low mass of these triaxially reinforced samples leads to a quick recovery. However, the distance of the heat lamp and the sample have to be well defined, not to overheat the samples.
For the investigation of the shape adjustment process the samples equipped with the actuator patches are placed in a thermal chamber exhibiting the recovery temperature. After a settling time and a certain recovery time the samples are removed from the thermal chamber and cooled down in a RT ($\approx 21^oC$) environment. This is a very pragmatic approach, which leads to satisfactory results.

8. The Actuator-Structure Interface

8.1. Parametric Study on the Load Introduction Capability

In Chapter 3.2.2 a couple of analytical methods can be found, which can be used for the analytical evaluation of the load introduction of actuator patches. In this chapter these equations are applied to shape memory polymer actuator patches. It is shown that some unconventional phenomenons appear due to the uncommon stiffness and thickness ratios. Parametric studies are performed using a finite element model and the results are compared with the analytical solutions. A model of a simply supported beam, equipped with two actuators at the top and bottom side is built (Figure 8.1).

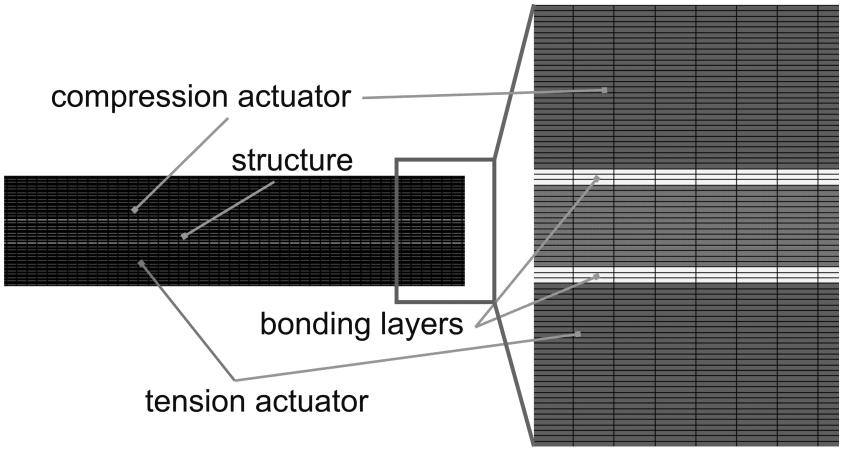

Figure 8.1.: Finite element model for the parametric study on the load introduction.

A 2-dimensional FE model with plain strain plane elements of type *PLANE183* is used. The constant behavior in width direction has been verified with a 3D model. It is assumed that the structure and the actuators have the same width. The actuator placed on top of the structure is operated in compression mode, while the actuator on the bottom side is operated in tensile mode. The adhesive layer is modeled with 3 elements in thickness direction. To verify the finite element model, it is compared to the solutions of the Euler-Bernoulli model and the model with constant strain for conventional stiffness ratios. Figure 8.2 shows the comparison of the models.

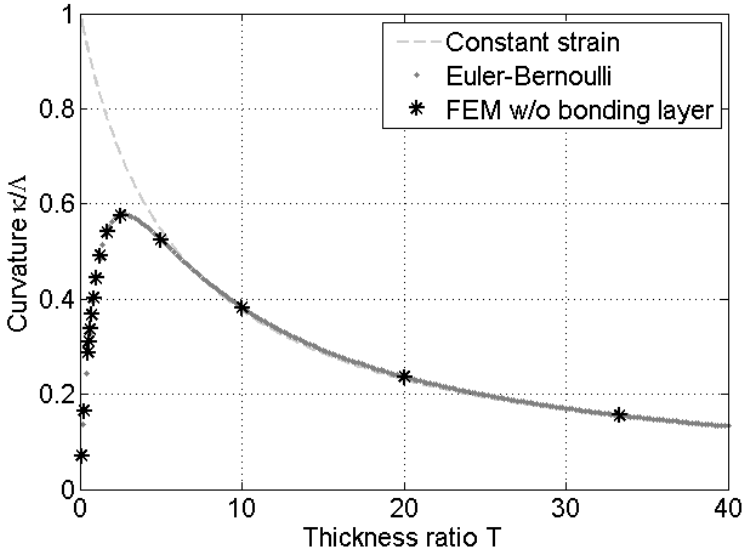

Figure 8.2.: Comparison of the FE model, Euler-Bernoulli model and model with constant strain (all with infinite bonding stiffness), with respect to the thickness ratio T for a stiffness ratio of $\Psi = 1$.

It can be seen that the results of the FE model are very close to the Euler-Bernoulli model's results for a conventional stiffness ratio of $\Psi = 1$.
The reference configuration for the parametric study is a 1 mm thick substrate with a Young's modulus of 50 GPa. The actuator has a thickness of 2 mm and a Young's modulus of 4.5 MPa. These parameters result in a thickness ratio of $T = 0.5$, a Young's modulus ratio of $E_S/E_A = 11111$ and a stiffness ratio of $\Psi = 5555$. The bonding layer has a Young's modulus of 1 GPa, a Poission's ratio of 0.3 and a thickness of 0.2 mm. A free actuation strain of 66% is modeled. The reference parameters are summarized in Table 8.1. Figure 8.3 shows the normalized introduced curvatures regarding the thickness ratio T for the analytical

Table 8.1.: Reference parameters for the parametric study regarding the structure-actuator interface.

Parameter	Value
Substrate Young's Modulus	50 [GPa]
Substrate thickness	1 [mm]
Actuator Young's modulus	4.5 [MPa]
Actuator thickness	2 [mm]
Adhesive Young's modulus	1 [GPa]
Adhesive Poission's ratio	0.3
Adhesive layer thickness	0.2 [mm]

Euler-Bernoulli model with (w) and without (w/o) bonding layer in comparison with the finite element analysis with a bonding layer.

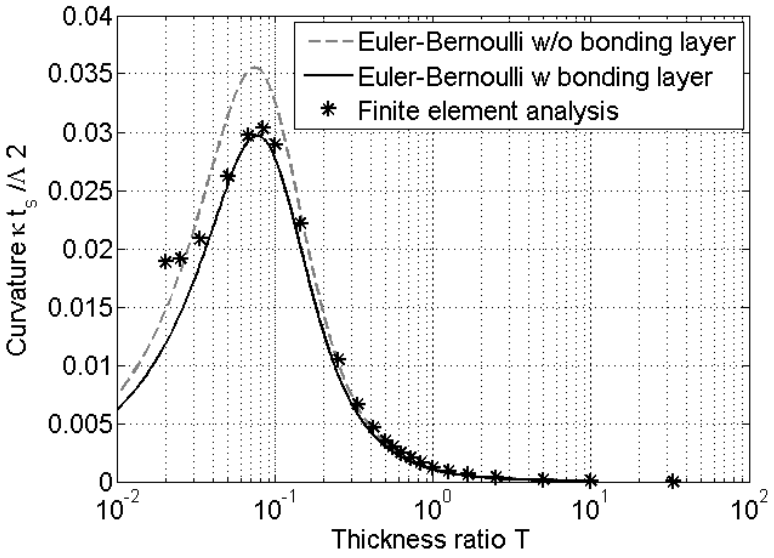

Figure 8.3.: Normalized introduced curvatures with respect to the thickness ratio T for the Euler Bernoulli model without (w/o) bonding layer and with (w) bonding layer and the finite element model with bonding layer.

It can be seen that in general the introduced curvature is much less than for conventional stiffness ratios. This can be explained with the very low stiffness of the actuator material (compare with Figure 3.14). The analytical model with the shear lag term shows expected lower efficiency than the model w/o bonding layer. However, the finite element model shows surprisingly higher curvature introductions, and high differences compared to the analytical model of up to 60%, which shows the necessity of the finte element modeling.

To investigate the thickness of the bonding layer, the reference configuration (tabel 8.1) is used and only the adhesive layer thickness is changed. The simulation results for the reference configuration are indicated by asterisks in Figure 8.4. The introduced curvatures normalized by the introduced curvature of a perfect bonded actuator are shown.

It can be seen that an optimum of a bonding layer thickness of 0.6 mm exists, where an improvement of about 18% is achieved compared with an infinite bonding stiffness. This behavior can be explained with an increase of the lever arm for the actuator patch regarding the neutral axis of the beam. However, this behavior only applies for very high stiffness ratios Ψ (Equation 3.18). If the stiffness ratio is reduced, the shear lag effect dominates and the positive influence of the additional lever arm diminishes. The squares in Figure 8.4 indicate this behavior.
In practice the optimum of 0.6 mm of bonding layer thickness is not used since the adhesion strength has its optimum between 0.05 mm and 0.2 mm (compare Section 8.2). Hence in the following a bonding layer thickness of 0.2 mm is considered, which leads to a theoretical

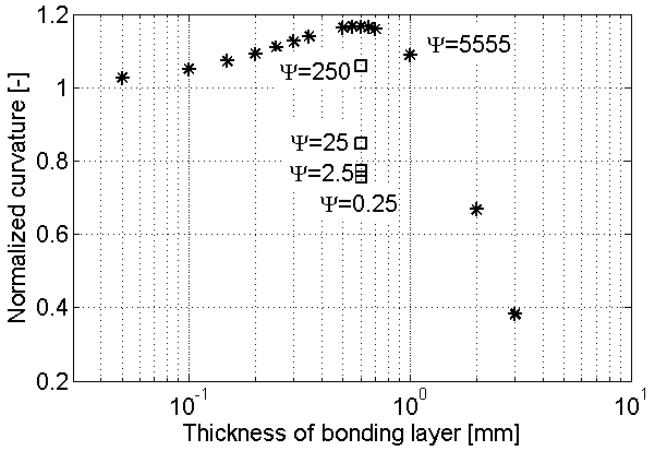

Figure 8.4.: Introduced curvature normalized by the curvature of a perfect bonded actuator with respect to the bonding layer thickness.

load introduction improvement of 9%.
Another investigated parameter is the Young's modulus of the bonding layer. For stiff actuator materials, such as SMAs or piezoceramics, the structure and the actuator have Young's moduli in the range of, or larger than the adhesive. In this case it is assumed that with increasing bonding layer stiffness, the introduced forces will increase also. However, for weak materials such as SMPs, an optimum exists at the actuator stiffness (here 4.5 MPa)(Figure 8.5).

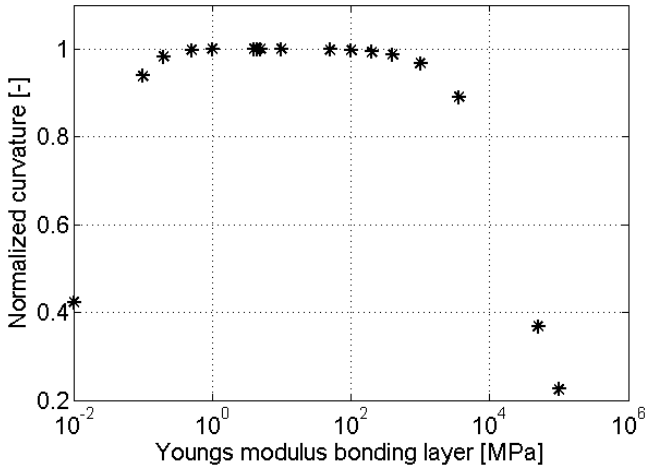

Figure 8.5.: Normalized load introduction with respect to the Young's modulus of the adhesive.

It can be seen that the optimum with respect to the stiffness of the adhesive layer is quite flat. However, for very high or very low stiffnesses the efficiency of the load introduction

drops down significantly. Thus adhesives with low Young's moduli between 0.1 MPa and 1000 MPa should be chosen for proper load introduction of SMP actuators.
Another approach to explain this extraordinary behavior is the characteristic of the shear factor Γ. For conventional material properties the shear factor increases with decreasing thickness ratios T and Young's modulus ratios E_s/E_a (Figure 3.18 and 8.6 (left)). However, for large stiffness ratios Ψ a minimum can be found for certain thickness ratios T (Figure 8.6 (left)).

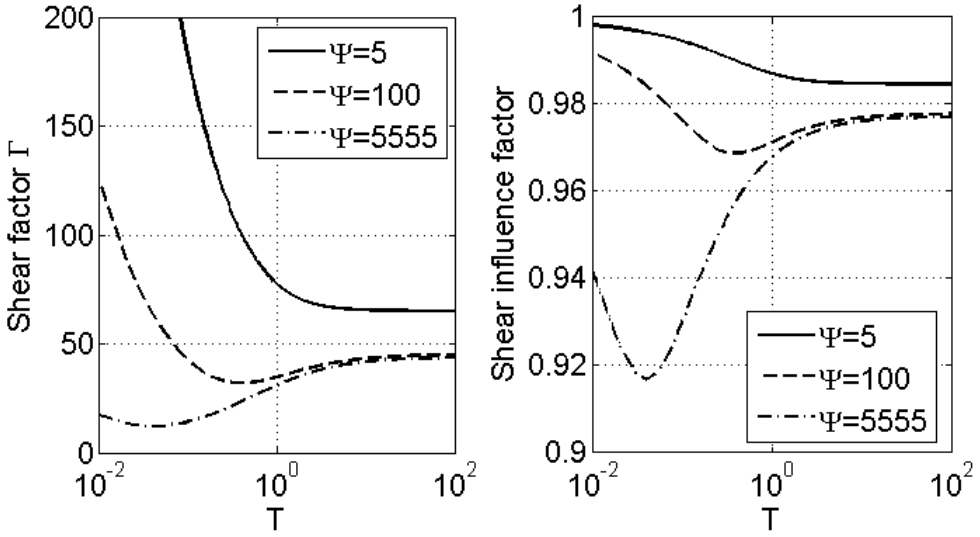

Figure 8.6.: Shear factor (left) and normalized curvature (right) with respect to the thickness ratio T for different stiffness ratios Ψ.

The bump for high stiffness ratios in the shear factor characteristic leads to an unconventional influence of the thickness ratio T on the curvature introdcution. This behavior is illustrated in Figure 8.6 (right). For low stiffness ratios the influence increases with increasing thickness ratios and the load introduction becomes worse. For high stiffness ratios the efficiency of the load introduction does not decrease monotonically, but has a distinct bump. Because of this behavior an additional loss of efficiency has to be taken into account, which is 4% for the SMP-CFRP combination on hand.

In summary: the existing analytical models shouldn't be used for soft actuator materials. A similar behavior can be expected for soft structures. Remarkable results are optima for the adhesive layer thickness and modulus.

8.2. Peel and Shear Stresses in the Actuator-Structure Interface

The adhesion of the actuator patch on the composite structure is an important part in the shape adjustment process chain. Although adhesive layers have been discussed regarding the posssible load introduction, their adhesion properties have not been addressed yet. Only if a proper adhesion is achieved, the load can be transferred reliably to the structure. Adhesion and adhesive technology is a very wide field, where still a lot of research is done. However, conventional models and theories cannot, or only with limitations, be applied to the application on hand. The inherent force generation by the shape memory effect leads to a different stress distribution in the adhesive layer, compared to conventional adhesive bondings. Furthermore, the unconventional stiffness and thickness ratios lead to a different load distribution in the bonding joint. Hence, finite element simulations are performed to determine peel and shear stresses, which might lead to deponding. The simulations are supplemented by experiments. The presented results have been determined within a student project by Mrs. Eva Graf [163].

8.2.1. Finite Element Model

For the investigation of the bonding stresses a simply supported beam, equipped with an SMP actuator patch, is modeled. As mentioned, the effects in width direction of the actuator can be neglected, thus 2D plane stress elements of type plane183 are used for the parametric study. The model is built in a Cartesian x-y-coordinate system, where x is the actuator length direction and y is the actuator thickness direction (Figure 8.7).

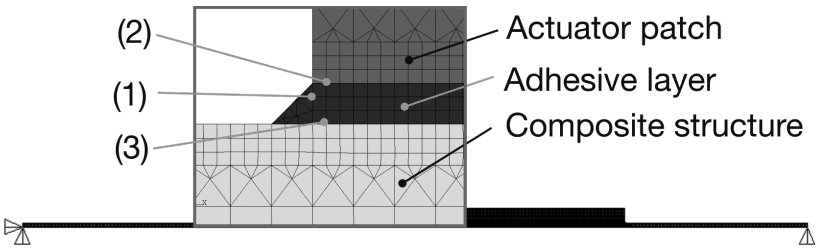

Figure 8.7.: 2D finite element model for the parametric study on peel and shear stresses.

Figure 8.7 shows the standard configuration, which is used for comparison of all parameter variations. The structure is modeled with a thickness of 0.5 mm and a Young's modulus of 70 GPa. The adhesive layer has a thickness of 0.2 mm and a Young's modulus of 3.5 MPa. A fillet is modeled at the actuator edges. The actuator patch is modeled with a thickness of 2mm and a Young's modulus of 3.2 MPa. The shape memory effect is considered by a adjusted *analogy of thermal expansion* (Chapter 6). The stimulus is applied by a negative thermal load on the actuator patch. For the evaluation three nodes are chosen in the adhesive

layer ((1)-(3) in Figure 8.7). At location (1) the normal stress in y-direction σ_y is evaluated while at location (2) and (3) the shear stress τ_{xy} is evaluated. The investigated parameters are the adhesive layer thickness, the adhesive Young's modulus, the actuator length and the mounting angle.

8.2.2. Thickness of the Adhesive Layer

Different adhesive layer thicknesses between 0.05 and 0.6 mm are simulated. All stress components show the same characteristic of a decreasing stress with increasing layer thickness. This can be explained by a larger volume in which stresses are degraded. The results are illustrated in Figure 8.8.

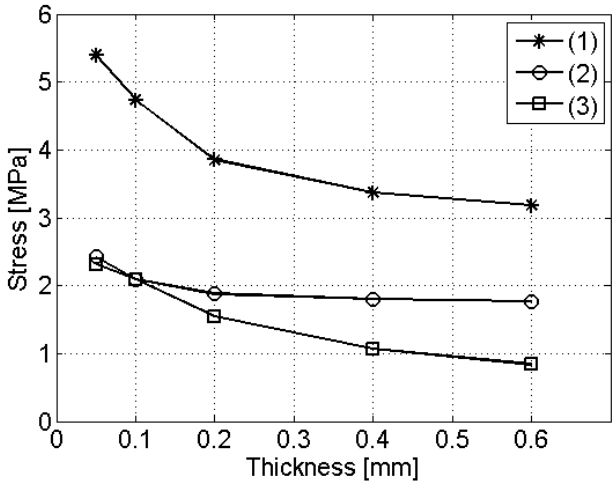

Figure 8.8.: Stresses in the adhesive layer with respect to the bonding layer thickness.

For the thickness increase of 0.55 mm a stress reduction of 28% is achieved for location (1). For the shear stresses in (2) and (3) the reduction is smaller. This behavior suggests a high bonding layer thickness, however, it is well known, that the bonding strength of adhesives is also a function of the bonding layer thickness (Figure 8.9).

It can be seen that there is an optimum of bonding strength regarding the bonding layer thickness, which is in the range of 0.05 mm to 0.2 mm. In the region below 0.05 mm the bonding strength decreases rapidly. This can be explained with touching substrate surfaces because of surface finish tips, which are locations of stress concentrations. Above 0.2 mm bonding layer thickness, the strength is decreasing slowly, which can be related to an increasing Poisson's ratio effect and increasing internal stress effects due to curing shrinkage. Because of this behavior a bonding layer thickness of 0.2 mm is chosen, which is still in a good strength range, limits the stresses and gives acceptable load introduction efficiency.

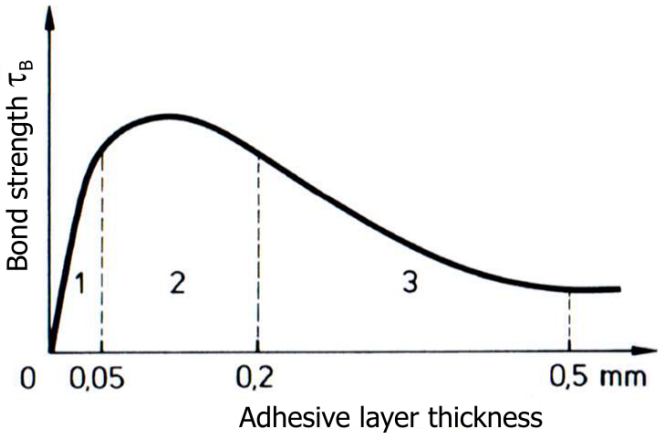

Figure 8.9.: Bonding strength with respect to bonding layer thickness [43].

8.2.3. Young's Modulus of the Adhesive Layer

It has been shown that the optimal load introduction is achieved with a Young's modulus of the adhesive, which is in the same range as the Young's modulus of the actuator. To investigate the resulting stress, the Young's modulus is varied in the range between 0.5 MPa to 10000 MPa, which is in the range of optimum load introduction. The simulation results are summarized in Figure 8.10.

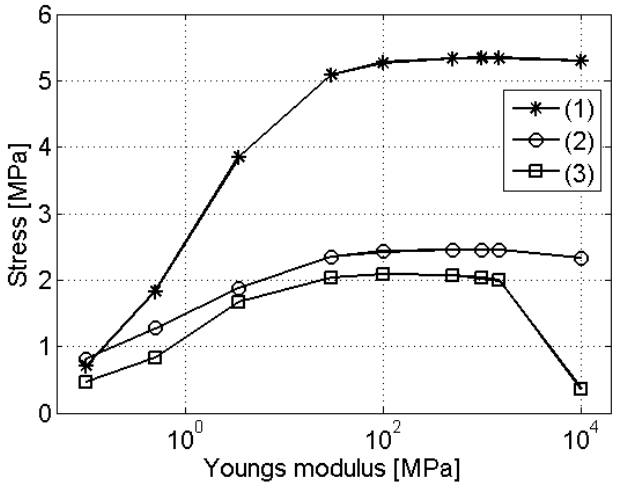

Figure 8.10.: Stresses with respect to the adhesive layer modulus.

It can be seen that the resulting peel stress (1) increases and reaches a saturation. While the shear stress between the actuator and the adhesive layer (2) almost stays constant for higher moduli of the bonding layer, the shear stress at location (3) drops down. This can be

explained with the stress degradation in the upper parts of the stiff bonding layer, thus no stress is transferred to the lower sections of the adhesive layer. For low moduli the stresses drop down, however, the load introduction efficieny drops down also. Commercially available adhesives are able to sustain the determined maximal load of 5.3 MPa.

8.2.4. Actuator Length

The actuator length seems to be an interesting parameter, since for conventional bonding joints especially the shear stress distribution along the bonding length varies a lot. For long bonding lengths, high stress peaks arise at the layer edges, which are reduced for shorter bonding lengths. For the example on hand, the stress in the bonding layer increases with increasing actuator length and reaches a saturation (Figure 8.11).

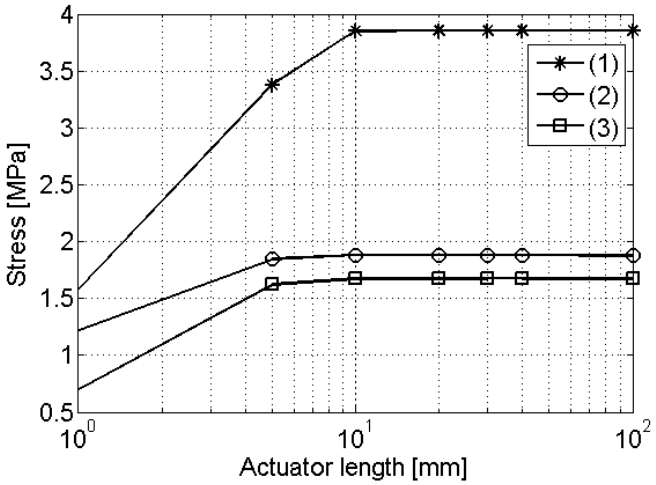

Figure 8.11.: Stresses with respect to the actuator length.

This behavior can be explained with increasing shear losses in the actuator for shorter actuators, thus actuators with low aspect ratios. However, it has to be taken into account that with increasing actuator length the introduced overall force increases, which is the major difference to conventional adhesive bondings. Therefore the evaluated stresses are related to the actuator volume of the standard configuration. The result is a decrease of the relative stress with increasing actuator length (Figure 8.12).

In conclusion: A large actuator length is desired to decrease the relative stress and increase the load introduction efficiency, since a saturation stress of 4 MPa can be sustained by conventional adhesives.

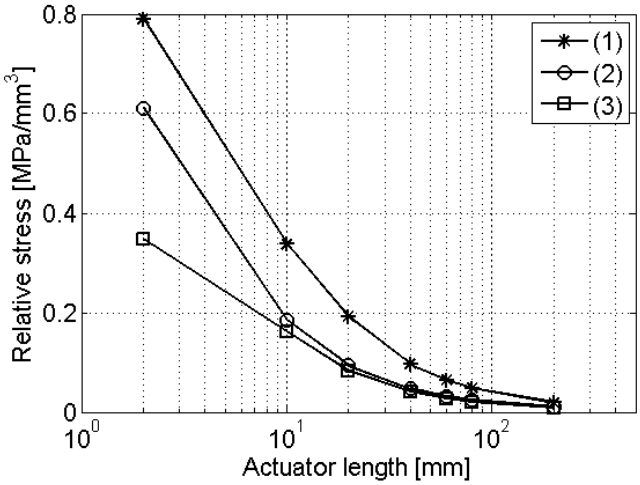

Figure 8.12.: Relative stresses with respect to the actuator length.

8.2.5. Actuator Mounting

An established method to improve the load path in bonding joints is the use of mountings. Mountings reduce the change in stiffness at the bonding edge. To investigate this behavior, mountings between $\alpha = 0^o$ and $\alpha = 80^o$ are modeled for the actuator edges (Figure 8.13).

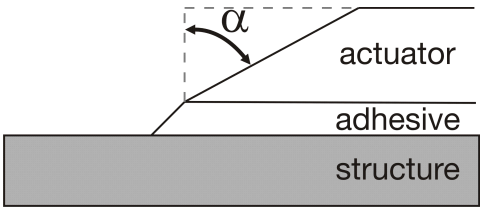

Figure 8.13.: Definition of mounting angle.

The resulting peel and shear stresses at locations (1) to (3) are illustrated in Figure 8.14.

It can be seen that the stresses decrease continuously with increasing mounting angle. For the shear stress at location (2) a small increase can be seen first. This might be explained with locking effects due to element warping. Especially the peel stresses can be reduced a lot (94%). The small reduction of actuator volume is neglected in this case.

8.2.6. Combined Adhesive Bonding

A more sophisticated technique to reduce stress peaks at the bonding layer edges is the combination of different adhesives. Weaker adhesives at the bonding edges reduce the stress peaks and transfer the load further into the middle of the bonding. Figure 8.15 shows a

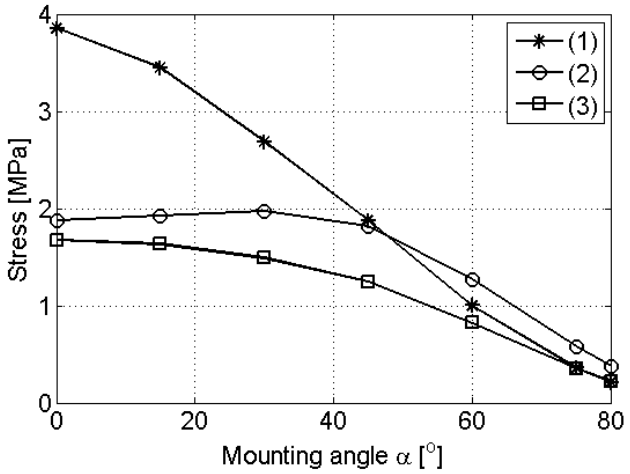

Figure 8.14.: Stresses in the bonding layer with respect to the mounting angle α.

sketch of this behavior (a) and a result of a finite element simulation for the current case (b).

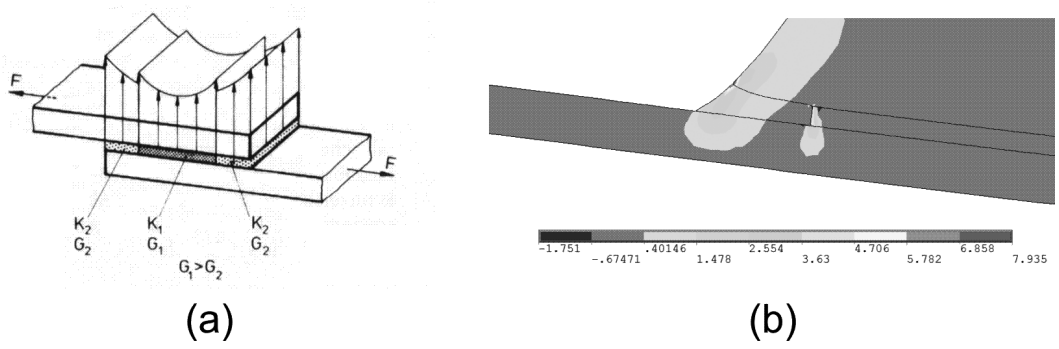

Figure 8.15.: (a) Sketch of the stress peak distribution [43]; (b) Contour plot of the peel stresses σ_y

The contour plot (b) shows the peel stress distribution σ_y. It can be seen that a second stress peak arises at the boundary between the two adhesives. This second stress peak reduces the peak at the outer side of the bonding.

From this simulation results supplementing experiments are derived.

8.3. Experimental Investigation of the Actuator Patch Adhesion

In an experimental investigation of the adhesion of SMP actuator patches on CFRP surfaces the mentioned parameters, adhesive Young's modulus, and mounting are investigated. Other process parameters such as the surface pre-treatment, the process temperature, and the temperature gradient, which couldn't be simulated, are investigated too. All parameter variations and samples can be found in Appendix A.5. To evaluate the adhesion, programmed actuator patches are applied to CFRP plate surfaces. After the curing time of 48 hours the samples are placed in a thermal chamber. During the recovery process the patches are visually monitored and the time of debonding is recorded.

The manufacturing process for the samples is illustrated in Figure 8.16.

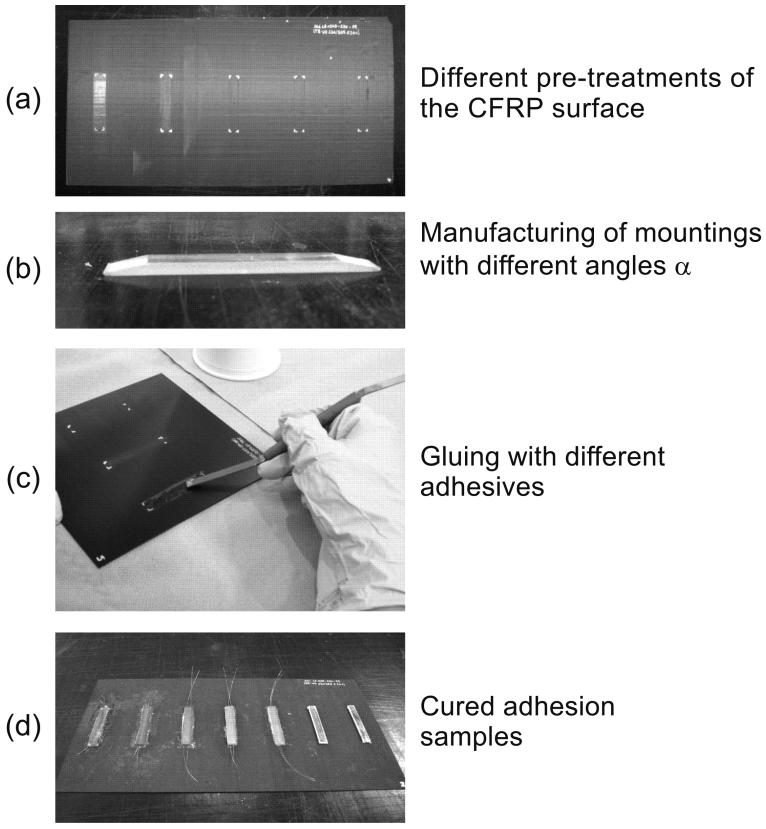

Figure 8.16.: Manufacturing process for adhesion samples: (a) Surface treatment; (b) Patch mounting; (c) Gluing process; (d) Cured samples.

(a) The surfaces of the CFRP samples are pre-treated with different procedures including mechanical treatment, sand blasting and ball blasting. The SMP patches are pre-treated by mechanical treatment and sand blasting. (b) The actuator patches are equipped with a mounting with different angels. (c) An adhesion process is applied. (d) The samples are

cured under a pressure of about 0.02 MPa for 48 hours at room temperature (RT $\approx 21^oC$). The recovery, thus the adhesion test is performed in a thermal chamber at 80^oC. The samples are programmed with a high programming strain of 175% to provoke debonding. The samples stay 4 minutes in the thermal chamber, or until they show debonding effects. The experimental results are evaluated by the time upon debonding is observed. They are structured regarding the varied parameter.

8.3.1. Adhesive

Different adhesives with different Young's moduli are used to investigate their adhesion strength and Young's modui influences. The test results also include the different adhesion strengths, however, some effects can clearly be related to the stiffness influence. The used adhesives, their Young's moduli, the debonding times and the fracture mechanisms are summarized in Table 8.2.

Table 8.2.: Adhesives and their adhesion properties.

Adhesive	Young's modulus [MPa]	Debonding time [s]	Fracture mechanism
PATEX Montageklebstoff	3.5	120	mixed debonding
DELO-DUOPOX AD895	2400	330	debonding between CFRP and adhesive
DELO-DUOPOX AD895	2400	220	debonding between patch and adhesive
Araldite AV 138	4700	140	debonding between CFRP and adhesive
Araldite AV 138	4700	160	debonding between CFRP and adhesive
CM (*TML*)	-	110	debonding between CFRP and adhesive
CM (*TML*)	-	420	debonding between CFRP and adhesive

The different adhesives show a wide range of performance and fracture mechanisms. The *PATEX Montageklebstoff*, which is the standard adhesive because of several advantages such as load introduction and processability, shows debonding already after 120 seconds. The *DELO-DUPOPOX AD895* shows a much better performance with up to 330 seconds. The *Araldite AV 138* shows debonding after 140 to 160 seconds. Here clearly the brittle behavior of the adhesive can be seen (Figure 8.17(a)). The *CM* adhesive, which is used for application of strain gages shows very different performances between 110 seconds and 420 seconds. Figure 8.17 (b) shows the sample after 420 seconds. The much better peformance

compared to the *Araldite AV 138* sample can be seen. The variety between the samples can be explained with the very narrow adhesive gap. Because this adhesive has a very low viscocity, the distance wires are not used and only a thin film is applied on the parts. This implies a high sensitivity regarding the bonding process.

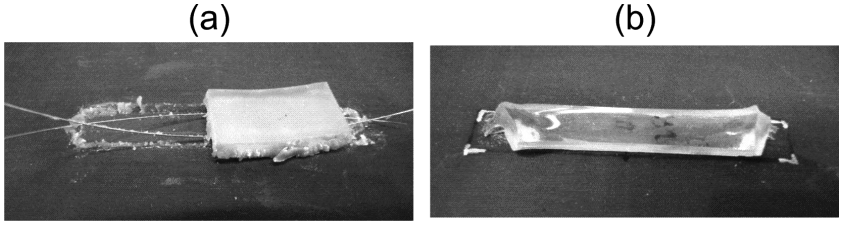

Figure 8.17.: Debonding effects: (a) Brittle debonding of Araldite AV138 (160 sec.); (b) Good performing CN strain gage adhesive (420 sec.)

8.3.2. Recovery Temperature

A process parameter, which cannot be simulated if the analogy of thermal expansion is used, is the real recovery temperature T_r. However, this process parameter has a large influence on the adjustment process performance. On the one hand all material properties change if the temperature is increased. On the other side the shape memory effect is affected. Only in the range of, or above, the transition temperture T_{Trans} the effect arises. To determine the effect of different recovery temperatures, standard samples are heated up to temperatures between 50^oC and 90^oC. The resulting debonding times and mechanisms are summarized in Table 8.3.

Table 8.3.: Adhesives and their adhesion properties.

Temperature $[^oC]$	Debonding time [s]	Fracture mechanism
50	-	no debonding
60	-	no debonding
70	300	debonding between patch and adhesive
80	165	debonding between patch and adhesive
90	90	debonding between patch and adhesive

The corresponding samples after debonding can be seen in Figure 8.18

For temperatures below T_{Trans} no debonding can be observerd. For 70^oC, which is slightly above the transition temperature first debonding can be observed after 300 seconds. The higher temperature samples show debonding already after 165 seconds and 90 seconds respectively. In Figure 5.15 it can be seen that the recovery temperature has negligible influence on the recovery energy, as long as it is above the transition temperature. Only the recovery

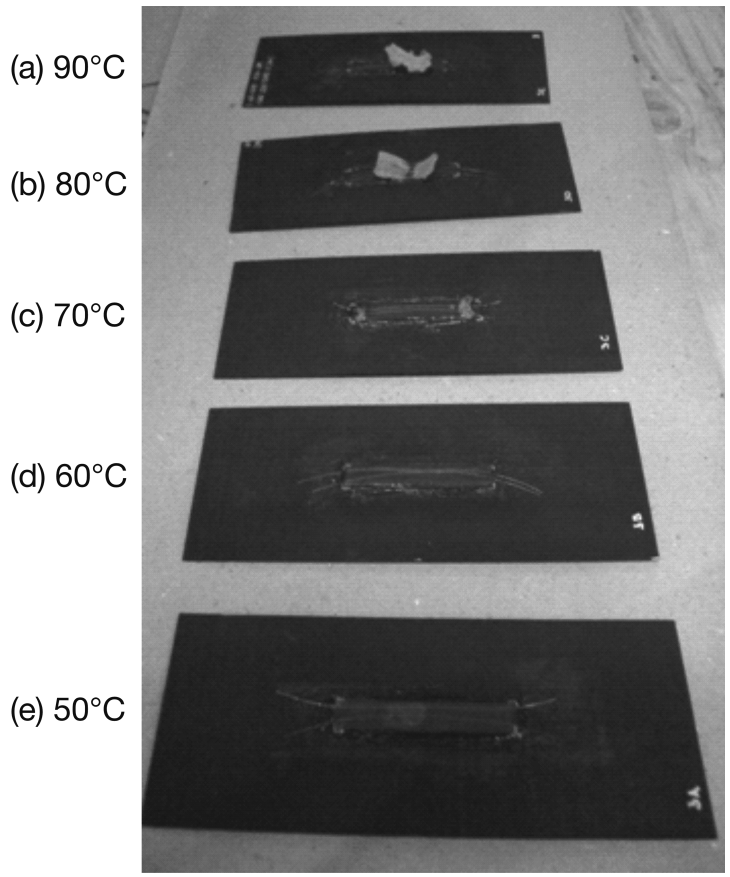

Figure 8.18.: Debonding for different recovery temperatures.

rate $\dot{\varepsilon}_r$ is reduced by reducing the recovery temperature. Therefore a recovery temperature of approximately T_{Trans} is recommended to avoid debonding effects.

8.3.3. Surface Treatment

The surface treatment of the CFRP plates shows only negligible effects. However, the sand blasting of the SMP patch improves the adhesion and changes the fracture mechansims. While the untreated samples debond between the SMP patch and the adhesive after 120 seconds, the roughened actuator only debonds after 180 seconds. The roughened and sand blasted sample shows debonding between the CFRP and the adhesive after 240 seconds.

8.3.4. Actuator Mounting

The results of the mounted actuators are unexpected. With increasing mounting angle the debonding times reduce. This might be explained with the missing pressure at the mounted edges during the curing. Because of the triangular geometry and the distributed pressure

by a wooden plate from the top, no pressure is applied at the patch ends for the mounted samples.

8.3.5. Conclusion

The avoidance of the debonding effects of shape memory actuator patches on CFRP surfaces could not be fully accomplished within this work. More research has to be conducted to improve adhesion. Adequate adhesive-actuator-structure combinations have to be found or other surface treatments such as plasma treatment might be applied. Furthermore, with proper recovery temperatures debonding can be reduced.

9. Shape Error Minimization of Distorted Parts

It is an established approach to optimize actuator or sensor locations for best optimal shape observability and control. In Chapter 4 an optimization of sensor locations has been introduced for shape reconstruction. Here the focus is on the controllability, or more precisely the shape adjustment.
For this purpose it is searched for an actuator configuration, which leads to a minimal structural shape error besides a minimal total mass for actuation.

9.1. The Discrete Actuator Approach - Linear Programming

The approach for dynamic or static shape control found mostly in the literature is a full occupancy or an equal distribution of actuator patches across the structure [3, 19, 24, 27, 49, 106]. For this approach the optimization variables are the stimulation parameters, for example the electric field for piezo-ceramic actuators. This leads to a linear programming since only the applied actuation forces change and the stiffness of the sytstem remains constant. The linear programming is a simple approach leading to a very efficient computation and short optimization times. Figure 9.1 shows a represtenative example of such an actuator configuration.

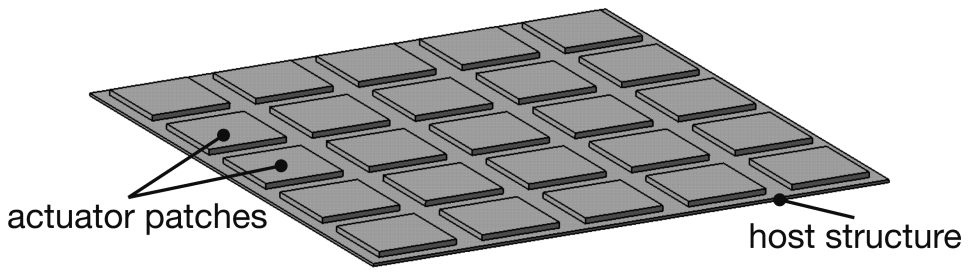

Figure 9.1.: 3D CAD model of a plate integrated with 25 actuator patches.

Due to the small computational effort even very fine patch discretizations can be used. However, the actuation orientation cannot be changed due to the fixed actuator configuration.

This approach is also immune to unknown and changing global distortions, how they occur for example due to thermal loads, since the total structure is covered by actuators and several distortions can be balanced. Additionally energy [106] and stress [19] constraints were integrated in the optimization, however, mass constraints cannot be considered since the actuator configuration is not a design variable. This is disadvantageous for the post manufacturing shape adjustment on hand since the deformation is known and the actuator configuration can be optimized regarding this special deformation and minimal actuation mass. However, the insight for the necessary actuator configuration is difficult and generally cannot be determined from the examination of the distorted shape. Furthermore, the shape memory effect is a quasi discrete process, thus discrete optimization variables are necessary for every patch. The shape distortions furthermore might be local and irregular effects which can hardly be compensated by equally oriented actuator patches. Figure 9.2 shows an representative example of a possible actuator configuration for a post manufacturing shape adjustment application.

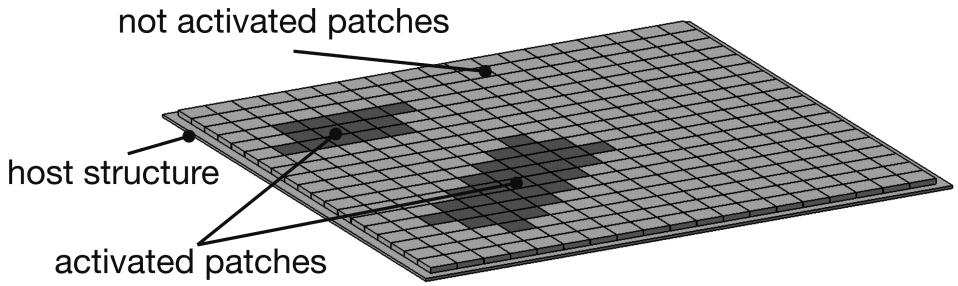

Figure 9.2.: 3D CAD model of a composite plate integrated with 324 actuator patches.

The shown example is comparable with the example shown in Figure 9.3. This exemplary configuration requires 324 discrete variables and 324 additional continuous variables for the actuation orientation. Additional manufacturing constraints are required. Because of these limitations of the linear programming and the equally distributed actuators and the difficult insight for the necessary actuator configuration, another approach is followed. The actuator geometries, locations and orientations are chosen as optimization variables. This leads to smaller numbers of design variables, however, a necessary update of the stiffness matrix in every optimization iteration.

9.2. The Actuator Placement Approach

The alternative to the introduced discrete distribution of actuators, is the continuous placement optimization of actuator patches. The advantages are a possible integration of mass constraints and a reduction of the optimization variables. These optimization variables are summarized in the vector $\vec{x}$. For the shape optimization on hand these parameters consist of geometric parameters and the stimulation parameter ΔS. For the optimization 2 dimensional

feasible regions are considered. For the most general case the design variable vector can be written as:

$$\vec{x}^T = \{x_1, y_1, \alpha_1, l_1, b_1, \Delta S_1, ..., x_N, y_N, \alpha_N, l_N, b_N, \Delta S_N\}^T \tag{9.1}$$

where x and y are the x- and y-coordinates of the actuator center of gravity, α is the rotational angle about the z-axis, l and b are the length and width of the actuator patch, ΔS is the stimulation value and N is the number of actuators. This approach leads to a number of variables of $n = 6 \cdot N$. Figure 9.3 illustrates the optimization variables.

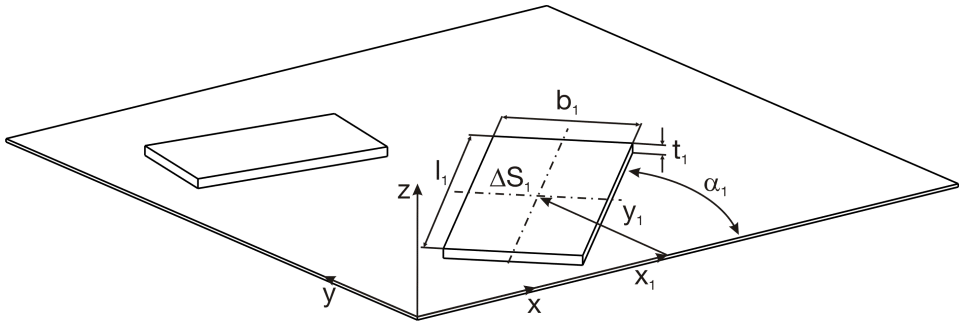

Figure 9.3.: Definition of optimization variables.

9.3. Formulation and Implementation of the Optimization Problem

The goal of the applied optimization algorithm is the minimization of shape errors and total mass for actuating. Thus from a general point of view a multiobjective function is present. However, the problem can also be stated as a single objective optimization with an additional restriction. Either the shape error is minimized with a mass restriction or the mass is minimized with a shape error restriction. For the introduction of the developed optimization algorithm the optimization of the shape error under a mass constraint is considered. Further constraints, considering geometric limitations such as the forbidden intersection of actuators, are included. Side constraints regarding the minium and maximum allowable actuator lengths and widths as well as x- and y-coordinates are included.

The problem can be formulated as:

$$\text{minimize} \quad z = f(\vec{x}) = \sqrt{\frac{\sum_{i=1}^{n} (\overline{w}_i - \hat{w}_i)^2}{n}} \tag{9.2}$$

$$\text{so that} \quad m = f(\vec{x}) < m_{max} \tag{9.3}$$

$$\text{and} \quad A_k \subseteq A_0 \quad , k = l...N \tag{9.4}$$

$$\text{and} \quad A_k \cap A_l = \emptyset \quad , k \neq l, \quad k, l = 1...N \tag{9.5}$$

$$\text{and} \quad \vec{x}_{lb} \leq \vec{x} \leq \vec{x}_{ub} \tag{9.6}$$

where z is the objective function dependent on the design variable vector $\vec{x}$. The objective is the RMS shape error, calculated by the differences of the actual displacements after adjustment $\hat{w}_i$, and the desired displacements $\overline{w}_i$, at every location i for n evaluation points. The mass m shall be smaller than a maximum mass m_{max}. All actuator areas A_k shall be a subset of the feasible region A_0. No actuator area A_k shall intersect another A_l. The design variables $\vec{x}$ shall not fall below the lower bound $\vec{x}_{lb}$ and not exceed the upper bond $\vec{x}_{ub}$. The design variable vector $\vec{x}$ includes geometric parameters and the stimulation parameter ΔS (Section 9.2). This optimization problem is implemented using the simulation software *MATLAB* and the finite element software *ANSYS*. Figure 9.4 shows a flowchart of the optimization process.

The simulation software *MATLAB* provides the environment for the numerical optimization. Within this environment the finite element software *ANSYS* is integrated for the determination of the system equations. The used integrated optimization environment was developed by Mr. Erich Wehrle at the Institute of Lightweight Structures. Displacements w_i, resulting from the patch actuation, are calculated using the finite element model. Since the small curing distortions have a negligible effect on the structural stiffness, an ideal shape of the structure is modeled. Thus superpositioning the calculated displacements from the finite element simulation with the measured shape, the resulting shape can be calculated in *MATLAB*. This resulting shape is evaluated by comparing it with the desired shape and calculating the RMS shape error. Additionally the mass is calculated in *MATLAB* using the design variable vector. After checking the convergence and the feasibility, the optimization loop either is stopped and the results are discussed or the design variable vector is changed by the optimization algorithm. Here a special feature is implemented in the optimization loop. To avoid element warpage errors in *ANSYS* and thus an interrupt of the optimization loop a geometry check is performed before the ANSYS call. The following properties are checked.

- All actuators k must lay completely inside the feasible region A_0: $A_k \subseteq A_o$
- No actuator shall intersect another actuator: $A_k \cap A_l = 0$

In the following the different elements of the optimization process will be discussed in more detail.

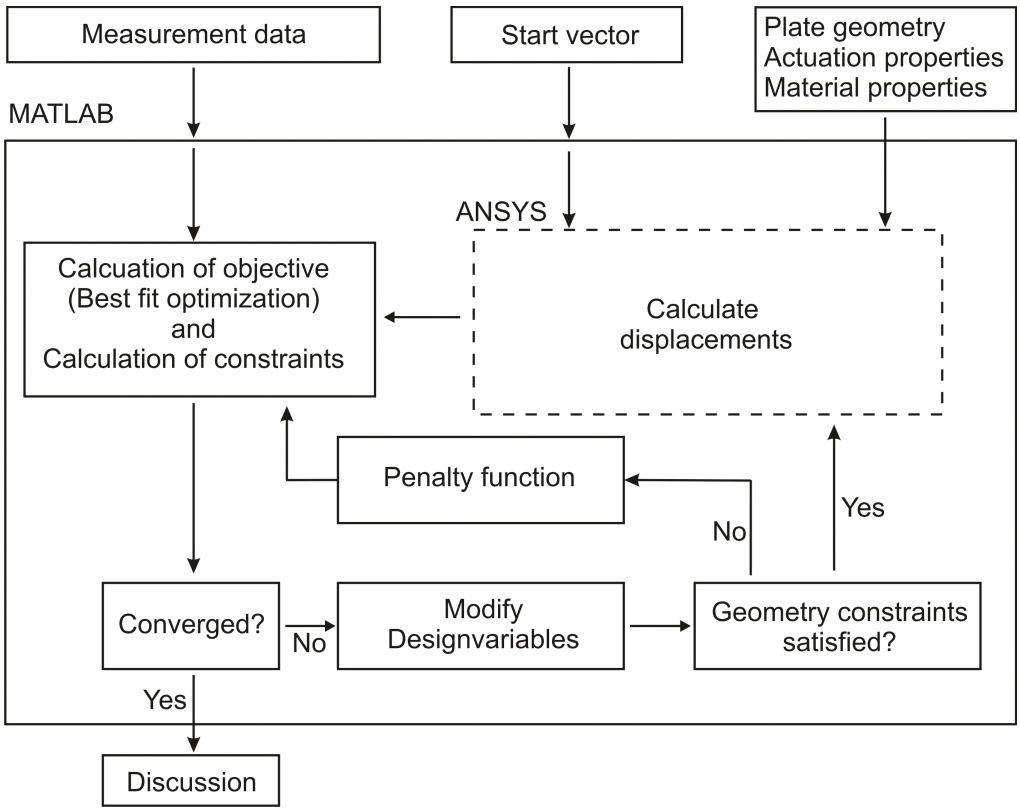

Figure 9.4.: Flowchart of the optimization process.

9.4. The Finite Element Model

The finite element modeling is performed regarding the description in Chapter 6. The composite structure is modeled with ideal geometry using layered shell elements. The shape memory polymer patches are modeled using volumetric brick elements and the material parameters determined with the process introduced in Chapter 6. For the optimization, however, the adhesive layer is neglected to save computational time. The resulting underestimation of the load introduction of about 9% (see Chapter 8) is neglected. Figure 9.5 shows a finite element model used for the optimization.

9.5. Objective Function

The objective function of the optimization is a best fit root mean square (RMS) shape error (Equation 4.1). The inputs for the calculation are the current state of deformation due to warpage, given as a vector of out-of-plane deformations $\vec{\tilde{w}}$, the deformation field calculated by the finite element simulation $\vec{w}$, and the desired deformation field $\vec{\overline{w}}$. Superpositioning the

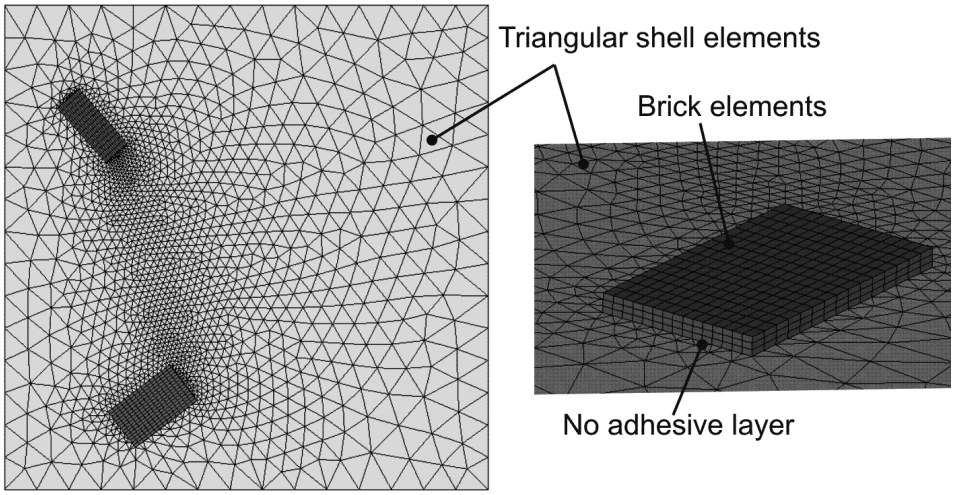

Figure 9.5.: Finite element model for the optimization process, neglecting the adhesive layer.

calculated deformation field with the actual field the actual deformation field after adjustment is calculated to:

$$\vec{\hat{w}} = \vec{\tilde{w}} + \vec{w} \tag{9.7}$$

Depending on the chosen boundary conditions in the finite element simulation, different rigid body motions occur. However, for the shape adjustment only the elastic deformations are relevant. Hence, a best fit optimization of the deformation field $\vec{\tilde{w}}$ with respect to the desired deformation field $\vec{\overline{w}}$ is performed. In our case the desired shape is a planar plane, why it is possible to use one of the planes of the Cartesian coordinate sytem as the reference plane. Here the z-x plane is used as the reference plane. The optimization is performed in a two step process. First the deformation field $\vec{\hat{w}}$ is translated into the coordinate origin, before the minimum RMS error regarding the z-x-plane is determined by optimizing the rotational angles about the x- and z-axis, α_{opt} and β_{opt}. As a third optimization variable the translation in y-direction y_{opt} is necessary. The process is illustrated in Figure 9.6.

The resulting objective function of the best fit optimization is a rotational and translational matrix $F = f(\alpha_{opt}, \beta_{opt}, y_{opt})$.

$$F = \begin{bmatrix} 0 & 0 & 0 \\ cos(\alpha_{opt}) \cdot sin(\beta_{opt}) & cos(\alpha_{opt}) \cdot cos(\beta_{opt}) & -sin(\alpha_{opt}) \\ 0 & 0 & 0 \end{bmatrix} \cdot \begin{pmatrix} x - x_m \\ y - y_{opt} \\ z - z_m \end{pmatrix} \tag{9.8}$$

Only the second line shows entries, since only the out-of-plane coordinate y is considered for the error calculation. The translation to the origin is performed by the translation by x_m and z_m. The optimization is performed in *Matlab* using the *lsqnonlin* function of the optimization toolbox.

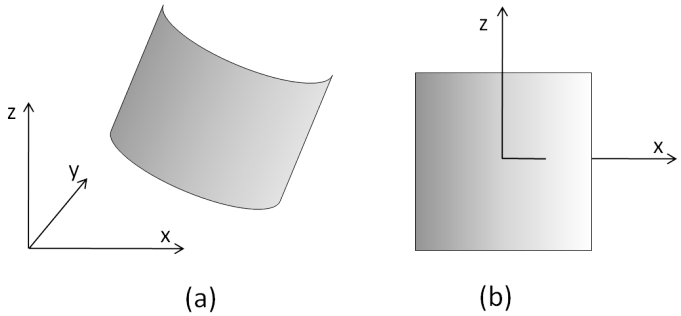

Figure 9.6.: Illustration of the best-fit RMS determination: (a) starting configuration; (b) translation to origin and optimal rotation and translation in y-direction.

9.6. Constraints

If not a multiobjective optimization is performed a mass constraint is used. Since the goal is the minimization of shape errors with a minimum weight increase, the mass m is limited to a certain limit m_{max}. The resulting constraint function is:

$$1 - \frac{m}{m_{max}} \geq 0 \tag{9.9}$$

The mass constraint function is implemented in the constraint functions of the optimization algorithms. As a measure for the mass the total surface area of the actuator is used, which is feasible for a constant thickness.

Besides the mass constraint, more complex geometric constraints have to be considered including the prohibition of intersecting actuators and the avoidance of infeasable actuator locations outside the structure. Figure 9.7 illustrates such an infeasible configuration.

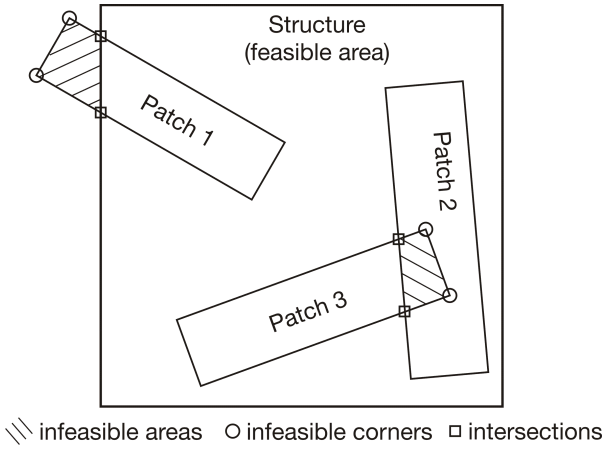

Figure 9.7.: Illustration of geometry constraints.

While patch actuator 1 violates the constraint of laying outside the feasible area, patches 2 and 3 intersect each other and build an overlapping area.
These constraints are implemented in a geometry checking function. The function has been developed within a student project at the Institute of Lightweight Structures (LLB) [168]. The function inputs are the design variables and its outputs are a feasibility flag (infeasible: 1; feasible: 0) and a penalty function f. The programm calculates overlapping areas between actuators or between the actuators and the outer, infeasable regions. The sum of the overlapping areas a_{ovlap} is added with a weighting factor γ to an offset C, which results in the penalty function f.

$$f = C + \gamma \cdot a_{ovlap} \tag{9.10}$$

Using this approach a weighting of the infeasibility is achieved and the gradient based optimization algorithm does not get stucked in an infeasible region with no gradient. In this case a gradient away from the overlapping geometry exists.

Calculation of overlapping areas of actuator and structure
The flowchart in Figure 9.8 illustrates the determination of the cumulated overlapping area of all actuators $i = 1...N$ with the outer boundary of the structure.

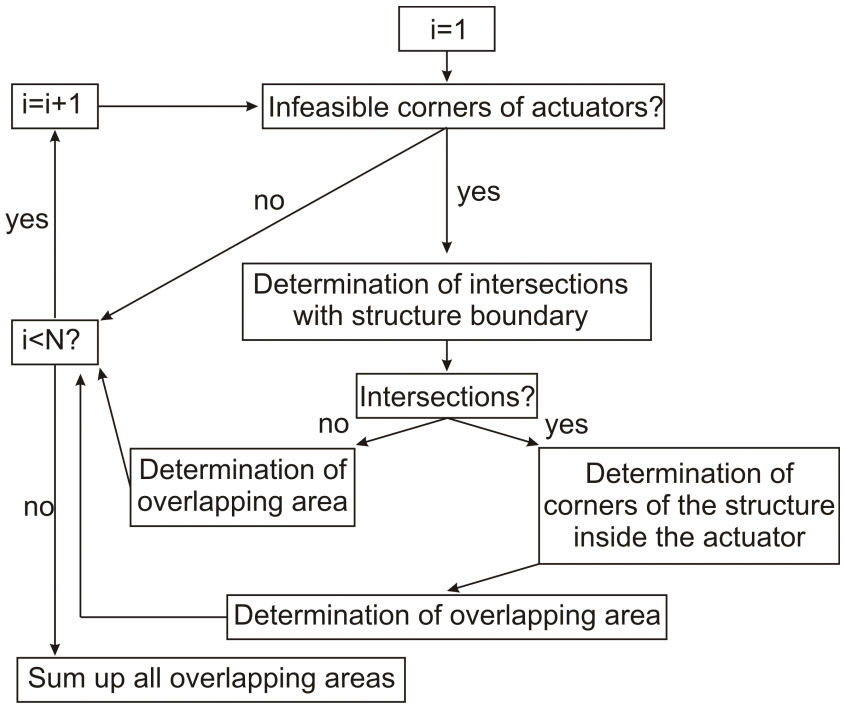

Figure 9.8.: Flowchart of the geometry feasibility evaluation function.

The first step is the checking, if actuator corners are outside the structural area. Is this not the case there is no infeasibility and the algorithm jumps to the next actuator. If there are corners of actuators outside the structures boundary, for each side of the rectangular actuator

a linear equation is determined, which is used to calculate the intersections with the plate boundary. If there are no intersections, the actuator is either fully capturing the structure or the acutator is laying completely outside the structure boundaries. In both cases the overlapping area can be calculated by vector opertations. After the calculation the algorithm jumps to the next actuator.
If there are intersections of the actuator edges with the structure boundary a inner loop calculates the overlapping areas. Within this calculation further possible corners of the structure inside the actuator have to be calculated. This is necessary to determine the number of corners of the overlapping area. Figure 9.9 illustrates an actuator overlapping with a second actuator with a tetragon and a pentagon. If the maximum number of actuators N is achieved all overlapping areas are summed up and saved as an output variable.

Calculation of overlapping areas of actuators with actuators
The basic principle for the determination of overlapping actuators is the same as for the overlapping of actuators with the structure. In this case one of the actuators is defined as the structure, thus the same algorithm can be used. However, a coordinate transformation has to be performed, such that the actuator denoted as the structure is parallel to the global Cartesian coordinate system (Figure 9.9).

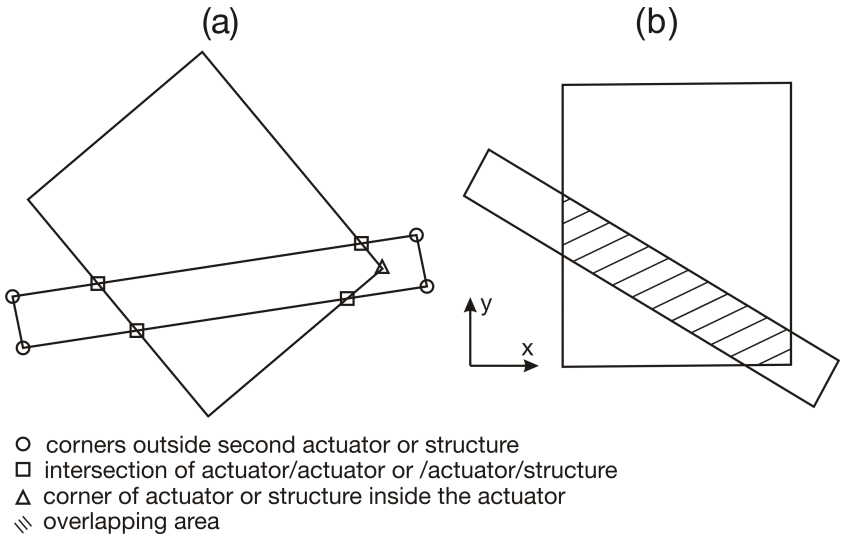

Figure 9.9.: Illustration of the determination of overlapping areas; (a) definition of different points; (b) rotated system.

The overlapping of different actuators has to be performed for all actuator pairs. The number of actuator pairs n is:

$$n = \frac{(N-1)N}{2} \tag{9.11}$$

Equation 9.11 describes a classical power sum. Including several special cases, for example multiple overlapping of more than two actuators, the overall overlapping sum is built for N

actuators. Using this overlapping area, the penalty function f (Equation 9.10) is calculated. For the performed optimization a offset penalty of $C = 1$ is chosen. Compared with desired objective function values of smaller than 0.1, this is a high value. The overlapping area is added with a weighting factor of $\gamma = 100$.

9.7. Algorithms

For the optimization itself three algorithms implemented in *MATLAB*, *fmincon*, *MatlabGA* and *GAmultiobj* are used.

9.7.1. Fmincon

Fmincon is a gradient based optimization algorithm for minimizing constrained functions. Using a given start design vector, the system equations are solved and the objective function and restrictions are calculated as well as the gradient regarding all design variables. With this approach the direction of steepest descent, the search direction $\vec{s}$, is found. The design variable vector is changed by a certain step size $\Delta\vec{x}$ in search direction and the system equations are evaluated again. This optimization cycle is repeated until the convergence criterion is fulfilled. These criterions are: a maximum change in the objective function value, the step length, or the contraint function values. The advantage of gradient based algorithms is the small number of necessary system evaluations and the high probability of finding at least a local optimum. The drawback is that the algorithm gets stucked in local optima. Therefore several starting vectors are necessary to get a high probability to find a global optimum.

9.7.2. MatlabGA

MatlabGA is a genetic algorithm based on genetic principles. Using an initial population of individual design variable vectors, a high number of system evaluations is performed. Evaluating the results leads to the survival of the best solution. These best design variable vectors are recombined by different principles and the system equations are evaluated again. The optimization cycle is repeated as long as the convergence criterion is not fulfilled. The advantage of this optimization strategy is the global view. Since a lot of individual solutions are generated, the probability of finding the global optimium is high. However, since the strategy is probabilistic, the exact optimum is hardly found. A further disadvantage is a very high necessary number of system evaluations.

9.7.3. Combined Strategy

For the optimization of the actuator configuration also a combination of the genetic algorithm and the gradient based algorithm is used. Using the genetic algorihm it is tried to find the global optimum. Using the determined optimal design variable vector as a start design for a subsequent gradient based optimization, may lead to a further improvement of the solution.

9.7.4. GAMultiObj

Besides the single objective optimization with constraints, a multiobjective optimization can be performed. In the case of shape optimization the two objectives might be the shape error and the actuator mass. Multiobjective optimizations can be performed either by a sum of weighted single objectives (Equation 9.12) or a multiobjective genetic algorithm.

$$\min \quad \gamma_1 \cdot f_1(\vec{x}) + \gamma_2 \cdot f_2(\vec{x}) \tag{9.12}$$

where $\gamma_{1,2}$ are weighting factors and $f_{1,2}$ are the objective functions. With a variation of the weighting factors the optimization leads to designs with smaller mass or with smaller shape error. A genetic multiobjective algorithm uses a population of individuals and evaluates all objectives. Individuals which do not have advantages in one objective compared to other individuals will not survive. The result of such an optimization is a *Pareto Front*. The Pareto front gives a good insight in the system behavior. Figure 9.10 illustrates the development of a Pareto front during a genetic multiobjective optimization.

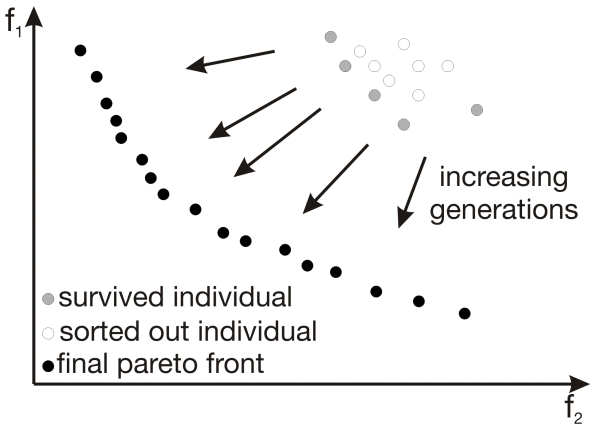

Figure 9.10.: Illustration of the development of a pareto front during a genetic multiobjective optimization.

More information about optimization algorithms can be found in [124].

9.8. Optimization Examples

To verify the developed optimization algorithm it is applied to a asymmetric distorted, quadratic fiber composite plate. The distorted shape, measured with dot-projection photogrammetry shows an RMS shape error (Equation 4.1) of 0.1263 mm. The results presented here are partly based on a student project, which has been conducted at the Institute of Lightweight Structures (LLB) [168]. Figure 9.11 shows the measured surface.

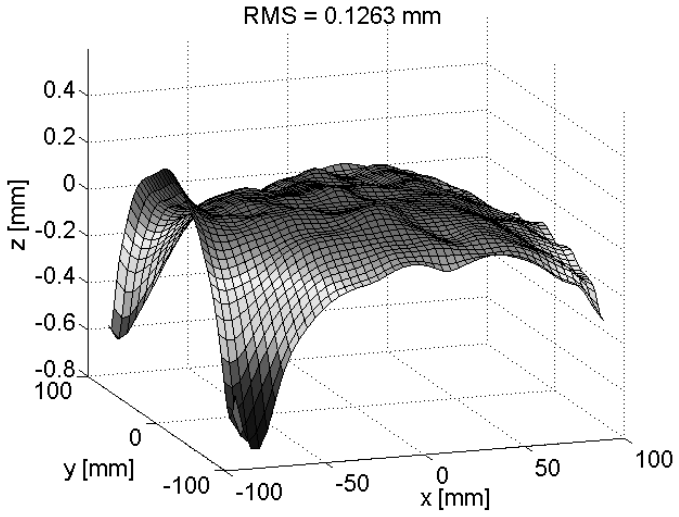

Figure 9.11.: Distorted shape of a CFRP plate; related shape error is RMS = 0.1263 mm. (Note scale of z-axis.)

The bumpy surface can be explained with the measurement accuracy of the dot projection photogrammetry of >0.03 mm (standard deviation of measured targets).
The plate is modeled with the dimensions of 184 mm × 184 mm × 1 mm, regarding the modeling introduced in Chapter 6.

Different optimization algorithms, constraints, design variable vectors, upper and lower bounds and optimization parameters are used to investigate the optimization loop itself. In the following one of these examples is described in detail, while for some others the results are presented only.
A genetic algorithm with a subsequent gradient based algorithm is applied to minimize the RMS shape error with a mass constraint and geometric constraints regarding Equation 9.2. A number of n=2209 points are used for the evaluation of the objective function. The mass is represented by an area, calculated from the design variables length and width. It is constrained to a maximum of $m_{max} = 1500\ mm^2$. A number of two actuators is chosen. The resulting design variable vector is defined as:

$$\vec{x}^T = \{x_1, y_1, \alpha_1, l_1, b_1, S_1, x_2, y_2, \alpha_2, l_2, b_2, S_2\}^T \tag{9.13}$$

The thickness of the actuators is t=2 mm. The design variables are normalized to ranges between -1 and $+1$. The lower and upper bounds are defined as:

$$\vec{x}_{lb}^T = \{-0.9, -0.9, 0.0, +0.05, +0.05, +0.0, -0.9, -0.9, 0.0, +0.05, +0.05, 0.0\}^T \quad (9.14)$$

$$\vec{x}_{ub}^T = \{+0.9, +0.9, +1.0, +0.4, +0.4, +1.0, +0.9, +0.9, +1.0, +0.4, +0.4, +1.0\}^T \quad (9.15)$$

With a population size of 20 individuals and after 7 generations a local minimum is found by the genetic optimization algorithm. The found RMS error is 0.0802 mm with a mass of 1231 (Figure 9.12 top, left). The resulting design variable vector is used as a start vector $\vec{x}_0$ for the subsequent gradient based optimization. After 38 iterations an optimal RMS shape error of 0.054 mm is found. Figure 9.12 shows the development of the designs.

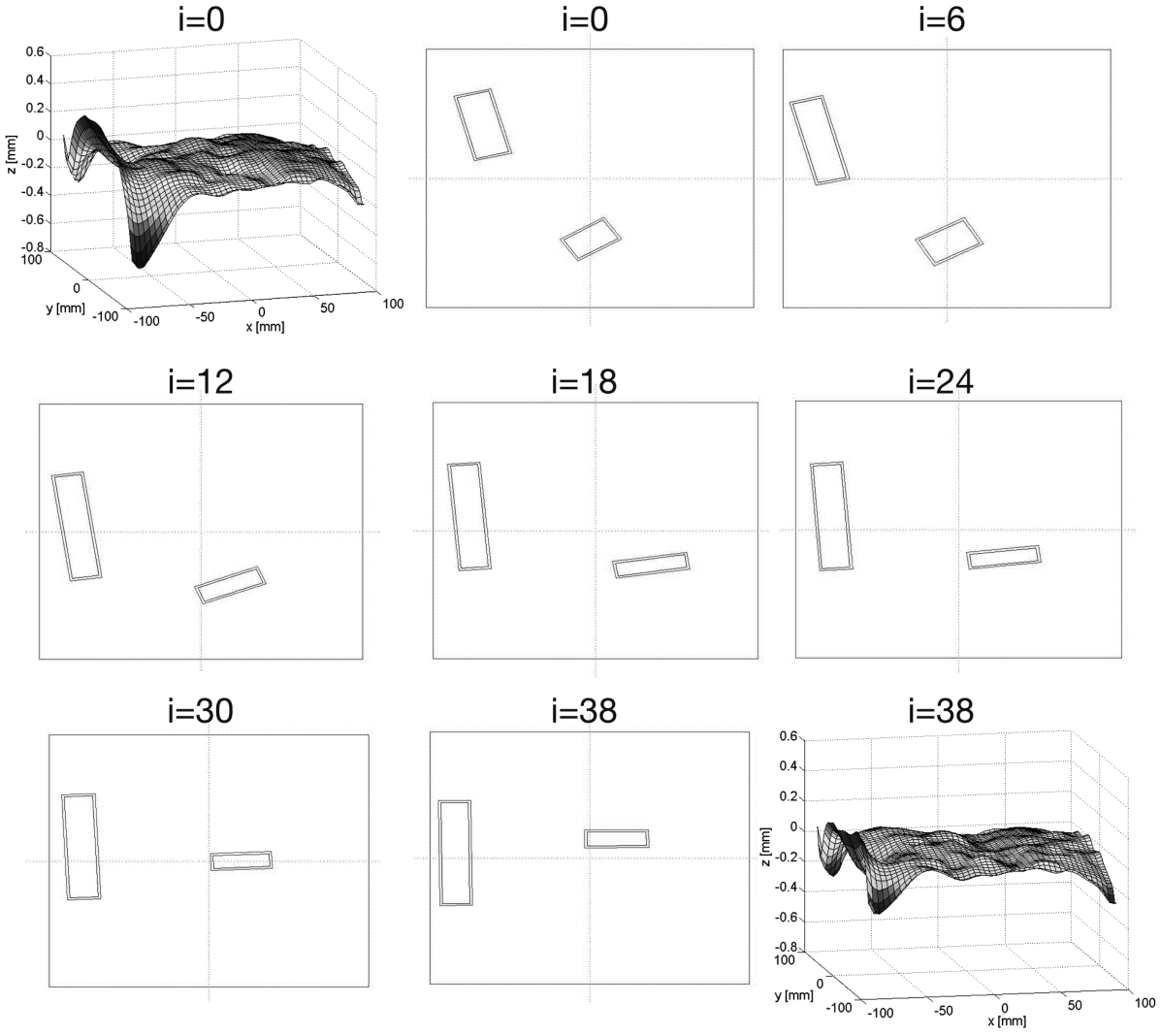

Figure 9.12.: Development of the actuator configurations during the gradient based design optimization; i denotes the iteration number.

On the top left corner the design (RMS = 0.0802 mm) after the GA optimization can be seen as well as the optimal design of actuator locations, orientations and dimensions (i=0). The different figures show the actuator configurations for the noted iteration numbers. On the bottom right corner the final shape of the optimized CFRP plate (RMS = 0.054 mm) can be seen. The corresponding design variable vector is

$$\vec{x}^T = \{0.17, 0.16, 0.004, 0.19, 0.05, 0.89, -0.84, 0.035, 0.50, 0.4, 0.086, 1.0\}^T \qquad (9.16)$$

The convergence criterion is a minimum change of the objective function lower than the tolerance and the total actuator mass is 1500 mm^2. The upper bounds $\vec{x}_{ub}(10)$ and $\vec{x}_{ub}(12)$ are active. This indicates that a longer actuator 2, which lays on the left side, could have improved the results. It is clear that the upper bound 12 is active, since only if the maximum possible energy output is recalled a minimum actuator mass is possible. Therefore it is more remarkable that upper bound 6 is not active. This is only possible because mass is not an objective but a constraint. This means that only 89% of the possible energy output of actuator 1 is used. Both actuators work in the tensile mode. In general it can be concluded that the optimization algorithm leads to plausible results and an improvement of the shape error of 57% is achieved. The complex geometry checking function is a stable and reliable tool to avoid actuator intersections. Using different upper and lower bounds and mass constraints as well as more actuators might lead to a further improvement.

The discrete variable, number of actuators N, is not included in the design variable vector, however, different numbers of actuators are investigated subsequently. In the following the final designs and resulting shapes are shown and interpreted. Figure 9.13 shows the final designs for the combined genetic and subsequent gradient based optimization for 3, 4 and 5 actuator patches and the resutling part shapes.

The corresponding shape errors are 0.055 mm, 0.058 mm and 0.073 mm. This shows that there is an optimal number of actuators. Due to the lower bound for the actuator lengths and widths actuators cannot diminish, which leads to an interference between the actuators. This is also indicated by the active lower bounds of lengths and widths for the actuators marked with $*$ and $**$. Furthermore, the resulting stimulation levels ΔS are near zero for these actuators. For the other actuators of the configurations with 3 and 4 actuators the upper bound for the stimulation level is active, which indicates a saturation of the energy output. The upper bound for one actuator is active only, in the configuration with 5 actuators. Thus in general this configuration is not using the optimal energy output.
To conclude the investigation of the number of actuators it can be mentioned that an increasing number of actuators does not improve necessarily the adjustment quality. Due to the continuous characteristic of this optimization algorithm the actuators cannot diminish and small actuators at the lower bound of their dimensions remain. Not to influence the shape adjustment, their stimulaton level ΔS becomes zero, which leads to a mass increase only and not to a shape error reduction. In the introduced example two actuators are sufficient and give the best result.

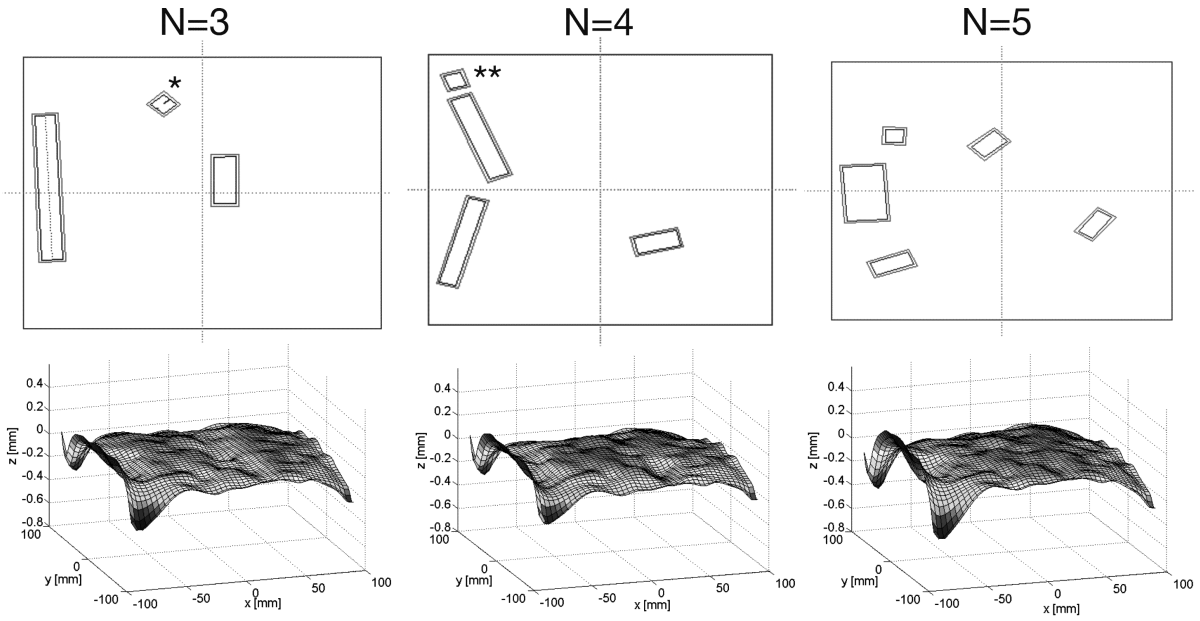

Figure 9.13.: Actuator configurations and resulting part shapes for N=3, 4 and 5 actuators.

The application of a multiobjective algorithm gives even more insight in the optimization problem. Using the *Matlab* multiobjective optimization algorithm *Multiobj* the RMS shape error and the mass are optimized. Using two actuators a pareto front is determined (Figure 9.14).

The figure shows a population of designs along a Pareto front. Some representative designs, thus actuator configurations, are shown as well as the corresponding shapes at the ends of the Pareto front.

The developed shape optimization method shows good optimization results. For the shown representative example, a shape improvement of 57% is achieved with the use of two actuators and a mass of $m = 1500\ mm^2$. It is shown that increasing actuator numbers do not necessarily lead to better shapes.
In Chapter 11.2 two further optimization examples are shown.

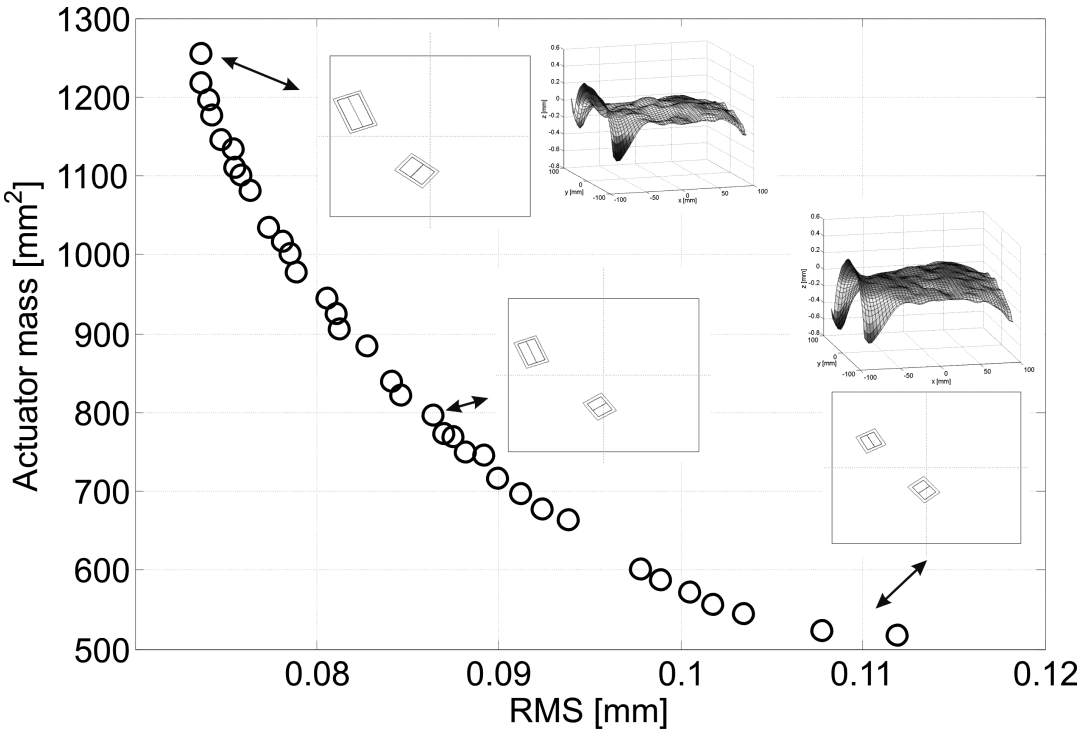

Figure 9.14.: Pareto front for the minimization of the RMS shape error and mass using 2 actuators.

10. Operational Considerations

In the operation phase of the adjusted composite parts, harsh environmental conditions, especially for space applications have to be sustained. Besides the vacuum condition, leading to the outgasing phenomenon of polymers, large temperature swings of for example $\pm 100^o C$, and the radiation hardness are considerable issues. For all applications, space or terrestrial, the constant static load in the actuator patches, resulting from the elastic deformation of the structure, leads to relaxation and creep effects in the actuator patch. A selection of these topics is presented here.

10.1. Relaxation and Creep

Because of the possible presence of viscoelasticity, yielding below the yield strength and at room temperature might occur in polymers. Therefore a temperature and time dependent Young's modulus, called creep modulus $E_c(t, T)$, has to be considered.
Two effects are distinguished within this behavior:

- Creep
- Relaxation

Creep
Creep is the increase of mechanical strain over time caused by a constant stress. This behavior occurs if polymers are exposed for a long time to a constant stress, and might even lead to breakage. The behavior is illustrated in Figure 10.1.

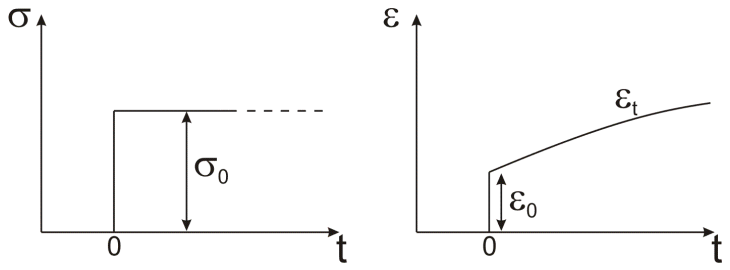

Figure 10.1.: Stress and strain characteristics for typical creep behavior of polymers.

Relaxation
Relaxation is the reduction of stress over time caused by a constant mechanical strain. Elastic

deformation is transformed by the slippage of molecule chains in plastic deformation. Figure 10.2 shows this behavior.

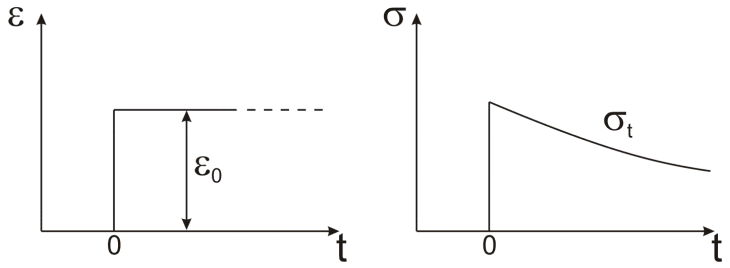

Figure 10.2.: Strain and stress characteristics of a typical relaxation behavior of polymers.

For creep and relaxation, yielding effects lead to irreversible plastic deformations. For the relaxation, high impellent forces lead to high stresses, which are decreasing with increasing strain. This leads to fast yielding at the beginning, which decreases over time. This can be expressed by a degressively decreasing relaxation modulus $E_r(t)$. For creep, however, the stress is constant and the strain increases degressively. However, since these differences are small, both effects can be treated similarly in a first order approximation.

The only standardized experimental procedure to determine creep properties is the creep rupture test, where the deformation for a constant load is recorded for a long time. Using such creep characteristics for different load levels, it is possible to determine isochrone stress-strain curves from which the creep modulus $E_c(t)$ can be extracted directly by:

$$E_c(t) = \frac{\sigma_0}{\varepsilon(t)} \tag{10.1}$$

For the polystyrene based SMP *Veriflex*, a creep rupture test is performed at three temperatures of -40^oC, 10^oC and ambient room temperature (uncontrolled, $\approx 21^oC$). The applied load is representative 1.5 MPa. The test results are shown in Figure 10.3.

The creep strain shown in the figure is referenced to the starting strain, thus all creep curves start in the origin for better visualization. At room temperature, a significant creep can be observed. A linear approximation of the creep curve leads to a creep strain rate of approximately $\dot{\varepsilon}_c = 2 \cdot 10^{-9}$ [1/s] for a load of 1.5 MPa. For a temperature of $+10^oC$, the creep rate is reduced to about half and a linear creep rate of $\dot{\varepsilon}_c = 7 \cdot 10^{-10}$ [1/s] can be derived. For a temperature of -40^oC no creep can be observed within the first 24 hours.
Based on these results, creep might be a serious limitation of the shape adjustment process. However, there are possiblities to reduce or even avoid creep effects, which will be introduced in the following.

- **Use of polymers with small creep susceptibility**
  Different polymers show different creep behavior [29]. While thermoplastic polymers show a strong trend to creep or relax, thermoset polymers show much lower creep effects. Especially epoxy-based polymers hardly show creep. Epoxy-based shape memory polymers were developed [63] and might be an alternative.

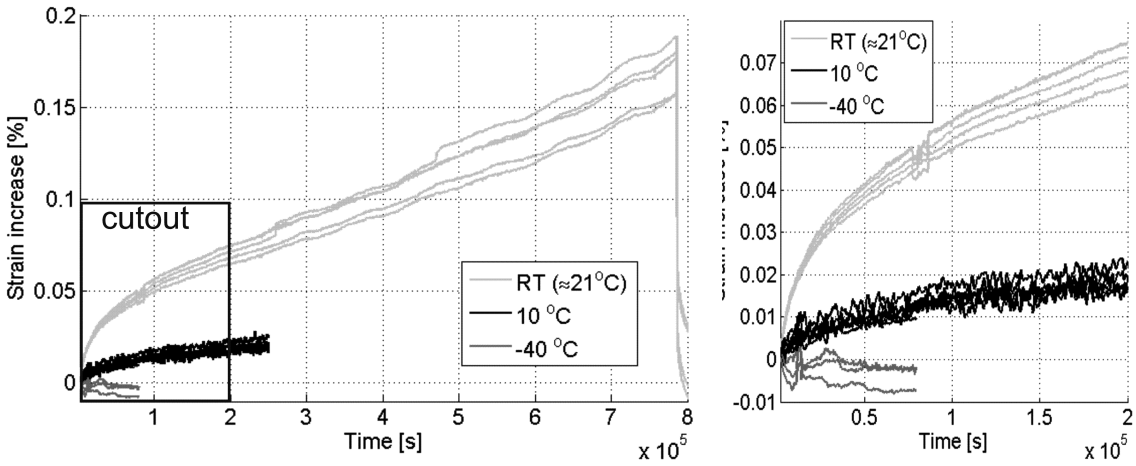

Figure 10.3.: Measurments of a creep rupture test with a 1.5 MPa load at RT ($\approx 21^oC$), 10^oC and -40^oC.

- **Use of fillers to reduce creep in polymers**
  The effect of fillers on the stress relaxation and creep behavior was investigated in the past. Bills et al. [10] showed an increase of the relaxation modulus by approximately 2 orders of magnitude using highly filled (up to 62%) polymers. They also showed an increase of the glass transition temperature of 16^oC for a filler content of 62 %. This increase of the glass transition temperature leads to a shift of the viscoelastic behavior to higher temperatures, and the glassy behavior might be available at the operational temperatures. Yang et al. [131] investigated the tensile creep resistance of polyamide 66 nanocomposites. Compared with the pure matrix the creep strain and the creep rate decreased by 62% and 67% respectively for a nanocomposite with 3.4 weight percent of TiO_2 nanofillers.

- **Limitation of programming strain and thus the operational load**
  The creep behavior of polymers is strongly dependent on the load level [131]. If the load level falls below a certain limit, creep is even stopped. To reduce the load of the shape memory polymer patches in operation smaller programming strains have to be used which leads to smaller recovery stresses. This of course has the drawback of necessary larger actuator cross-sections to maintain the required actuation forces for the shape adjustment.

- **Use of shape memory alloys as an alternative**
  Although shape memory alloys (SMAs) have not been discussed so far, SMAs could be an alternative if relaxation effects are a criterion, since they show no creep. The basic methods and principles introduced in this thesis can be applied for SMAs as well. Only technical solutions, such as the programming and the application and stimulation have to be changed. The drawbacks of SMAs such as the high mass density, the possible incompatibility with composite structures, and possibly high stimulation temperatures have to be accepted in this case.

In conclusion: creep is a property of shape memory polymers which cannot be neglected for the introduced shape adjustment application. However, there are methods to reduce or avoid this phenomenon.

10.2. Thermal Distortions

In general, every integrated actuator may also be a disturbance of the structure. Besides the active behavior, the actuator patches also show a conventional structural passive behavior. Due to possible thermo-elastic incompatibilities with the structure, thermal loads can lead to additional thermal stresses in the structure, which lead to distortions. This is investigated with a finite element analysis for the example of a planar plate.
The same quadratic plate is used as for the investigation of the optimization algorithms. The original shape distortions resulted in an RMS shape error of 0.1263 mm. Using two optimized actuators a minimal RMS shape error of 0.055 mm, which is a shape error ruduction of 57%, was achieved (Section 9.8). Figure 10.4 shows the distorted (a) and adjusted shape (b).

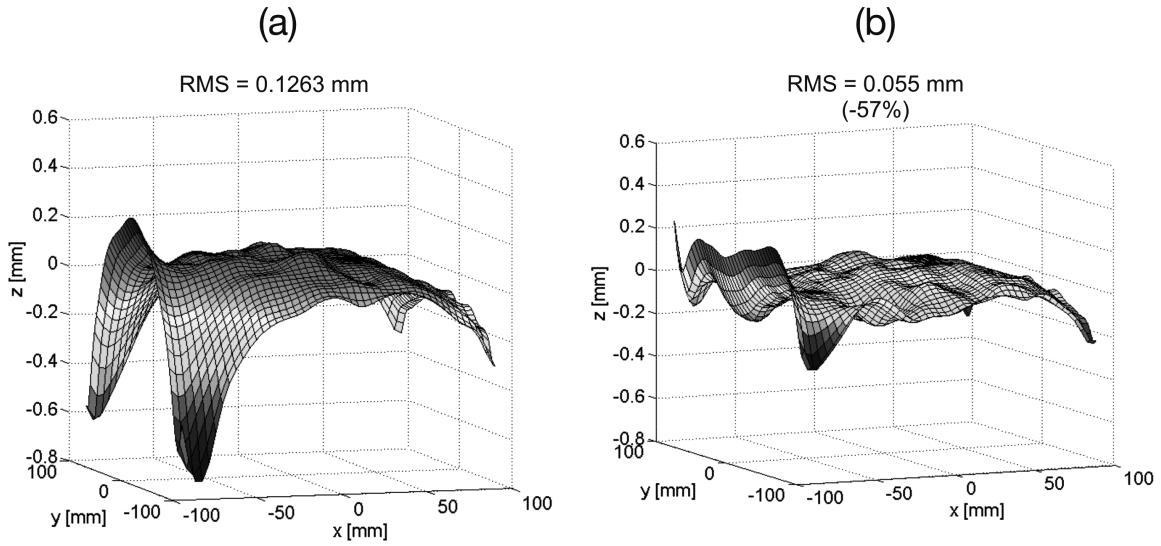

Figure 10.4.: Distorted (a) and adjusted (b) shape of a quadratic plate.

Thermal loads of ΔT of $+100\ ^oC$ and -100 ^oC are applied to the adjusted shape. The Young's moduli of the patches are chosen according to the temperature, with a modulus of 3.2 MPa for the hot case and a modulus of 800 MPa for the cold case. The results can be seen in Figure 10.5.

Since the composite plate has a symmetric layup, and local anisotropies of fiber volume fraction and fiber orientation are not modeled, the thermal strains of the plate do not have an effect on the out-of-plane deformations. Only the thermal strains of the actuator patches introduce distortions in this modeled case. It can be seen that, for the hot case, the shape

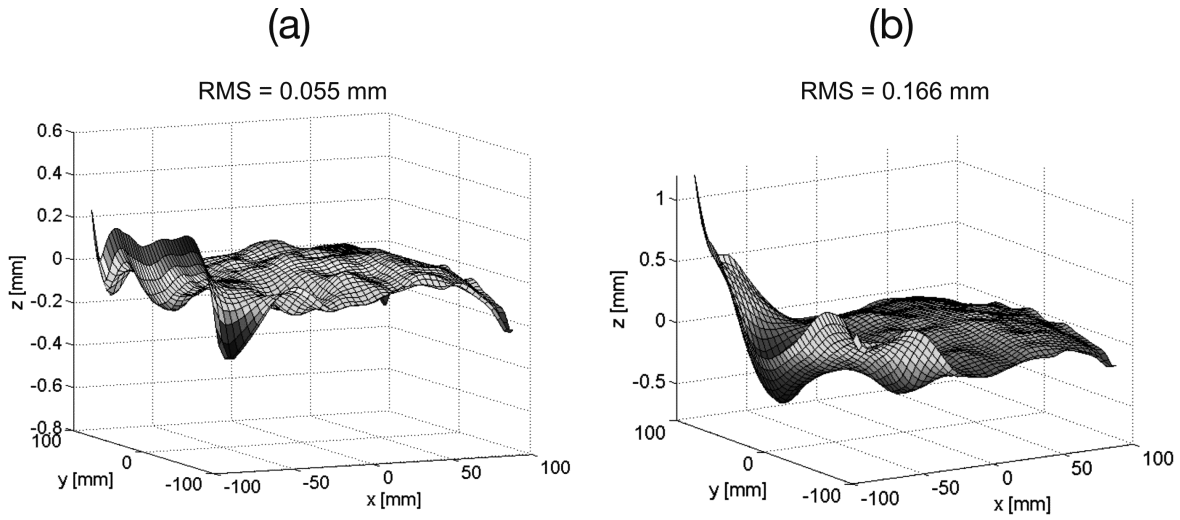

Figure 10.5.: (a) Negligible thermal distortion due to hot load case; (b) Significant thermal distoriton due to the cold case.

does not change, reflected by an unchanged RMS shape error of 0.055 mm. For the cold case, however, the thermal load leads to strong distortions of the shape and an RMS shape error of 0.166 mm, which is even worse when compared to the initial situation of 0.1263 mm.

It can be concluded that, for cold cases, the actuator patches introduce significant additional distortions. For the hot case, however, the distortions are negligible. For the operation in cold environment it might be an approach to include the thermal loads in the optimization algorithm to get the best average shape for the designated temperature ranges. Furthermore, there might be several applications, especially in the field of highly precise instruments, where a thermally controlled environment ist necessary.

11. Examples

11.1. Example 1 - Curved Plates

In a first example, the measurement technique, the simulation model, and the application and stimulation process are verified. For this purpose single curved CFRP shells are used due to their easy predictability and deformability. The results presented here are partly based on a diploma thesis, which has been conducted at the Institute of Lightweight Structures (LLB) [162].

11.1.1. Single curved CFRP Shells

Because of their easy predictability, high deformability and low stiffness, thin-walled, asymmetric CFRP shells are used for this first experiment. They consist of a $[0/90]$ laminate from *Sigratex Prepreg CE 1250-230-39* UD plys. The size is 180 mm $\times$ 180 mm and the resulting laminate thickness is approximately 0.5 mm. The resulting average curvature radii are 285 mm. Figure 11.1 shows representative samples. One surface of the samples is coated matt white for the measurement using dot projection photogrammetry.

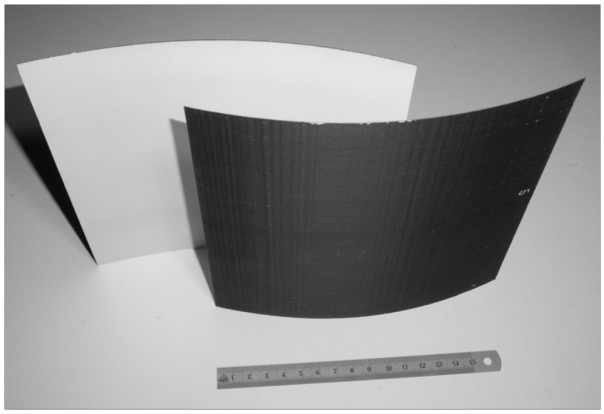

Figure 11.1.: Coated single curved CFRP shells for Example 1.

11.1.2. Shape Measurement with Dot Projection Photogrammetry

The shape of the matt white coated plates is measured with the introduced method of dot-projection photogrammetry using the *AICON DPA Pro* measurement system. Figure 11.2 (a) shows the measurement setup. Five pictures are taken each from six different camera locations. The determination of the 3D data points is performed with the software *AICON 3D Studio*. The postprocessing is performed with the software *Matlab*. Figure 11.2 (b) shows the measurement points and the interpolated surface for sample 1.1.

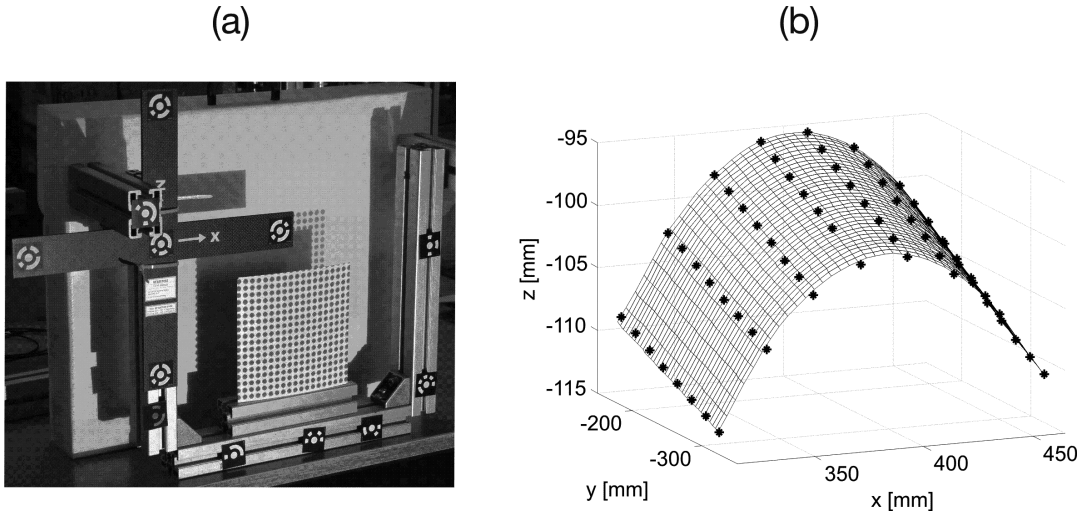

Figure 11.2.: (a) Measurement setup for dot projection photogrammetry of curved shells; (b) Interpolated surface of sample 1.1 after curing; asterisks mark measurement data.

For the single curved shell the maximum out-of-plane deformation Δz in the middle of the plate is used for the quantitative evalutaion of the shape (Figure 11.3).

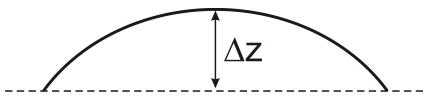

Figure 11.3.: Illustration of the evalutation parameter Δz for Example 1.

For the calculation of the deformation reduction δ, Equation 11.1 is used.

$$\delta = \frac{\Delta z_1 - \Delta z_2}{\Delta z_1} \cdot 100[\%] \tag{11.1}$$

where Δz_1 and Δz_2 are the out-of-plane deformations before and after the shape adjustment.

The samples show out-of-plane deformations between $\Delta z_1 = 9.49mm$ and $\Delta z_1 = 11.42mm$. The measurement results are summarized in Table 11.1

Table 11.1.: Maximum shape distortions Δz_1 before shape adjustment for samples 1.1 to 1.4

Sample No.	Deformation Δz_1 [mm]
1.1	9.65
1.2	9.49
1.3	11.42
1.4	10.73

11.1.3. Investigated Actuator Configurations

To verify the simulation model, and the programming, application and stimulation process, samples with different actuator configurations are used. For sample 1.1 and sample 1.2 compression mode actuators with different adhesives and a programming strain of $\varepsilon_{prog} = 33\%$ are used. For sample number 1.1, a two-component epoxy based adhesive *GP 14*, with a high modulus, for sample 1.2, a flexible adhesive (*PATEX Montageklebstoff*) with a low Young's modulus is used. This parameter variation is performed to investigate the adhesion and to verify the results of the paramter study of the structure-actuator interface (Chapter 8). Remember - the Young's modulus of the adhesive should be as similar to the Young's modulus of the actuator as possible, to guarantee optimal load introduction. For the samples number 1.3 and 1.4, tensile actuators with programming strains of $\varepsilon_{prog} = 85\%$ and $\varepsilon_{prog} = 170\%$ respectively are used. For reasons of comparability, approximately the same actuator volume is used for each test. The configurations of the performed tests are summarized in Table 11.2.

Table 11.2.: Summary of actautor configurations for Example 1

Nr.	Adhesive	Mode	$\varepsilon_{prog}/\varepsilon_{free}$ [%]	Actuator geometry $[mm^3]$	Actuator configuration
1.1	stiff	compression	33.3 / 50	$100 \times 20 \times 4.5$	1
1.2	flexible	compression	33.3 / 50	$100 \times 20 \times 4.5$	1
1.3	flexible	tension	85 / 46	$100 \times 12 \times 2.2$	3 parallel
1.4	flexible	tension	170 / 63	$150 \times 11 \times 2$	3 parallel

11.1.4. Simulation of the Shape Adjustment

For the example of the asymmetric laminates, with the large distortions, the geometric change cannot be neglected. Therefore the distorted shape is modeled using the measurement data

as an input. The thickness of the [0/90] asymmetric laminate has been determined to be 0.56 mm and is implemented in the model. The actuator patches are modeled as described in Section 6. For a used programming strain of 170%, an actuation stress of 3.1 MPa is extracted from the actuation stress characteristic (Figure 5.16) for the tensile case. The corresponding recovery strain of 63% leads to an effective Young's modulus of 4.92 MPa (Equation 6.6). For compression actuators, a recovery stress is used for the modeling, since for compression an unknown, only small influence of the thermal stress is assumed. For the achieved programming strain of 33%, a blocking recovery stress of 0.25 MPa can be extracted from Figure 5.14. The corresponding free recovery strain is 50%, which leads to an effective Young's modulus of 0.5 MPa. Figure 11.4 shows the finite element model of sample number 1.4. The CFRP plate is modeled using layered shell elements. The adhesive layer and the actuator patch are modeled using volume elements.

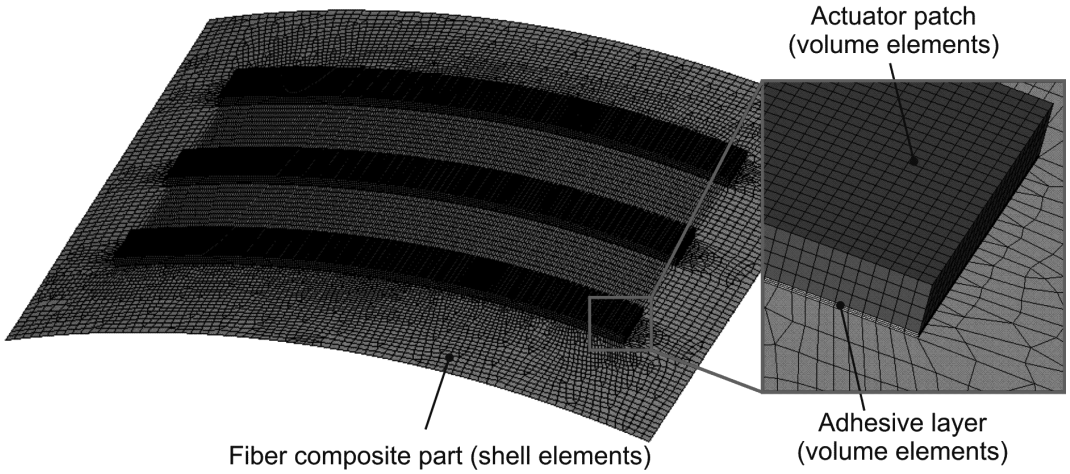

Figure 11.4.: Finite element model of sample number 1.4.

A representative example for the simulated shape adjustment is shown in Figure 11.5.

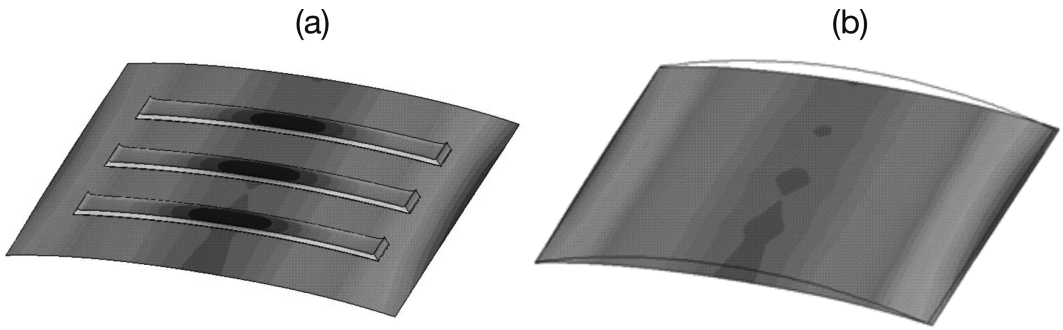

Figure 11.5.: Simulation of shape adjustment for sample number 1.4; (a) deformation field including acutators; (b) out-of-plane deflection (plotted to scale).

The simulation results, in terms of reduction of the out-of-plane deformation, are summarized in Table 11.3 and illustrated in Figure 11.8. It can be seen that the compression actuators

show a much lower performance than the tensile actuators. This can be explained with their lower recovery stress (see also Section 5). The different adhesive moduli show only negligible influence, which can be explained with the flat optimum regarding the adhesive modulus (Figure 8.5). From the results of sample 1.3 and 1.4 it can be seen that with increasing programming strain, the shape adjustment performance improves as expected (see also Section 5). Overall a maximum deformation reduction of 91.7% is achieved in the simulation.

11.1.5. Programming of Actuators

The programming of the actuators is performed in two steps for the curved geometry as described in Chapter 7. In a first step the actuator green body is tensioned or compressed in axial direction. In a second step the curvature is manufactured in a mould. Especially the compressing of the tiny actuator patches leads to difficulties in terms of wrinkles, which limited the programming compression strain to 33%.

11.1.6. Application and Stimulation Process

The application of the actuator patches is performed by an established gluing process (Chapter 7). After the marking of the actuator locations, the surfaces of the CFRP shells and the actuators are mechanically pre-treated by sand blasting. Thereafter the surfaces are cleaned using *Acetone*. The adhesive is applied to the surface and distributed avoiding bubbles using a spatula. Distance wires are placed in the adhesive layer to maintain the desired adhesive gap. The actuator is placed on the marked area without integrating bubbles in the adhesive layer. The acutator is pressed to the surface and cured for at least 48 hours. Figure 11.6 shows the cured sample number 1.1 with an intregrated compression actuator.

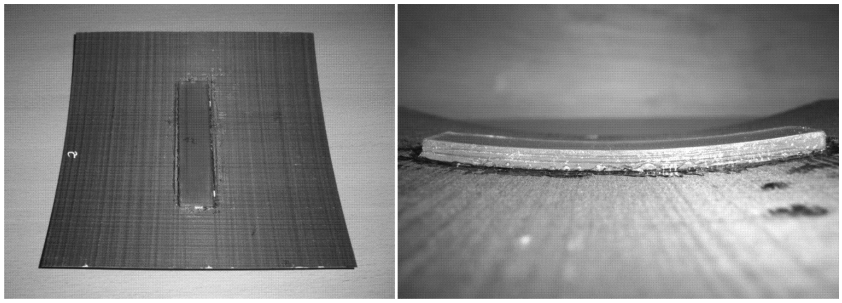

Figure 11.6.: Sample number 1.1 after curing.

The stimulation is performed in a thermal chamber at $T_r = 88^oC$. The recovery time t_r is approximately 5 minutes.

11.1.7. Results

After the stimulation, the CFRP shells are measured again. Moderate to large improvements are achieved. Figure 11.7 shows the measured cross section of sample number 1.4 before and after the adjustment process. It can be seen that the edges still show large distortions since the actuator has a limited length and the edges are not adjusted. However, the middle part of the plate shows a significant ruduction of the distortion.

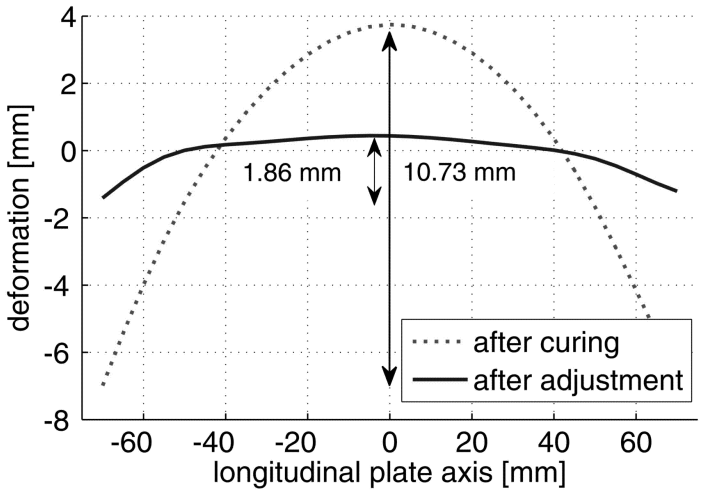

Figure 11.7.: Cross section of sample number 1.4 after curing and after adjustment.

The results are summarized in Table 11.3 and illustrated in Figure 11.8.

Table 11.3.: Deformation reductions for both simulation and experiment

Sample Nr.	Deformation reduction δ (Simulation) [%]	Deformation reduction δ (Experiment) [%]	Difference Sim.-Exp. [%]
1.1	15.0	14.6	+0.4
1.2	15.3	16.0	-0.7
1.3	50.6	51.6	-1
1.4	91.7	82.7	+9.0

It can be seen that in general the simulation model can predict the shape adjustment process very well. The larger difference of 9% between simulation and experiment for sample number 1.4 can be explained by beginning debonding of the actuator patches in the experiment, which leads to a reduction of the adjustment efficiency. It can be noticed that the adhesive has only a small influence on the adjustement performance. However, the soft adhesive performed better. The compression actuators show a much lower performance than the tensile actuators (see also Section 5). Furthermore, it can be seen that with increasing programmed strain the shape adjustment performance improves as expected.

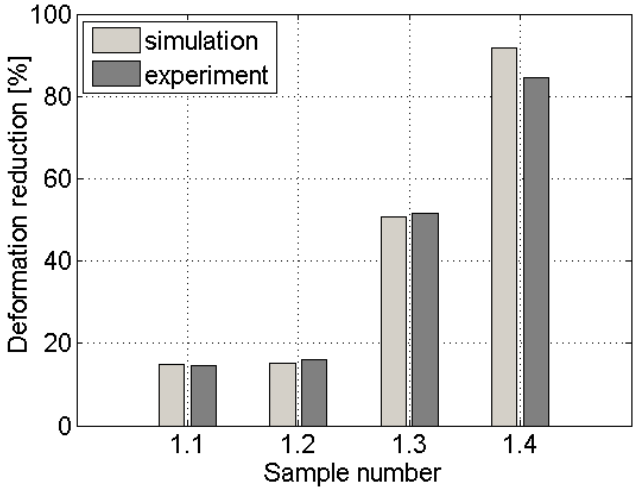

Figure 11.8.: Results of simulation and experiment for Example number 1.

Overall a maximum deformation reduction of 82.7 % has been achieved in the experiments. Overall the experiment shows the high potential of the suggested method. In further examples, the approach is applied to more complex structures, incorporating the optimization algorithm to determine optimal actuator configurations.

11.2. Example 2 - Planar Plate

To demonstrate the developed shape adjustment approach, including the shape optimization, the example of a planar rectangular plate with asymmetic distortions is investigated.

11.2.1. Curing of the Sample

A $[90/0/0/90]$ laminate is manufactured using *Sigratex Prepreg CE 1250-230-39* UD plys. The sample size is 200 mm $\times$ 200 mm $\times$ 1 mm. The sample is cured under vacuum conditions. Peel ply is used on both sides to get a rough textured surface, which is advantageous for the actuator bonding. The setup for the curing can be seen in Figure 11.9.

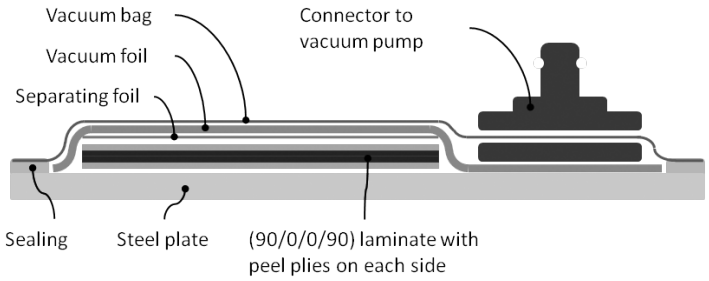

Figure 11.9.: Schematic of the setup for the curing of the samples.

After curing, warpage effects can be observed. The reason in this case is the tool-part interaction between the steel mould and the sample. To quantify the distortions and to apply the simulation and optimization process, the surface is measured by dot projection photogrammetry.

11.2.2. Shape Measurement with Dot Projection Photogrammetry

Before the sample can be measured, one surface must be coated matt white to obtain the high contrast between the surface and the projected black targets. The settings for the dot projection are as follows. A grid of 19×19 circular targets, with a spacing of approximately 10.7 mm is used. The target diameter is approximately 7 mm. The projector is set up in a distance of 1300 mm to the sample. A coordinate system and 8 coded markers are used. The camera settings can be found in Appendix A.2. The measurement setup and the resulting scatter plot can be seen in Figure 11.10. The out-of-plane measurements show a standard deviation of 30-150 μm. The plate shape is evalutated by a best fit RMS shape error (Equation 4.1). For the error calculation an interpolated surface with 49×49 evaluation points is used. This best fit surface regarding the x-y-plane is shown in Figure 11.11.

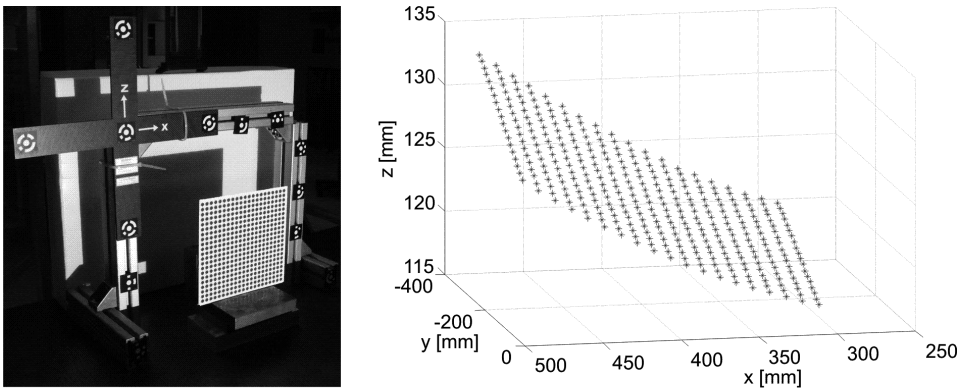

Figure 11.10.: Measurement after curing; (a) setup; (b) scatter plot.

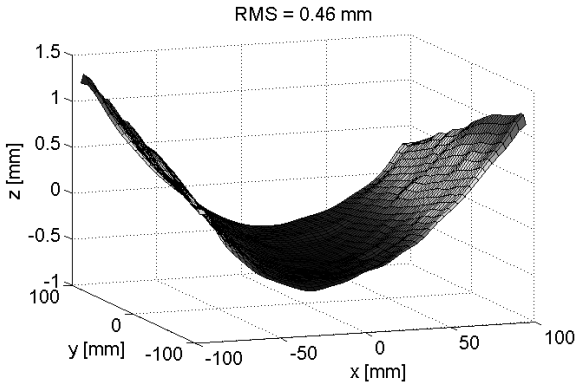

Figure 11.11.: Interpolated best fit surface of sample 2.1.

It can be seen that there is a dominant curvature about an axis, which is rotated about 75^o regarding the x-axis. Furthermore, the corners of the laminate show different amplitudes of distortions. The resulting RMS error for this surface regarding the best fit plane is 0.46 mm. To reduce this error the shape adjustment process is applied.

11.2.3. Finite Element Model

The finite element model is built following the instructions in Chapter 6. However, since an optimization process is applied and high computational effort shall be avoided, the adhesive layers are not modeled to reduce the model size. Tensile actuators are used for this example. For the applied programming strain of 150% an actuation stress of 3 MPa can be extracted from the actuation stress characteristic (Figure 5.16). From these values, the free recovery strain ε_{free} of 60% and an effective Young's modulus E_{eff} of 5 MPa can be calculated. These values are used for modeling. Since the tensile mode is used, the actuators are applied on the convex side of the plate. All degrees of freedom of the plate are constrained at one

corner node. The finite element model of the optimized configuration can be seen in Figure 11.12.

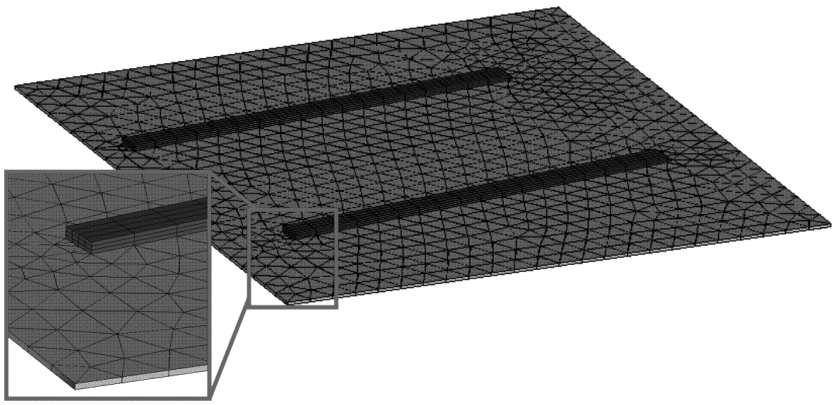

Figure 11.12.: Finite element model of the optimized actuator configuration.

11.2.4. Shape Optimization

The introduced shape optimization algorithm is applied on this example to determine the optimal actuator configuration. A combination of a genetic algorithm (*MatLabGA*) optimization and a subsequent gradient based optimization (*fmincon*) is used. For this example, two actuators are chosen. The design variable vector is defined as:

$$\vec{x} = \{x_1, y_1, \alpha_1, L_1, W_1, x_2, y_2, \alpha_2, L_2, W_2\}^T$$

where x is the x-coordinate, y is the y-coordinate, α is the angle of the actuator axis and the positiv x-axis, and L and W are the length and width of the actuator. The thickness of the actuator is kept constant at t_a= 2 mm. Only a tensile mode with full recovery is allowed, thus the stimulation parameter is a constant and not a design variable.
The objective function of the optimization is the RMS shape error (Equation 4.1) regarding a best fit plane. The restrictions are a mass limit and geometrical limits. For both actuators only tensile mode with full recovery is allowed. The full optimization statement is given in Equation 9.2 and the following. The resulting actuator configuration and the corresponding optimized shape can be seen in Figure 11.13 (a) and (b). The RMS errors decreased from 0.46 mm to 0.032 mm, which is a reduction of 93%.

11.2.5. Adjustment - Application and Stimulation

Two actuator patches are manufactured, regarding the results obtained by the optimization process. Rectangular samples are tensioned in an INSTRON tensile testing machine at a programming temperature of $T_{prog} = 90^oC$ and a strain rate of v=62 mm/min to a maximum strain of $\varepsilon_{prog} = 150\%$. After the programming the actuators are cut to the

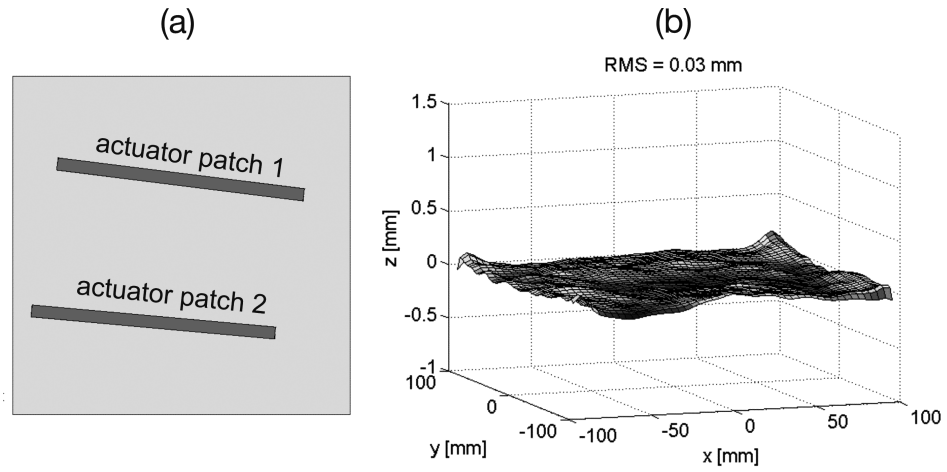

Figure 11.13.: (a) Optimized actuator configuration and (b) corresponding optimal best fit shape (RMS = 0.03 mm).

determined rectangular dimensions and applied to the structural back side following the introduced gluing process. A contact pressure of 0.01 MPa is applied for the curing at room temperature for 48 hours. Figure 11.14 shows the CFRP plate with the applied actuator patches after curing.

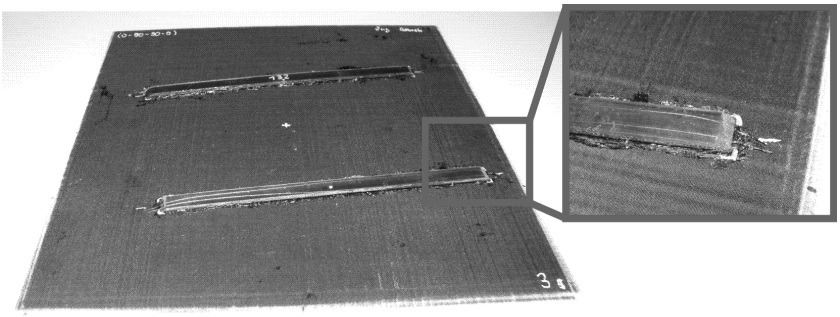

Figure 11.14.: CFRP plate integrated with two SMP actuator patches.

After the curing the plate is placed in a thermal chamber for approximately four minutes at a recovery temperature of T_r of 67^oC. After four minutes deponding started and the plate is removed from the thermal chamber. Figure 11.15 shows the debonding of one of the actuators.

After cool down and resting for 4 hours the sample is measured. For the measurement the standard camera settings are used (see Appendix A.2). A grid of 21 $\times$ 21 targets with a spacing of approximately 9.5 mm is used. The target size is about 6.5 mm. For the RMS error calculation a grid of 48 $\times$ 48 evaluation points is used. The corresponding interpolated surface can be seen in Figure 11.16 (b) in comparison with the original shape (a). The RMS error is reduced about 58.7% from 0.46 to 0.19 mm.

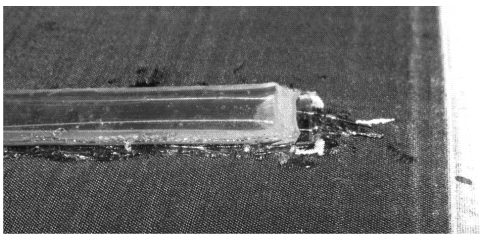

Figure 11.15.: Debonding of the actuator because of peel stresses and limited adhesive forces.

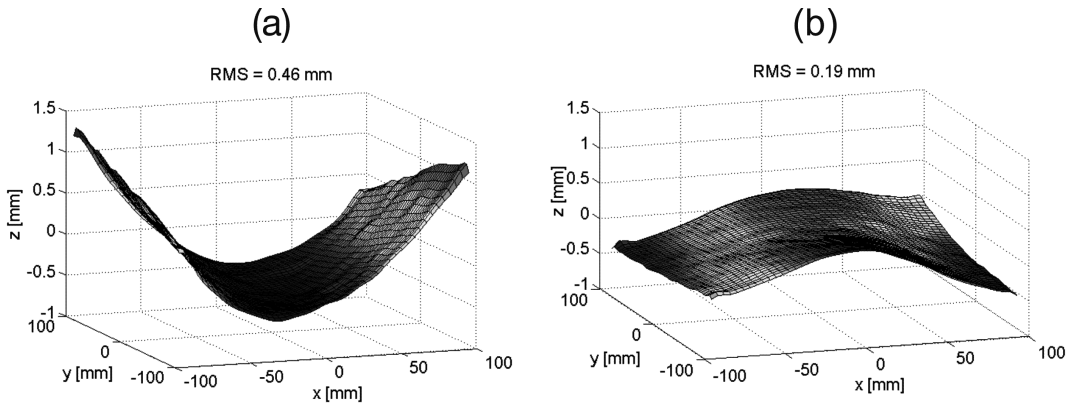

Figure 11.16.: (a) Plate shape after curing; (b) Plate shape after adjustment.

However, it can be seen that, compared with the simulation (reduction of 93%), the optimal shape is not achieved (reduction of 58%). The underestimation of the adjustment performance can be explained with an unsatisfactory thickness modeling of the plate and not considering the adhesive layer. For the optimization a plate thickness of 1 mm has been assumed. Post-test measurements, however, gave an average plate thickness of 0.92 mm. For an adhesive layer of 0.2 mm an increase of the actuator efficiency of 9.3% is determined (Figure 8.4). Thus, the acutuators deform the plate more than expected, and a curvature in the opposite direction is induced. Using this additional information in a second finite element simulation the experimental result and the simulation agree surprisingly well. The resulting RMS shape error for the corrected simulation is 0.17 mm (reduction of 63%), compared to the measured shape error of 0.19 mm (reduction of 58%). Figure 11.17 shows the measured (a) and corrected, simulated (b) plate shapes.

As it can be seen in Chapter 10, relaxation and creep might affect the performance of the shape adjustment in an opertational environment. At room temperature a significant creep could be observed and a creep rate of approximately $\dot{\varepsilon}_c = 2 \cdot 10^{-9}$ [1/s] has been obtained for a load of 1.5 MPa. This behavior is verified with Example 2.1. After 65 days the sample has been measured again, and the resulting best fit shape can be seen in Figure 11.18.

Compared with Figure 11.17 (a) a clear reduction of the deformation can be observed indicating creep of the actuator material. Using iterative finite element simulations a backward calculation of the prevailing creep modulus E_c can be calculated. Using the creep modulus

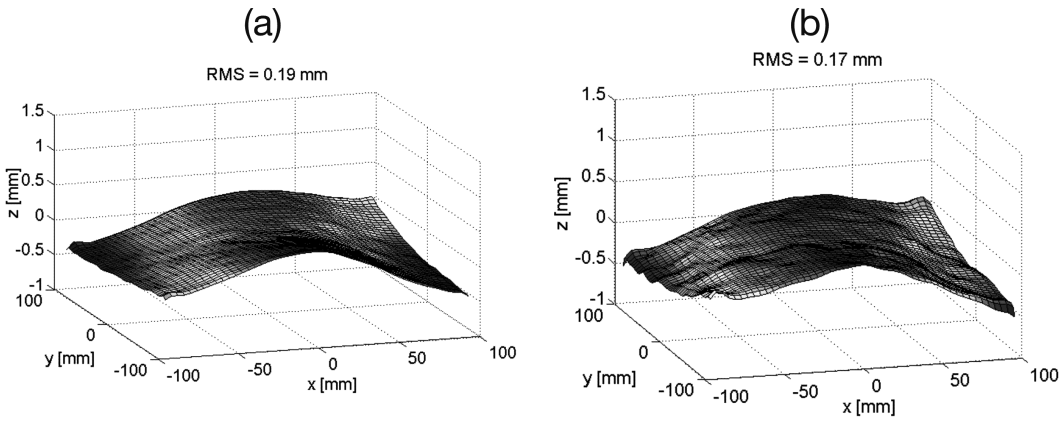

Figure 11.17.: Good agreement between measured shape (a) and corrected simulation (b).

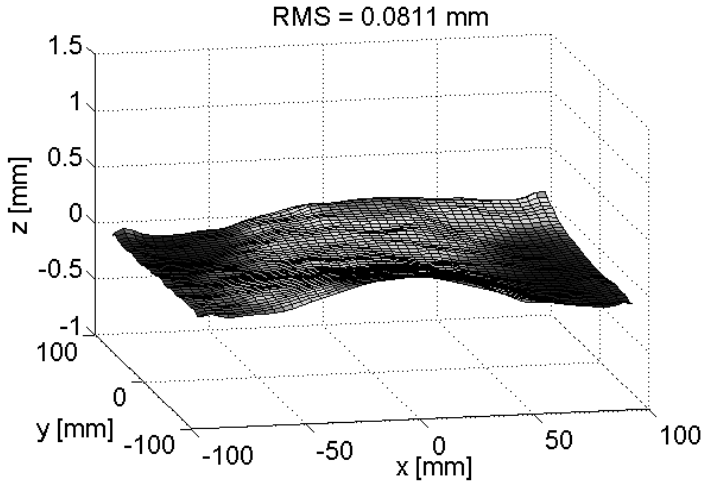

Figure 11.18.: Best fit shape of sample 2.1 after a storage time of 65 days.

E_c the actual strain increase can be calculated using Equation 10.1. With this calculations a creep rate of $\dot{\varepsilon}_c = 1.7 \cdot 10^{-8}$ [1/s] is determined, which is one order of magnitude larger than the one determined by the creep rupture test (Section 10). This discrepancy might be explained with an increased temperature during the storage of the sample and the higher load of approximately 3 MPa compared to the 1.5 MPa used in the creep rupture test.

11.2.6. Further Example

In addtion to the example introduced in detail, another example shall be shown briefly. The same material, layup, manufacturing, measurement, modeling and optimization processes as in the previous example are used.

The interpolated best fit shape after curing of Example 2.2 is shown in Figure 11.19.

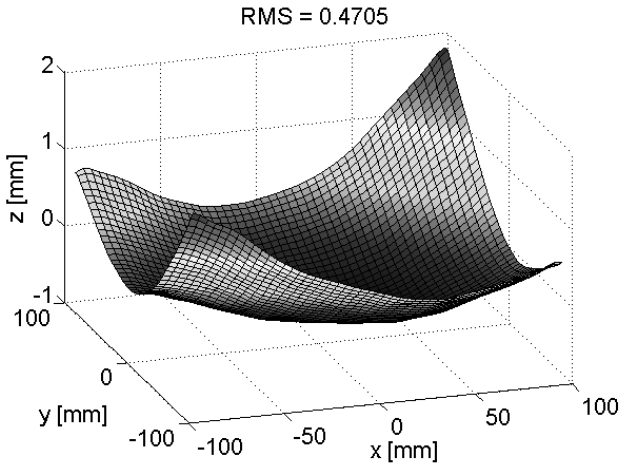

Figure 11.19.: Best fit shape of sample number 2.2 with a shape error of 0.47 mm.

The corresponding best fit shape error is 0.47 mm. With the optimization using 2 actuators only an optimal best fit shape error of 0.24 mm is found. This unsatisfactory result can be explained with the double curved distorted shape, which requires more sophisticated actuator configurations. Hence the number of actuators is increased to N=3, N=4 and N=5. The results are summarized in Table 11.4 and illustrated in Figure 11.20.

Table 11.4.: Simulated optimization results for Example 2.2.

Number of actuators N	RMS [mm]	Reduction [%]	mass [mm^2]
0	0.46	0	-
2	0.240	47.8	2381
3	0.142	69.1	3000
4	0.128	72.2	3000
5	0.184	60.0	2993

It should be mentioned that, for 3 and 4 actuators the mass restriction is active and for 5 actuators the restriction is close to active, which indicates that the mass is the limiting constraint. For two actuators, however, the mass constraint is not active, but no better shape is found by the optimization algorithm. This might be explained with the limited flexibility of this configuration. The best solution is found for a configuration of 4 actuators.

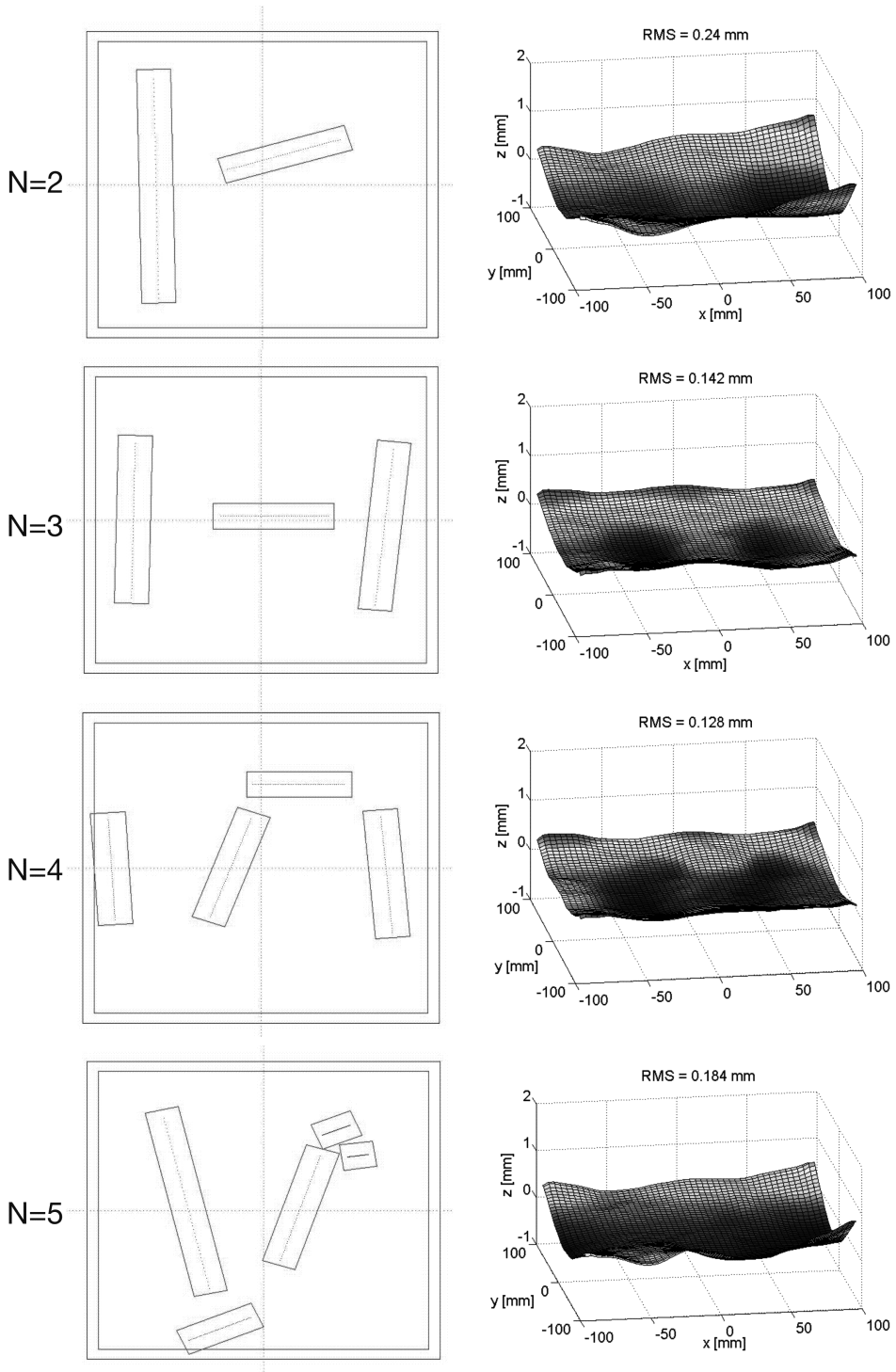

Figure 11.20.: Optimized actuator configurations and resulting best fit shapes for N=2,3,4 and 5 actuators.

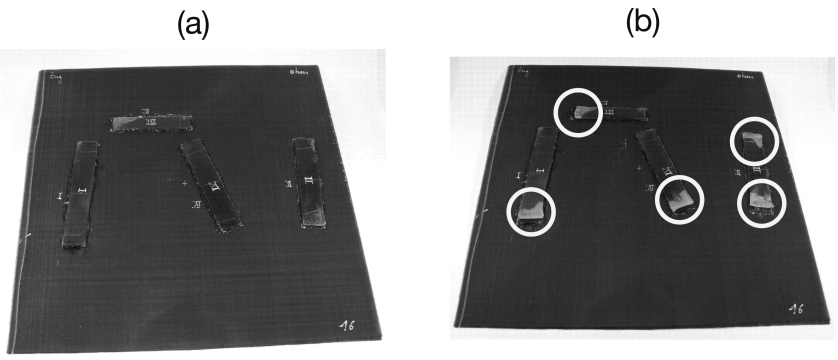

Figure 11.21.: Sample number 2.2; (a) unsatisfactory sample with bubbles in adhesive layers; (b) strong debonding (marked with circles) of actuators after stimulation at 70^oC.

This configuration is further investigated with an experiment. The sample can be seen in Figure 11.21 (a). Unfortunately, unsatisfactory gluing has been performed. Bubbles have been integrated in the bonding layers of acatuators II and III (Figure 11.21 (a)). Hence, during the recovery strong debonding effects occured, which resulted in a large reduction of the shape adjustment performance. Figure 11.21 (b) shows the debonding actuators after recovery.

The resulting shape of the structure with a best fit shape error of 0.31 mm, which is a distortion reduction of 32.7%, can be seen in Figure 11.22.

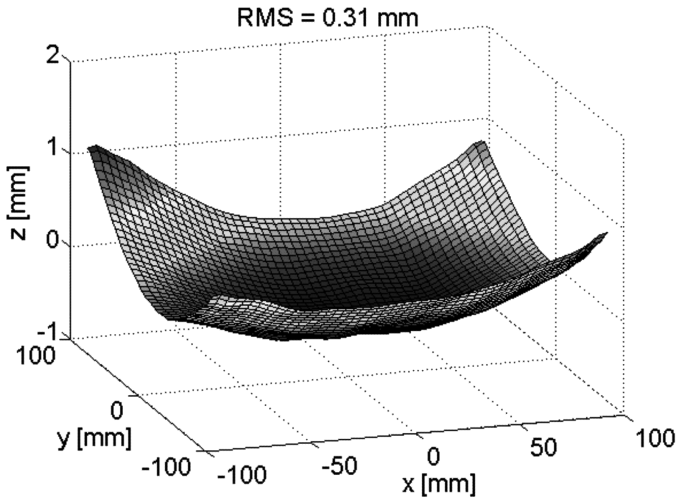

Figure 11.22.: Measured best fit shape of sample number 2.2 after adjustment (RMS = 0.31 mm; reduction of 32.7%).

11.3. Example 3 - Antenna Waveguide

The introduced shape adjustment approach is suited especially for thin-walled high performance composite structures. Thin-walled structures are more susceptible to warpage effects than thicker laminates. Furthermore, the limited available actuation stress for SMPs is well suited to parts with low stiffness. In high performance structures, even very small distortions in the range of microns may be significant and may reduce the functional performance. One example for such parts are high frequency (antenna) waveguides.

11.3.1. Lightweight Intersatellite Antenna - LISA

Due to the demand for increasing data rates for satellite and inter-satellite links an increasing bandwidth is required, which is possible using high frequencies such as the Ka-band. Especially for small satellites, lightweight and compact high gain antennas have to be developed. In the project, named Lightweight Inter-Satellite Link Antenna (LISA), funded by the German Aerospace Center (DLR), a lightweight and compact inter-satellite link antenna for Ka-band has been developed. Figure 11.23 shows a 3D CAD model of the S-Band variant, mounted on top of a representative satellite.

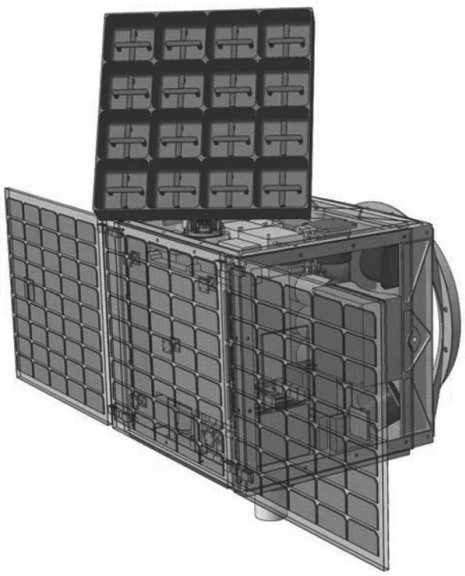

Figure 11.23.: 3D CAD model of the Lightweight Inter-Satellite Link Antenna (LISA) on top of a satellite [Institute of Astronautics (LRT), TUM].

The project has been led by the Institute of Astronautics (LRT, TUM), which has been responsible for system aspects. While the company NTP has accomplished the radio frequency (RF) design, the Institute of Lightweight Structures (LLB) has been responsible for the structural concept and the mechanical design. For compact antennas with the dimensions of 400 mm $\times$ 400 mm, direct radiating arrays offer the optimal gain. A further advantage of direct

radiating arrays is the possible electrical beam steering [148]. In a first step an antenna for S-Band has been developed with rectangular radiating elements and a conventional electrical cable network on a conductor plate [75, 156] (Figure 11.23). In a further project phase, a K_a-Band antenna has been developed. Due to the higher frequencies and the resulting unavoidable electrical losses, the waveguide technology has been applied. The used waveguides with a cross-sectional area of approximately 4.4 mm $\times$ 8.8 mm build a complex and dense network for the required, compact high gain antenna. The aperture consists of 8 $\times$ 8 optimized horns, with a total size of 400 mm $\times$ 400 mm. Figure 11.23 (a) shows a 3D CAD model of the antenna system mounted on a satellite surface, (b) shows the complex waveguide network.

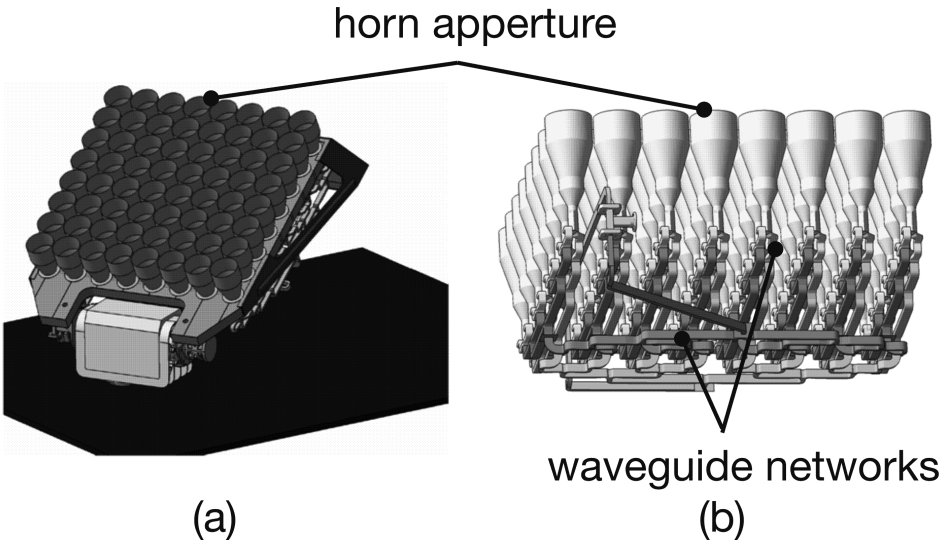

Figure 11.24.: 3D-CAD model of the horn array and the waveguide network of LISA II.

The challenge within this development has been the manufacturing of the very compact and complex waveguide network. Conventional manufacturing techniques and flanging the parts together have been avoided due to mass penalties of the flanges, electrical losses and limited accessibility. Therefore different integral manufacturing techniques have been investigatd. Besides the direct metal laser sintering (DMLS) with aluminum powder and a copper electro-forming technique (which is finally chosen), a CFRP-copper variant has been investigated. The DMLS technique failed because of the poor quality of achievable surface roughness, a function of to low laser power, low focussing performance, and graining of the alumium powder. The copper electro-forming technique leads to very good electrical performance. However, the mass density of copper is high ($8.9g/cm^3$) and thus the resulting mass is very high. To reduce mass, a hybrid technique using a thin layer of copper and a structural stiffening laminate is investigated. Figure 11.25 shows M-shaped test sample waveguides, built with these manufacturing techniques. More information about the manufacturing techniques can be found in [146, 156]

Although the electrical performance of the hybrid waveguide is similar to the pure copper

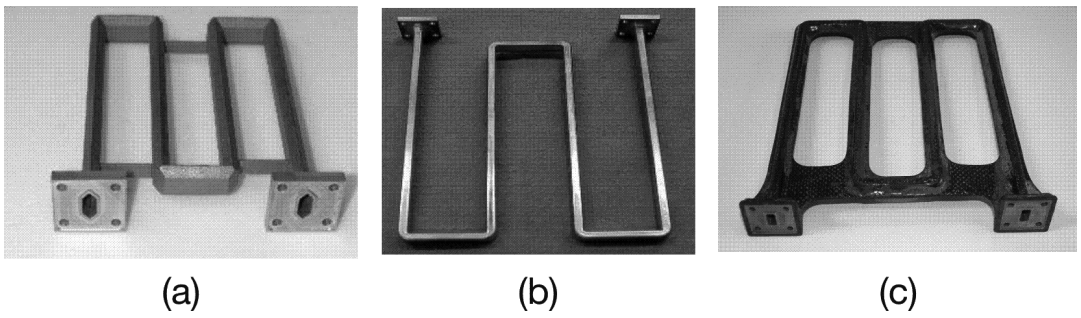

Figure 11.25.: Waveguides for Ka-Band manufactured differently: (a) Direct metal laser sintering; (b) Copper electro-forming; (c) Hybrid CFRP-copper.

waveguide, distortion effects can be seen with straight samples, which might affect the high frequency performance. The parallelity of the two opposing surfaces is important for the high frequency performance of antenna waveguides (see Section 11.3.2). Curved CFRP structures, however, show a strong trend to the distortion effect of spring-in (Section 3.1). In Figure 11.26, a cross-section of a hybrid waveguide manufactured during the LISA project is shown.

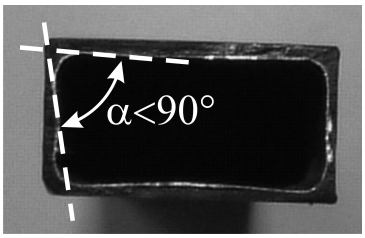

Figure 11.26.: Cross-section of a hybrid CFRP-copper waveguide showing spring-in effect.

A clear spring-in effect can be observed. Due to this apparent warpage effect the developed shape adjustment approach is applied to a sample of a waveguide.

11.3.2. Waveguides

Waveguides are electrically conductive structural elements that can guide electromagnetic waves in the frequency range of typically 3 GHz to 300 GHz. The advangage of waveguides over cables is the very low electrical loss factor. Typical shapes are circular, elliptical or rectangular cross-sections.

Physical Background

If an electromagnetic wave strikes a conductive surface perpendicularly, it is reflected. If a second conductive surface is aligned parallel in a proper distance, a standing wave is formed, and a stationary wave field becomes apparent. The resonance frequencies in this field are depending on the distance of the parallel surfaces. In a waveguide, however, electromagnetic

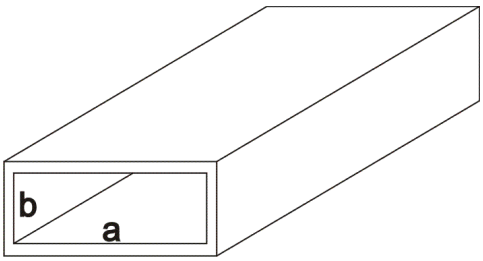

Figure 11.27.: Schematic illustration of a rectangular waveguide.

waves have to travel along the tubes. This is achieved by chosing the distance of the walls slightly smaller than the used wavelength. In this case the waveform only fits into the waveguide if it has an inclination. Thus the wave travels along a zig-zag path along the tube. The minimum width a of a waveguide is slightly smaller than the half of the transported wavelength λ. In this case one half wave is fitting into the waveguide. The corresponding wavelength is called the critical wavelength λ_c and is calculated by Equation 11.2

$$\lambda_c = 2 \cdot a \tag{11.2}$$

where a is the longer side of the waveguide (Figure 11.27).

For common frequency bands, the frequencies, the band names and the waveguide dimensions are listed in Table 11.5

Table 11.5.: Typical communication bands.

Name	Frequency band [GHz]	Waveguide width a [mm]
L	1 - 2.6	165.1
S	2.6 - 3.95	72.14
C	4.64 - 7.05	40.39
X	8.2 - 12.4	22.86
K_a	26.5 - 40	8.64
W	75 - 110	2.54

In this table a aspect ratio of a:b of 2:1 is assumed.

Architectures and Materials

Conventional waveguides are built from aluminum or copper because of their outstanding electric properties. Using conventional manufacturing techniques such as milling or casting, straight, curved or even intersecting waveguides are built. Using flange connections they are assembled to quite complex waveguide networks for different high frequency (HF) applications such as radar or communication antennas.
For space applications CFRP waveguides are used to reduce mass. The company *INVENT* built, in cooperation with *EADS Astrium GmbH*, several hundred rectangular waveguides for

X-band with the dimensions of 9 mm × 11 mm to 10 mm × 20 mm and a length of 400 mm for the radar satellite *TerraSar X*. *EADS Astrium GmbH* also built straight CFRP waveguides for the *Sentinal 1* radar antenna [4].

11.3.3. Sample Waveguide

The used waveguide samples have inner dimensions of 47.5 mm × 23.7 mm × 100 mm, which corresponds to an L-Band waveguide. A symmetric [0/90/90/0] layup, using UD layers of the prepreg *SIGRATEX PREPREG CE 1250-230-39*, supplied by *SGL*, is laminated. The resulting rectangular CFRP tubes are shown in Figure 11.28.

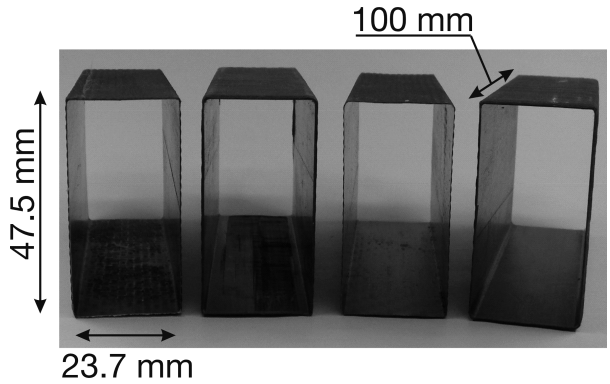

Figure 11.28.: Rectangular waveguide samples after curing.

11.3.4. Shape Measurement

Since the functional surface of the waveguide is the inner side, the actuator patches have to be mounted on the outside of the waveguide, and the measurements have to be performed at the inner side. This is not possible with the dot projection photogrammetry, thus the measurement is performed with the 3D-NC measurement (see Section 4.1). The measurement is performed with a *Zeiss RT 05-800* machine. The measurement accuracy is 0.01 mm and the minimal measurement force is 0.1 N. This leads to negligible measurement errors for the waveguide samples (see Section 4.1). A ball pin of 8 mm diameter is used. The waveguide is clamped using magnets at two perpendicular walls. The opposing long side wall a of the waveguide is measured as a representative geometric measure. This is valid since the parallelity of the two opposing long side walls is a significant geometric property for the reflectivity of the electromagnetic waves. A measurement grid of 23 × 10 points with a spacing of 4.25 mm is used. The test setup can be seen in Figure 4.1. The scatter plot of the measured 3D coordinates is shown in Figure 11.29.

A spring-in effect is clearly visible by means of the concave deformation of the waveguide wall. Using a grid with a spacing of 1 mm the best fit RMS shape error regarding a best fit

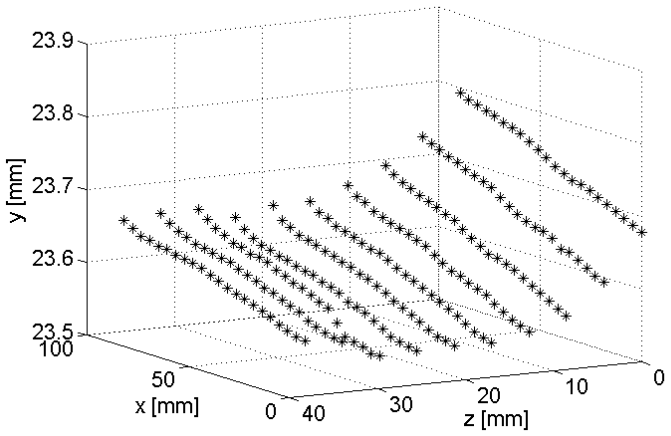

Figure 11.29.: Measurement pattern along the side wall of a waveguide test sample.

plane is calculated. The best fit interpolated surface can be seen in Figure 11.31 (a). The resulting RMS error is 0.026 mm.

11.3.5. Finite Element Modeling

The CFRP waveguide is modeled using shell elements of the type *shell181*. The waveguide thickness is 0.95 mm with a [0/90/90/0] layup, where the 0^o direction is in waveguide axial direction. The actuators are modeled using *solid45* volume elements. Figure 11.30 shows a representative finite element model.

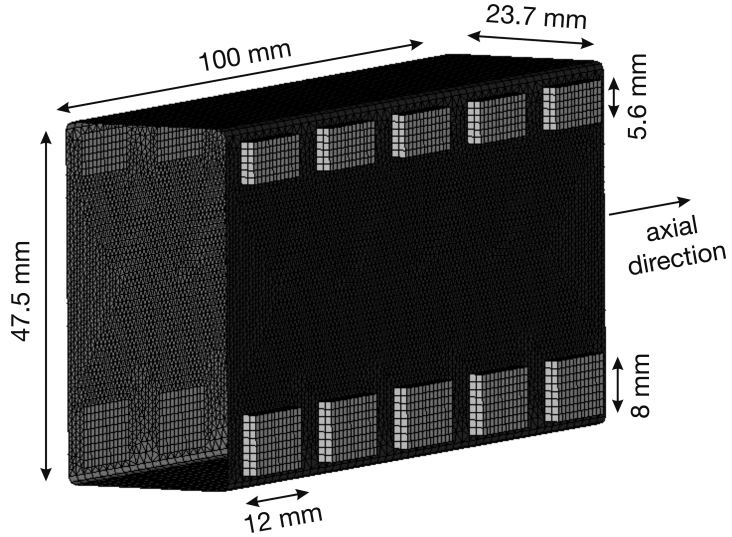

Figure 11.30.: Finite element model of the waveguide including actuators.

11.3.6. Shape Adjustment

Due to the simple geometry of the distortion the optimization process is assumed not to be necessary. Instead a finite element analysis is carried out and a parametric study is performed to find an appropriate actuator configuration. Only tensile acutators are used since the manufacturing is much easier and the actuation performance is better in terms of actuation stress. A further geometric constraint for this example is the limited width of the actuators due to their availability. The final actuator configuration can be seen in Figure 11.30. At the top edge 5 patches with lengths of 5.6 mm and widths of 12 mm are applied side by side. At the bottom edge, 5 patches with lengths of 8 mm and widths of 12 mm are applied side by side. All patches have a thickness of the required 2 mm. Due to the large thickness to length ratio, this leads to disadvantageous load introduction due to high shear losses. New manufacturing technologies for the production of thin actuators or even active membranes would improve the situation. The resulting best fit surface can be seen in Figure 11.31 (b). The corresponding shape error is RMS=0.0091 mm, which is, compared to the initial RMS error of 0.026 mm, a error reduction of 65%.

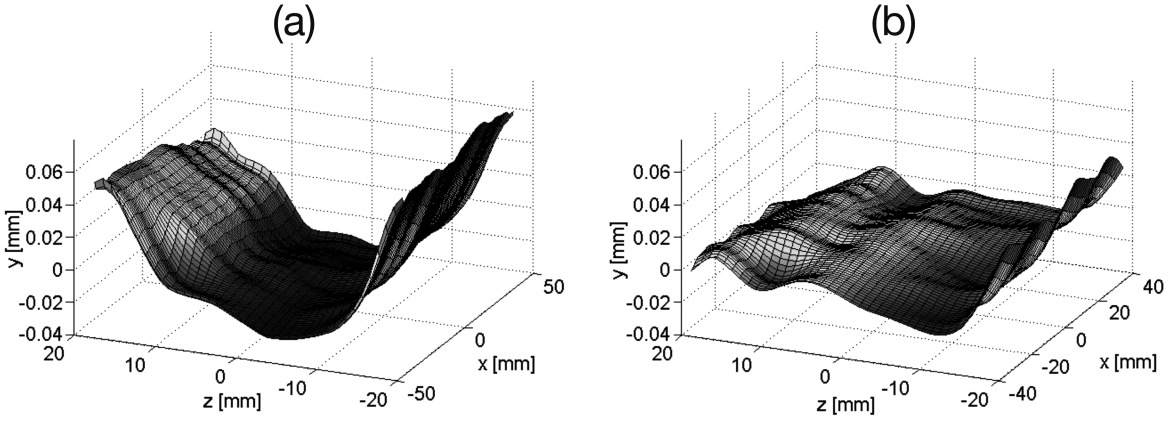

Figure 11.31.: Shape of the waveguide wall; (a) Best-fit shape after manufacturing (RMS=0.026 mm); (b) Best-fit shape after simulated adjustment (RMS=0.009 mm).

To summarize this feasiblity investigation, it appears to be possible to improve the shape of composite waveguides significantly (here a reduction of 65% is achieved in the simulation). These results should be validated with experiments in the future.

12. Summary, Future Work and Outlook

12.1. Summary

A comprehensive literature review showed that shape distortions of composite parts remain a drawback of composite manufacturing despite several optimization approaches. A novel post manufacturing shape adjustment process using shape memory polymer (SMP) actuator patches to compensate manufacturing distortions was developed in this work.
Different 3D shape measurement techniques were introduced and discussed. The conventional 3D-NC shape measurement showed fast and reliable results with a resolution of 0.01 mm. However, due to the inherent drawback of a necessary minimal sensing force of 0.01 N, this measurement technique could not be applied to all of the investigated thin-walled composite parts. The discussed dot projection photogrammetry is a non-contact measurement technique which is well suited for laborous measurements. For the measurements performed in this work an accuracy of 0.005-0.015 mm was achieved. As an alternative a shape reconstruction method based on the strain measurement using fiber Bragg grating sensors and a modal transformation matrix was introduced. For a dynamic experiment, it was shown that part shapes could be reconstructed with a RMS shape error of smaller than 2%. This more complex technique, however, was not well suited for the investigation of the shape adjustment process in the laboratory. But for industrial applications it seems to be an appropriate approach.
A novel experimental method was developed for the determination of comprehensive actuator property characteristics. Load controlled thermomechanical cycles were performed to simulate arbitrary working points of the smart material. Recovery stress and energy density characteristics with respect to the recovery ratio and the programmed strain were determined for the tensile and compression case. For tension, actuation stresses of 3 MPa were obtained, while for compression, the actuation stress was below 1 MPa. The determined energy densities were in the range of 0.15 [J/g], which is a competitive value compared to other smart materials.
A finite element modeling technique for the shape memory polymer patch actuation was developed using an adapted *analogy of thermal expansion*. The simulation results agreed very well with experiments. For curved CFRP plates and asymmetric distorted planar plates the shape adjustment could be predicted with an error smaller than 10%. The simulation of a composite waveguide with integrated SMP patches showed the possibility of the modeling and simulation of more complex structurs. Furthermore, the models could be integrated in

an optimization algorithm for the evaluation of the system equations.
An optimization algorithm was developed for the determination of optimal actuator configurations for the shape error minimization. The given asymmetric shape distortions and mass constraints led to the approach of a continuous variation of actuator locations and orientations in the optimization process. Therefore nonlinear optimization was necessary because of nonlinear geometry constraints and the necessary update of the stiffness matrix in every iteration. Gradient based and genetic algorithms were used in combination to obtain optimal results. For representative examples shape error reductions of up to 92% could be achieved in the simulation with optimized actuator configurations.
Practical and operational considerations were carried out. Programming, application and stimulation techniques were investigated. While the programming in a tensile testing machine and a thermal chamber, and the stimulation by heat lamps or a thermal chamber worked very well, the application process led to unsatisfactory results and debonding of the patch actuators was observed. A creep rupture test was performed at different temperatures in which a creep rate of $\dot{\varepsilon}_c = 2 \cdot 10^{-9}[1/s]$ was obtained for 21^oC ambient temperature. For -10^oC no creep could be observed. The use of fillers, polymers with low creep susceptibility, or lower operational loads was suggested to avoid creep. Furthermore, the influence of thermal loads during operation was investigated. It was shown that negative temperature shifts lead to significant shape distortions caused by the actuator patches. It was mentioned that these load could be included in the optimization process for a best performance in the assumed environment.
Three examples including a curved and a planar plate, and a rectangular waveguide were used to show the entire shape adjustment process. For the curved plate shape error reductions of up to 82.7% were achieved in the experiment. For the planar plate with asymmetric distortions a shape error reduction of 58% was achieved using the optimized actuator configuration. For the composite waveguide a shape error reduction of 65% was simulated.

12.2. Critique, Future Work and Outlook

In this work the feasibility and the potential of the post manufacturing process was shown. However, more experiments have to be performed, for a reliable proposition on the achievable shape adjustment quality and especially repeatability. The prevention of the debonding of the actuator patches could not be fully accomplished within this work. The determination of actuation stresses for the compression case could not be performed with the used experimental setup. The inclusion of thermal loads into the optimization algorithm was not performed. From this critique future work can be derived.
A comprehensive investigation of the adhesion between the SMP and composite parts has to be performed to find appropriate surface treatments, adhesives and bonding processes. This is essential for reliable and repeatable shape adjustment results. Many similar shape adjustment experiments have to be performed to show the repeatability and reliability of the process and carry out statistical data of the shape adjustment quality. Furthermore, experiments with more complex parts, such as the waveguide, have to be conducted. Other

applications like space reflectors or structures of physical instruments should be considered also. Actuation stresses for compression, have to be determined by the development of an improved experimental method. Thermal loads should be included in the optimization process. To reduce the susceptibility to creep, the effect of fillers or the performance of other shape memory polymers have to be investigated. The use of shape memory alloys (SMAs) for the introduced method might be investigated, due to their benefitial, higher recovery stresses.
As an outlook further interesting scientific work or applications shall be suggested or pointed out. For the patch actuation the 2D programming could be an interesting option. Mechanisms would have to be developed for a 2D programming, then however, further improvements of the shape adjustment and reduction of actuation mass could be achieved. For the manufacturing of more complex actuator geometries the rapid prototyping (RP) technology could be an attractive option. Especially laser stereo-lithography is able to manufacture polymer parts in arbitrary shape directly using 3D CAD data. This technique would improve and accelerate the actuator manufacturing. Since shape memory polymers are well suited for deployment applications due to their outstanding recovery strains, deployment of space structures should be considered as one of the future applications. Especially if a very high precision is not required the recovery ratios of 99% may be enough for reliable deployment. Another property of shape memory polymers is the pseudo-plasticity, describing the effect of large reversible strain. This property can be used for parts, where changable material properties are necessary. One such application are morphing wings. While a lot of actuation principles and mechanisms were suggested in the past, the wing skin for morphing applications is an unsolved problem. The challenge for these skins are the contradictory requirements of flexibility for morphing and stiffness for carrying the aerodynamic loads. Shape memory polymers could offer a solution since they show stiff properties in their glassy, and flexible properties in their rubbery state, and the pseudo-plasticity for the necessary reversible large deformations.

12.3. Conclusion

With this work the feasibility and potential of the post manufacturing shape adjustment, using shape memory polymers, was demonstrated. Developed tools, such as the experimental method for the determination of actuation properties, the 3D shape measurement techniques, the modelling approach, and the optimization process, can be used in future studies. The application of the suggested methods for creep and debonding reduction, and a certain amount of experimentally verified examples and the resulting statistics, will push the method further into the direction of industrial application.

13. Bibliography

13.1. Literature

[1] Abrahamson, E. R., Lake, M. S., Munshi, N. A., and Gall, K. Shape memory mechanics of an elastic memory composite resin. *Journal of Intelligent Material Systems and Structures 14* (2003), 623–632.

[2] Agrawal, B. N., and Treanor, K. E. Shape control of a beam using piezoelectric actuators. *Smart Materials and Structures 8* (1999), 729–740.

[3] Agrawal, S. K., and Tong, D. Modeling and shape control of piezoelectric actuator embedded elastic plates. *Journal of Intelligent Material Systems and Structures 5* (1994), 514–521.

[4] Aicher, U., Huchler, M., Alberti, M., Haas, C., and Kling, G. Sentinel 1 antenna tile structure design. In *Proceedings of the 11th European Conference on Spacecraft Structurs, Materials and Mechanical Testing (ECSSMMT)* (2009).

[5] Albert, C., and Fernlund, G. Spring-in and warpage of angled composite laminates. *Composites Science and Technology 62* (2002), 1895–1912.

[6] Austin, F., Rossi, M. J., Nostrand, W. V., and Knowles, G. Static shape control for adaptive wings. *AIAA Jounal 32* (1994), 1895–1901.

[7] Baer, G., Wilson, T. S., Matthews, D. L., and Maitland, D. J. Shape-memory behavior of thermally stimulated polyurethane for medical applications. *Journal of Applied Polymer Science 103* (2006), 3882–3892.

[8] Balta, J. A., Bosia, F., Michaud, V., Dunkel, G., Botsis, J., and Manson, J.-A. Smart composites with embedded shape memory alloy actuators and fibre bragg grating sensors: activation and control. *Smart Materials and Structures 14* (2005), 457–465.

[9] Barrett, R., Francis, W., Abrahamson, E., and Lake, M. S. Qualification of elastic memory composite hinges for spaceflight applications. In *47th AIAA/ASME/ASCE/AHS/ASC Structures, Structural Dynamics, and Materials Conference* (2006).

[10] Bills, K. W. J., S., K. H., and Salcedo, F. S. The tensile porperties of highly filled polymers. effect of filler concentration. *Journal of Applied Physics Science 4* (1960), 259–268.

[11] Binette, P., Dano, M.-L., and Gendron, G. Active shape control of composite structures under thermal loading. *Smart Materials and Structures 18*, 025007 (200).

[12] Böl, M., and Reese, S. Computer simulations of temperature induced shape memory polymers by means of a finite element method. In *Proceedings of 5th European Conference on Constitutive Models of rubber* (2008), pp. 93–99.

[13] Bruck, H. A., Moore, C. L., and Valentine, T. L. Repeatable bending actuation in polyurethanes using opposing embedded one-way shape memory alloy wires exhibiting large deformation recovery. *Smart Materials and Structures 11(2002)* (2002), 509–518.

[14] Buehler, W. J., Gilfrich, J. V., and Wiley, R. C. Effects of low temperature phase changes on the mechanical properties of alloys near composition tini. *Journal of Applied Physics 34* (1963), 1475.

[15] Bushnell, D. Control of surface configuration by application of concentrated loads. *AIAA Journal 17* (1979), 71–77.

[16] Cadogan, D. P., Scarborough, S. E., Lin, J. K., and George, H. S. Shape memory composite development for use in gossamer space inflatable structures. In *43th AIAA/ASME/ASCE/AHS/ACC Structures, Structural Dynamics, and Materials Conference and Exhibit* (2002).

[17] Capehart, T. W., Muhammmad, N., and Kia, H. G. Compensating thermoset composite panel deformation using corrective molding. *Journal of Composite Materials 14* (2007), 1675–1701.

[18] Chang, L. C., and Read, T. A. Plastic deformation and diffusionless phase changes in metals the goldcadmium beta phase. *Trans. AIME 191* (1951), 47–52.

[19] Chen, W. M., Wang, D. J., and Li, M. Static shape control employing displacement-stress dual criteria. *Smart Materials and Structures 13* (2004), 468–472.

[20] Chung, T., Romo-Uribe, A., and Mather, P. T. Two-way reversible shape memory in a semicrystalline network. *Macromolecules 41* (2008), 184–192.

[21] Crawley, E. F. Intelligent strucutres for aerospace: A technology overview and assessment. *AIAA Journal 32* (1994), 1689–1699.

[22] Crawley, E. F., and Anderson, E. H. Detailed models of piezoceramic actuation of beams. *Journal of Intelligent Material Systems and Structures 1* (1990), 4–25.

[23] Crawley, E. F., and de Luis, J. Use of piezoelectric actuators as elements of intelligent structures. *AIAA Jounal 25* (1987), 1373 – 1385.

[24] Crawley, E. F., and Lazarus, K. B. Induced strain actuation of isotropic and anisotropic plates. *AIAA Journal 29* (1989), 944 – 951.

[25] Datashvili, L., and Baier, H. Precision deployable shell-membrane antenna reflector for space applications. In *Proceedings of 58th International Astronautical Congress 2008* (2008).

[26] Datashvili, L., Baier, H., Wehrle, E., Kuhn, T., and Hoffmann, J. Large shell-membrane space reflectors. In *51st AIAA/ASME/ASCE/AHS/ASC Structures, Structural Dynamics, and Materials Conference* (2010).

[27] Dawood, M. S. I. S., Iannucci, L., and Greenhalgh, E. S. Three-dimensional static shape control analysis of composite plates using distributed piezoelectric actuators. *Smart Materials and Structures 17* (2008), 025002.

[28] Diani, J., Liu, Y., and Gall, K. Finite strain 3d thermoviscoelastic constitutive model for shape memory polymers. *Polymer Engineering and Science 46* (2006), 486–492.

[29] Domininghaus, H. *Die Kunststoffe und ihre Eigenschaften*. Springer, 1998.

[30] Dong, C. *Dimension Variation Prediction and Control for Composites*. PhD thesis, Florida State University, 2003.

[31] Elspass, W. J., and Flemming, M. *Aktive Funktionsbauweisen - Eine Einführung in die Struktronik*. Springer, 1998.

[32] Fernlund, G., Poursartip, A., Twigg, G., and Albert, C. Residual stress, spring-in and warpage in autoclaved composite parts. In *Proceedings of the14th International Conference on Composites 2002* (2002).

[33] Fernlund, G., Rahman, N., Courdji, R., Bresslauer, M., Poursartip, A., Willden, K., and Nelson, K. Experimental and numerical study of the effect of cure cycle, tool surface, geometry, and lay-up on the dimensional fidelity of autoclave-processed composite parts. *Composites Part A 33* (2002), 341–351.

[34] Foss, G. C., and Haugse, E. D. Using modal test results to develop strain to displacement transformation. In *Proceedings 13th IMAC* (1995), pp. 112–118.

[35] Friebele, E., Askins, C., Bosse, A., Kersey, A., Patrick, H., Pogue, W., Putnam, M., Simon, W., Tasker, F., Vincent, W., and Vohra, S. Optical fiber sensors for spacecraft applications. *Smart Materials and Structures 8* (1999), 813–838.

[36] Gall, K., Dunn, M. L., and Liu, Y. Internal stress storage in shape memory polymer nanocomposites. *Applied Physics Letters 85* (2004), 290–292.

[37] Gall, K., Mikulas, M., Munshi, N., Beavers, F., and Tupper, M. Carbon fiber reinforced shape memory polymer composites. *Journal of Intelligent Material Systems and Structures 11* (2000), 877–886.

[38] Gausepohl, H., and Gellert, R. *Kunststoff Handbuch 4*. Hanser Verlag, 1996.

[39] Ghosh, K., and Batra, R. C. Shape control of plates using piezoeceramic elements. *AIAA Journal, Technical Notes 33* (1995), 1354–1357.

[40] Giesecke, P. *Dehnungsmessstreifentechnik - Grundlagen und Anwendungen in der industriellen Messtechnik*. Vieweg, 1994.

[41] Grellmann, W., and Seidler, S. *Kunststoffprfung*. Hanser Fachbuchverlag, 2005.

[42] Ha, S. K., Keilers, C., and Chang, F.-K. Finite element analysis of composite structures containing distributed piezoceramic sensors and actuators. *AIAA Journal 30* (1992), 772 – 780.

[43] Habenicht, G. *Kleben*. Springer Verlag, 2006.

[44] Haftka, R. T., and Adelman, H. M. An analytical investigation of shape control of large space structures by applied temperatures. *AIAA Journal 23* (1983), 450–457.

[45] Huang, C. K., and Yang, S. Y. Study on accuracy of angled advanced composite tools. *Materials and Manufacturing Processes 12* (1997), 473–486.

[46] Irschik, H. A review on static and dynamic shape control of structures by piezoelectric actuation. *Engineering Structures 24* (2002), 5–11.

[47] Jain, L. K., and Mai, Y.-W. On residual stress induced distortions during fabrication of composite shells. *Jorunal of Reinforced Plastics and Composites 15* (1996), 793–805.

[48] Ji, F., Zhu, Y., Hu, F., Liu, Y., Yeung, L.-Y., and Ye, G. Smart polymer fibers with shape memory effect. *Smart Materials and Structures 15* (2006), 1547–1554.

[49] Jin, D., Sun, D., Chen, W., Wang, D., and Tong, L. Static shape control of repetitive structures integrated with piezoelectric actuators. *Smart Materials and Structures 14* (2005), 1410–1420.

[50] Johnston, A., Vaziri, R., and Poursartip, A. A plane strain model for process-induced deformation of laminated composite structures. *Journal of Composite Materials 35* (2001), 1435–1469.

[51] Jones, R. T., Bellemore, D. G., Berkoff, T. A., Sirkis, J. S., Davis, M. A., Putnam, M. A., Friebele, E. J., and Kersey, A. D. Determination of cantilever plate shapes using wavelength division multiplexied fiber bragg grating sensors and a least-squares strain-fitting algorithm. *Smart Materials and Structures 7* (1998), 178–188.

[52] Jr., D. A. D., and Smith, L. V. Isolating components of processing induced warpage in laminated composites. *Journal of Composite Materials 36* (2002), 2407–2419.

[53] Kabashima, S., Ozaki, T., and Takeda, N. Structural health monitoring using fbg sensor in space environment. In *Proceeding of the Smart Structures and Materials 2001: Industrial and Commercial Applications of Smart Structures Technologies* (2001).

[54] Kang, L., Kim, D., and Han, J. Estimation of dynamic structural displacements using fiber bragg grating strain sensors. *Journal of Sound and Vibration 305* (2007), 534–542.

[55] Kirby, G. C., and Lindner, D. K. Optimal sensor layout for shape estimation from strain sensors. In *Smart Materials and Structures 1995: Smart Sensing, Processing and Instrumentation* (1995).

[56] Koconis, D. B., Kollr, L. P., and Springer, G. S. Shape control of composite plates and shells with embedded actuators. ii desired shape specified. *Journal of Composite Materials 28* (1994), 459–482.

[57] Kukula, S., Saito, M., Kikuchi, N., Shimeno, T., and Muranka, A. Warpage in incection molded frp: Establishing causes and cures using numerical analysis.

[58] Lake, M. S., and Campbell, D. The fundamentals of designing deployable structures with elastic memory composites. In *2004 IEEE Aerospace Conference Proceedings* (2004).

[59] Lan, X., Liu, Y., Wang, X., Leng, J., and Du, S. Fiber reinforced shape-memory polymer composite and its application in a deployable hinge. *Smart Materials and Structures 18* (2009), 024002.

[60] Lan, X., Wang, X., Lu, H., Liu, Y., and Leng, J. Shape recovery performances of a deployable hinge fabricated by fiber-reinforced shape memory polymer. In *Smart Structures and Materials - Behavior and Mechanics of Multifunctional Materials and Composites III* (2009).

[61] Lang, M., Baier, H., and Datashvili, L. High presision thin shell reflectors - design concepts, structural optimization and shape adjustment techniques high precision thin shell reflectors - design concepts, structural optimization and shape adjustment techniques. In *Proceedings of the European Conference of Space Structures* (2005).

[62] Lendlein, A., and Kelch, S. Formgedächtnispolymere. *Angewandte Chemie 114* (2002), 2139–2162.

[63] Leng, J., and Du, S. *Shape Memory Polymers and Multifunctional Composites*. CRC Press, Taylor & Francis Group, 2010.

[64] Leng, J., Liu, Y., and Lan, X. Advance in shape-memory polymer actuation. In *Proc. SPIE Conf. on Smart Structures and Materials 2009, San Diego* (2009), no. 7287.

[65] Leng, J., Lv, H., Liu, Y., and Du, S. Electroactivate shape-memory polymer filled with nanocarbon particles and short carbon fibers. *Applied Physics Letters 91* (2007), 144105.

[66] Leng, J. S., Huang, W. M., Lan, X., Liu, Y. J., and Du, S. Y. Significantly reducing electrical resistivity by forming conductive ni chains in a polyurethane shape memory polymer-carbon-black composite. *Applied Physics Letters 92* (2008), 204101.

[67] Leng, J. S., Lan, X., Liu, Y. J., Du, S. Y., Huang, W. M., Liu, N., Phee, S., and Yuan, Q. Electrical conductivity of thermoresponsive shape-memory polymer with embedded micron sized ni powder chains. *Applied Physics Letters 92* (2008), 014104.

[68] Li, C.-J. High-precision measurement of tool-tip displacement using strain gauges in precision flexible line boring. *Mechanical Systems and Signal Processing 13* (1999), 531–546.

[69] Lin, C.-C., and Hsu, C.-Y. Satic shape control of smart beam plates laminated with sine sensors and actuators. *Smart Materials and Structures 8* (1999), 519–530.

[70] Lin, J. K., Knoll, C. F., and Willey, C. E. Shape memory rigidizable inflatable (ri) structures for large space systems applications. In *47th AIAA/ASME/ASCE/AHS/ACC Structures, Structural Dynamics, and Materials Conference and Exhibit* (2006).

[71] Liu, C., Qin, H., and Mather, P. T. Review of progress in shape-memory polymers. *Journal of Material Chemistry 17* (2007), 1543–1558.

[72] Liu, Y., Gall, K., Dunn, M. L., and McCluskey, P. Thermomechanical recovery couplings of shape memory polymers in flexure. *Smart Materials and Structures 12* (2003), 947–954.

[73] Liu, Y., Ken Gall, M. L. D., Greenberg, A. R., and Diani, J. Thermomechanics of shape memory polymers: Uniaxial experiments and constitutive modeling. *International Journal of Plasticity 22* (2006), 279–313.

[74] Lively, P. S., Atalla, M. J., and Hagood, N. W. Investigation of filgering techniques applied to the dynamic shape estimation problem. *Smart Materials and Structures 10* (2001), 264–272.

[75] Lundin, R., Nathrath, N., Fasold, D., Trmper, M., Letschnik, J., and Walter, U. A compact and lightweight inter-satellite antenna for s-band. In *Proceedings of the second European conference on antennas and propagation (EUCAP 2007)* (2007).

[76] Manzo, J., and Garcia, E. Demonstration of an in situ morphing hyperelliptical cambered span wing mechanism. *Smart Materials and Structures 19* (2010), 025012.

[77] Mckenzie, I., and Karafolas, N. Fiber optic sensing in space structures: The experience of the european space agency. In *17th International Conference on Optical Fibre Sensors* (2005).

[78] Meirovitch, L. *Dynamics and control of structures*. John Wiley and Sons, Inc., 1990.

[79] Meng, Q., Hu, J., and Yeung, L. An electro-active shape memory fibre by incorporating multi-walled carbon nanotubes. *Smart Materials and Structures 16* (2007), 830–836.

[80] Mueller, U. C. *Structural Monitoring and Displacement Field Estimation based on Distributed Fiber Bragg Grating Sensors*. PhD thesis, Technische Universitt Mnchen, 2010.

[81] Mueller, U. C., and Baier, H. Strain and temperature measurement with fiber optic sensors in composite structures. In *GESA Symposium 2005* (2005).

[82] Mueller, U. C., Zeh, T., Koch, A. W., and Baier, H. Fiber optic bragg grating sensors for high-precision structural deformation control in optical systems. In *Smart Structrues and Materials 2006 - Smart Sensor Monitoring and Applications* (2006).

[83] Murayama, H., Kageyama, K., Naruse, H., Shimada, A., and Uzawa, K. Application of fiber-optic distributed sensors to health monitoring for full-scale composite structures. *Journal of Intelligent Material Systems and Structures 14* (2003), 3–13.

[84] Nguyen, T. D., Qi, H. J., Castro, F., and Long, K. N. A thermoviscoelastic model for amorphous shape memory polymers - incorporating structural and stress relaxation. *Journal of the Mechanics and Physics of Solids 56* (2008), 2792–2814.

[85] Ni, Q.-Q., sheng Zhang, C., Fu, Y., Dai, G., and Kimura, T. Shape memory effect and mechanical properties of carbon nanotube/shape memory polymer nanocomposites. *Composite Structures 81* (2007), 176–184.

[86] Nielsen, L. E. Cross-linking - effect on physical properties of polymers. *J. of Macromolecular Science - Reviews Macromolecualar Chemistry C3* (1969), 69–103.

[87] O, H. K., Y, F., C, J. D., and S, K. B. Photosensitivity in optical fiber waveguides: Application to reflection filter fabrication. *Applied Physics Letter 32* (1978), 647ff.

[88] Olivier, P., and Cottu, J. P. Optimisation of the co-curing of two different composites with the aim of minimising residual curing stress levels. *Composites Science and Technology 58* (1998), 645–651.

[89] Peng, F., Hu, Y.-R., and Nguyen, A. Development of ga-based control systm for active shape control of inflatable space structures. In *Proceedings of hte 2005 IEEE Conference on Control Applications* (2005).

[90] Pisoni, A. C. Displacements in a vibrating body by strain gauge measurements. In *Internatinal Conference on Modal Analysis* (1995).

[91] Pons, J. *Emerging Actuator Technologies - A Micromechanic Approach*. KLUWER ACADEMIC PUBLISHERS, 2002.

[92] Prasatya, P., McKenna, G. B., and Simon, S. L. A viscoelastic model for predicting isotropic residual stresses in thermosetting materials: effects of processing parameters. *Composite Materials 35* (2001), 826–848.

[93] Preumont, A. *Vibration Control of Active Structures - An Introduction*. WILEY, 2005.

[94] Qi, H. J., Nguyen, T. D., Castro, F., Yakacki, C. M., and Shandas, R. Finite deformation thermo-mechanical behavior of thermally induced shape memory polymers. *Journal of the Mechanics and Physics of Solids 56* (2007), 1730–1751.

[95] Radford, D. W. Volume fraction gradient induced warpage in curved composite plates. *Composite Engineering 5* (1995), 923–934.

[96] Radford, D. W., and Diefendorf, R. J. Shape instabilities in composites resulting from laminate anisotropy. *Journal of Reinforced Plastics and Composites 12* (1993), 58–75.

[97] Radford, D. W., and Rennick, T. S. Separating sources of manufacturing distortion in laminated composites. *Journal of Reinforced plastics and composites 19* (2000), 621–641.

[98] Ratna, D., and Karger-Kocsis, J. Recent advances in shape memory polymers and composites - a review. *Journal of Material Science 43* (2008), 254–269.

[99] Roose, S., Stockman, Y., Rochus, P., Kuhn, T., Lang, M., Baier, H., Langlois, S., and Casarosa, G. Optical methods for non contact measurements of membranes. *Acta Astronautica 65* (2009), 1317–1329.

[100] Salama, M., Umland, J., Bruno, R., and Garba, J. Shape adjustment of precision truss structures: analytical and experimental validation. *Smart Materials and Structures 2* (1993), 240 – 248.

[101] Sofla, A. Y. N., Elzey, D. M., and Wadley, H. N. G. Shape morphing hinged truss structures. *Smart Materials and Structures 18* (2009), 065012.

[102] Song, G., Kelly, B., and Agrawal, B. N. Active position control of s a shape memory alloy wire actuated composite beam. *Smart Materials and Structures 9* (2000), 711–716.

[103] Song, G., Kelly, B., Agrawal, B. N., Lam, P. C., and Srivatsan, T. S. Application of shape memory alloy wire actuator for perecision position control of a composite beam. *Journal of Materials Engineering and Performance 9* (2000), 330–333.

[104] Spröwitz, T., Kleineberg, M., and Tessmer, J. Prozesssimulation in der faserverbundherstellung - spring-in. *NAFEMS-Magazin 9* (2008), 43–52.

[105] Sun, D., and Tong, L. Adhesive element modelling and weighted static shape control of composite plates with piezoelectric actuator patches. *International Journal for Numerical Methods in Engineering 60* (2004), 1911–1932.

[106] Sun, D., and Tong, L. Static shape control of structures using nonlinear piezoelectric actuators with energy constraints. *Smart Materials and Structures 13* (2004), 1059–1068.

[107] Svanberg, J. M. Prediction of shape distortions for a curved composite c-spar. *Reinforced plastics and composites 24* (2005), 323–339.

[108] Svanberg, J. M., and Holmberg, J. A. An experimental investigation on mechanisms for manufcturing induced shape distortions in homogeneous and balanced laminates. *Composites Part A 32* (2001), 827–838.

[109] Svanberg, J. M., and Holmberg, J. A. Pediction of shape distortions part 1. fe-implementation of a path dependent constitutive model. *Composites Part A 35* (2004), 711–721.

[110] Svanberg, J. M., and Holmberg, J. A. Prediction of shape distortions part ii. experimental validation and analysis of boundary conditions. *Composites Part A 35* (2004), 723–734.

[111] Sweeting, R., Liu, X. L., and Paton, R. Prediction of processing-induced distortion of curved flanged composite laminates. *Composite Structures 57* (2002), 79–84.

[112] Tabata, M., and Natori, M. C. Active shape control of a deployable space antenna reflector. *Journal of Intelligent Material Systems and Structures 7* (1996), 235–240.

[113] Tan, D. Compensation for thermal deformation of paraboloid shell using distributed structural actuation. *International Journal of solids and structures 38* (2001), 2893 – 2919.

[114] Tanaka, N., Okabe, Y., and Takeda, N. Temperature-compensated strain measurement using fiber bragg grating sensors embedded in composite laminates. *Smart Materials and Structures 12* (2003), 940–946.

[115] Tobushi, H., Hara, H., Yamada, E., and Hayashi, S. Thermomechanical properties in a thin film of shape memory polymer of polyurethane series. *Smart Materials and Structures 5* (1996), 483–491.

[116] Tobushi, H., Hashimoto, T., Hayashi, S., and Yamada, E. Thermomechanical constitutive modeling in shape memory polymer of polyurethane series. *Intelligent Material Systems and Structures 8* (1997), 711–718.

[117] Tobushi, H., Hayashi, S., and Kojima, S. Mechanical properties of shape memory polymer of polyurethane series (basic characteristics of stress-strain-temperature relationship. *JSME International Journal 35* (1992), 296–302.

[118] Tupper, M., Gall, K., and Jr., M. M. Developments in elastic memory composite materials for spacecraft deployable structures. In *Proceedings of IEEE Aerospace Conference 2001* (2001), no. 5 2541-2547.

[119] Tuttle, M. E., Koehler, R. T., and Keren, D. Controlling thermal stresses in comosites by means of fiber prestress. *Composite Materials 30* (1996), 486–502.

[120] Twigg, G., Poursartip, A., and Fernlund, G. An experimental method for quantifying tool-part shear interaction during composites processing. *Composites science and technology 63* (2003), 1985–2002.

[121] Twigg, G., Poursartip, A., and Fernlund, G. Tool-part interaction in composites processing. part i: experimental investigation and analytical model. *Composites Part A 35* (2004), 121–133.

[122] Twigg, G., Poursartip, A., and Fernlund, G. Tool-part interaction in composites processing. part ii: numerical modelling. *Composites Part A 35* (2004), 135–141.

[123] Udd, E. Fiber grating sensors for structural health monitoring of aerospace structures. In *Smart Structures and Materials 2006 - Smart Sensor Monitoring Systems and Applications* (2006).

[124] Vanderplaats, G. N. *Multidiscipline Design Optimization*. 2007.

[125] Wang, Z., huan Chen, S., and Han, W. The static shape control for intelligent structures. *Finite Elements in analysis and design 26* (1997), 303–314.

[126] Wei, Z. G., and Sandstroem, R. Review - shape-memory materials and hybrid composites for smart systems: Part i shape-memory materials. *Journal of materials science ee* (1998), 3743–3762.

[127] Wei, Z. G., and Sandstroem, R. Review - shape-memory materials and hybrid composites for smart systems: Part ii shape-memory hybrid composites. *Journal of materials science ee* (1998), 3763–3783.

[128] White, S. R., and Hahn, H. T. Process modeling of composite materials: Residual stress development during cure. part i. model formulation. *Journal of Composite Materials 26* (1992), 2402–2422.

[129] White, S. R., and Hahn, H. T. Cure cycle optimization for the reduction of processing-induced residual stresses in compsite materials. *Composite Materials 27* (1993), 1352–1378.

[130] Wu, X., Liu, Y., and Leng, J. Investigation of mechanical behavior of epoxy shape memory polymers. In *Smart Structures and Materials - Behavior and Mechanics of Multifunctional Materials and Composites III* (2009).

[131] Yang, J.-L., Zhang, Z., Schlarb, A. K., and Friedrich, K. On the characterization of tensile creep resistance of polyamide 66 nanocomposites. part i. experimental results and general discussion. *Polymer Engineering and Science 47* (2006), 2791–2801.

[132] Yates, B., McCalla, B. A., Phillips, L. N., Kingston-Lee, D. M., and Rogers, K. F. The thermal expansion of carbon fibre-reinforced plastics part 5: the influence of matrix curing characteristics. *Jorunal of Material Science 14* (1979), 1207–1217.

[133] Yi, S., Hilton, H. H., and Ahmad, M. F. A finite element approach for cure simulation of thermosetting matrix composites. *Computers and Structures 64* (1997), 383–388.

[134] Yin, W., Fu, T., Liu, J., and Leng, J. Structural shape sensing for variable camber wing using fbg sensors. In *Proc. SPIE Conf. on Smart Structures and Materials 2009, San Diego* (2009), no. 7292.

[135] Yu, K., Yin, W., Sun, S., Liu, Y., and Leng, J. Design and analysis of morphing wing based on smp composite. In *Smart Structures and Materials - Behavior and Mechanics of Multifunctional Materials and Composites III* (2009).

[136] Zhou, B., Liu, Y., Wang, Z., and Leng, J. Modeling the shape memory effect of shape memory polymer. In *Second International Conference on Smart Materials and Nanotechnology in Engineering* (2009).

[137] Zhu, Q., Geubelle, P. H., Li, M., and III, C. L. T. Dimensional accuracy of thermoset composites: Simulation of process-induced residual stresses. *Composite Materials 35* (2001), 2171–2205.

[138] Zhu, Y., and Geubelle, P. H. Dimensional accuracy of thermoset composites: Shape optimization. *Journal of Composite Materials 36* (2002), 647–672.

13.2. Own Publications - Author and Co-Author

[139] Baier, H., Datashvili, L., and Rapp, S. Functional membranes - a basis for satellite architectures of the future. In *European Conference on Aerospace Science (CEAS)* (2007).

[140] Baier, H., Datashvili, L., and Rapp, S. Enhancing space satellite performance by integrating smart sensors and actuators for sensing and shape morphing. In *2nd International Conference on Smart Materials and Nanotechnology in Engineering* (2009).

[141] Baier, H., Datashvili, L., Rapp, S., and Hoffmann, J. Shape morphing and control of flexible surfaces for aerospace applications. In *International Scientific Conference on Advanced Lightweight Structures and Reflector Antennas* (2009).

[142] Baier, H., Datshivili, L., and Rapp, S. Smart membranes for aerospace applications. In *Proc. of the Int. Conf. on Smart Materials and Nanotechnology in Engineering* (2007).

[143] Baier, H., Mueller, U., and Rapp, S. Fiber optic sensor networks in smart structures. In *Smart Structures and NDE 2008 - Smart Sensor Phenomena, Technology, Networks and Systems* (2008), no. 6933-09.

[144] Baier, H., Mueller, U., and Rapp, S. Fibre optic sensor networks for monitoring displacement and temperature fields in smart structures. In *Proc. SPIE Conf. on Smart Structures and Materials* (2008).

[145] Baier, H., and Rapp, S. In-orbit monitoring and re-adjustment of satellite structures. In *European Conference on Aerospace Science (CEAS)* (2007).

[146] Nathrath, N., Trümper, M., Rapp, S., Harder, J., and Walter, U. Manufacturing technologies for lisa. In *3rd European Conference on Antennas and Propagation (EUCAP)* (2009).

[147] Rapp, S. Deformation field estimation using fiber bragg gratings. In *European Conference on Aerospace Science (CEAS)* (2007).

[148] Rapp, S., and Baier, H. New materials and structural concepts for compact waveguide antennas including shape memory polymers for actuation. In *European Conference of Spacecraft Structures, Materials and Mechanical Testing* (2009).

[149] Rapp, S., and Baier, H. Reconstruction of temperature and displacement fields in satellite sandwich panels based on integrated fiber optic sensors. In *Proc. SPIE Conf. on Smart Structures and Materials 2009, San Diego* (2009).

[150] Rapp, S., and Baier, H. Determination of recovery energy densities of shape memory polymers via closed loop, force controlled recovery cycling. *Smart Materials and Structures 19* (2010), 045018.

[151] Rapp, S., and Baier, H. Integrated fiber optic sensors for hot spot detection and temperature field reconstruction in satellites. *Smart Materials and Structures 19* (2010), 075007.

[152] Rapp, S., and Baier, H. Shape memory polymer actuators for shape adjustment of fiber comosite parts. In *Proc. of Actuator 2010, 12 International Conference on New Actuators* (2010), no. P80.

[153] Rapp, S., Baier, H., Zuknik, K.-H., and Reutlinger, A. Temperature monitoring in satellite sandwich panels using integrated fiber optic sensors. In *ESA workshop on Fiber Optic Sensors for Space Application* (2009).

[154] Rapp, S., Kang, L., Han, J., Mueller, U., and Baier, H. Displacement field estimation for a 2-dimensional structure using fiber bragg grating sensors. *Smart Materials and Structures 18* (2009).

[155] Rapp, S., Kang, L., Mueller, U., Han, J.-H., and Baier, H. Dynamic shape estimation by modal approach using fiber bragg grating strain sensors. In *Smart Structures and Materials 2007 - Sensors and Smart Structures Technologies* (2007), vol. 6529.

[156] Rapp, S., Lang, M., Letschnik, J., Nathrath, N., Trümper, M., Fasold, D., Walter, U., Baier, H., and Krmer, L. Cfk struktur einer leichten intersatelliten antenne (lisa). In *Proc. der DGLR Tagung* (2008).

[157] Rapp, S., Zuknik, K., Reutlinger, A., and Baier, H. A demonstrator for an integrated temperature sensor network for satellite panels. In *Proceedings of the 4th European Workshop on Structural Health Monitoring* (2008), no. p. 89-96.

[158] Rapp, S., Zuknik, K., Reutlinger, A., and Baier, H. An integrated temperature sensor network for satellite sandwich panels. In *Proceedings of the IAC Congress 2008* (2008), no. IAC-08-C2.5.4.

[159] Reutlinger, A., Glier, M., Zuknik, K.-H., Hoffmann, L., Mueller, M., Rapp, S., Kurvin, C., Ernst, T., Mckenzie, I., and Karafolas, N. Fiber optic sensing for telecommunication satellites. In *SPIE - 18th Optical Fiber Sensing* (2008).

13.3. Student Projects Supervised by Author

[160] Endler, S. Expansion of the structural concept and finite element analysis of a lightweight intersatellite antenna lisams. Diploma thesis, Technische Universität München, 2009.

[161] Ferber, C. Experimental determination of acutation performance maps for shape memory polymers. Semester thesis, Technische Universität München, 2009.

[162] Ferber, C. Simulation and experimental investigation of warpage reduction in composite parts using shape memory polymer actuator patches. Diploma thesis, Technische Universität München, 2010.

[163] Graf, E. Investigation of the adhesion of shape memory polymer patches on cfrp surfaces. Semester thesis, Technische Universität München, 2010.

[164] Harikrishnan, J. Characterization of shape memory polymers and composites. Semester thesis, Technische Universität München, 2008.

[165] Hörmann, P. Simulation of the force introduction of shape memory polymer actuator patches into thin-walled cfrp parts. Semester thesis, Technische Universität München, 2009.

[166] Ickes, A. Thermo-elastic deformation of asymmetric laminates. Semester thesis, Technische Universität München, 2009.

[167] Kim, S. Experimental investigation of blocking and actuator stresses of shape memory polymers. Semester thesis, Technische Universität München, 2010.

[168] Knyrim, T. Shape optimization of distorted composite parts using smp actuator patches. Semester thesis, Technische Universität München, 2011.

[169] Lässig, H. Design of a demonstrator for the visualization of the shape memory effect of polymers. Semester thesis, Technische Universität München, 2008.

[170] Loos, C. Experimental determination of actuation figures of merit of an shape memory polymer. Semester thesis, Technische Universität München, 2008.

[171] Murtomäki, J. Constructive improvement of a fiber optic temperature sensor transducer. Bachelor thesis, Technische Universität München, 2010.

[172] Nixdorf, D. Variation of the fiber volume fraction in the interface layer of cfrp-metal-composites for the reduction of thermal stresses. Semester thesis, Technische Universität München, 2009.

[173] Oezbek, M. Thermo-elastic analysis of a hybrid cfrp-copper waveguide for an intersatellite link antenna (lisa). Semester thesis, Technische Universität München, 2009.

[174] Patscheider, J. Constitutive model for shape memory polymers for simulation using finite elements. Semester thesis, Technische Universität München, 2009.

[175] Roos, C. Investigation of the influence of the adhesive layer on the actuatorpatch-structure-interaction using fem. Semester thesis, Technische Universität München, 2009.

[176] Schröter, J.-W. Modelling and experimental investigation of relaxation effects of shape memory polymers. Semester thesis, Technische Universität München, 2010.

[177] Stakelies, M. Parameter survey of a hyrbrid copper-cfrp horn of a satellite antenne using finite element analysis. Semester thesis, Technische Universität München, 2010.

[178] Weichenrieder, C. Literature research about warpage and spring-in - causes, modelling, simulation and counter measures. Semester thesis, Technische Universität München, 2009.

[179] Weidner, P. Improvement of the design and detailled finite element analysis of a lightweight in-tersatellite antenna. Diploma thesis, Technische Universität München, 2010.

[180] Weiss, M. Investigation of the influence of integrated heating wires on the load capacity of shape memory parts. Semester thesis, Technische Universität München, 2010.

A. Appendix

A.1. Test Sample Geometries

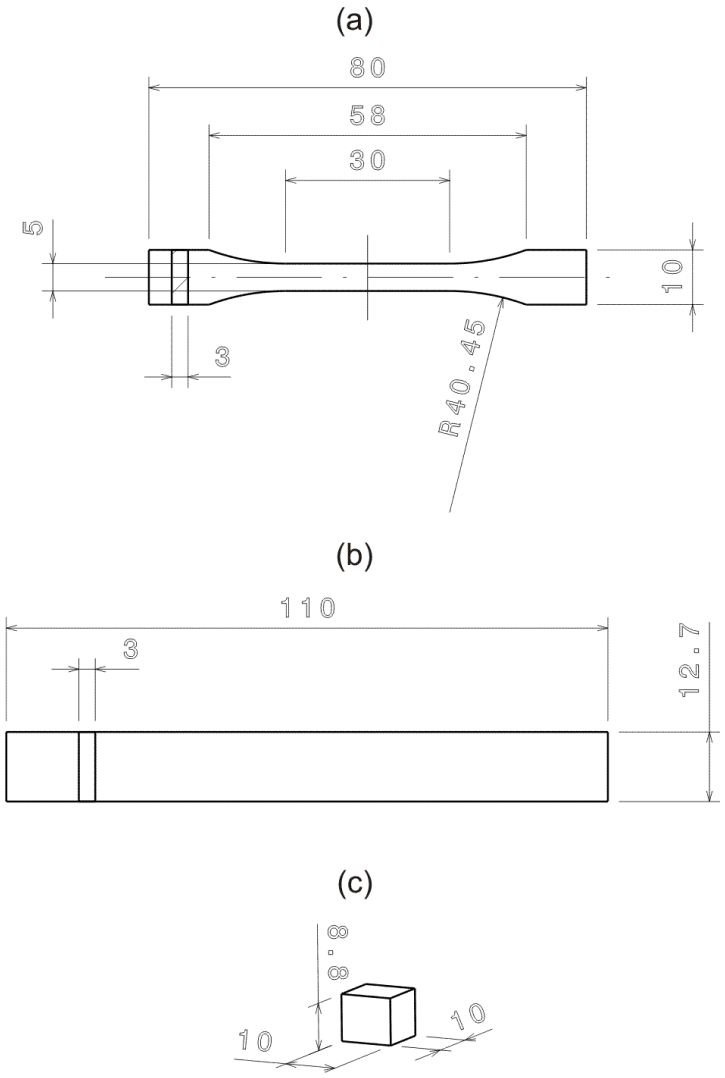

Figure A.1.: Sample geometries for the determination of actuation properties: (a) Sample regarding DIN EN ISO 527-1BA; (b) Multipurpose sample [41]; (c) Non standard compression sample.

A.2. Photogrammetry Camera Settings

Table A.1.: Camera settings for dot projection photogrammetry.

Setting	Value
aperture	8
focus	2 [m]
sensitivity	ISO 400
white balance	A
shutter speed	1/60 [s]
long exposure	active

Table A.2.: Experimental set up for photogrammetry measurement.

Setting	Value
Distance of projector to object	1.3 [m]
Distance of camera to object	1.3 - 2.5 [m]
Target size	7 [mm]
Target spacing	10 [mm]
Background color	white

A.3. Test parameters for the determination of the actuation properities.

Table A.3.: Test parameters for the determination of actuation properties.

Parameter	Symbol	Tension	Compression
Programming temperature	T_{prog}	80 $[^oC]$	80 $[^oC]$
Storage temperature	T_S	RT	RT
Storage time	t_S	120-180 [s]	120-180 [s]
Recovery temperature	T_r	50-90 $[^oC]$	50-90 $[^oC]$
Programming strain rate	$\dot{\varepsilon}$	62 [mm/min]	5 [mm/min]
Programming strain	ε_{prog}	50-233 %	20-80 %
Recovery stress range	R_{sigma}	0.01 [MPa]	0.005 [MPa]
Machine speed during recovery	v	2-50 [mm/min]	0.5-2 [mm/min]

A.4. Material Data

Table A.4.: Material data for CFRP UD ply.

Property	Material data
E_x	120000 [MPa]
E_y	8440 [MPa]
E_z	8440 [MPa]
ν_{xy}	0.3
ν_{xz}	0.3
ν_{yz}	0.3
G_{xy}	4615 [MPa]
G_{yz}	3246 [MPa]
G_{xz}	4615 [MPa]

Table A.5.: Material data for SMP used for finite element modeling.

Property	Material data
E_{eff}	3.2-5.4[MPa]
ν_{xy}	0.0-0.4
α_x	109.5 $[\cdot 10^{-6} 1/K]$
α_y	0 $[\cdot 10^{-6} 1/K]$
α_z	0 $[\cdot 10^{-6} 1/K]$

Table A.6.: Material data for adhesive used for finite element modeling

Property	Material data
E	3.5 [MPa]
ν_{xy}	0.45

A.5. Adhesion Samples

Table A.7.: Adhesives and their adhesion properties.

Nr.	Mounting	Ad.	Temp.	Heating Rate	SMP	CFRP
1	-	**1**	**80^o**	-	**sand paper**	**peel ply**
2	*45^o*	1	80^o	-	sand paper	peel ply
3	*60^o*	1	80^o	-	sand paper	peel ply
4	*75^o*	1	80^o	-	sand paper	peel ply
5	-	1	$< 80^o$	*1^o/min*	sand paper	peel ply
6	-	1	$< 80^o$	*10^o/min*	sand paper	peel ply
7	-	**1**	**80^o**	-	**sand paper**	**peel ply**
8	-	*2*	80^o	-	sand paper	peel ply
9	-	*2*	80^o	-	sand paper	peel ply
10	-	*3*	80^o	-	sand paper	peel ply
11	-	*3*	80^o	-	sand paper	peel ply
12	-	*4*	80^o	-	sand paper	peel ply
13	-	*4*	80^o	-	sand paper	peel ply
14	-	1	*50^o*	-	sand paper	peel ply
15	-	1	*60^o*	-	sand paper	peel ply
16	-	1	*70^o*	-	sand paper	peel ply
17	-	**1**	**80^o**	-	**sand paper**	**peel ply**
18	-	1	*90^o*	-	sand paper	peel ply
19	-	1	80^o	-	sand paper	*peel ply - sand blasted*
20	-	1	80^o	-	sand paper	*peel ply - roughend*
21	-	**1**	**80^o**	-	**sand paper**	**peel ply**
22	-	1	80^o	-	*sand blasted*	peel ply
23	-	1	80^o	-	*roughend*	peel ply
24	-	1	80^o	-	sand paper	*w/o peel ply*
25	-	1	80^o	-	sand paper	*w/o peel ply - roughend*
26	-	1	80^o	-	sand paper	*w/o peel ply - sand blasted*

Standard parameters, *Varied parameters*

A.6. Optimization Parameters

Table A.8.: Optimization parameters and optimization results.

No.	N	GA PopSize	GA Elite	Gen	RMS_{GA} $[\mu m]$	$mass_{GA}$	Iter	RMS $[\mu m]$	mass $[mm^2]$
220996	2	20	default	7	80	1231	38	52	1500
221146	3	30	3	7	90	1674	58	55	1500
221141	4	60	4	7	96	1442	26	58	1489
221142	5	75	5	7	83	2966	14	73	1471

A.7. Veriflex Data Sheets

Veriflex® Shape Memory Polymer Resin

Description:

Veriflex® is a two-part, fully formable, thermoset shape memory polymer (SMP) resin system.

Cured Veriflex has unique "shape memory" properties. When heated above its activation temperature (T_g), Veriflex changes from a rigid plastic to a flexible elastomer. In its elastic state, it can be twisted, pulled, bent, and stretched, reaching up to 200% elongation. If cooled while constrained in this new shape, the polymer hardens and can maintain its new shape. When heated, unconstrained, above its T_g, this polymer returns to the shape in which it was cured. This process can be repeated indefinitely without loss of the memory shape or degradation of the material.

Standard Veriflex resin is engineered with a T_g of 62 °C (144 °F). Uncured Veriflex resin has a low viscosity that makes it easy for RTM or VARTM processing and composite fabrication.

Typical applications include customizable and reusable molds, toys, architectural applications, furniture, deployment mechanisms, containers, shipping and packaging, thermal sensors, and actuators.

Features & Benefits:

- Unique shape memory properties
- Can be reshaped and recover original shape repeatedly
- Reversibly transforms from rigid polymer to soft elastomer
- Up to 200% elongation in elastic state
- Toughened polymer for increased durability
- Low viscosity and easily processable (uncured resin)

866.341.2744 x165 huelskampsr@crg-industries.com crg-industries.com

Cured Material Properties:

Property	Value	Unit	Value	Unit	Method
Mechanical					
Tensile strength	23.0	MPa	3,330	psi	ASTM D638
Tensile modulus	1.24	GPa	180	Ksi	ASTM D638
Tensile elongation to break	3.90	%			ASTM D638
Flexural strength	37.1	MPa	4,600	psi	ASTM D790
Flexural modulus	1.24	GPa	180	Ksi	ASTM D790
Compressive strength	32.4	MPa	4,700	psi	ASTM D695
Compressive elastic modulus	1.45	GPa	210	Ksi	ASTM D695
Thermal					
Glass transition temperature (T_g)	62	°C	144	°F	
Thermal conductivity at 18.9 °C (65 °F)	0.17	W/(m*K)	0.10	Btu*ft/(h*ft^2* °F)	
Material density	0.92	g/cm^3	57.4	lbs/ft^3	
Max service temperature	130	°C	266	°F	

Unless otherwise noted, all measurements were taken below the T_g of Veriflex.

Curing Conditions:

Veriflex must be cured in a closed system mold. Below is a suggested cure cycle:

- Ramp from room temperature to 75 °C (167 °F) with a heating rate of 1 °C (1.65 °F)/minute
- Soak at 75 °C (167 °F) for 3 hours
- Ramp from 75 °C (167 °F) to 90 °C (194 °F) with a heating rate of 15 °C/180 minutes
- Ramp from 90 °C (194 °F) to 110 °C (230 °F) with a heating rate of 20 °C/120 minutes
- Do not heat above 135 °C (275 °F)

866.341.2744 x165 huelskampsr@crg-industries.com crg-industries.com

Storage:

Resin should be stored in tightly closed containers in a flammables storage cabinet. Resin should be kept away from sources of ignition and strong oxidizers.

Handling & Safety Precautions:

Uncured, this material should be handled using a NIOSH/OSHA approved respirator, and with a fume hood or mechanical exhaust. Compatible, chemical-resistant gloves and safety goggles should also be worn. The user should wash thoroughly after handling and wash any contaminated clothing before reuse. Resin should be kept away from sources of ignition and strong oxidizers. User should avoid breathing vapors. Resin contact with skin, eyes, and clothing should be avoided. Prolonged or repeated exposure should also be avoided. Please consult the MSDS for more safety information.

For More Information:

CRG Industries is a manufacturer and supplier of various high-tech, high-performance materials and products:

- Syntactic Foams
- Shape Memory Patch Systems
- Shape Memory Resins
- Shape Memory Composites
- Shape Memory Mandrels for Custom Tooling
- Precision Injection-Molded Parts
- Precision Stamped Metal
- Non-contact Magnetic Transmissions

For quotes, orders and product information please call 866-341-2744 toll-free or email huelskampsr@crg-industries.com

Any suggestion or information contained in CRG Industries literature is based solely on limited data available to CRG Industries, LLC and our experience with the general properties of any specified product. Accordingly, no express or implied representation or warranty is made either as to the accuracy of any such suggestion or information or as to the results which may be obtained from, or the consequences of the use or application of, any product or of any such suggestion or information. In no event is any such suggestion or information to be considered or represented to be a recommendation or a final or preliminary engineering or other design. EXCEPT FOR SUCH EXPRESS WRITTEN WARRANTY, IF ANY, AS CRG INDUSTRIES LLC OR THE MANUFACTURER OR SUPPLIER MAY ISSUE TO THE PURCHASER, CRG INDUSTRIES LLC MAKES NO WARRANTY, EXPRESS OR IMPLIED, WITH RESPECT TO ANY PRODUCT, INCLUDING, BUT NOT BY WAY OF LIMITATION, THE MERCHANTABILITY OR FITNESS FOR ANY PARTICULAR PURPOSE OF SUCH PRODUCT. The purchaser assumes sole and full responsibility for being familiar with all characteristics of all products and for determining and satisfying itself as to the content of all products and the suitability of all products for the uses and applications contemplated by the purchaser and others, as well as for complying with all laws, regulations and standards applicable to the possession, handling, processing, and use of all products. The purchaser also assumes all risks and liabilities arising out of or in connection with the use of all products, and of the results obtained by the use of all products, whether used alone or in combination with other material, including, without limitation, all risks and liabilities with respect to patent and proprietary rights of third parties. Copyright © 2008 CRG Industries, LLC. All rights reserved. CRGIPDVTS0108